

CHEMIA

**STUDIA
UNIVERSITATIS BABEŞ-BOLYAI
CHEMIA**

4 / 2012

EDITORIAL BOARD
STUDIA UNIVERSITATIS BABEȘ-BOLYAI
CHEMIA

ONORARY EDITOR:

IONEL HAIDUC - Member of the Romanian Academy

EDITOR-IN-CHIEF:

LUMINIȚA SILAGHI-DUMITRESCU

EXECUTIVE EDITOR:

GABRIELA NEMEȘ

EDITORIAL BOARD:

PAUL ȘERBAN AGACHI, Babeș-Bolyai University, Cluj-Napoca, Romania

LIVAIN BREAU, UQAM University of Quebec, Montreal, Canada

HANS JOACHIM BREUNIG, Institute of Inorganic and Physical Chemistry,
University of Bremen, Bremen, Germany

JEAN ESCUDIE, HFA, Paul Sabatier University, Toulouse, France

ION GROSU, Babeș-Bolyai University, Cluj-Napoca, Romania

EVAMARIE HEY-HAWKINS, University of Leipzig, Leipzig, Germany

FLORIN DAN IRIMIE, Babeș-Bolyai University, Cluj-Napoca, Romania

FERENC KILAR, University of Pecs, Pecs, Hungary

BRUCE KING, University of Georgia, Athens, Georgia, USA

ANTONIO LAGUNA, Department of Inorganic Chemistry, ICMA, University of
Zaragoza, Zaragoza, Spain

JURGEN LIEBSCHER, Humboldt University, Berlin, Germany

KIERAN MOLLOY, University of Bath, Bath, UK

IONEL CĂTĂLIN POPESCU, Babeș-Bolyai University, Cluj-Napoca, Romania

CRISTIAN SILVESTRU, Babeș-Bolyai University, Cluj-Napoca, Romania

<http://chem.ubbcluj.ro/~studiachemia/>; studiachemia@chem.ubbcluj.ro

http://www.studia.ubbcluj.ro/serii/chemia/index_en.html

STUDIA UNIVERSITATIS BABEȘ-BOLYAI CHEMIA

4

Desktop Editing Office: 51ST B.P. Hasdeu, Cluj-Napoca, Romania, Phone + 40 264-40.53.52

CUPRINS – CONTENT – SOMMAIRE – INHALT

NABEEL E. ARIF, ROSLAN HASNI, Second Order and Second Sum Connectivity Indices of Tetrathiafulvalene Dendrimers.....	7
CORNELIA BOGĂȚAN (POP), MIRCEA NĂSUI, TRAIAN PETRIȘOR JR., MIHAI GABOR, TANIA RISTOIU, LELIA CIONTEA, TRAIAN PETRIȘOR, On the Way of Growing $YBa_2Cu_3O_{7-x}$ Superconducting Thin Films from a Fluorin-Free Water Based Propionate Precursor Solution.....	13
O. COZAR, C. COTA, N. CIOICA, E.M. NAGY, L. ȚIBRE, FT – IR Investigation of the Plasticizers Effects on the Native Corn Starch Macrostructure.....	23
DIJE DEHARI, FETAH PODVORICA, SHEFKET DEHARI, MUHAMET SHEHABI, Synthesis and Characterization of Co(II) Complexes with Tridentate (ONO) Schiff Bases	33
DRAGAN M. ĐORĐEVIĆ, MAJA N. STANKOVIĆ, MILOŠ G. ĐORĐEVIĆ, NENAD S. KRSTIĆ, MILA A. PAVLOVIĆ, ALEKSANDAR R. RADIVOJEVIĆ, IVAN M. FILIPOVIĆ, FTIR Spectroscopic Characterization of Bituminous Limestone: Maganik Mountain (Montenegro).....	39
MOHAMMAD REZA FARAHANI, MIRANDA PETRONELLA VLAD, On the Schultz, Modified Schultz and Hosoya Polynomials and Derived Indices of Capra-Designed Planar Bezenoids.....	55
MODJTABA GHORBANI, MOHAMMAD A. HOSSEINZADEH, MIRCEA V. DIUDEA, On Topological Polynomials of Weighted Graphs.....	65
ASMA HAMZEH, ALI IRANMANESH, SAMANEH HOSSEIN-ZADEH, MIRCEA V. DIUDEA, Generalized Degree Distance of Trees, Unicyclic and Bicyclic Graphs	73

ANIKÓ KILLYÉNI, MARIA E. YAKOVLEVA, CLEMENS K. PETERBAUER, DÓNAL LEECH, LO GORTON, IONEL CATALIN POPESCU, Effect of Enzyme Deglycosylation on the Amperometric Detection of Glucose at PDH-Modified Electrode	87
ISTVAN KOCSIS, NICULINA HĂDADE, ION GROSU, Synthesis and Structural Analysis of Some New Arylbromide Decorated Azobenzene Derivatives.....	101
TEODORA MARCU, OVIDIU NEMES, MILICA TODEA, DAN LEORDEAN, CATALIN POPA, Characterization of Hydroxyapatite Coatings on Different Pretreated Ti ₆ Al ₇ Nb Alloy Substrates	109
RALUCA MATIES, BEATA SZEFLER, IOANA IONUT, BRANDUSA TIPERCIUC, QSPR Study on the Chromatographic Behavior of a Set of Thiazole Derivatives by Auto-Correlation Analysis	121
HORIA MOCUTA, MARIETA MUREȘAN-POP, IRINA KACSÓ, GHEORGHE BORODI, SIMION SIMON, IOAN BRATU, Physical-Chemical and Structural Characterization of Ambazone and of Its Synthesis Secondary Product.....	135
CRISTINA MORAR, CARMEN SACALIS, PEDRO LAMEIRAS, IOAN BRATU, OANA MOLDOVAN, YVAN RAMONDENC, MIRCEA DARABANTU, Novel 1,3-Thiazolidines. Synthesis of 2-ARYL-4,4-BIS(Hydroxymethyl)-1,3-Thiazolidines by Direct Thioaminalisation	145
OANA PONTA, ENDRE JAKAB, IOAN BURDA, ARTHUR TUNYAGI, ANDREEA SILAGHI, SIMION SIMON, AFM Investigation of Morphological Changes to <i>Staphylococcus Aureus</i> Surface Induced by AgNO ₃ and Oxacillin Addition.....	157
MIHAELA POPA, AMALIA MESAROS, RALUCA A. MEREU, IOANA PERHAITA, LELIA CIONTEA, TRAIAN PETRISOR, Thermal Decomposition and Kinetics of the Precursors for Obtaining ZnO and Teah Modified ZnO Nanopowders	167
DEJAN PRVULOVIĆ, MILAN POPOVIĆ, DJORDJE MALENČIĆ, MIRJANA LJUBOJEVIĆ, GORAN BARAĆ, VLADISLAV OGNJANOV, Phenolic Content and Antioxidant Capacity of Sweet and Sour Cherries	175
MONICA PUSTIANU, ADINA BUCEVSCHI, POPA ALEXANDRU, ERZSEBET AIRINEI, Analysis and Interpretation of Colours Characteristics of the Dyed Samples, Based on Remission Curves	183
LORÁND ROMÁNSZKI, JUDIT TELEGDI, LAJOS NYIKOS, Ultrathin Organic Coatings on Copper, Copper Alloys and Stainless Steel for Controlling the Microbiologically Influenced Corrosion.....	191
EMILIA SABĂU, NICOLAE BÂLC, PAUL BERE, OVIDIU NEMEȘ, New Materials from Waste Glass Fibre	201
ANDRA TĂMAȘ, SORINA BORAN, Comparative Study of Turbulence Promoters on Pressure Loss in Heat Transfer	209
FARDAD KOOHYAR, HASAN GHASEMNEJAD-BOSRA, MEYSAM SHARIFIRAD, Investigation on Thermodynamic Properties for Binary Systems of Water + Formic, Acetic, Trichloroacetic, Lactic, and Citric Acid at $T = 292.15$ k and Atmospheric Pressure	217

Studia Universitatis Babes-Bolyai Chemia has been selected for coverage in Thomson Reuters products and custom information services. Beginning with V. 53 (1) 2008, this publication is indexed and abstracted in the following:

- Science Citation Index Expanded (also known as SciSearch®)
- Chemistry Citation Index®
- Journal Citation Reports/Science Edition

SECOND ORDER AND SECOND SUM CONNECTIVITY INDICES OF TETRATHIAFULVALENE DENDRIMERS

NABEEL E. ARIF^a, ROSLAN HASNI^b

ABSTRACT. The m -order connectivity index is an extension of the Randić (simple) connectivity index that counts the connectivity of all paths of length m in G . The m -sum connectivity index changes the multiplication with addition, in the above index. A dendrimer is a hyperbranched molecule built up from branched units called monomers. In this paper, the 2-order connectivity and 2-sum connectivity indices of an infinite family of tetrathiafulvalene dendrimer are computed.

Key words: *Randić connectivity index, Sum-connectivity index, Dendrimers.*

INTRODUCTION

A simple graph $G=(V,E)$ is a finite nonempty set $V(G)$ of objects called vertices together with a (possibly empty) set $E(G)$ of unordered pairs of distinct vertices of G called edges. In chemical graphs, the vertices of the graph correspond to the atoms of the molecule, and the edges represent the chemical bonds.

A single number which characterizes the graph of a molecule is called a graph theoretical invariant or topological index. Among the many topological indices considered in chemical graph theory, only a few have been found worthy in practical application, the connectivity index (Randić, 1975) being one of them [1]. This index has been used in predicting physico-chemical properties such as boiling point and solubility partition. The molecular connectivity index χ is related to the branching of molecules. Next, Kier and Hall (1986) extended this to higher orders and introduced modifications to account for heteroatoms [2].

Molecular connectivity indices are the most popular topological indices (Trinajstić, 1992), used in predicting physicochemical properties such as boiling point, solubility partition, coefficient etc, (Murray et al., 1975; Kier and Hall, 1976) or biological activities (Kier et al., 1975; Kier and Murray, 1975) [2].

^a School of Mathematical Sciences, Universiti Sains Malaysia 11800 USM, Penang, Malaysia

^b Department of Mathematics, Faculty of Science and Technology Universiti Malaysia Terengganu 21030, Kuala Terengganu, Terengganu, Malaysia

Let G be a simple connected graph of order n . For an integer $m \geq 1$, the m -order connectivity index of the graph G associated to a covalently bonded molecule is defined as

$${}^m \chi(G) = \sum_{i_1 \dots i_{m+1}} \frac{1}{\sqrt{d_{i_1} \dots d_{i_{m+1}}}},$$

where $i_1 \dots i_{m+1}$ runs over all paths of length m in G and d_i denotes the degree of vertex v_i . In particular, the 2-order connectivity index is defined as follows:

$${}^2 \chi(G) = \sum_{i_1 i_2 i_3} \frac{1}{\sqrt{d_{i_1} d_{i_2} d_{i_3}}}.$$

Recently, a variant of the Randić connectivity index, called the sum-connectivity index was introduced by Zhou and Trinajstić [3,4]. For a simple connected graph G , its sum-connectivity index $X(G)$ is defined as the sum over all edges of the graph of the terms $(d_u + d_v)^{-1/2}$, that is

$${}^s X(G) = \sum_{u,v} \frac{1}{\sqrt{d_u + d_v}},$$

where d_u and d_v are the degrees of the vertices u and v , respectively. It has been found that the sum-connectivity index correlates well with π -electronic energy of benzenoid hydrocarbons, and it is frequently applied in quantitative structure property QSPR and structure-activity QSAR studies [2,5].

The m -sum connectivity index of G is defined as

$${}^{ms} X(G) = \sum_{i_1 \dots i_{m+1}} \frac{1}{\sqrt{d_{i_1} + d_{i_2} + \dots + d_{i_{m+1}}}},$$

where $i_1 i_2 \dots i_{m+1}$ runs over all paths of length m in G . In particular, the 2-sum connectivity index is defined as

$${}^{2s} X(G) = \sum_{i_1 i_2 i_3} \frac{1}{\sqrt{d_{i_1} + d_{i_2} + d_{i_3}}}.$$

Dendrimers are hyper-branched macromolecules, with a rigorously tailored architecture. They can be synthesized, in a controlled manner, either by a divergent or a convergent procedure. Dendrimers have gained a wide range of applications in supra-molecular chemistry, particularly in host guest reactions and self-assembly processes. Their applications in chemistry, biology and nano-science are unlimited. Recently, some researchers investigated the m -order connectivity index and m -sum connectivity index in some dendrimer nanostars, where $m = 2$ and 3 (see [6,7,8,9,10]).

In this paper, we shall study the 2-connectivity and 2-sum connectivity indices of an infinite family of tetrathiafulvalene dendrimers.

RESULTS AND DISCUSSIONS

In this section, we first study the 2-order connectivity index of some infinite family of dendrimers. We consider the tetrathiafulvalene dendrimer of generation G_n (i.e. grown in n stages). We denote this graph by $TD_2[n]$. Figure 1 shows the generation G_2 dendrimer.

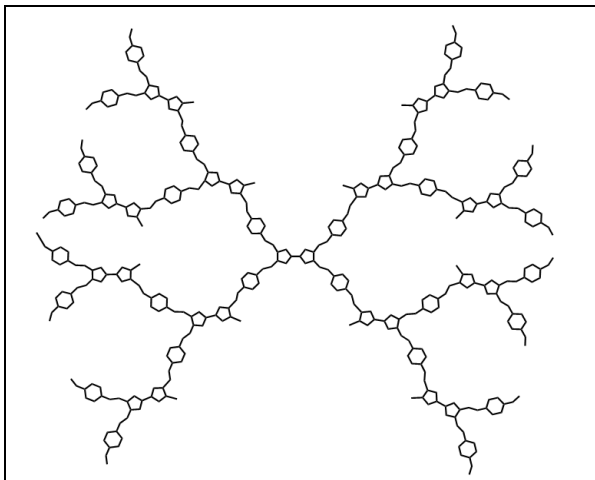


Figure 1. Tetrathiafulvalene dendrimer of generation G_n ; $n=2$, symbolized $TD_2[2]$

We can now give our main results.

Theorem 1. Let $n \in \mathbb{N}_0$. The second-order connectivity index of $TD_2[n]$ is computed as follows

$${}^2\chi(TD_2[n]) = \begin{cases} \frac{1}{3}(8\sqrt{2}+27\sqrt{3}+2\sqrt{6}), & \text{if } n = 0; \\ \frac{1}{3}(8\sqrt{2}+27\sqrt{3}+2\sqrt{6}) + \frac{1}{3}(15\sqrt{2}+31\sqrt{3}+2\sqrt{6}+2)(2^{n+1}-2), & \text{if } n \geq 1. \end{cases}$$

Proof. The core of the structure means the stage zero. Firstly, we compute ${}^2\chi(TD_2[0])$. Let $d_{i_1 i_2 i_3}$ denote the number of 2-paths whose three consecutive vertices are of degree i_1, i_2, i_3 , respectively. In the same way, we use $d_{i_1 i_2 i_3}^{(n)}$ to mean $d_{i_1 i_2 i_3}$ in n -th stages. Particularly, $d_{i_1 i_2 i_3}^{(n)} = d_{i_3 i_2 i_1}^{(n)}$. It is easy to see that

$$d_{123}^{(0)} = 4, \quad d_{223}^{(0)} = 24, \quad d_{232}^{(0)} = 30, \quad d_{233}^{(0)} = 12, \quad d_{323}^{(0)} = 4.$$

Therefore, we have

$$\begin{aligned} {}^2\chi(TD_2[0]) &= \frac{4}{\sqrt{1 \times 2 \times 3}} + \frac{24}{\sqrt{2 \times 2 \times 3}} + \frac{30}{\sqrt{2 \times 3 \times 2}} + \frac{12}{\sqrt{2 \times 3 \times 3}} + \frac{4}{\sqrt{3 \times 2 \times 3}} \\ &= \frac{1}{3}(8\sqrt{2} + 27\sqrt{3} + 2\sqrt{6}). \end{aligned}$$

Secondly, we construct the relation between ${}^2\chi(TD_2[n])$ and ${}^2\chi(TD_2[n-1])$ for $n \geq 1$.

By simple reduction, we have

$$\begin{aligned} d_{123}^{(n)} &= d_{123}^{(n-1)} + 2 \times 2^n, \quad d_{132}^{(n)} = d_{132}^{(n-1)} + 2 \times 2^n, \quad d_{133}^{(n)} = d_{133}^{(n-1)} + 2 \times 2^n, \\ d_{223}^{(n)} &= d_{223}^{(n-1)} + 28 \times 2^n, \end{aligned}$$

$$d_{232}^{(n)} = d_{232}^{(n-1)} + 34 \times 2^n, \quad d_{233}^{(n)} = d_{233}^{(n-1)} + 22 \times 2^n, \quad d_{323}^{(n)} = d_{323}^{(n-1)} + 8 \times 2^n,$$

and for any $(i_1 i_2 i_3) \neq (123), (132), (133), (223), (232), (233), (323)$, we have $d_{i_1 i_2 i_3}^{(n)} = 0$.

Therefore,

$$\begin{aligned} {}^2\chi(TD_2[n]) &= {}^2\chi(TD_2[n-1]) + \frac{2 \times 2^n}{\sqrt{1 \times 2 \times 3}} + \frac{2 \times 2^n}{\sqrt{1 \times 3 \times 2}} + \frac{2 \times 2^n}{\sqrt{1 \times 3 \times 3}} + \frac{28 \times 2^n}{\sqrt{2 \times 2 \times 3}} \\ &\quad + \frac{34 \times 2^n}{\sqrt{2 \times 3 \times 2}} + \frac{22 \times 2^n}{\sqrt{2 \times 3 \times 3}} + \frac{8 \times 2^n}{\sqrt{3 \times 2 \times 3}} \\ &= {}^2\chi(TD_2[n-1]) + \frac{1}{3}(15\sqrt{2} + 31\sqrt{3} + 2\sqrt{6} + 2) \times 2^n. \end{aligned}$$

From the above recursion formula, we have

$$\begin{aligned} {}^2\chi(TD_2[n]) &= {}^2\chi(TD_2[n-1]) + \frac{1}{3}(15\sqrt{2} + 31\sqrt{3} + 2\sqrt{6} + 2) \times 2^n \\ &= {}^2\chi(TD_2[n-2]) + \frac{1}{3}(15\sqrt{2} + 31\sqrt{3} + 2\sqrt{6} + 2)(2^n + 2^{n-1}) \\ &\quad \vdots \\ &= {}^2\chi(TD_2[0]) + \frac{1}{3}(15\sqrt{2} + 31\sqrt{3} + 2\sqrt{6} + 2)(2^n + 2^{n-1} + \dots + 2^2 + 2). \end{aligned}$$

Thus,

$${}^2\chi(TD_2[n]) = \frac{1}{3}(8\sqrt{2} + 27\sqrt{3} + 2\sqrt{6}) + \frac{1}{3}(15\sqrt{2} + 31\sqrt{3} + 2\sqrt{6} + 2)(2^{n+1} - 2).$$

The proof is now complete.

Now, we shall study the 2-sum connectivity index of the same family of dendrimer as shown in Figure 1.

Theorem 2. Let $n \in \mathbb{N}_0$. The second-sum connectivity index of $TD_2[n]$ is

$${}^{2s}\chi(TD_2[n]) = \begin{cases} \frac{1}{21}(14\sqrt{6}+162\sqrt{7}+42\sqrt{8}), & \text{if } n = 0; \\ \frac{1}{21}(14\sqrt{6}+162\sqrt{7}+42\sqrt{8}) + \frac{1}{84}(56\sqrt{6}+768\sqrt{7}+315\sqrt{8})(2^{n+1}-2), & \text{if } n \geq 1. \end{cases}$$

Proof. We first compute ${}^{2s}\chi(TD_2[0])$. Let $d_{i_1 i_2 i_3}$ denote the number of 2-paths whose three consecutive vertices are of degree i_1, i_2, i_3 , respectively. Similarly we use $d_{i_1 i_2 i_3}^{(n)}$ to mean $d_{i_1 i_2 i_3}$ in n -th stages. Particularly, $d_{i_1 i_2 i_3}^{(n)} = d_{i_3 i_2 i_1}^{(n)}$.

It is easy to see that

$$d_{123}^{(0)} = 4, d_{223}^{(0)} = 24, d_{232}^{(0)} = 30, d_{233}^{(0)} = 12, d_{323}^{(0)} = 4.$$

Therefore, we have

$$\begin{aligned} {}^{2s}\chi(TD_2[0]) &= \frac{4}{\sqrt{1+2+3}} + \frac{24}{\sqrt{2+2+3}} + \frac{30}{\sqrt{2+3+2}} + \frac{12}{\sqrt{2+3+3}} + \frac{4}{\sqrt{3+2+3}} \\ &= \frac{1}{21}(14\sqrt{6} + 162\sqrt{7} + 42\sqrt{8}). \end{aligned}$$

By using the same way in Theorem 1, we can find the relation between ${}^{2s}X(TD_2[n])$ and ${}^{2s}X(TD_2[n-1])$ for $n \geq 1$.

We have

$$\begin{aligned} d_{123}^{(n)} &= d_{123}^{(n-1)} + 2 \times 2^n, d_{132}^{(n)} = d_{132}^{(n-1)} + 2 \times 2^n, d_{133}^{(n)} = d_{133}^{(n-1)} + 2 \times 2^n, \\ d_{223}^{(n)} &= d_{223}^{(n-1)} + 28 \times 2^n, \\ d_{232}^{(n)} &= d_{232}^{(n-1)} + 34 \times 2^n, d_{233}^{(n)} = d_{233}^{(n-1)} + 22 \times 2^n, d_{323}^{(n)} = d_{323}^{(n-1)} + 8 \times 2^n, \text{ and for any} \\ &(i_1 i_2 i_3) \neq (123), (132), (133), (223), (232), (233), (323), \text{ we have } d_{i_1 i_2 i_3}^{(n)} = 0. \end{aligned}$$

Therefore,

$$\begin{aligned} {}^{2s}\chi(TD_2[n]) &= {}^{2s}\chi(TD_2[n-1]) + \frac{2 \times 2^n}{\sqrt{1+2+3}} + \frac{2 \times 2^n}{\sqrt{1+3+2}} + \frac{2 \times 2^n}{\sqrt{1+3+3}} + \frac{28 \times 2^n}{\sqrt{2+2+3}} \\ &\quad + \frac{34 \times 2^n}{\sqrt{2+3+2}} + \frac{22 \times 2^n}{\sqrt{2+3+3}} + \frac{8 \times 2^n}{\sqrt{3+2+3}} \\ &= {}^{2s}\chi(TD_2[n-1]) + \frac{1}{84}(56\sqrt{6} + 768\sqrt{7} + 315\sqrt{8}) \times 2^n. \end{aligned}$$

From the above recursion formula, we have

$${}^{2s}\chi(TD_2[n]) = {}^{2s}\chi(TD_2[n-1]) + \frac{1}{84}(56\sqrt{6} + 768\sqrt{7} + 315\sqrt{8}) \times 2^n$$

$$\begin{aligned}
 &= {}^{2s}\chi(TD_2[n-2]) + \frac{1}{84}(56\sqrt{6} + 768\sqrt{7} + 315\sqrt{8})(2^n + 2^{n-1}) \\
 &\quad \vdots \\
 &= {}^{2s}\chi(TD_2[0]) + \frac{1}{84}(56\sqrt{6} + 768\sqrt{7} + 315\sqrt{8})(2^n + 2^{n-1} + \dots + 2^2 + 2).
 \end{aligned}$$

Hence,

$${}^{2s}\chi(TD_2[n]) = \frac{1}{21}(14\sqrt{6} + 162\sqrt{7} + 42\sqrt{8}) + \frac{1}{84}(56\sqrt{6} + 768\sqrt{7} + 315\sqrt{8})(2^{n+1} - 2).$$

The proof is now complete.

CONCLUSION

In this paper, we have discussed the 2-order- and 2-sum connectivity indices of tetrathiafulvalene dendrimers. We believe the technique used in this paper can be extended to study the connectivity indices of some other families of dendrimers as well. In our next papers, we will determine the m -order and m -sum connectivity indices of tetrathiafulvalene dendrimers, where $m = 3$ and 4.

REFERENCES

1. M. Randic, *J. Am. Chem. Soc.*, **1975**, *97*, 6609.
2. L.B. Kier and L.H. Hall, *Molecular connectivity in structure activity analysis*, John Wiley, London, **1986**.
3. B. Zhou, N. Trinajstic, *J. Math. Chem.*, **2010**, *47*, 210.
4. B. Zhou, N. Trinajstic, *J. Math. Chem.*, **2009**, *46*, 1252.
5. R. Todeschini and V. Consonni. *Handbook of Molecular Descriptors*. Wiley-V CH, Weinheim, **2000**.
6. A.R. Ashrafi, P. Nikzad, *Digest J. Nanomater. Biostruct.*, **2009**, *4(2)*, 269.
7. M.B. Ahmadi, M. Sadeghimehr, *Digest J. Nanomater. Biostruct.*, **2009**, *4(4)*, 639.
8. S. Chen, J. Yang, *Internatl. Math. Forum*, **2011**, *6(5)*, 223.
9. A. Madanshekaf, M. Ghaneei, *Digest J. Nanomater. Biostruct.*, **2011**, *6(2)*, 433.
10. J. Yang, F. Xia, S. Chen, *Int. J. Contemp. Math. Sci.*, **2011**, *6(5)*, 215.

ON THE WAY OF GROWING $\text{YBa}_2\text{Cu}_3\text{O}_{7-x}$ SUPERCONDUCTING THIN FILMS FROM A FLUORIN-FREE WATER BASED PROPIONATE PRECURSOR SOLUTION

CORNELIA BOGĂȚAN (POP)^a, MIRCEA NĂSUI^a, TRAIAN PETRIȘOR JR.^a,
MIHAI GABOR^a, TANIA RISTOIU^a, LELIA CIONTEA^a,
TRAIAN PETRIȘOR^a

ABSTRACT. $\text{YBa}_2\text{Cu}_3\text{O}_{7-x}$ thin films were successfully deposited from a water-based propionate precursor solution. In order to determine the thermal decomposition behaviour of the deposited precursor solution during the pyrolysis, the precursor powder, as- obtained by drying the precursor solution, was submitted to thermal analysis (DTA – TG). The precursor films were deposited on (100) SrTiO_3 single crystalline substrates by spin-coating and subjected to a single – step thermal treatment comprising both pyrolysis and crystallization. The as-obtained $\text{YBa}_2\text{Cu}_3\text{O}_{7-x}$ films were structurally and morphologically investigated by X-ray diffraction and atomic force microscopy, respectively. The electrical characterization of the films was made by the four point method.

Keywords: *YBCO thin films, superconductivity, spin coating deposition, thermal analysis, film characterization*

INTRODUCTION

$\text{YBa}_2\text{Cu}_3\text{O}_{7-x}$ (YBCO) films have gained considerable interest due to their intrinsic properties. Because of these properties the YBCO superconducting films are very promising for power applications. These films can be obtained by both physical, and chemical methods [1,2]. The chemical solution deposition (CSD) is a low cost, high rate and a non-vacuum method which complies with the industrial demands [3].

The most common CSD method used in order to obtain superconducting YBCO films is the metal-organic decomposition of trifluoroacetates (TFA-MOD) [4]. By this method epitaxial YBCO films with very good superconducting properties ($J_c \approx 10 \text{ MA/cm}^2$) were obtained [5]. However, this method has a major drawback: during the thermal decomposition of the precursor solution, highly toxic and corrosive acid is released, namely the hydrofluoric acid (HF).

^a *Technical University of Cluj-Napoca, Materials and Environmental Faculty, 28 Memorandumului Street, RO-400114, Cluj-Napoca, Romania, corneliapop@yahoo.com*

To overcome this disadvantage, several research groups have begun to investigate fluorine-free precursor solutions using different combinations of starting reagents and solvents.

Thus, several groups have succeeded to obtain superconducting YBCO films with good superconducting properties using the corresponding metal acetylacetonates and both pyridine, and propionic acid as solvents [6]. In order to obtain epitaxial YBCO films they have used a low-cost vacuum technique during the thermal treatment.

Another research group have used Y, Ba, Cu trimethylacetates and a combination of propionic acid and amines as solvents [7]. Good results have also been reported when using metal acetates dissolved in a mixture of water and acetic acid [8].

The aim of this work was to find a new, simpler and more ecologic precursor solution (in our case a water based precursor solution) from which YBCO superconducting films can be obtained.

RESULTS AND DISCUSSION

Precursor Powder Characterization

The precursor powder has been obtained by drying the final precursor solution in air at 60°C on a hot plate (the preparation of the final precursor solution is detailed in the **Experimental section**).

The thermal decomposition behavior of the precursor powder gives us important clues regarding the thermal treatment used for obtaining YBCO films. In order to find out the optimal conditions for the thermal treatment, the precursor powder was subjected to thermal analyses. The analyses were performed in dry and humid oxygen, from room temperature up to 500°C, at different heating rates. These different heating rates are needed for the highly exothermic reactions that take place during the decomposition of the propionate complex. The DTA – TG curves of the precursor powder are presented in figure 1.

As it can be seen, the thermal decomposition of the precursor solution ends around 400°C both in dry, and humid oxygen atmosphere. According to figure 1 the thermal decomposition of the precursor powder takes place as follows:

- In the first stage, in the temperature range 20°C – 200°C, the precursor powder goes through a dehydration process indicated on the DTA curves by an endothermic peak at 197°C. In this stage the thermogravimetric curves show a weight loss of 4%, both in humid and in dry oxygen atmosphere.

- In the temperature range $200^\circ\text{C} - 260^\circ\text{C}$, the second stage of the thermal decomposition performed in dry oxygen, begins the decomposition of the organic part of the precursor powder. This is indicated by a weight loss of 23% on the TG curve and by two exothermic peaks on the DTA curve at 238°C and 252°C , respectively.
- The third stage of the decomposition process for the precursor powder treated in dry oxygen atmosphere is in the temperature range $260^\circ\text{C} - 300^\circ\text{C}$. In this stage it can be easily observed that the TG curve registers a slight weight increase that reveals the oxidation of Cu(I) to Cu(II) [9].
- For the precursor powder thermally treated in humid oxygen atmosphere the second stage of the decomposition process takes place in the temperature range $200^\circ\text{C} - 300^\circ\text{C}$. During this stage the beginning of the organic part decomposition is indicated by a weight loss of 25 % on the TG curve and by the presence of two exothermic peaks on the DTA curve at 235°C and 270°C .
- The last stage of the thermal decomposition of the precursor powder thermally treated both in dry and humid oxygen atmosphere is in the temperature range $300^\circ\text{C} - 400^\circ\text{C}$. The DTA curve registered in dry oxygen atmosphere presents three exothermic peaks at 366°C , 384°C and at 398°C showing the finalization of the organic part decomposition. The corresponding thermogravimetric curve reveals a weight loss of 19%. In humid oxygen the DTA curve presents only two exothermic peaks: a small peak at 321°C and a very sharp peak at 398°C , indicating that the decomposition reactions are partially overlapped. The corresponding TG curve registers a weight loss of 21%.

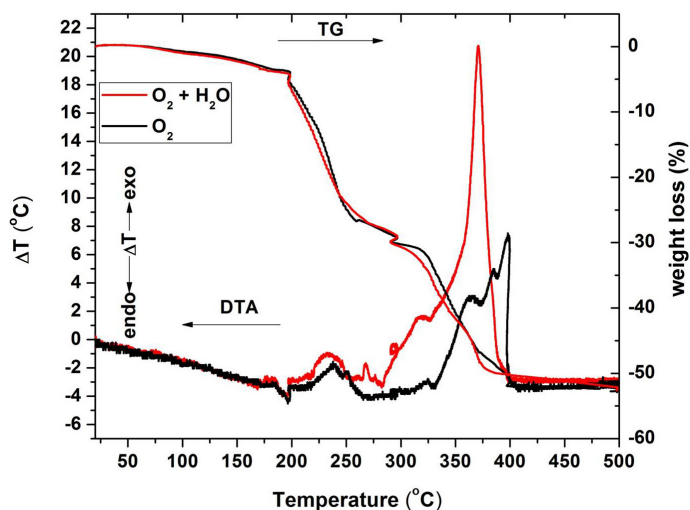


Figure 1. DTA – TG analyses performed under dry and humid oxygen atmosphere

Above of 400°C the TG – DTA curves are stable, indicating that the thermal decomposition of the sample is complete.

In order to identify the crystalline phases that are present in the powder sample during the thermal decomposition process the precursor powders thermally treated at different temperatures (300°C, 400°C and 500°C) were subjected to X-ray diffraction. The X-ray patterns are presented in figure 2.

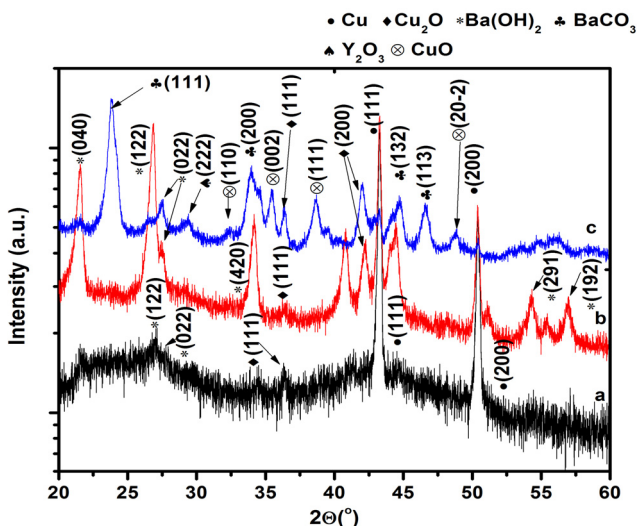


Figure 2. X-ray diffraction patterns of the precursor powders thermally treated at: (a) 300°C, (b) 400°C and (c) 500°C

As it can be observed at the temperature of 300°C in the precursor powder are present the following crystalline phases: metallic Cu – (111)Cu and (200)Cu, Cu₂O – (111)Cu₂O, and Ba(OH)₂ – (122)Ba(OH)₂ and (022)Ba(OH)₂. As it can be seen at 400°C the intensity of the peaks corresponding to metallic Cu phase decreases, while the intensity and the numbers of the peaks corresponding to Cu₂O phase are increasing. This indicates the oxidation of a large amount of metallic Cu to Cu₂O. It can also be observed that the peaks corresponding to Ba(OH)₂ are more intense, indicating a more advanced crystallization of barium hydroxide. At 500°C along with the Cu₂O phase, the CuO phase is present proving the Cu(I) to Cu(II) oxidation supposition. Also at 500°C the X-ray diffraction pattern exhibits peaks corresponding to Y₂O₃ phase. At this temperature Ba(OH)₂ reacts with the atmospheric CO₂ and peaks corresponding to BaCO₃ can be observed in the X-ray diffraction patterns.

The crystalline phases present in the precursor powder (and also in the film) after the pyrolysis are: Y₂O₃, CuO și BaCO₃.

YBCO thin films characterization

The quality of a pyrolysed film is first indicated by its surface. The surface of the YBCO films after pyrolysis has to be smooth, without cracks or defects. According to the thermal analyses, the precursor powder decomposition is completed after 400°C . Thus, the pyrolysis temperature was selected in the temperature range $400^\circ\text{C} - 500^\circ\text{C}$. The best results were obtained for the pyrolysis performed at 500°C in humid oxygen atmosphere. The pyrolysed YBCO film surface was investigated by optic microscopy. In figure 3 is presented the microphotography of the YBCO film surface pyrolysed at 500°C in humid oxygen atmosphere. As it can be seen, the pyrolysed film surface is crack-free, smooth and presents only a “comet – type” spinning defect.

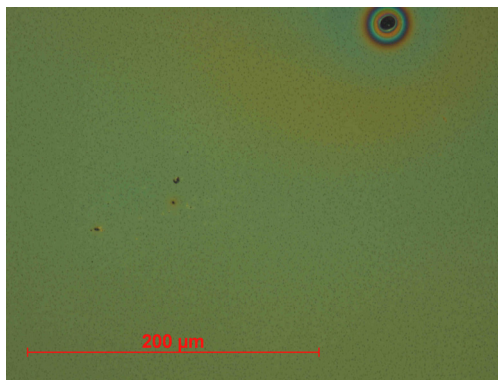


Figure 3. Microscopic image of the YBCO film pyrolysed at 500°C in humid oxygen atmosphere

The final YBCO films were structurally, morphologically and electrically investigated by X-ray diffraction, atomic force microscopy and by the four points method, respectively.

The structural investigation (presented in figure 4) indicates that the film has a high degree of (00l) orientation. The X-ray pattern of the crystallized YBCO film reveals only the presence of (00l)YBCO peaks and the peaks corresponding to the SrTiO_3 (STO) single crystalline substrate. No other orientations of YBCO or other phases are detected. The peaks intensities reveal a good crystallization of the YBCO phase.

The three-dimensional characteristics of the particles were assessed by atomic force microscopy, AFM (figure 5). These investigations reveal a continuous surface with a small degree of porosity. Furthermore, the grains with the a/b-axis oriented perpendicular to the substrate are observed on the surface. These grains are not detected by the X-ray diffraction due to

the detection limit of the X-ray diffractometer (about 5%). From the AFM investigations the root-mean-square (rms) roughness and the peak-to-valley distance were calculated. It was found that rms roughness has the value of 36.5 nm and the peak-to-valley distance has the value of 472.8 nm, indicating a strong crystallization of the particles located on the film surface.

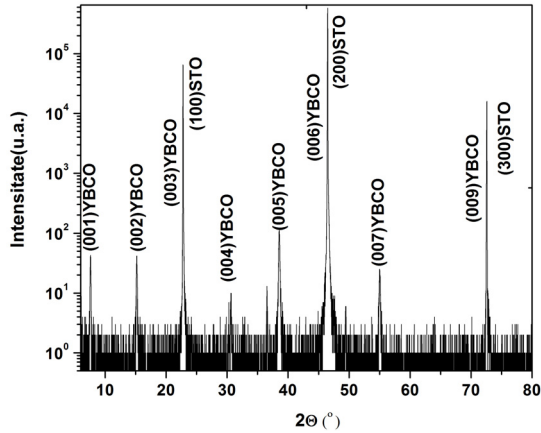


Figure 4. X-ray pattern for the YBCO film

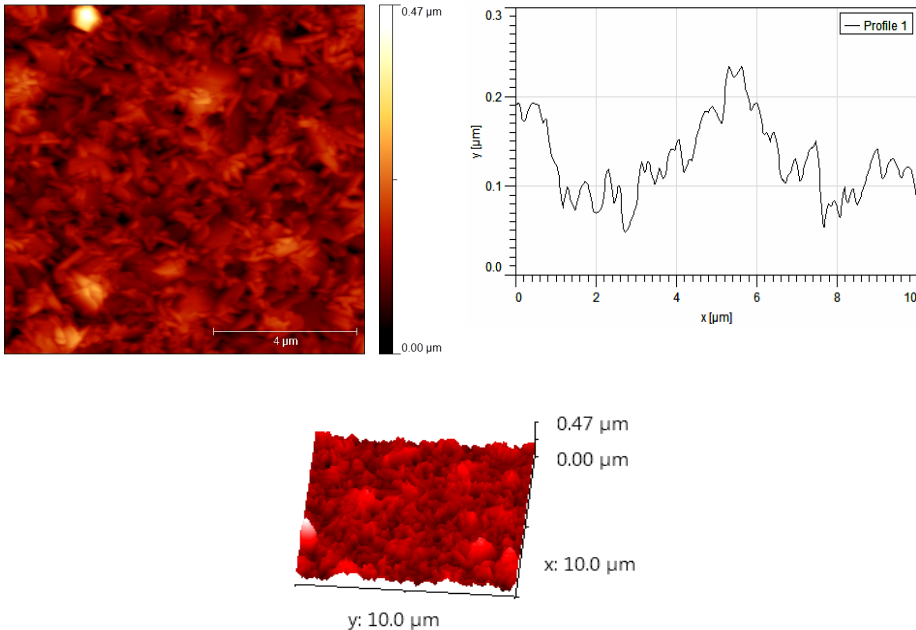


Figure 5. Two dimensional, 3D AFM images and the profile of an analysed line for the YBCO films

The electrical characterization of the YBCO films was performed using the four points method. In figure 5 is presented the temperature dependence of the electrical resistance of the YBCO thin film. The transport measurements show a transition temperature to the superconductive state of the YBCO thin film of 88.7K, with a $\Delta T_C \sim 3\text{K}$.

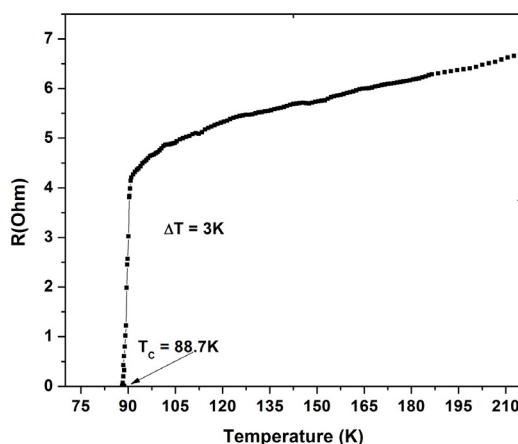


Figure 6. Temperature dependence of the electrical resistance of the YBCO film

CONCLUSIONS

A fluorine-free water-based solution was prepared starting from metal acetates dissolved in water and propionic acid. In order to optimize the low temperature thermal treatment, the precursor powder was subjected to thermal analyses. It was found that above 400°C the organic part of the precursor powder is completely decomposed to oxides. The precursor solution was deposited by spin coating on (100)STO single crystalline substrates and subjected to a single-step thermal treatment. The as-obtained YBCO films were structurally, morphologically and electrically characterized. The structural investigations show that the films are highly (00l) oriented. No other phases or other orientations were detected. The AFM measurements reveal a rms roughness of 36.5 nm and a peak-to-valley distance of 472.8 nm. The AFM images present characteristic cross-needles which represent unwanted a-axis crystallites growth. The needles grow parallel to the edge of the substrate.

The critical temperature is 88.7K with a $\Delta T \sim 3\text{K}$, indicating that the YBCO films have good superconducting properties.

All the investigations have proved that it is possible to obtain YBCO films with good superconducting properties from a fluorine-free water based solutions in a single step thermal treatment.

EXPERIMENTAL SECTION

1. Precursor solution and precursor powder synthesis

The precursor solution was prepared starting from yttrium acetate – $Y(CH_3COO)_3 \cdot 4H_2O$ (Alfa Aesar), barium acetate – $Ba(CH_2COO)_2 \cdot H_2O$ (Alfa Aesar) and copper acetate – $Cu(CH_3COO)_2 \cdot H_2O$ (Alfa Aesar). These acetates were individually dissolved in deionized water and an excess of propionic acid. Ammonium hydroxide was added to the Ba and Cu solutions until they become clear. The as-obtained solutions were mixed in an ultrasound bath for about 10 minutes and then concentrated by vacuum distillation under severe conditions. The stoichiometric ratio of the metal ions in the final precursor solution is Y:Ba:Cu = 1:2:3. The concentration of the metal ions in the final precursor solution is 1.5M.

2. Precursor powder characterization

In order to obtain the precursor powder, the as-prepared precursor solution was dried on a hot plate at 60°C in air. The as-obtained precursor powder was subjected to thermal analyses (DTA – TG) using a Q – derivatograph. The thermal analyses were performed both in dry, and humid oxygen atmosphere from room temperature up to 500°C with the following heating rates: from room temperature to 200°C with 5°C/min, from 200°C to 300°C with 3°C/min and from 300°C to 500°C the samples are heated with 2°C/min, to simulate the pyrolysis thermal treatment of the YBCO thin films.

3. Film deposition, thermal treatment and characterization

The precursor solution was spin coated on $SrTiO_3$ (STO) single crystalline substrates with a spinning rate of 6000 rpm for about 120 seconds. The as-deposited precursor film was subjected to a single-step thermal treatment, as shown in figure 6. The thermal treatment takes place in a tube furnace under controlled atmosphere.

The single-step thermally treated YBCO thin films are structurally, morphologically and electrically characterized. The structural investigations were made by X-ray diffraction using an X Brucker AXS Discover 8 diffractometer ($Cu K\alpha = 0.1541 \text{ nm}$). The X-ray diffractometer has a detection limit of 5% (in order for a crystalline phase to be detected it has to be in amount of more than 5%).

Atomic force microscopy was used to characterize the films morphology. The morphological investigations were made using a Veeco Dimension 3100 atomic force microscope. The electrical properties of the YBCO films were determined by Rvs.T measurements by using the four-probe technique.

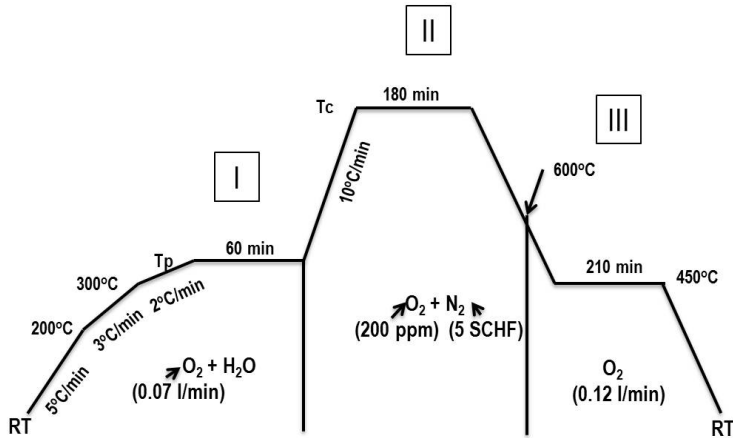


Figure 7. The thermal treatment diagram for YBCO films
 I – pyrolysis ($T_p = 500^\circ\text{C}$); II – crystallization ($T_c = 850^\circ\text{C}$); III - oxygention

ACKNOWLEDGMENTS

This paper was supported by the project “Doctoral studies in engineering sciences for developing the knowledge based society-SIDOC” contract no. POSDRU/88/1.5/S/60078, project co-funded from European Social Fund through Sectorial Operational Program Human Resources 2007-2013 and partially by CNCISIS – UEFISCU, project number PN II – IDEI cod 106/2010.

REFERENCES

1. L. Ciontea, T. Petrișor, A. Giurgiu, *Applied Superconductivity, World Congress on Superconductivity Proceedings of the 3rd International Conference and Exhibition, 1993*, 1, 853 – 857.
2. A. Armenio, A. Augieri, L. Ciontea, G. Contini, I. Davoli, V. Galluzzi, A. Mancini, A. Rufoloni, T. Petrișor, A. Vannozzi, G. Celentano, *Superconductor Science and Technology*, **2008**, 21, 7.
3. W. Cui, J.L. Tanner, T.W. Button, J.S. Abell, *Journal of Physics: Conference Series*, **2008**, doi: 10.1088/1742-6596/97/1/012257.
4. X. Obradors, T. Puig, A. Pomar, F. Sandiumenge, N. Mestres, M. Coll, A. Cavallaro, N. Romà, J. Gazquez, O. Castaño, J. Gutierrez, A. Palau, K. Zalamova, S. Morlens, A. Hasini, M. Gibert, S. Ricart, J.M. Moretó, S. Piñol, D. Isfort, J. Bock, *Superconductor Science and Technology*, **2006**, 19, S13 – S26.

5. T. Araki, I. Hirabayashi, *Superconductor Science and Technology*, **2003**, *16*, R71 – R97.
6. I. Yamaguchi, M. Sohma, K. Tsukada, W. Kondo, K. Kamiya, S. Mizuta, T. Kumagai, *IEEE Transactions on Applied Superconductivity*, **2005**, *15*, 2927 – 2930.
7. Y. Zhang, X. Yao, J. Lian, L. Wang, A. Li, H. K. Liu, H. Yao, Z. Han, L. Li, Y. Xu, D. Shi, *Physica C*, **2006**, *436*, 62 – 67.
8. P. Vermeir, I. Cardinael, M. Backer, J. Schanbroeck, E. Schacht, S. Hoste, I. Van Driessche, *Superconductor Science and Technology*, **2009**, *22*, 075009.
9. M. Nasui, R.B. Mos, T. Petrisor Jr., M.S. Gabor, R.A. Varga, L. Ciontea, T. Petrisor, *Journal of Analytical and Applied Pyrolysis*, **2011**, doi:10.1016/j.jaap. 2011.08.005

FT – IR INVESTIGATION OF THE PLASTICIZERS EFFECTS ON THE NATIVE CORN STARCH MACROSTRUCTURE

O. COZAR^{a,b,c}, C. COTA^b, N.CIOICA^b, E.M. NAGY^b, L. ŢIBRE^a

ABSTRACT. The influence of the water and glycerol in various contents and ratios on the native corn starch is investigated by FT-IR spectroscopy. The changes in intensity of the bands from 1000 cm⁻¹ region characteristics of amylose and amylopectin are correlated with the amorphous – crystalline forms of the studied starch samples. The increase of water and glycerol content until 10 – 12% leads to the prevalence of the amorphous phase.

Keywords: starch, water, glycerol, FT-IR

INTRODUCTION

Starch is a biopolymer with a very complex structure, formed by glycosidic linkages between glucose units, and presenting functional properties which make the polymer very helpful for the paper industry, the textile industry, and mainly the food industry. The ratio between amylose and amylopectin is fundamental in determining the functional properties of the starch [1,2].

Amylose is a molecule which is essentially linear, formed by D-glucose residues linked by $\alpha(1-4)$ bonds in a helicoidal structure; inside the helix it contains hydrogen atoms, which characterizes amylose as a hydrophobic species. This hydrophobic characteristic is very important in the biological medium, and allows the complexation with free fatty acids, and also with alcohols or iodine. On the other hand, amylopectin is a highly branched polymer formed by D-glucose units linked in an $\alpha(1-4)$ fashion, and containing only 5–6% $\alpha(1-6)$ bonds in the structure [1-3].

Many physical-chemical characteristics and properties of starch as viscosity, gelation power, adhesion etc., are strongly influenced by the amylose to amylopectin ratio [4].

^a Babes-Bolyai University, Faculty of Physics, RO-400084 Cluj-Napoca, Romania

^b National Institute of Research - Development for Machines and Installations designed to Agriculture and Food Industry-INMA Bucuresti – Cluj-Napoca branch, RO-400458 Cluj-Napoca, Romania

^c Academy of Romanian Scientists, 54 Splaiul Independentei, RO-050094, Bucharest, Romania

The vibrational spectroscopic techniques, such as IR spectroscopy and Raman spectroscopy are successfully used in the quantitative investigation of control analysis of starch for the food industry, characterization of some medical polysaccharides and quantitative investigation of amylose and amylopectin content in different starch samples [5-12].

Fechner et al. [5] have investigated the retrogradation of untreated wild-type starches (potato, corn and wheat) by employing Raman spectroscopy. The studies of potato starch retrogradation were also made by FT-IR spectroscopy [6]. Zhbakov et al. [7] characterized some medical polysaccharides, including amylose and amylopectin, by FT-IR and FT-Raman spectroscopy, whereas Schuster et al. [8] presented a novel approach to monitor starch hydrolysis by FT-Raman spectroscopy.

Flores-Morales et al. [9] determined the structural changes on retrograded starch of maize tortillas by FT-IR, Raman and CP/MAS ¹³C NMR spectroscopy.

Iizuka and Aishima [10] directly observed some changes related to the gelation process of starch by using FT-IR / ATR spectroscopy.

Kizil et al. [11] applied FT-IR and FT-Raman methods, as well as discriminant analysis, for the rapid characterization and classification of selected irradiated starch samples. Sohn et al. [12] employed FT-Raman and near-IR reflectance spectroscopy to compare calibration models for determination of rice cooking quality parameters such as apparent amylose and protein.

Most native starches are non-plastic due to their crystallinity of about 20- 45% [2]. Amylose and the branching points of amylopectin form amorphous regions. The short-branched chain in the amylopectin is the main crystalline component in granular starch. Crystalline regions are present in the form of double helices with a length of ~5nm. The amylopectin segments in the crystalline regions are all parallel to the axis of the large helix. The molecular weight of amylopectin is about 100 times higher than that of amylose. The ratio of amylose / amylopectin depends upon the source and age of the starch.

Thermoplastic extrusion is a thermo-mechanical processing used to disrupt and transform the semi-crystalline structure of starch granules to form a homogeneous and amorphous material. This transformation is usually accomplished by small amounts of molecular substances commonly known as plasticizers. The most used plasticizers are water, a volatile plasticizer and glycerol, a non-volatile plasticizer [13, 14].

The plasticizing – antiplasticizing effects of water and glycerol contents on starch samples and also the amylose / amylopectin ratios were recently investigated by various methods [15-18].

FT – IR investigation of various ratios contents of the water and glycerol on the macrostructure of native corn starch is also reported in this paper.

RESULTS AND DISCUSSION

Figs.1 and 2 show the characteristic IR spectra of starch samples with different amounts of volatile (water) and non-volatile (glycerol) plasticizer agents. The representative bands are situated in the following five regions: 3300 cm^{-1} , 2900 cm^{-1} , 1610 cm^{-1} , 1300 cm^{-1} and 1000 cm^{-1} . The two bands at 3300 cm^{-1} and 1610 cm^{-1} are ascribed to water stretching and bending vibrations [9, 10]. The other three absorptions are originated mainly from the vibrational modes of the amylose and amylopectin, the principal components of starch [9].

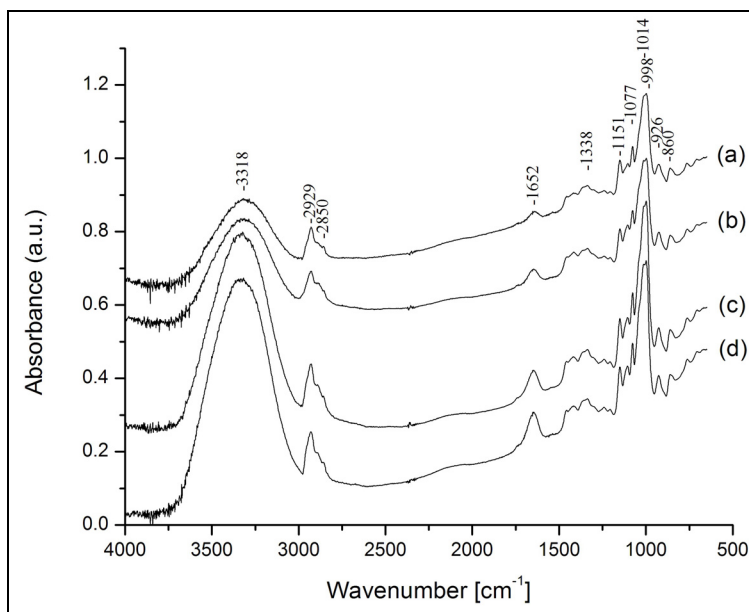


Figure 1. FT-IR spectra of samples with 4:1 starch:glycerol constant ratio and various water contents: 0%(a); 2.5%(b); 10%(c), 15%(d).

The two absorption bands from at 2930 cm^{-1} and 2850 cm^{-1} are assigned to vibrations of CH_2 groups [9]. The absorptions from 1350 cm^{-1} region are due to bending modes of O-C-H, C-C-H and C-O-H angles from amylose and amylopectin formations [19].

The strong absorption peaks appeared in the $1150 - 900\text{ cm}^{-1}$ region are assigned to C-C and C-O stretching vibrations [20]. The bands at 1000 cm^{-1} and 850 cm^{-1} are sensitive to changes in crystallinity and the intensity of 1000 cm^{-1} band determines the orientation in intermolecular H – bonding of CH and CH_2 in CH_2OH [9, 21].

It can be seen that the main intensity variations of the absorption bands without those of water 3318 cm^{-1} , 1652 cm^{-1} , with the content and ratio of the added plasticizers appear in the 1000 cm^{-1} region. These changes may be related with crystalline – amorphous forms ratio of the corn starch in the investigated samples. In principle, the amorphous regions are determined by amylose and branching points of amylopectin, while crystalline component by the short-branched chains from amylopectin [2].

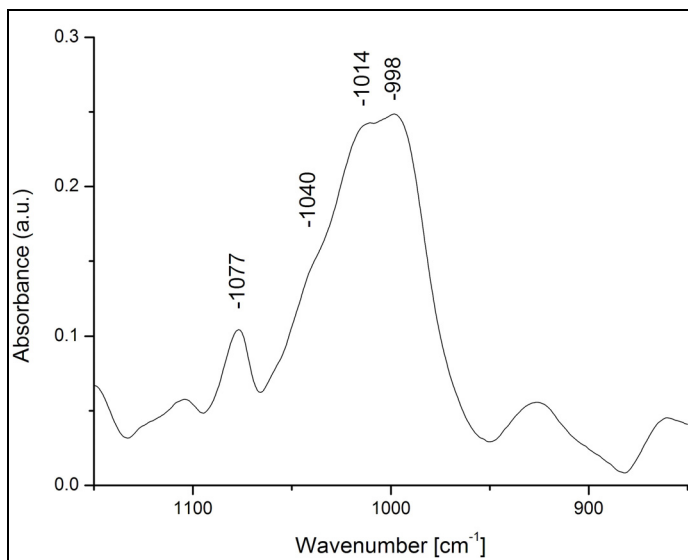


Figure 2. Extended region of 1000 cm^{-1} absorption of (b) IR spectrum from Figure 1.

On the other hand very little changes appear in the $2930\text{--}2850\text{ cm}^{-1}$ and 1350 cm^{-1} region bands with the modifications of the plasticizers content in the starch samples.

Taking into account the small changes in the intensity of 2928 cm^{-1} band for all the samples, the ratios of $998 / 2928\text{ cm}^{-1}$ and $1014 / 2928\text{ cm}^{-1}$ band intensities versus water and glycerol content are shown in Figs. 3 and 4, respectively.

According to Capron et al. [18] the intense absorption from 998 cm^{-1} may be assigned to hydrated crystalline domains whereas the band at 1014 cm^{-1} reveals the amorphous contribution of plasticizers in starch formulas. Iizuka and Aishima [10] mentioned also that the absorption peaks from 1000 cm^{-1} region assigned to C-C and C-O stretching modes of the polysaccharide backbone of amylose and amylopectin, increase in intensity with temperature, being closely related with gelatinization process.

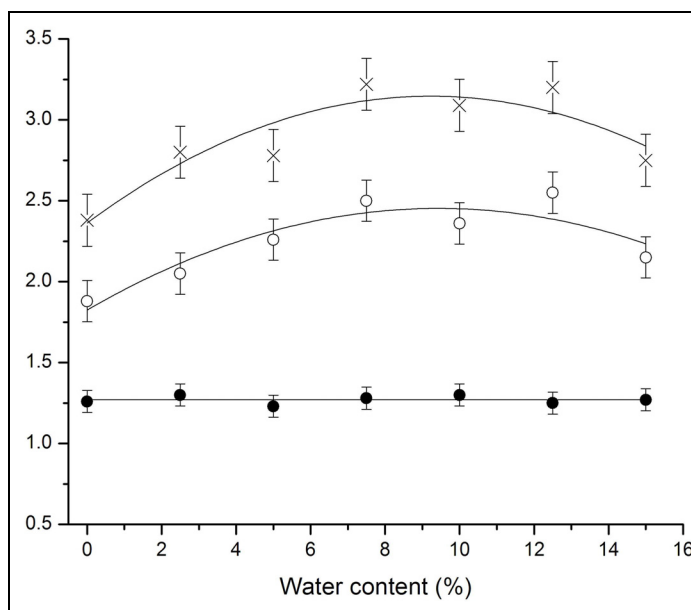


Figure 3. The dependence of 998 / 2929(x), 1014/2929(o) and 998/1014(•) ratios band intensities versus water content. (The errors bars are under 5% error limits)

A simultaneously increase of the 998 and 1014 cm^{-1} bands intensities with the increasing of water content until 10% and then a decreasing is observed in Fig. 3 for the samples with a fixed ratio of 4:1 between starch and glycerol (17-20%).

In agreement with NMR relaxation measurements [26] this fact suggested the appearance of new interactions between amorphous components at a larger spatial distance, which finally lead to a collapse of these components into a single amorphous phase for the studied starch samples. Also no change in the intensity of ratio 998 / 1014 cm^{-1} was observed (Fig. 3.) with varying water content suggesting an absence of structural order at the FTIR observation range. A similar situation is also mentioned for the 1000 / 1022 cm^{-1} ratio in the case of extruded starch and granular starch with water content fewer than 20% [18].

Many correlations between changes in the some band intensities from the 1000 cm^{-1} region (994, 1000, 1022, 1040, 1047, 1053 cm^{-1}) and the crystalline and amorphous phases (forms) of different starches are given in papers [6,9,17,18].

Analog results were also obtained in the case of samples where ratio between starch and water (12.5-15%) remains constant (5.66:1) and the

glycerol increases from 0 to 16.5% (Fig. 3). The little increase of the 998 / 1014 cm^{-1} ratio versus glycerol content may be attributed to the reaching of the double helices on a more ordered structure [18].

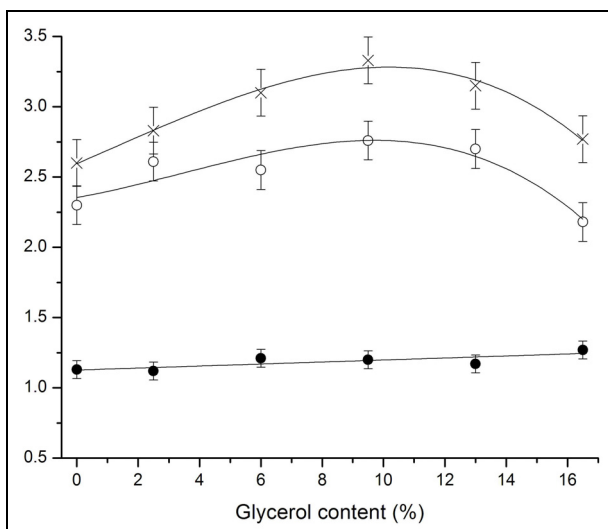


Figure 4. The dependence of 998/2929(x), 1014/2929(o) and 998/1014(•) ratios band intensities versus glycerol content. (The errors bars are under 5% error limits)

NMR relaxation data show also for these samples an increase content of lateral branches and free – end chain segments correlated with the decrease content of less mobile segments located in amylopectin core banches. In the same time the content of segments adjacent to junctions seems to be less affected by the increase of glycerol content.

The changes of the band intensities from 1000cm^{-1} region may be related with plasticizing – antiplasticizing effects of water and glycerol in function of their content in the studied starch samples. An analogous behavior amorphous – crystalline function of glycerol content in these samples was also emphasized in paper [26]. Raman and MAS-NMR data on these samples and their processing are in progress.

CONCLUSIONS

FT-IR spectra of the native corn starch with water and glycerol in various ratios and contents show the changes in intensity of the bands from 1000 cm^{-1} region characteristics to C-C and C-O stretching modes of the polysaccharide backbone from amylose and amylopectin.

These changes are correlated with the amorphous – crystalline forms of the investigated starch samples in function of plasticizers (water, glycerol) content.

In agreement with our NMR relaxation data on these starch samples results that the amorphous phase prevail until 10 – 12% water and glycerol content. The additional increasing of plasticizes content leads to the appearance of the crystalline form.

EXPERIMENTAL SECTION

The normal corn starch used in this study was obtained from SC Amylon Sibiu, Romania, having water content on wet basis (wt.b) of 10.76 %, a density of 0.561 g/cm³ and an amylose content of 21%. The glycerol used in formulas was purchased from SC Nordic Invest SRL Cluj Napoca and had a concentration of 99.5% and a density of 1.262 g/cm³. The water used was from the water supply system.

Table 1 shows the ratio of the components in the used formulas. For homogenization, the components were thoroughly mixed and stored in sealed containers for 24 hours before performing the tests.

Table 1. The ratio of the components starch-glycerol-water in the used formulas

Sample	Starch [%]	Glycerol [%]	Water [%]	Starch/ Glycerol	Starch/ Water
1	100	0	0	-	-
2	80	20	0	4	-
3	78	19.5	2.5	4	31.2
4	76	19	5	4	15.2
5	74	18.5	7.5	4	9.87
6	72	18	10	4	7.2
7	70	17.5	12.5	4	5.6
8	68	17	15	4	4.53
9	71	16.5	12.5	4.3	5.68
10	74	13	13	5.69	5.68
11	77	9.5	13.5	8.1	5.68
12	80	6	14	13.33	5.68
13	83	2.5	14.5	33.2	5.68
14	85	0	15	-	5.68

FT-IR/ATR spectra were recorded at room temperature on a conventional Equinox 55 (Bruker, Germany) spectrometer equipped with a DTGC detector, coupled with an ATR sampling device (Miracle, Pike Techn.). The resolution was of 2 cm^{-1} . The ATR crystal is of ZnSe and we made 40 acquisitions for obtaining IR spectra.

ACKNOWLEDGMENTS

This work was supported by CNCSIS –UEFISCDI, project number PN II – IDEI code 284/2011.

REFERENCES

1. M.R. Almeida, R.S. Alves, L.B.L.R. Nascimbem, R. Stephani, R.J. Poppi, L.F.C. de Oliveira, *Anal. Bioanal. Chem.*, **2010**, 397, 2693.
2. H. Liu, F. Xie, L. Yu, L. Chen, L. Li, *Progress in Polymer Science*, **2009**, **34**, 1348.
3. Buléon, P. Colonna, V. Planchot, S. Ball, *Int. J. Biol. Macromol.*, **1998**, **23**, 85.
4. E.R. Daiuto, M.P. Cereda, L.J.C.B. Carvalho, *Braz. J. Food Technol.*, 2002, **5**, 217.
5. P.M. Fechner, S. Wartewig, P. Kleinebudde, R.H.H. Neubert, *Carbohydrate Research*, **2005**, **340**, 2563.
6. J.J.G. van Soest, D. de Wit, H. Toumois, J.F.G. Vliegthart, *Starch/Stärke*, **1994**, **46**, 453.
7. R.G. Zhabankov, S.P. Firsov, E.V. Korolik, P.T. Petrov, M.P. Lapkovski, V.M. Tsarenkov, M.K. Marchenwka, H. Ratajczak, *J. Mol. Struct.*, **2000**, **555**, 85.
8. K.C. Schuster, H. Ehmoser, J.R. Gapes, B. Lendl, *Vibr. Spectrosc.*, **2000**, **22**, 181.
9. A.F. Morales, M.J. Estrada, R.M. Escobedo, *Carbohydrate Polymers*, **2012**, **87**, 61.
10. K. Iizuka, T. Aishima, *J. Food Science – Chemistry / Biochemistry*, **1999**, **64**, 653.
11. R. Kizil, J. Irudayaraj, K. Seetharaman, *J. Agric. Food Chem.*, **2002**, **50**, 3912.
12. M. Sohn, D.S. Himmelsbach, F.E. Barton, *Cereal Chem.*, **2004**, **81**, 429.
13. Tan, C.C. Wee, P.A. Sopade, P.J. Halley, *Carbohydrate Polymers*, **2004**, **58**, 191.
14. A.L. Da Roz, A.J.F. Carvalho, A. Gandini, A.A.S. Curvelo, *Carbohydrate Polymers*, **2006**, **63**, 417.
15. Y.P. Chang, A.B. Karim, C.C. Seow, *Food Hydrocolloids*, **2006**, **20**, 1.
16. P. Liu, F. Xie, M. Li, X. Liu, L. Yu, P.J. Halley, L. Chen, *Carbohydrate Polymers*, **2011**, **85**, 180.
17. N. Katayama, M. Kondo, M. Miyazawa, *J. Molec. Struct.*, **2010**, **974**, 179.
18. Capron, P. Robert, P. Colonna, M. Brogly, V. Planchot, *Carbohydrate Polymers*, **2007**, **68**, 249.

19. V. Bellon-Maurel, C. Vallat, D. Goffinet, *Appl. Spectroscopy*, **1995**, 49, 556.
20. R.H. Wilson, P.S. Belton, *Carbohydr. Res.*, **1988**, 180, 339.
21. M. Kacurakova, M. Mathlouthi, *Carbohydrate Res.*, **1996**, 284, 145.
22. A.M. Benzerdjeb, I.N.T. Mokhtari, M.S. Rahal, *Spectrochim. Acta Part A*, **2007**, 68, 284.
23. A. Synytsya, J. Copikova, P. Matejka, V. Machovic, *Carbohydr. Polym.*, **2003**, 54, 97.
24. N.A. Nikonenko, D.K. Buslov, N.I. Sushko, R.G. Zhbakov, *J. Mol. Struct.*, **2005**, 752, 20.
25. L. Yang, L.M. Zhang, *Carbohydr. Polym.*, **2009**, 76, 349.
26. N. Cioica, R. Fechete, C. Cota, E.M. Nagy, L. David, O. Cozar, *J. Mol. Struct.* (in press).

SYNTHESIS AND CHARACTERIZATION OF Co(II) COMPLEXES WITH TRIDENTATE (ONO) SCHIFF BASES

DIJE DEHARI^a, FETAH PODVORICA^b, SHEFKET DEHARI^a,
MUHAMET SHEHABI^a

ABSTRACT. Complexes of Co(II) with tridentate (ONO) Schiff bases have been prepared in the reaction of Co(II) acetate, ethanolamine and 5-X salicylaldehyde (X= Br, Cl) in nitrogen atmosphere. Bis(2-hydroxyethylimino) methyl-4-bromophenolato)cobalt(II) and bis(2-hydroxyethylimino)methyl-4-chlorophenolato)cobalt(II) were characterized by elemental analysis, IR spectroscopy and ESI mass spectrometry.

Keywords: Schiff base, cobalt(II) complexes, IR spectroscopy, mass spectrometry

INTRODUCTION

Schiff bases are versatile ligands that may be used for different purposes. For exemple Hodnett and Dunn (1970), El-masry et al. (2000), Holla et al. (2006), Jarrahpour et al. (2007) and Hania (2009) investigated antitumoral, antimicrobial, antibacterial, antifugal, antiviral and anticancer properties of Schiff bases as free ligands [1-5]. Schiff bases are also used as ligands in the complexes with transit metals [6-12]. Azomethine group of Schiff bases forms stable complexes in the presence of another atom or group susceptible to act as a ligand [6]. When salicylaldehyde reacts with ethanolamine the resulted Schiff base can act as tridentate, ligand, for example with nickel ions octahedral complexes were obtained [7]. If hydroxyl group of ethanolamine do not take part in the complexation then the previous Schiff base acts as a bidentate ligand [8].

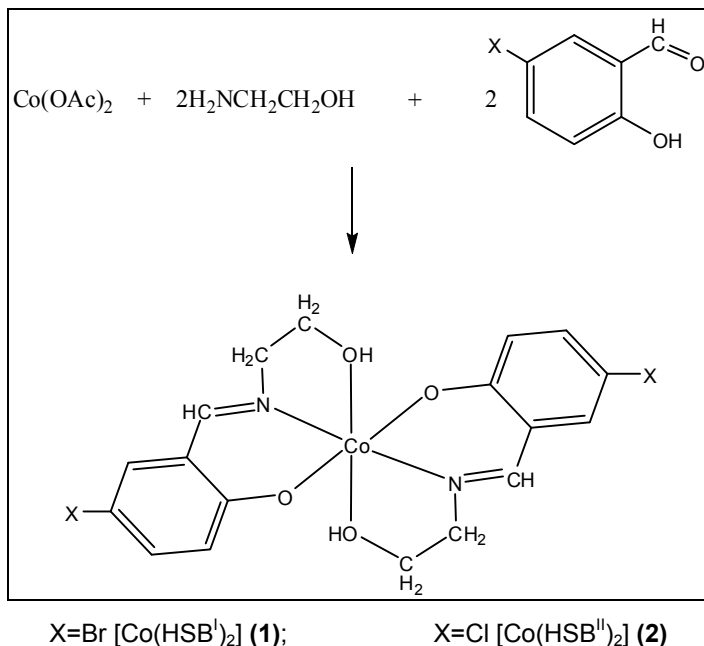
When the reaction of Co(II) ions with Schiff bases is performed in the air presenceoxidation to Co(III) occurs and anionic complexes are formed due to the deprotonation of OH groups [9]. Schiff bases as ligands form complexes with metal ions of Mn(II), Co(II) and (III), Ni(II), Cd(II), Fe(III), Zn(II) and Cu(II) [10-12]

^a State University of Tetovo, Faculty of Mathematical and Natural Sciences, Department of Chemistry, 1200 Tetovo, Macedonia

^b University of Prishtina, Faculty of Mathematical and Natural Sciences, Department of Chemistry, "Nëna Terezë" 10000 Prishtinë, Republic of Kosovo

RESULTS AND DISCUSSION

In this paper we report the ability of cobalt (II) to form stable complexes with ethanolamine and 5-bromo or 5-chloro salicylaldehyde "in situ" under nitrogen atmosphere (Scheme 1).



Scheme 1

The elemental analysis data fit very well with those calculated and they show that cobalt is coordinated with Schiff bases in 1:2 ratio. The molecular ions are present in the ESI-MS spectra of the two complexes. The mass spectrum of complex **(1)** is shown in the fig. 2. Based on the elemental analysis and mass spectra the formula, $[\text{Co}(\text{HSB})_2]$ (HSB = Schiff base), was suggested for the both complexes therefore an octahedral geometry around Co(II) was assumed with three dentate ligands.

IR spectrum of ligand

The reaction of transformation of C=O group of salicylaldehyde into azomethine in reaction with the primary amine is quantitative as the carbonyl vibration in the region 1682 cm^{-1} and the bands in the region $3600\text{-}3400 \text{ cm}^{-1}$ corresponding to the primary amine are not present.

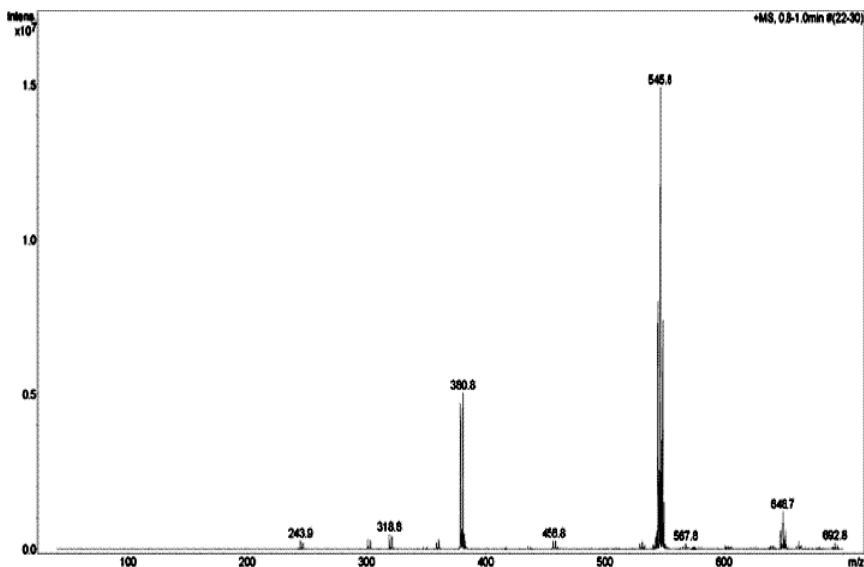


Figure 2. Mass spectrum of $[\text{Co}(\text{HSB})_2]$ complex

IR spectra of the complexes

The IR spectra of complexes are very clear and the characteristic absorptions of O-H and C=N bands which are present in complexes are easily identified. The broad bands at 3500-3300 cm^{-1} [12,13] with a maximum absorption at 3423 cm^{-1} (**1**) and 3432 cm^{-1} (**2**) suggest the coordination of the hydroxyl groups in the protonated form. The azomethine groups (C=N) in both of complexes appear with as a strong stretching absorption band at 1636 cm^{-1} (**1**) respectively 1634 cm^{-1} (**2**) [12,13]. The spectrum of the free ligand shows a band at 1650 cm^{-1} for C=N that means that lower values for complexes are due to the coordination of cobalt ions through the nitrogen of azomethine group. This interaction between Co ion and nitrogen of azomethine group reduces the electron density on nitrogen atom [14]. The strong band at 1306 cm^{-1} was assigned to C-O stretching of the phenolic group, compared to the phenolic C-O stretching of free ligand Schiff base observed at 1240 cm^{-1} . This shift of the band at higher frequency is attributed to the coordination of cobalt ion through the phenolic oxygen atom [15,16]. Finally the existence of two bands at 635 and at 470 cm^{-1} corresponding to Co-N and Co-O stretching vibrations in the case of complex indicates the coordination of the Schiff base to the cobalt ion, as shown previously in the literature. [17]

CONCLUSIONS

The data of elemental analysis, IR spectra and mass spectra show that Schiff bases synthesized “in situ” reaction are coordinated with cobalt(II) ion and form bis(2-hydroxyethylimino)methyl-4-bromophenolato) cobalt(II) and bis(2-hydroxyethylimino)methyl-4-chlorophenolato)cobalt(II). The Schiff bases are coordinated to the Co(II) ion through phenolic oxygen, azomethine nitrogen and alcoholic oxygen.

EXPERIMENTAL SECTION

Material and methods

All reagents and chemicals were used as obtained from Aldrich and Acros organics. The infrared spectra were measured on a Perkin-Elmer System 2000 FT-IR spectrometer with KBr pellets. The mass spectra were obtained on an FT-ICR-MS Bruker-Daltonics ESI spectrometer (APEX II, 7 Tesla). Elemental analyses were performed on a VARIO EL microanalyzer (Heraeus).

Preparation of complex (1)

0.5 mmol of $\text{Co}(\text{OAc})_2 \cdot 4\text{H}_2\text{O}$ are dissolved in a mixture of 10 mL ethanol + 5mL H_2O at 50 °C under nitrogen atmosphere. A second solution of 1mmol of 2-aminoethanol and 1mmol of 5-bromosalicylaldehyde dissolved in 15 mL of absolute ethanol at 50°C was added and the mixture was refluxed for 20 min. The orange precipitate was filtered and washed with acetone and diethyl ether.

IR spectrum (KBr) cm^{-1} : 3423, 1636 (C=N vibrations), 1458 (C=C), 1380 (C=C), 1305 (δ OH), 1174 (ν OH), 824, 684 (C-H aromatic);

IR spectrum of the ligand (KBr, cm^{-1}): 3174, 1650, 1515, 1350, 1240, 1165, 825, 725;

ESI-MS spectrum: m/z 545.8 ($\text{M}+\text{H}^+$);

Elemental analysis: Calc. for $\text{C}_{18}\text{H}_{18}\text{Br}_2\text{CoN}_2\text{O}_4$: C, 39.66 %; H, 3.33%; N, 5.14%. Found: C, 38.93%; H, 3.19%; N, 4.87%,

Mp: 245°C(decomp).

Preparation of complex (2)

A solution of 1mmol of 2-aminoethanol and 1mmol of 5-chlorosalicylaldehyde in 15 ml absolute ethanol prepared at 50°C was added to the solution obtained by solving 0.5mmol $\text{Co}(\text{OAc})_2 \cdot 4\text{H}_2\text{O}$ in a mixture of 10 ml ethanol + 5ml H_2O at 50°C under nitrogen atmosphere. The mixture was refluxed for 20 minute. The orange precipitate was filtered were filtered, washed with acetone and diethyl ether.

IR spectrum (KBr) cm^{-1} : 3432, 1634, 1459, 1381, 1306, 1176, 825, 705;
ESI-MS spectrum: m/z 455.9 ($\text{M}+\text{H}^+$);
Elemental analysis: Anal. Calc. for $\text{C}_{18}\text{H}_{18}\text{Cl}_2\text{CoN}_2\text{O}_4$: C, 47.39 %; H, 3.98%; N, 6.14%. Found: C, 46.96%; H, 3.89%; N, 5.92%,
Mp: 245°C(decomp).

ACKNOWLEDGMENTS

D.D. and Sh.D. thank the DAAD Programme "Stability Pact for South Eastern Europe" for financial support during their stay at the Faculty of Chemistry and Mineralogy, Universität Leipzig, Germany and at the Faculty of Chemistry and Chemical Engineering, Babes-Bolyai University, Cluj-Napoca.

REFERENCES

1. A.H. El-Masry, H.H. Fahmy, S.H. Ali Abdelwahed, *Molecules*, **2000**, 5, 1429.
2. E.M. Hodnett, W.J. Dunn, *Journal of Medicinal Chemistry*, **1970**, 13, 768.
3. B.S. Holla, B.S. Rao, K. Sarojini, M. Akberali, N.S. Kumari, *European Journal of Medicinal Chemistry*, **2006**, 41, 657.
4. A. Jarrahpour, D. Khalili, E. De Clercq, C. Salmi, J.M. Brunel, *Molecules*, **2007**, 12, 1720.
5. M. Hania, *E-Journal of Chemistry*, **2009**, 6, 629.
6. P. Dholakiya, M. N Patel, *Synthesis and Reactivity in Inorganic and Metal- Organic Chemistry*, **2004**, 34, 553.
7. M. Dey, C.P. Rao, P.K. Saarenketo, K. Rissanen, *Inorganic Chemistry Communications*, **2002**, 5, 924.
8. K. Iijima, I. Oonishi, F. Muto, A. Nakahara, *Bulletin of the Chemical Society of Japan*, **1970**, 43, 1040.
9. L.R. De, K. Samanta, K. Maiti, E. Keller, *Inorganica Chimica Acta*, **2001**, 316, 113.
10. N.H. Patel, H. M. Parekh, M. N. Patel, *Transition Metal Chemistry*, **2005**, 30, 13.
11. G.G. Mohamed, M.M. Omar, A.M. Hindy, *Turkish Journal of Chemistry*, **2006**, 30, 361.
12. A.P. Mishra, M. Khare, S.K. Gautam, *Synthesis and Reactivity in Inorganic and Metal- Organic Chemistry*, **2002**, 32, 1485.
13. R.M. Silverstein, G.C. Bassler, T.C. Morrill, "Spectrometric Identification of Organic Compounds", John Wiley & Sons, New York Chichester Brisbane Toronto Singapore, **1991**, 5, 102.

14. R. Karvembu, S. Hemalatha, R. Prabhakaran, K. Natarajan, *Inorganic Chemistry Communications*, **2003**, 6, 486.
15. S.H. Baiu, M.M. El-Ajaily, N.M. El-Barasi, *Asian Journal of Chemistry*, **2009**, 21, 5.
16. A.A. Ahmed, S.A. BenGuzzi, O.M. Ahshad, *Rasayan Journal of Chemistry*, **2009**, 2, 781.
17. E. Pretsch, P. Buhlmann, M. Badertscher, "Structure Determination of Organic Compounds", Springer-Verlag Berlin Heidelberg, **2009**, 4, 296.

FTIR SPECTROSCOPIC CHARACTERIZATION OF BITUMINOUS LIMESTONE: MAGANIK MOUNTAIN (MONTENEGRO)

DRAGAN M. ĐORĐEVIĆ^{a*}, MAJA N. STANKOVIĆ^a,
MILOŠ G. ĐORĐEVIĆ^a, NENAD S. KRSTIĆ^b, MILA A. PAVLOVIĆ^c,
ALEKSANDAR R. RADIVOJEVIĆ^d, IVAN M. FILIPOVIĆ^d

ABSTRACT. FTIR spectroscopy has been used to detailed study of bituminous limestone samples from two different locations at Maganik Mountain (Montenegro). Bituminous limestone at Maganik Mountain occurs as carbonate sediments in three levels and belongs to the early Cretaceous. Our specimens come from the oldest sediments of this limestone belonging to Barremian age. Particular attention has been given to investigation of isolated asphaltenes and kerogens. The FTIR technique provides fine determination of various organic and inorganic functional groups, as well as aliphatic and aromatic carbon and hydrogen. Due to the structural complexity of kerogens and asphaltenes, in this study we have done correlations of particular infrared absorptions to various functional groups. The asphaltenes of studied samples show higher contribution of aromatic structures than the kerogens. Notable differences in FTIR spectra of some samples that are reflected as shift of peak locations and a variety of intensities are attributed to eventual differences in the microbial precursors and/or depositional environments, conditions of sedimentation and/or genesis.

Keywords: FTIR analysis, kerogen, asphaltenes, Maganik Mountain

INTRODUCTION

The organic matter (OM) of bituminous limestone is composed mainly of two fractions – bitumen, the term assigned to soluble component (e.g. asphaltenes, resins, polar fraction) and kerogen, representing the insoluble component [1]. The solubility is here related to organic solvents.

^a *Laboratory for Geochemistry, Cosmochemistry and Astrochemistry, Faculty of Sciences and Mathematics, University of Niš, Višegradska 33, P.O. Box 224, 18000 Niš, Serbia, dragance73@yahoo.com*

^b *Department of Chemistry, Faculty of Sciences and Mathematics, University of Niš, Višegradska 33, P.O. Box 224, 18000 Niš, Serbia*

^c *Faculty of Geography, University of Belgrade, Studentski trg 3/III, 11000 Belgrade, Serbia*

^d *Department of Geography, Faculty of Sciences and Mathematics, University of Niš, Višegradska 33, P.O. Box 224, 18000 Niš, Serbia*

A careful study of the bituminous organic matter requires investigating the three main components: kerogen, bitumen, and mineral matrix [2]. Kerogens are complex, heterogeneous mixture of organic matter [3] produced primarily by geological processing of biogenic materials [4]. They are classified into three types depending on its origin and maturity. Types I, II or III are associated to distinct depositional environments: lacustrine, marine, and continental, respectively [5-7]. These types display difference in the elemental composition, primarily in H/C and O/C ratios [8].

However, modern understanding of kerogen nature exceeds this way of classification [9]. On the other hand, asphaltenes are much smaller molecules compared to kerogens and represent fragments of kerogens structure. They are mostly composed of polycyclic-aromatic and naphthenic rings bonded by aliphatic chains and heteroatoms (N, O, and S). Due to the heterogeneity and complexity of kerogens, characterization of the structural functional groups can help understanding their nature and maturity. The asphaltenes of OM from bituminous limestone (locality Maganik) were also determined, because they exhibit close structural similarities to their precursors, kerogens [10, 11].

Fourier Transform Infrared spectroscopy (FTIR) is widespread used tool for molecular structure identification of the geological organic constituents. This technique provides fine determination of various organic and inorganic functional groups, as well as aliphatic and aromatic carbon and hydrogen. Due to the structural complexity of kerogens and asphaltens, in this study we have done correlations of particular infrared absorptions to various functional groups.

Geological setting and sampling

The specimens were sampled from geological section of Barremian age, occurring in the south-western flank of the Maganik Mountain. Maganik, 20 km long and 10 km wide mountain range is placed in the middle part of Montenegro, among the rivers of Zeta, Morača and Mrtica (Fig. 1). This massif represents a group of limestone formations of Cretaceous period. The base of this mountain massif from the side of the city of Nikšić and the Morača River valley is made up of Triassic limestone. Bituminous limestone at Maganik Mountain occurs as carbonate sediments in three levels and belongs to the early Cretaceous. Our specimens come from the oldest sediments of this limestone belonging to Barremian age.

The layers of bituminous limestone of Barremian age are thick, usually from 0.1 to 0.3 m, rarely up to 0.8 m. They are dark brown-to-black, depending on the proportion of bitumen, break with irregular fracture and always smell on bitumen when cracked with hammer. Basically, these rocks are of carbonate composition, but some layers contain ingredients of detrital aluminosilicate rocks (mostly clays). The bitumen is manifested as completely

impregnated in the layer of limestone, but of varying intensity in the same layer, as well as in all the layers that make up this formation. The texture of the limestone formation is laminated and striped.

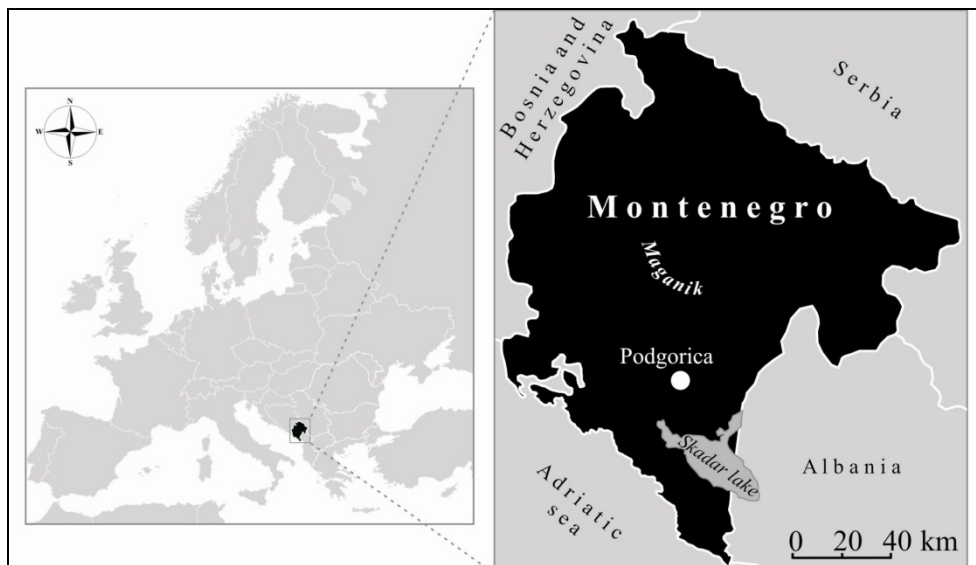


Figure 1. Geographical map of Maganik Mountain

The ESR spectroscopic investigation of vanadyl ions incorporated into the structure of kerogens from this locality has been performed by Premović et al. [12]. However, no comprehensive studies on the quantitative characteristics of the bituminous limestone and the qualitative characteristics of the isolated asphaltenes and kerogens were available to date.

In this study have been analyzed four samples (132, 425, 3149 and 3150) from the Maganik Mountain. Three of them (132, 3149, and 3150), have been collected from the locality Rekočica (altitude ca. 1550 m), and the fourth sample (425) has been collected from the locality Tuvertina greda (altitude ca. 1530 m).

RESULTS AND DISCUSSION

Bituminous limestone samples 3150 and 425 contain relatively little OM (0.6 % and 2.5 %, respectively), sample 3149 has medium content of OM (17 %), whereas the sample 132 shows relatively high content of OM (54 %, Table I). Comparison of results of OM fractions represents that kerogen made 50-87 % of total OM in investigated samples. Kerogen concentration in the sedimentary rocks is considered to be reflection of the organic productivity

as well as the general sedimentation pattern during geological period of formation and diagenesis [1]. Asphaltenes are presented in range of 0.1 % (sample 3150) to 6.0 % (sample 132).

Table I. Fractional analysis of samples [± 5 wt%]

	Samples			
	132	425	3149	3150
Cold HCl	32.0	96.0	79.0	99.0
Hot HCl	2.0	0.5	1.0	0.1
HF/HCl	12.0	1.0	3.0	0.3
<i>Total of inorganic matter</i>	<i>46.0</i>	<i>97.5</i>	<i>83.0</i>	<i>99.4</i>
Polar fraction	0.5	0.1	0.5	0.1
Resin	0.5	0.1	1.0	0.1
Asphaltene	6.0	0.3	1.5	0.1
Kerogen	47.0	2.0	14.0	0.3
<i>Total of organic matter</i>	<i>54.0</i>	<i>2.5</i>	<i>17.0</i>	<i>0.6</i>

Comparing the FTIR spectra of the samples 425, 3149 and 3150 (Fig. 2) the dominance of inorganic fraction bands towards organic fraction bands is obvious, contrary to FTIR spectrum of sample 132, where organic fraction bands are significant. These results are in accordance with results of the fractional analysis.

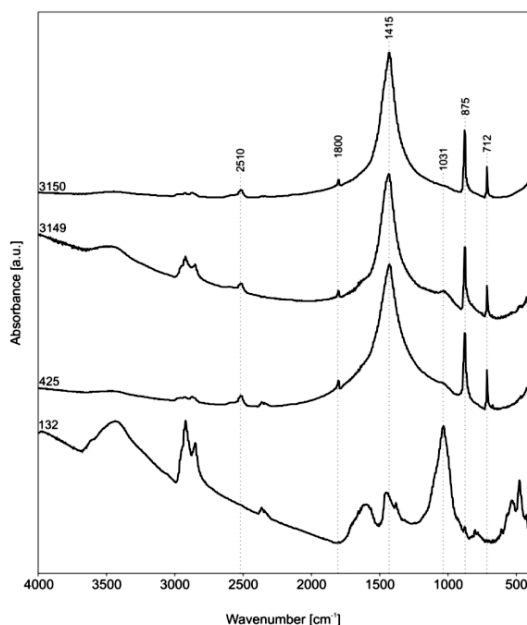


Figure 2. FTIR spectra of untreated samples 132, 425, 3149, and 3150

The FTIR spectra of the samples 425, 3149 and 3150 featured the following bands at: 2500, 1800, 1415, 875 and 712 cm^{-1} characteristic for carbonate minerals, precisely for calcite with minor aragonite [13]. These bands are absent in the FTIR spectrum of sample 132 indicating the inorganic fraction is, probably, composed mainly of silicate and aluminosilicate minerals.

Significant differences are evident in the relative intensity of the peak at 1031 cm^{-1} . This absorption is the most intense in the sample 3149 (if neglected sample 142), then in the sample 425, and at least in sample 3150. This is in accordance to analytical data of inorganic matter where the carbonate fraction (cold HCl soluble fraction) is the most existing in samples 3150, 425 and 3149, with 99 %, 96 % and 79 % of carbonate, respectively.

It should be mentioned that in the FTIR spectrum of sample 132 the bands of carbonate minerals are comparatively weak due to presence of intensive bands corresponding to silicate and aluminosilicate minerals, although there is higher account of the carbonate fraction (32 %) than of the silicate fraction (12 %).

FTIR spectra after treatment with (cold and hot) HCl

In the FTIR spectra of all the samples treated with cold/hot HCl featured the common bands, corresponding to the inorganic minerals, at: 3623, 1095, 1030, 920, 789, 777, 527, 470 and 417 cm^{-1} [13]. In Figure 3 are featured the FTIR spectra of the residues after treatment with cold/hot HCl, in the fingerprint region (1400-400 cm^{-1}), since the peak at 3623 cm^{-1} is not spectral interesting.

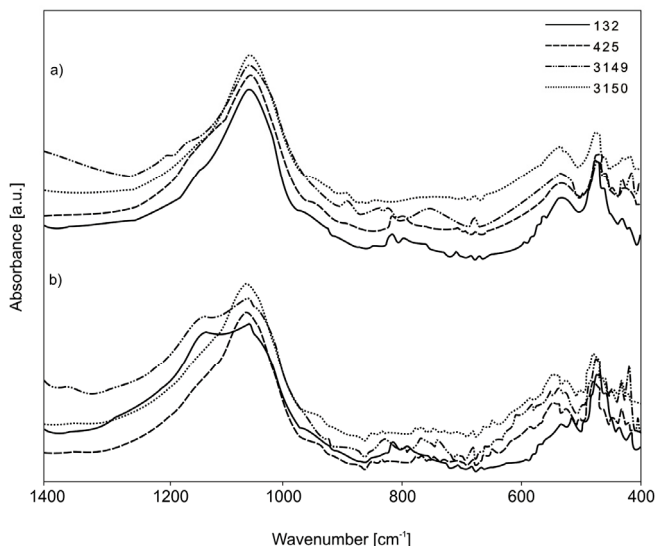


Figure 3. FTIR spectra of the studied samples in 1400-400 cm^{-1} region: a) after treatment with cold HCl; b) after treatment with hot HCl

It is almost impossible unambiguously determinate minerals responsible for above mentioned bands, because they are insufficiently separated. Although, it could be claimed that these absorptions probably correspond to the following silicate/aluminosilicate minerals: montmorillonite, illite, secondary aluminous chlorite, interstratified montmorillonite/illite, interstratified montmorillonite/chlorite, cristobalite, and quartz. We believe that dominant species are secondary aluminous chlorite, interstratified montmorillonite/illite, and interstratified montmorillonite/chlorite. Quartz is presented in the traces. Our further studies will be performed in aim to get a more precise answer about nature of presented inorganic minerals.

Comparing the spectra of the residues after cold HCl treatment to those treated with hot HCl, the latter show neglected differences, primarily due to removal of less soluble carbonates and easily soluble silicate/aluminosilicate minerals. This difference is the most obvious in the spectra of the samples 132 and 3149 which is expected due to these samples have higher contribution of hot HCl soluble fraction, 2 % and 1 %, respectively.

Chemical characterization of asphaltenes

The FTIR spectra of carbonate isolated asphaltenes from all studied samples are presented at Fig. 4a. It can be seen that IR spectra show a combination of aliphatic and aromatic structures. The aliphaticity is presented by the intense bands in the regions between $2970\text{--}2850\text{ cm}^{-1}$ and $1455\text{--}1350\text{ cm}^{-1}$ [14]. The aromatic groups are indicated by the stretching vibrations at 3050 cm^{-1} and deformation vibrations between 900 and 700 cm^{-1} .

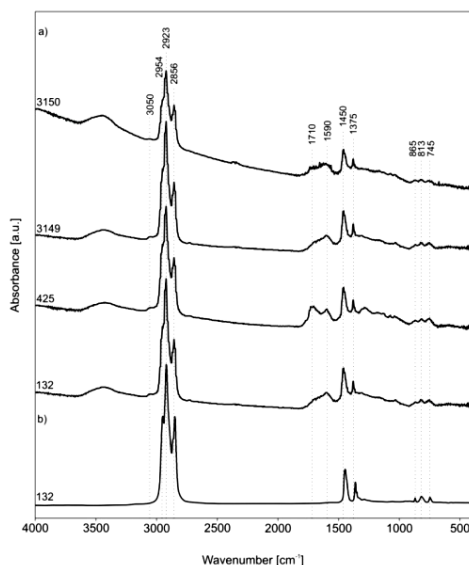


Figure 4. FTIR spectra of asphaltenes of studied samples
a) KBr pellets method, b) in Nujol

The absorption at 1710 cm^{-1} , observing in all samples spectra is assigned to stretching of carbonyl groups mainly occurring as free carbonyl-group, not as part of carboxyl-group, due to the absence of $-\text{OH}$ band in the $3600\text{-}2500\text{ cm}^{-1}$ region (the broad band around 3300 cm^{-1} originated from moisture, what was confirmed by FTIR spectra of samples dispersed in Nujol as matrix, Fig. 4b). More intense band at 1710 cm^{-1} in the spectra of sample 425 in comparison to spectra of samples 132, 3149 and 3150 could be a sign of higher contribution of oxygen, and as follows the pronounced aromaticity of this asphaltene and its lower degree of evolution [15].

The presence of polyaromatic groups in the structures of all four samples is indicated by weak bands at 3050 , 865 , 813 and 745 cm^{-1} (Table II). The shoulder appearing in the domain 1700 and 1600 cm^{-1} corresponds to olefinic or aromatic ring $\text{C}=\text{C}$ stretching and is hard to observe it in the spectra due to the overlapping with deformation absorption of water, and $\text{C}=\text{O}$ vibration of aromatic quinines [14, 15].

Table II. Characteristic band assignments

Wavenumber (cm^{-1})	Assignment
3400	hydroxyl, OH^- stretching
3080-3000	aromatic C-H bonds
2956	asymmetric CH_3 stretching
2925	asymmetric C-H stretching of methylene group
2872	symmetric CH_3 stretching
2850	symmetric C-H stretching of methylene group
1745-1680	carbonyl $\text{C}=\text{O}$ stretching $\text{C}=\text{C}$ bonds, H_2O deformation, aromatic ring
1650-1580	stretching
1520-1500	aromatic rings
1450	asymmetric CH_2 and CH_3 bending
1380-1370	CH_3 and cyclic CH_2 vibrations
1250	phenolic C-O bond
1050	C-O bonds of alcohols
980-890	$\text{C}=\text{C}$ bonds
900-700	aromatic out-of-plane deformation
725-720	aliphatic chains longer than C_4

In our spectra this shoulder is shifted to 1590 cm^{-1} and represents the sum of the bands originated from $\text{C}=\text{C}$ stretching vibrations of polyaromatic structures, bending vibrations of molecular water and unsaturated hydrocarbons chains. This shift to lower frequencies could be the sight of higher level of maturity [15, 16].

As crucial for understanding the asphaltenes is the nature of their aliphatic and aromatic structures, the attention is paid to the absorptions that can provide information about these structures.

The analysis of aliphatic bands in the 3000-2800 cm^{-1} region

It was necessary to apply deconvolution in this region, because it helps to determine position, width and areas of each band (Fig. 5). The aliphatic bands in the 3000-2800 cm^{-1} region actually represent a sum of the following mutually overlapped single bands:

- asymmetric stretching of $-\text{CH}_3$ located at 2954 cm^{-1} ;
- asymmetric stretching of $-\text{CH}_2-$ located at 2923 cm^{-1} ;
- stretching of CH located at 2900 cm^{-1} ;
- symmetric stretching of $-\text{CH}_3$ located at 2870 cm^{-1} ;
- asymmetric stretching of $-\text{CH}_2-$ located at 2856 cm^{-1} .

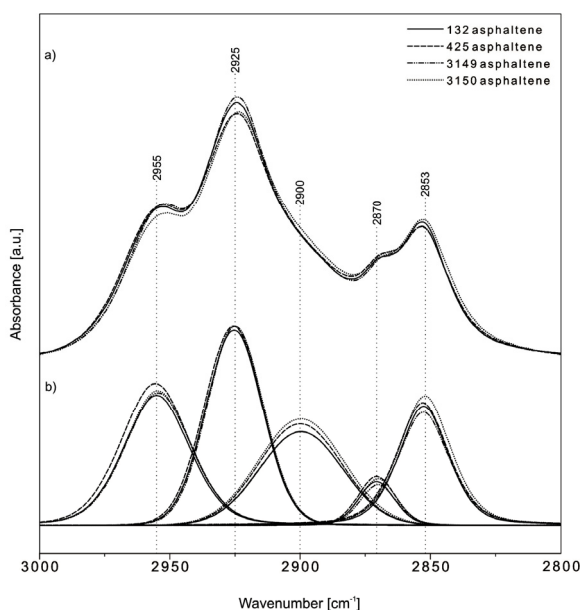


Figure 5. Deconvolution of region from 3000 to 2800 cm^{-1} ;
a) original spectra, b) deconvolution bands

The spectra show no differences in the peak positions, but only in their intensities. For interpreting the nature of the aliphatic structure is essential knowledge of the relationship between the methyl ($-\text{CH}_3$) and methylene ($-\text{CH}_2-$) groups which absorbed at 2955 cm^{-1} and 2925 cm^{-1} , respectively. The methyl/methylene bands ratio of the FTIR spectra were studied by curve-fitting analysis.

The ratio of these bands (I_{2955}/I_{2925}) gives an approximate picture of the aliphatic-chain length of hydrocarbons and the degree of branching of these structures [17, 18]. If this ratio has lower value the structure is dominated by long, straight aliphatic groups. The higher ratio values indicate existence of shorter and more branched aliphatic-chains. Increasing of this ratio is in accord to the decreasing of the H/C ratio which acts as a parameter of maturation, implying higher degree of maturation.

The analysis of aromatic bands in the 900-700 cm^{-1} region

In this region are occurring three bending aromatic bands at 865 cm^{-1} (corresponding to aromatic structures with isolated aromatic hydrogen), 813 cm^{-1} and 745 cm^{-1} , with two and four vicinal hydrogen atoms per cycle, respectively (Fig. 6) [19]. The number of vicinal aromatic hydrogen atoms per cycle could indicate the degrees of substitution and aromatic structure condensation. The intense band at 865 cm^{-1} accounts for the higher degrees of substitution and condensation, while weak bands at 815 cm^{-1} , and especially at 745 cm^{-1} show reversely. The spectra given in the Fig. 6 show no differences except in intensities of bands, and based on relative intensities of observed bands sample 3150 shows the highest degrees of substitution and condensation, followed by samples 3149, 425, and 132.

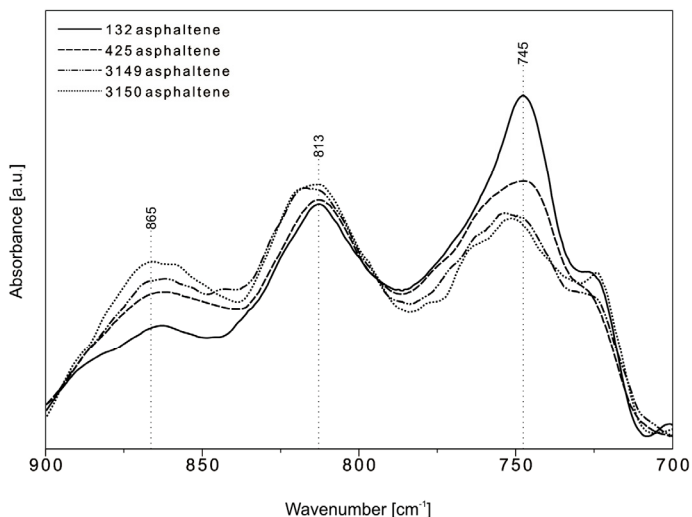


Figure 6. Enlarged FTIR spectra of asphaltenes of the studied samples in 900-700 cm^{-1} region.

In all spectra is presented comparative weak band around 720 cm^{-1} indicating low content of long aliphatic chains (with more than 4 methylene groups) in molecular structures of asphaltenes.

Chemical characterization of kerogens

The intense bands in the 2960-2850 cm^{-1} and 1455-1350 cm^{-1} regions are related to pronounced aliphatic structures into the kerogens of all four studied samples (Fig. 7). Also, the band at 1710 cm^{-1} corresponding to the carbonyl-group is presented in all spectra. This group is assigned mainly to free carbonyl-groups, out of carboxyl-group, due to the absence of $-\text{OH}$ band in the 3600-2500 cm^{-1} region (as mentioned for asphaltenes, the observed broad band at about 3300 cm^{-1} originated from moisture, confirmed by FTIR spectra of kerogen dispersed in Nujol as matrix, Fig. 7b).

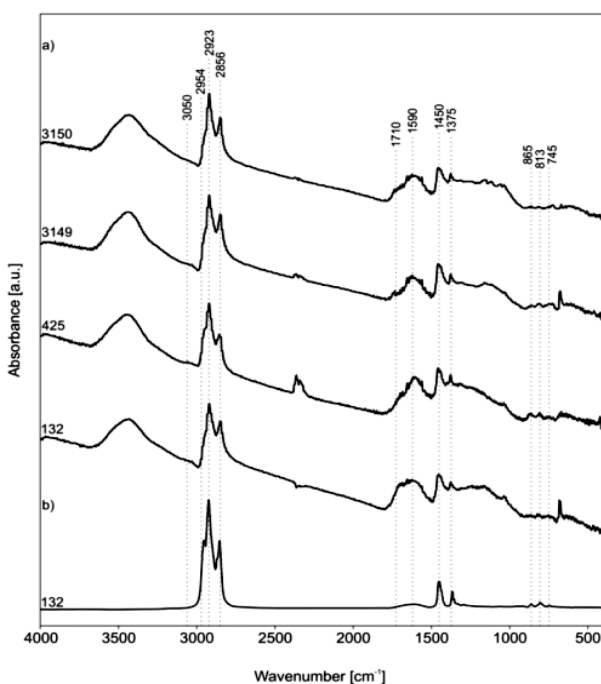


Figure 7. FTIR spectra of kerogens of studied samples
a) KBr pellets method, b) in Nujol

The presence of polyaromatic groups in the structures of all four samples is indicated by almost absent absorption at 3050 cm^{-1} and weak bands at 865, 813 and 745 cm^{-1} . The band at 1590 cm^{-1} is result of overlapping the bands associated to: C=C stretching vibrations of polyaromatic structures, bending vibrations of molecular water and unsaturated hydrocarbons chains. The knowledge of nature of aliphatic and aromatic structures of kerogens is crucial for their understanding, so our attention was paid to corresponding absorptions in the 3000-2800 cm^{-1} and 900-700 cm^{-1} regions.

The analysis of aliphatic bands in the 3000-2800 cm^{-1} region

The absorptions in the 3000-2800 cm^{-1} region assigned to aliphatic structures are result of composited, mutually overlapped bands (above mentioned, in section about asphaltenes) with presence of one more peak at 2833 cm^{-1} of unknown origin (Fig. 8).

The main differences in FTIR spectra of individual samples are the intensities of asymmetric stretching absorptions of methyl and methylene groups and symmetric stretching absorption of methylene group, resulting comparative high value for methyl/methylene ratio for sample 425 and low value of this ratio for sample 3150 (Fig. 9). This suggests that sample 425 is the most evolved cause methyl/methylene ratio tends to have higher value for kerogens with lower hydrogen content characteristic for the species of higher degree of maturity.

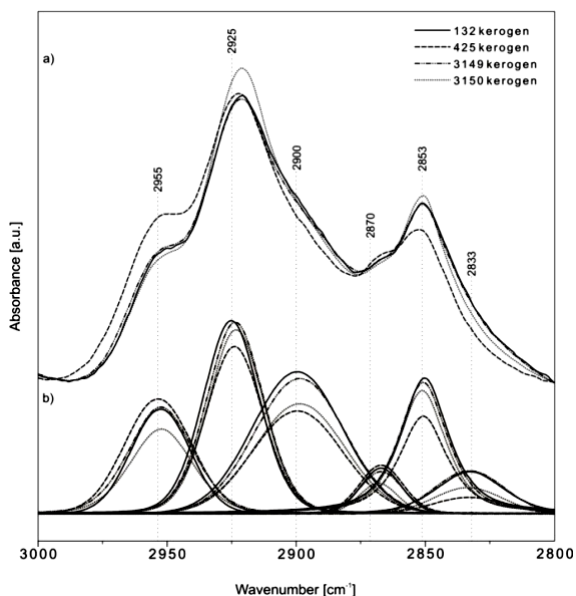


Figure 8. Deconvolution of region from 3000 to 2800 cm^{-1} ;
a) original spectra, b) deconvolution bands.

The methyl/methylene bands ratio, as well as for asphaltenes, shows lower value for the structure dominated by longer and straight aliphatic-chains, and higher values indicating dominating short and more branched aliphatic groups [17, 20, 21] in kerogen structure (Fig. 9). This ratio shows higher values for extracted asphaltenes indicating presence of shorter and more branched aliphatic structures, which is in correlation with the definition of these substances. However, one can observe that asphaltenes originating from kerogens give FTIR spectra similar to kerogens.

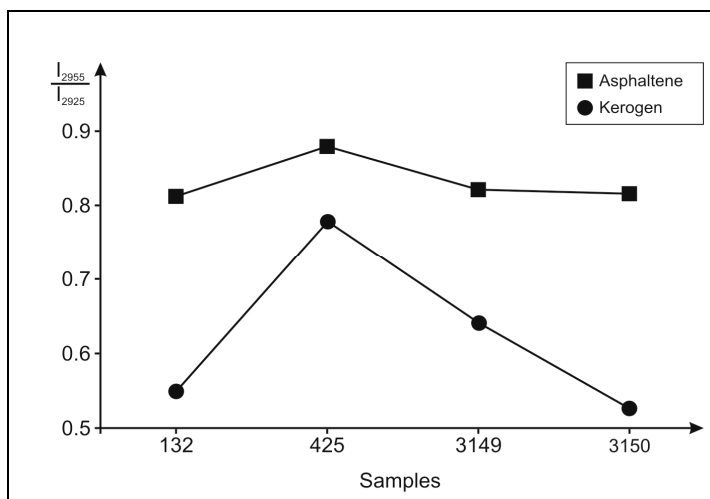


Figure 9. The I_{2955}/I_{2925} ratio for asphaltenes and kerogens of studied samples

The analysis of aromatic bands in the 900-700 cm^{-1} region

The differences in the peak positions, as well as in band intensities characterize the FTIR spectra of isolated kerogens in 900-700 cm^{-1} region (Fig. 10).

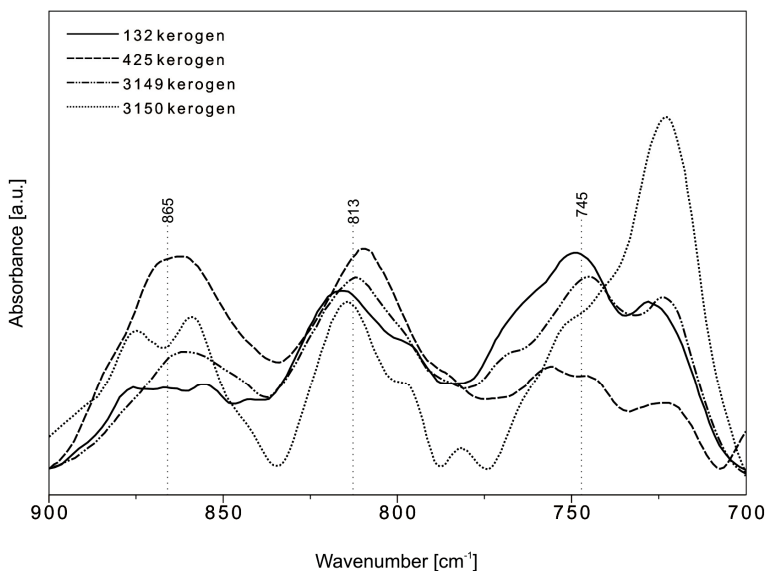


Figure 10. FTIR spectra of kerogens of the studied samples in 900-700 cm^{-1} region.

Bands that correspond to the aromatic out-of-plane deformation vibrations appear around 865, 813 and 745 cm^{-1} . In accordance with discussion for asphaltenes, the intense band at 865 cm^{-1} accounts for the higher degrees of substitution and condensation, while weak bands at 815 cm^{-1} , and especially at 745 cm^{-1} mean opposite. The sample 425 shows the highest degrees of substitution and condensation of aromatic structures, followed by samples 3149, 3150, and 132. It could be due to differences in the geological conditions of kerogen formation of sample 425. The FTIR spectrum of sample 3150 in this domain contains an intense band around 720 cm^{-1} due to CH_2 rocking vibrations in long chain aliphatic substances with more than 4 methylene groups, indicating high contribution of long, straight aliphatic-chains within kerogen structure.

Notable differences in FTIR spectra of samples 132 and 3150, such as peak locations and band intensities are attributed to eventual differences in the microbial precursors and/or depositional environments, conditions of sedimentation and/or genesis.

CONCLUSIONS

Successively dissolution and FTIR analysis show that the studied samples are mainly composed of inorganic matter (calcite with minor silicate and aluminosilicate minerals), except sample 132 that shows significant content of organic matter. Due to the FTIR spectra of untreated samples do not give useful information about the structures of organic matter because of interferences with the carbonate functional groups, extraction of asphaltene and kerogens have to be performed. According to the results of FTIR analysis of carbonate isolated organic matter, it may be concluded:

- The asphaltenes of studied samples show higher contribution of aromatic structures than the kerogens, and methyl/methylene ratio indicates existing shorter and more branched aliphatic-chains within the structures.
- The FTIR analyses of studied kerogens show very low aromaticity with aliphatic stretching vibrations in the 3000-2800 cm^{-1} as the most significant bands. The methyl/methylene ratio for kerogens, contrary to asphaltenes indicates higher contribution of longer and straight aliphatic-chains.

Notable differences in FTIR spectra of some samples that are reflected as shift of peak locations and a variety of intensities are attributed to eventual differences in the microbial precursors and/or depositional environments, conditions of sedimentation and/or genesis.

EXPERIMENTAL SECTION

Analysis and fractionation

Pre-treatment

Before extraction and treatment with mineral acids, the samples were grinded in a vibrating mill to particle size of 100 μm . To extract OM from source carbonate-bearing rocks, we followed the method of isolation by successively treating with HCl and HF [7, 22, 23] due to the presence of carbonates and clay minerals.

Demineralization of inorganic fractions

Ground samples of bituminous limestones were successively digested with appropriated mineral acids in order to remove carbonates and silicates. Dilution in HCl (6 M) at room temperature during 12 h was performed to remove most of the carbonates. The residues were then diluted in 6 M solution of HCl at 80 °C for 12 h for removing soluble silicates and less soluble carbonates and oxides. Insoluble residue after HCl-treatment was subjected to dissolution in mixture of (22 M) HF and (12 M) HCl (3:1, v/v) heated in a teflon glass at 80 °C. This mixture was used for removal of silicate minerals and silica.

Extraction of soluble OM

The separation of extractable OM from the insoluble residue after consecutive demineralization was performed in Soxhlet apparatus following the sketched fractionation procedure (Fig. 11).

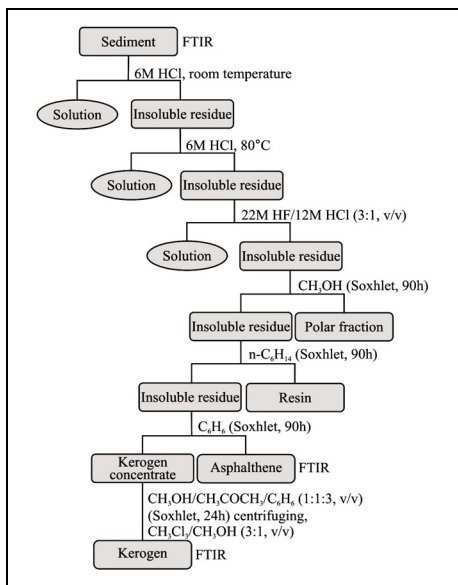


Figure 11. Flow chart of the fractionation procedure

The polar fraction was obtained from dried, finely powdered samples with methanol refluxing (Soxhlet) for 90 hours. The subsequent step was performed with n-hexane giving the resin fraction, and finally the asphaltene fraction was extracted with benzene. After solvent evaporation we get solid phase hereafter referred to as asphaltene.

Extraction of kerogen

In order to obtain the "cleaner" kerogen, the insoluble residue obtained after removal of the soluble fractions was extracted in Soxhlet apparatus with mixture of methanol/acetone/benzene (1:1:3, v/v) for 24 h. Also, the kerogen concentrate was subjected to centrifugation in the mixture of chloroform/methanol (3:1, v/v) in purpose to remove coarse pyrite and other HF/HCl insoluble minerals, as well as neoformed fluorides [24].

Fourier Transform Infrared (FTIR) Spectrometry

FTIR spectra were recorded, in absorbance mode, with a BOMEM Michelson Series MB FTIR spectrometer set to give undeformed spectra. Spectra were collected at room temperature, over the range of 4000-400 cm^{-1} with a spectral resolution of 4 cm^{-1} . 1.5 mg of a sample was ground with 150 mg of analytical quality KBr in a vibrating mill and sintered into a disk in a hydraulic press to obtain KBr pellets.

ACKNOWLEDGMENTS

The authors wish to thank M. T. Pajović from the Institute for Geological Exploration (Podgorica), who kindly provided the bituminous limestone samples. We would like to also thank to the Laboratory for Physical Chemistry, Faculty of Technology (Leskovac) for the FTIR analyses of samples. This work was partially funded by Ministry of Education and Science of Republic of Serbia within the project OI176008 and TR34008.

REFERENCES

1. M. Vandenbroucke, C. Largeau, *Organic Geochemistry*, **2007**, 38, 7.
2. M. Razvigorova, T. Budinova, B. Tsyntsarski, B. Petrova, E. Ekinci, H. Atakul, *Internacional Journal of Coal Geology*, **2008**, 76, 243.
3. Ö.M. Doğan, B.Z. Uysal, *Oil Shale*, **2002**, 19, 399.

4. B.N. Khare, W.R. Thompson, C. Sagan, E.T. Arakawa, C. Meisse, I. Gilmour, "Proceedings of the Second International Conference on Laboratory Research for Planetary Atmospheres", University of Virginia, Charlottesville, **1991**, 340.
5. B. Durand, J. Espitalie, *Compte Rendu de l' Academie des Sciences*, **1973**, 276, 2253.
6. B. Tissot, B. Durand, J. Espitalie, *American Association of Petroleum Geologists Bulletin*, **1974**, 58, 397.
7. B. Durand, G. Nicaise, "Kerogen-Insoluble Organic Matter from Sedimentary Rocks", B. Durand (ed.), Technip, Paris, **1980**, 35.
8. D.W. Van Krevelen, "Coal", Elsevier, Amsterdam, **1961**, chapter 7.
9. A. Hutton, S. Bharati, T. Robl, *Energy & Fuels*, **1994**, 8, 1478.
10. B.P. Tissot, D.H. Welte, "Petroleum formation and occurrence", Springer-Verlag, Berlin, **1984**, 2nd Edition.
11. R. Pelet, F. Behar, J. C. Monin, *Organic Geochemistry*, **1986**, 10, 481.
12. P.I. Premović, I.R. Tonsa, M.T. Pajović, L. Lopez, S. Lo Monaco, D.M. Đorđević, M. S. Pavlović, *Fuel*, **2001**, 80, 635.
13. H.W. Van der Marel, H. Beutelspacher, "Atlas of Infrared spectroscopy of clay minerals and their admixtures", Elsevier, Amsterdam, **1976**, 194.
14. P.C. Painter, R.W. Snyder, M. Starsinic, M.M. Coleman, D. Kuehn, A. Davis, *Applied Spectroscopy*, **1981**, 35, 474.
15. P.G. Rouxhet, P.L. Robin, G. Nicaise, "Kerogen-Insoluble Organic Matter from Sedimentary Rocks", B. Durand (ed.), Technip, Paris, **1980**, 163.
16. D.N. Kendal, "Applied infrared spectroscopy", Reinhold Publishing Corp., New York, **1966**, 5.
17. R. Lin, G.P. Ritz, *Organic Geochemistry*, **1993**, 20, 695.
18. S.H. Wang, P.R. Griffiths, *Fuel*, **1985**, 64, 229.
19. T.F. Yen, W.H. Wu, G.V. Chilingar, *Energy Sources*, **1984**, 7, 203.
20. G.P. Lis, M. Mastalerz, A. Schimmelmann, M. Lewan, B.A. Stankiewicz, *Organic Geochemistry*, **2005**, 36, 1533.
21. J.A. D'Angelo, *Ameghiniana*, **2006**, 43, 669.
22. J.D. Saxby, *Chemical Geology*, **1970**, 6, 173.
23. P.I. Premović, Lj.S. Jovanović, G.S. Nikolić, *Organic Geochemistry*, **1996**, 24, 801.
24. P.I. Premović, S.B. Zlatković, M.P. Premović, I.R. Tonsa, *Journal of Petroleum Geology*, **1998**, 21, 289.

ON THE SCHULTZ, MODIFIED SCHULTZ AND HOSOYA POLYNOMIALS AND DERIVED INDICES OF CAPRA- DESIGNED PLANAR BEZENOIDS

MOHAMMAD REZA FARAHANI^a, MIRANDA PETRONELLA VLAD^b

ABSTRACT. In this paper, Schultz, Modified Schultz and Hosoya polynomial and their topological indices of a benzenoid molecular graph constructed by Capra-map operation, $Ca(C_6)$, are calculated. Several examples are given.

Keywords: *Schultz polynomial; Modified Schultz polynomial; Hosoya polynomial; Wiener index; Capra-operated benzenoid.*

INTRODUCTION

Let $G=(V,E)$ be a simple connected graph of finite order $n=|V|$, such that it has the vertex set $V=V(G)$ and edge set $E=E(G)$. A general reference for the notation in Graph Theory is [1]. The distance between vertices u and v of G , denoted $d(u,v)$, is the number of edges in a shortest path connecting them. The largest distance in G is called the diameter, $d(G)$. Another invariant in graph is degree of a vertex $v \in V(G)$ that it is the number of edges incident in it and is denoted by δ_v .

In graph theory, several counting polynomials are known: Schultz polynomial $Sc(G,x)$, Modified Schultz polynomial $Sc^*(G,x)$, Hosoya polynomial $H(G,x)$, etc. Their first derivative (in $x=1$) define, in general, the corresponding topological indices.

Definitions of the above polynomials and indices are as follows:

$$Sc(G, x) = \frac{1}{2} \sum_{\{u,v\} \in E(G)} (\delta_u + \delta_v) x^{d(u,v)}$$
$$Sc^*(G, x) = \frac{1}{2} \sum_{\{u,v\} \in E(G)} (\delta_u \delta_v) x^{d(u,v)}$$

^a *Iran University of Science and Technology (IUST), Department of Mathematics, Narmak, Tehran 16844, Iran, MR_Farahani@Mathdep.iust.ac.ir*

^b *Dimitrie Cantemir University, Bucharest, Faculty of Economic Sciences, No 56 Teodor Mihali Street, 400591, Cluj Napoca, Romania, Mirandapv@yahoo.com*

$$H(G,x) = \sum_{i=0}^{d(G)} d(G,i)x^{d(u,v)}$$

$$Sc(G) = \frac{1}{2} \sum_{\{u,v\} \in E(G)} (\delta_u + \delta_v)d(u,v)$$

$$Sc^*(G) = \frac{1}{2} \sum_{\{u,v\} \in E(G)} (\delta_u \times \delta_v)d(u,v)$$

$$W(G) = \frac{1}{2} \sum_{v \in V(G)} \sum_{u \in V(G)} d(u,v) = \sum_{i=0}^{d(G)} d(G,i)d(u,v)$$

$$WW(G) = H'(1) + (1/2)H''(1)$$

The Schultz index was introduced by *Schultz* in 1989 [2] while the Modified Schultz index was defined by *Klavžar* and *Gutman* in 1997 [3]. The Schultz index, also called molecular topological index, was studied in many papers [2-17]. These indices have been computed in some nanotubes [12-14, 17-21].

Hosoya polynomial was introduced by *H. Hosoya*, in 1988 [16]. The first derivative of Hosoya polynomial is just the Wiener index; a Hyper-Wiener index, denoted $WW(G)$ (see above) can be computed from the first and second derivative of Hosoya polynomial. Wiener index had found numerous application and was reported in [8, 16, 21-32].

The coefficients of Hosoya polynomial can be calculated from layer/shell matrices, as shown by *Diudea* [33-35], who gave a “chemical” generalization in Hosoya-Diudea weighted polynomials.

In chemistry, physics and nanoscience, there are especially symmetric structures. Such molecular graphs are *Capra-designed planar benzenoids*. Capra Ca map operation (also called Septupling S_1) is a method of drawing and modifying the covering of a polyhedral structure, introduced by *Diudea* [36,37]. A detailed example is given in Figure 1.

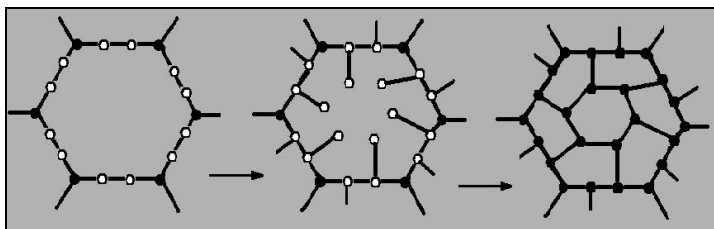


Figure 1. An example of Capra map operation on the hexagon face.

In this paper, we applied Capra operation on the benzene molecular graph C_6 to design planar benzenoid structures; the k -iterated benzenoids are denoted $Ca_k(C_6)$. The two first members of this series are shown in Figure 2.

Also, $Ca(C_6)$ is called Coronene H_2 and is the second member of the circumcoronene series of benzenoids H_k , $k \geq 1$. The first three members of circumcoronene series are shown in Figure 3.

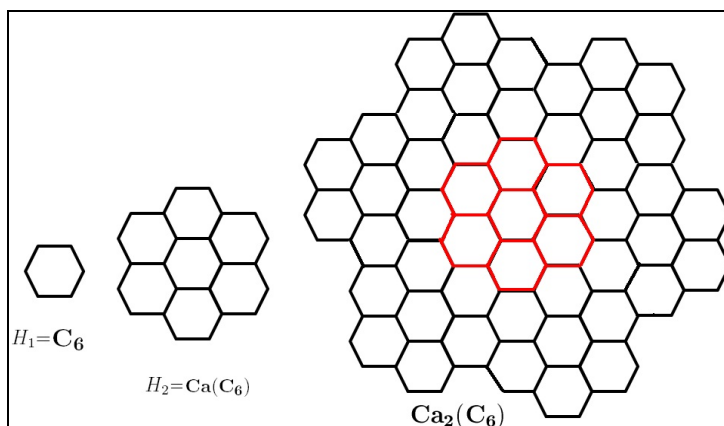


Figure 2. Benzenoid molecular graphs $H_2=Ca(C_6)$ and $Ca_2(C_6)$, representing the first two members of Capra-designed planar benzenoids.

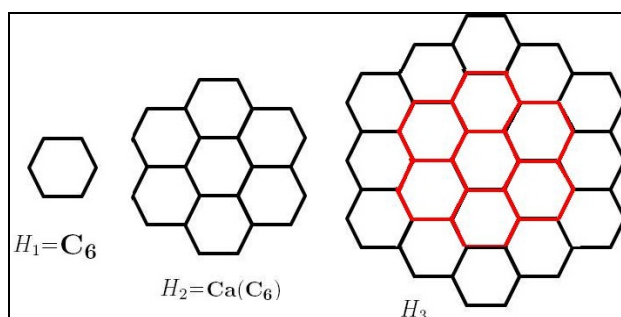


Figure 3. The first three graphs H_1 , H_2 and H_3 of the Circumcoronene series.

Within this paper, we focused on the Schultz, Modified Schultz and Hosoya polynomials and their topological indices of the Coronene $Ca(C_6)$ planar benzenoid structure.

Theorem 1. Let $G=Ca(C_6)$ be a Capra-designed planar benzenoid. Then the Schultz polynomial of G is equal to:

$$Sc(G,x)=156x+252x^2+294x^3+276x^4+222x^5+132x^6+48x^7$$

and the Schultz index $Sc(G)=4884$.

The Modified Schultz polynomial of G is equal to:

$$Sc^*(G,x)=204x+330x^2+381x^3+348x^4+267x^5+144x^6+48x^7$$

and the Modified Schultz index $Sc^*(G)=5934$.

Theorem 2. Let $G=Ca(C_6)$ be a Capra-designed planar benzenoid. Then, the Hosoya polynomial of G is equal to:

$$H(G,x)=24+30x^1+48x^2+57x^3+54x^4+45x^5+30x^6+12x^7$$

Also, the Wiener index is $W(G)=1002$, and Hyper Wiener index $WW(G)=2697$.

MAIN RESULTS

In this section we will prove the two above theorems. At first, we introduce some notations, related to Figure 4.

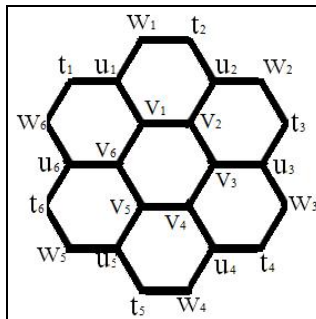


Figure 4. Capra-designed planar molecular graph: Coronene, $Ca(C_6)=H_2$ and the notation used in the text.

Let $V(G)$ be the vertex set of $G=Ca(C_6)$ with cardinality 24 and $E(G)$ the edge set, of cardinality 30. We describe each vertex of G by automorphism f , such that:

$$f: V(G) \rightarrow \{u_i, v_i, w_i, t_i \mid i \in \mathbb{Z}_6\}.$$

and

$$f: E(G) \rightarrow \{v_i v_{i+1}, v_i u_i, u_i w_i, u_i t_i, w_i t_{i+1} \mid i \in \mathbb{Z}_6\}.$$

According to the Figure 4, we have the vertices u_i, v_i of degree 3 and vertices w_i, t_i of degree 2, for all \mathbb{Z}_6 . $\mathbb{Z}_6 = \{0, 1, 2, 3, 4, 5\}$ is the cycle finite group of order 6 (or integer number of module 6).

Proof of Theorem 1: Let $G=Ca(C_6)$ be the Coronene graph. Since there exists 24 distinct vertices, we have $\binom{n}{2} = 276$ distinct shortest paths between vertices u and v of G . Also, in Coronene there are distances from one to seven, for every vertices $u, v \in V(G)$. In other words,

$$\forall u, v \in V(G), \exists d(u, v) \in \{1, 2, \dots, 7\}.$$

So, we will have seven partitions for proof.

I . If $d(u, v)=1$, then $D_1 = \{(v_i, v_{i+1}), (v_i, u_i), (u_i, w_i), (u_i, t_i), (w_i, t_{i+1}) \mid i \in \mathbb{Z}_6\}$ and $|D_1|=30$ (that is equal to $|E(G)|$). So, we have three subsets of it.

I -1. $\forall i \in \mathbb{Z}_6$, let $v=v_i$ and $u=u_i=v_{i+1}$. Since $\delta_{v_i} = \delta_{u_i} = 3$, hence $\delta_v + \delta_u = 6$ and $\delta_v \times \delta_u = 9$. Therefore $|\{(u, v) \mid u, v \in V(G), d(u, v) = 1 \ \& \ \delta_v + \delta_u = 6, \delta_v \times \delta_u = 9\}| = 6 \times 2$.

So, we have two terms $72x^1$, $108x^1$ of the Schultz polynomial and Modified Schultz polynomial, respectively.

I -2. $\forall i \in \mathbb{Z}_6$, let $v=t_i$, w_i and $u=u_i$. Since $\delta_{u_i} = 3$ and $\delta_{t_i} = \delta_{w_i} = 2$. So, $\delta_v + \delta_u = 5$ and $\delta_v \times \delta_u = 6$. Therefore $|\{(u, v) \mid u, v \in V(G), d(u, v) = 1 \ \& \ \delta_v + \delta_u = 5, \delta_v \times \delta_u = 6\}| = 6 \times 2$.

So, we have two sentences $60x^1$, $72x^1$ of the above polynomials.

I -3. $\forall i \in \mathbb{Z}_6$, let $v=w_i$ and $u=t_i$. Since $\delta_{t_i} = \delta_{w_i} = 2$. So, $\delta_v + \delta_u = 4$ and $\delta_v \times \delta_u = 4$.

Therefore $|\{(u, v) \mid u, v \in V(G), d(u, v) = 1 \ \& \ \delta_v + \delta_u = 4, \delta_v \times \delta_u = 4\}| = 6$.

In general, we have two terms $156x^1$, $204x^1$ for the Schultz polynomial and Modified Schultz polynomial, respectively.

II . If $d(u, v)=2$, then

$D_2 = \{(v_i, v_{i+2}), (v_i, u_{i+1}), (v_i, w_i), (v_i, t_i), (v_i, u_{i-1}), (u_i, t_{i+1}), (u_i, w_{i-1}), (w_i, t_i) \mid i \in \mathbb{Z}_6\}$ and $|D_2|=48$. Similarly, we have three subsets of it.

II -1. $\forall i \in \mathbb{Z}_6$, let $v=v_i$ and $u=v_{i+2}, u_{i+1}, u_{i-1}$ (or u_{i+5}). Since $\delta_{v_i} = \delta_{u_i} = 3$, hence $\delta_v + \delta_u = 6$ and $\delta_v \times \delta_u = 9$. Therefore $|\{(u, v) \mid u, v \in V(G), d(u, v) = 2 \ \& \ \delta_v + \delta_u = 6, \delta_v \times \delta_u = 9\}| = 6 \times 3$.

So, we have two terms $108x^2$, $162x^2$ for the Schultz polynomial and Modified Schultz polynomial, respectively.

II -2. $\forall i \in \mathbb{Z}_6$, let $(u=t_i, w_i \ \& \ v=v_i)$ or $(v=t_{i+1}, w_{i-1} \ \& \ u=u_i)$. Since $\delta_{v_i} = \delta_{u_i} = 3$ and $\delta_{t_i} = \delta_{w_i} = 2$, therefore $|\{(u, v) \mid u, v \in V(G), d(u, v) = 2 \ \& \ \delta_v + \delta_u = 5, \delta_v \times \delta_u = 6\}| = 24$. So, we have two sentences $120x^2$, $144x^2$ of these polynomials.

II -3. $\forall i \in \mathbb{Z}_6$, let $v=w_i$ and $u=t_i$. Since $\delta_{t_i} = \delta_{w_i} = 2$, therefore

$$|\{(u, v) \mid u, v \in V(G), d(u, v) = 2 \ \& \ \delta_v + \delta_u = 4, \delta_v \times \delta_u = 4\}| = 6.$$

Generally, we have two terms $252x^2$, $330x^2$ for the Schultz polynomial and Modified Schultz polynomial, respectively.

III. If $d(u, v) = 3$, then $D_3 = \{(v_i, v_{i+3}), (v_i, u_{i+2}), (v_i, u_{i-2}), (v_i, w_{i+1}), (v_i, t_{i+1}), (v_i, w_{i-1}), (v_i, t_{i-1}), (u_i, u_{i+1}), (t_i, t_{i+1}), (w_i, w_{i+1}) \mid i \in \mathbb{Z}_6\}$ and $|D_3| = 57$.

Similarly, we have three subsets of it.

III-1. $\forall i \in \mathbb{Z}_6$, let $v=v_i$ & $u=v_{i+3}, u_{i+2}, u_{i-2}$ or $v=v_{i+1}$ & $u=u_i$. Hence $\delta_v + \delta_u = 6$ and $\delta_v \times \delta_u = 9$. Therefore $|\{(u, v) \mid u, v \in V(G), d(u, v) = 3 \& \delta_v + \delta_u = 6, \delta_v \times \delta_u = 9\}| = 6 \times 3 + 3 = 21$

Then, we have $126x^3$ and $189x^3$ in these polynomials.

III-2. $\forall i \in \mathbb{Z}_6$, let $v=v_i$ & $u=t_{i+1}, t_{i-1}, w_{i+1}, w_{i-1}$. Thus

$|\{(u, v) \mid u, v \in V(G), d(u, v) = 3 \& \delta_v + \delta_u = 5, \delta_v \delta_u = 6\}| = 6 \times 4 = 24$.

So, we have $120x^3$ and $144x^3$.

III-3. $\forall i \in \mathbb{Z}_6$, let $v=w_i$ & $u=w_{i+1}$ or $v=t_i$ & $u=t_{i+1}$. Since $\delta_{t_i} = \delta_{w_i} = 2$, then

$|\{(u, v) \mid u, v \in V(G), d(u, v) = 3 \& \delta_v + \delta_u = 4, \delta_v \times \delta_u = 4\}| = 12$. Overall, there are the terms $294x^3, 381x^3$ for the Schultz polynomial and Modified Schultz polynomial, respectively.

IV. If $d(u, v) = 4$, then $D_4 = \{(v_i, u_{i+3}), (v_i, w_{i+2}), (v_i, w_{i-2}), (v_i, t_{i+2}), (v_i, t_{i-2}), (u_i, w_{i+1}), (u_i, t_{i-1}), (u_i, u_{i+2}), (w_i, t_{i+2}) \mid i \in \mathbb{Z}_6\}$ and $|D_4| = 54$. Similarly,

we have three subsets of D_4 .

IV-1. $\forall i \in \mathbb{Z}_6$, since $d(v_i, u_{i+3}) = d(u_i, u_{i+2}) = 4$, thus $|\{(u, v) \in V(G) \mid d(u, v) = 4 \& \delta_v + \delta_u = 6, \delta_v \times \delta_u = 9\}| = 12$. Thus, we have the term $72x^4$ for the Schultz polynomial and $108x^4$ for the Modified Schultz polynomial.

IV-2. $\forall i \in \mathbb{Z}_6$, let $(u=t_{i+2}, t_{i-2}, w_{i+2}, w_{i-2}$ & $v=v_i)$ or $(v=t_{i-1}, w_{i-1}, w_{i+1}$ & $u=u_i)$. Thus,

$|\{(u, v) \mid u, v \in V(G), d(u, v) = 4 \& \delta_v + \delta_u = 5, \delta_v \delta_u = 6\}| = 36$. So, we have the term $180x^4$ for the Schultz polynomial and $216x^4$ for the Modified Schultz polynomial.

IV-3. $\forall i \in \mathbb{Z}_6$, let $v=w_i$ & $u=w_{i+2}$. Thus,

$|\{(u, v) \in V(G) \mid u, v \in V(G), d(u, v) = 4 \& \delta_v + \delta_u = 4, \delta_v \delta_u = 4\}| = 6$.

Generally, the two terms for the Schultz polynomial and Modified Schultz polynomial are $276x^4, 348x^4$, respectively.

V. If $d(u, v) = 5$, then $D_5 = \{(v_i, t_{i+3}), (v_i, w_{i+3}), (u_i, w_{i+2}), (u_i, w_{i-2}), (u_i, t_{i+2}), (u_i, t_{i-2}), (u_i, u_{i+2}), (w_i, t_{i-1}) \mid i \in \mathbb{Z}_6\}$ and $|D_5| = 45$. Again, we have three

subsets of D_5 as above.

V-1. We have $|\{(u_i, u_{i+3}) \mid \forall i \in \mathbb{Z}_6, d(u_i, u_{i+3}) = 5 \& \delta_v + \delta_u = 5, \delta_v \times \delta_u = 9\}| = 3$. Hence, $18x^5$ and $27x^5$ are the terms for the Schultz polynomial and Modified Schultz polynomial, respectively.

V-2. $\forall i \in \mathbb{Z}_6$, let $(v=t_{i+2}, t_{i-2}, w_{i+2}, w_{i-2}$ & $u=u_i)$ or $(u=t_{i+3}, w_{i+3}$ & $v=v_i)$, therefore

$|\{(u, v) \mid u, v \in V(G), d(u, v) = 5 \& \delta_v + \delta_u = 5, \delta_v \delta_u = 6\}| = 36$. Thus, there is the term $180x^5$ for the Schultz polynomial and $261x^5$ for the Modified Schultz polynomial.

V -3. $\forall i \in \mathbb{Z}_6$ since $d(w_i, t_{i-1})=5$, $|\{(u,v) \in V(G) | d(u,v)=5 \& \delta_v + \delta_u = \delta_v \delta_u = 4\}|=6$.

In general, the terms are $222x^5$, $267x^5$ for these polynomials.

VI. If $d(u,v)=6$, then $D_6 = \{(u_i, t_{i+3}), (u_i, w_{i+3}), (w_i, w_{i+2}), (w_i, t_{i-2}), (t_i, t_{i+2}) | i \in \mathbb{Z}_6\}$ and $|D_6|=30$. It means that, we have two subsets of D_6 .

VI-1. We have $|\{(u_i, w_{i+3}), (u_i, t_{i+3}) | \forall i \in \mathbb{Z}_6, d(u,v)=6 \& \delta_v + \delta_u = 5, \delta_v \times \delta_u = 6\}|=12$. Then, $60x^6$ and $72x^6$ are the two terms for the Schultz polynomial and Modified Schultz polynomial, respectively.

VI-2. $\forall i \in \mathbb{Z}_6$, since $d(w_i, w_{i+2})=d(w_i, t_{i-2})=d(t_i, t_{i+2})=6$. Therefore, $|\{(u,v) | u,v \in V(G), d(u,v)=6 \& \delta_v + \delta_u = \delta_v \delta_u = 4\}|=18$. In general, we have $132x^6$ for the Schultz polynomial and $144x^6$ for the Modified Schultz polynomial.

VII. If $d(u,v)=7$, then $|D_7| = |\{\forall i \in \mathbb{Z}_6, (w_i, t_{i+3}), (w_i, w_{i+3}), (t_i, t_{i+3}) | d(u,v)=7 \& \delta_v + \delta_u = \delta_v \delta_u = 4\}|=12$. Thus, there is the same term $48x^7$ for the Schultz polynomial and Modified Schultz polynomial. Now, we enumerate all distinct shortest path of any $u, v \in V(G)$. Thus the Schultz polynomial of $Ca(C_6)$ is: $Sc(Ca(C_6), x) = 156x + 252x^2 + 294x^3 + 276x^4 + 222x^5 + 132x^6 + 48x^7$ and the Schultz index is $Sc(Ca(C_6)) = 4884$.

The Modified Schultz polynomial of $Ca(C_6)$ is:

$$Sc^*(Ca(C_6), x) = 204x + 330x^2 + 381x^3 + 348x^4 + 267x^5 + 144x^6 + 48x^7$$

and the Modified Schultz index $Sc^*(Ca(C_6)) = 5934$.

Thus, the *proof* of Theorem 1 is complete.

Proof of Theorem 2. Let $Ca(C_6)$ be the molecular graph of Coronene.

Since $D_i = D_i(3,3) \cup D_i(3,2) \cup D_i(2,2)$, $\forall i \in \{1, 2, \dots, 7\}$

therefore the set of distances in G is given by the following relation: $d(G, i) = |D_i| = |D_i(3,3)| + |D_i(3,2)| + |D_i(2,2)|$. Keeping in mind the definition of Hosoya polynomial and the data provided in the proof of Theorem 1, the formula of this polynomial in Coronene is:

$$H(G, x) = \sum_{i=0}^{d(G)} d(G, i)x^i = 24 + 30x + 48x^2 + 57x^3 + 54x^4 + 45x^5 + 30x^6 + 12x^7.$$

Hence, the Wiener and Hyper Wiener indices of Coronene are:

$$W(G) = \sum_{i=0}^{d(G)} i \times d(G, i) = 24 \times 0 + 30 \times 1 + 48 \times 2 + 57 \times 3 + 54 \times 4 + 45 \times 5 + 30 \times 6 + 12 \times 7 = 1002.$$

$$WW(G) = 1002 + (1/2)(48 \times 2 + 57 \times 3 \times 2 + 54 \times 4 \times 3 + 45 \times 5 \times 4 + 30 \times 6 \times 5 + 12 \times 7 \times 6) = 2697$$

Thus, the *proof* of Theorem 2 is complete.

CONCLUSIONS

In this paper, Schultz, Modified Schultz and Hosoya polynomials and their topological indices in the molecular graph of Coronene (constructed by Capra-operated benzenoid: $Ca(C_6)$ (or H_2)) are calculated. These polynomials and indices could be useful in the topological investigation of benzenoids molecules.

ACKNOWLEDGMENTS

The author is thankful to *Dr. Mehdi Alaeiyan* and *Seyed Hamid Hosseini* of Department of Mathematics, Iran University of Science and Technology (IUST) for their precious support and suggestions.

REFERENCES

1. D.B. West, "An Introduction to Graph Theory", Prentice-Hall, **1996**.
2. S. Klavžar and I. Gutman, *J. Chem. Inf. Comput. Sci.*, **1996**, 36, 1001.
3. A. Iranmanesh and Y. Alizadeh, *Digest. J. Nanomater. Bios.*, **2009**, 4, 67.
4. A.A. Dobrynin. *Croat. Chem. Acta*, **1999**, 4, 869.
5. M. Goldberg, *Tohoku Math. J.*, **1937**, 43, 104.
6. I. Gutman and S. Klavžar, *ACH Models Chem.*, **1996**, 133, 389.
7. H.P. Schultz, *J. Chem. Inf. Comput. Sci.*, **1989**, 29, 227.
8. H.P. Schultz, *J. Chem. Inf. Comput. Sci.*, **2000**, 40, 1158.
9. Y. Alizadeh, A. Iranmanesh and S. Mirzaie, *Digest. J. Nanomater. Bios.*, **2009**, 4, 7.
10. M.V. Diudea, *J. Chem. Inf. Comput. Sci.*, **1996**, 4, 833.
11. M.V. Diudea, *J. Chem. Inf. Comput. Sci.*, **1996**, 4, 535.
12. M. Eliasi and B. Taeri, *Appl. Anal. Discrete Math.*, **2008**, 2, 285.
13. O. Halakoo, O. Khormali and A. Mahmiani, *Digest. J. Nanomater. Bios.*, **2009**, 4(4), 687.
14. A. Heydari, *Digest. J. Nanomater. Bios.*, **2010**, 5, 51.
15. A. Heydari and B. Taeri, *MATCH Commun. Math. Comput. Chem.*, **2007**, 57, 665.
16. H. Hosoya, *Discrete Appl. Math.* **1988**, 19, 239.
17. S. Klavžar and I. Gutman, *J. Chem. Inf. Comput. Sci.*, **1997**, 37, 741.
18. A. Iranmanesh and Y. Alizadeh, *Int. J. Mol. Sci.*, **2008**, 9, 131.
19. A. Iranmanesh and O. Khormali, *MATCH Commun. Math. Comput. Chem.*, **2011**, 65, 93.

20. A. Iranmanesh and O. Khormali, *J. Comput. Theor. Nano Sci.*, **2008**, 5, 131.
21. A. Iranmanesh and Y. Alizadeh, *Digest. J. Nanomater. Bios.*, **2009**, 4, 607.
22. S. Klavžar and I. Gutman, *Disc. Appl. Math.*, **1997**, 80, 73.
23. W.C. Shiu and P.C.B. Lam, *Discrete Appl. Math.*, **1997**, 73, 101.
24. A.R. Ashrafi and M. Ghorbani, *Digest. J. Nanomater. Bios.*, **2009**, 4, 389.
25. A.R. Ashrafi and H. Shabani, *Digest. J. Nanomater. Bios.*, **2009**, 4, 453.
26. A.R. Ashrafi and S. Yousefi, *MATCH Commun. Math. Comput. Chem.*, **2007**, 4, 403.
27. M.V. Diudea, *Commun. Math. Comput. Chem. (MATCH)*, **2002**, 45, 109.
28. I. Gutman, *J. Chem. Inform. Comput. Sci.*, **1994**, 34, 1087.
29. H. Hosoya, *Bull. Chem. Soc. Jpn.*, **1971**, 44, 23.
30. H. Shabani and A.R. Ashrafi, *Digest. J. Nanomater. Bios.*, **2009**, 4, 423.
31. K. Xu, Computing, *Digest. J. Nanomater. Bios.*, **2011**, 6, 265.
32. Sh. Xu and H. Zhang, *J. Math. Chem.*, **2008**, 43, 2.
33. M.V. Diudea and A.R. Ashrafi, *Acta Chim. Sloven.*, **2010**, 57, 559.
34. M.V. Diudea, *MATCH Commun. Math. Comput. Chem.*, **2013**, 69, 93.
35. M.V. Diudea and M. Medeleanu, in: Gutman, B. Furtula (Eds.), "Distance in Molecular Graphs–Applications", Univ. Kragujevac, Kragujevac, MCM series **2012**, p. 27.
36. M.V. Diudea, *Studia UBB Chemia*, **2003**, 4, 3.
37. M.V. Diudea, *J. Chem. Inf. Model.*, **2005**, 45, 1002.

ON TOPOLOGICAL POLYNOMIALS OF WEIGHTED GRAPHS

MODJTABA GHORBANI^{a,*}, MOHAMMAD A. HOSSEINZADEH^b
and MIRCEA V. DIUDEA^c

ABSTRACT. Two edges e and f of a plane graph G are in relation opposite, e op f , if they are opposite edges of an inner face of G .

Relation op enables the partition the edge set of G into opposite edge strips ops. On this ground, Diudea defined Omega and Theta polynomial while Ashrafi et al. defined the Sadhana polynomial. In this paper a weighted version of these polynomials was introduced and several relations between them are demonstrated. Some molecular weights are suggested in view of using the derived topological indices in correlational studies.

Key Words: *Omega polynomial, Sadhana polynomial, Topological indices.*

INTRODUCTION

Mathematical chemistry is a branch of theoretical chemistry that studies molecular structures using mathematical methods, not necessarily referring to quantum mechanics. Chemical graph theory is an important tool for studying molecular structures. At the beginning, let us recall some definitions that will be used in this paper.

Let G be a simple molecular graph without directed and multiple edges and without loops, the vertex set $V(G)$ and edge-sets $E(G)$ of which representing the atoms and covalent bonds of the molecule. Suppose G is a connected molecular graph and $x, y \in V(G)$. The distance $d(x, y)$ between x and y is defined as the length of a minimum path between x and y . Two edges $e = ab$ and $f = xy$ of G are called co-distant, "e co f", if and only if $d(a, x) = d(b, y) = k$ and $d(a, y) = d(b, x) = k + 1$ or vice versa, for a non-negative

^a Department of Mathematics, Faculty of Science, Shahid Rajaee Teacher Training University, Tehran, 16785-136, I.R. Iran; * Corresponding author: mghorbani@srttu.edu

^b Department of Mathematical Science, Sharif University of Technology, Tehran, 11365-9415, I.R. Iran

^c Faculty of Chemistry and Chemical Engineering, Babes-Bolyai University, Arany Janos 11, 400028 Cluj, Romania

integer k . It is easy to see that the relation “ co ” is reflexive and symmetric but it is not necessarily transitive. Set $C(e) = \{ f \in E(G) \mid f \text{ } co \text{ } e \}$. If the relation “ co ” is transitive on $C(e)$ then $C(e)$ is called an orthogonal cut of G . The graph G is called a co-graph if and only if the edge set $E(G)$ is a union of disjoint orthogonal cuts. If any two subsequent edges of an edge-cut sequence are topologically parallel within the same face of the covering, such a sequence is called a quasi-orthogonal cut or *opposite edge strips ops s*. If G is a co-graph, then $|c_k| = |s_k|$, and $S(G) = \{s_1, s_2, \dots, s_k\}$ forms a partition of $E(G)$.

Diudea defined the Ω -polynomial of G on ops as $[1 - 4]$:

$$\Omega(x) = \sum_{i=1}^k x^{|s_i|}$$

Another polynomial also related to the ops in G , but counting the *non-opposite* edges is the *Sadhana* polynomial, defined by Ashrafi et al. [5] as:

$$Sd(x) = \sum_{i=1}^k x^{|E|-|s_i|}$$

The *Sadhana* index $Sd(G)$ was defined by Khadikar et al [6, 7] as:

$$Sd(G) = \sum_{i=1}^k |E(G)| - |s_i|.$$

From the definition of Omega polynomial, one can obtain the *Sadhana* polynomial by replacing $x^{|s_i|}$ with $x^{|E|-|s_i|}$ in the Omega polynomial. Then the *Sadhana* index will be the first derivative of $Sd(x)$ evaluated at $x = 1$, see for more details [8 - 14].

RESULTS AND DISCUSSION

Let $e=uv$ be an edge of G and v be an arbitrary vertex. Denote by $w_G(e)$ and $w_G(v)$ the weights of edge e and vertex v , respectively. For each strip s of G , the weight of s can be defined as:

$$w_{G,e}(s) = \sum_{e \in s} w_G(e),$$

$$w_{G,v}(S) = \sum_{v \in V(G[s])} w_G(v) = \sum_{uv \in s} (w_G(u) + w_G(v)).$$

where $G[s]$ is the induced subgraph in G by s . One can see that if G is a co-graph, then

$$w_e(G) = \sum_{e \in E(G)} w_G(e) = \sum_{s \in S} \sum_{e \in s} w_G(e).$$

By using the concept of weighted graph, we define three new versions of Omega polynomial: the edge weighted-, vertex weighted- and edge-vertex-weighted Omega polynomial. These new polynomials are defined as follows:

$$\begin{aligned}\Omega_e(G, x) &= \sum_{s \in S} \left[\frac{w_{G,e}(s)}{|s|} \right] m(G, s) x^{|s|}, \\ \Omega_v(G, x) &= \sum_{s \in S} m(G, s) x^{\lfloor \frac{w_{G,v}(s)}{2} \rfloor}, \\ \Omega_{ev}(G, x) &= \sum_{s \in S} \left[\frac{w_{G,e}(s)}{|s|} \right] m(G, s) x^{\lfloor \frac{w_{G,v}(s)}{2} \rfloor}.\end{aligned}$$

Obviously, if the weight of each edge and vertex is 1, then

$$\Omega_e(G, x) = \Omega_v(G, x) = \Omega_{ev}(G, x) = \Omega(G, x).$$

Analogously, for Theta and Sadhana polynomials we have:

$$\begin{aligned}\Theta_e(G, x) &= \sum_{c \in C} w_{G,e}(c) m(G, c) x^{|c|}, \\ \Theta_v(G, x) &= \sum_{c \in C} m(G, c) |c| x^{\lfloor \frac{w_{G,v}(c)}{2} \rfloor}, \\ \Theta_{ev}(G, x) &= \sum_{c \in C} w_{G,e}(c) m(G, c) x^{\lfloor \frac{w_{G,v}(c)}{2} \rfloor}, \\ Sd_e(G, x) &= \sum_{c \in C} m(G, c) x^{w_e(G) - w_{G,e}(c)}, \\ Sd_v(G, x) &= \sum_{c \in C} \left[\frac{w_{G,v}(c)}{2|c|} \right] m(G, c) x^{|E| - |c|}, \\ Sd_{ev}(G, x) &= \sum_{c \in C} \left[\frac{w_{G,v}(c)}{2|c|} \right] m(G, c) x^{w_e(G) - w_{G,e}(c)}.\end{aligned}$$

One can see again, if the weight of each edge and vertex be 1, then $\Theta_e(G, x) = \Theta_v(G, x) = \Theta_{ev}(G, x) = \Theta(G, x)$ and $Sd_e(G, x) = Sd_v(G, x) = Sd_{ev}(G, x) = Sd(G, x)$, respectively. Note that, in co-graphs, $|c_k| = |s_k|$, and the symbols c/s interchanges.

Let G and H be two edge weighted graphs. The Cartesian product graph of G and H is a graph with vertex set $V(G \times H) = V(G) \times V(H)$ and edge set

$$E(G \times H) = \{((a, b), (c, d)) : a=c, bd \in E(H) \text{ or } b = d, ac \in E(G)\}.$$

Then, the weight of an edge $((a, b), (c, d))$ is as follows:

If $a = c$, then $w_{G \times H}(((a, b), (c, d))) = w_H(bd)$,

If $b = d$, then $w_{G \times H}(((a, b), (c, d))) = w_G(ac)$.

In this section we compute the weighted Omega polynomial of Cartesian product of two weighted graphs.

Lemma 1. Let G and H be graphs. Then we have:

- (a) $|V(G \times H)| = |V(G)| |V(H)|$,
 $|E(G \times H)| = |E(G)| |V(H)| + |V(G)| |E(H)|$;
- (b) $G \times H$ is connected if and only if G and H are connected;
- (c) If (a, x) and (b, y) are vertices of $G \times H$ then
 $d_{G \times H}((a, x), (b, y)) = d_G(a, b) + d_H(x, y)$;
- (d) the Cartesian product is associative.

We recall that for a graph G and $e \in E(G)$,

$$N(e) = |E| - (n_e u(e|G) + n_e v(e|G)).$$

The following result is direct consequence of Lemma 1.

Lemma 2. Suppose $(a, x), (b, y)$ are adjacent vertices of $G \times H$, where G and H are co-graphs. Then

$$N_{G \times H}((a, x)(b, y)) = \begin{cases} |V(G)| N(f) & \text{for } a = b \text{ and } x y = f \in E(H) \\ |V(H)| N(g) & \text{for } x = y \text{ and } ab = g \in E(G) \end{cases}$$

$$w_{G \times H, e}(c) = \begin{cases} |V(G)| w_{H, e}(c) & \text{for } c = |V(G)| c_H \\ |V(H)| w_{G, e}(c) & \text{for } c = |V(H)| c_G \end{cases}$$

Theorem 3. Let G and H be connected co-graphs. Then

Proof. By using Lemmas 1 and 2 and definition of Omega polynomial of a graph, we have:

$$\Omega_e(G \times H, x) = \sum_{c_1} \left[\frac{w_{G, e}(c_1)}{|c_1|} \right] m_1 \cdot x^{|V(H)| c_1} + \sum_{c_2} \left[\frac{w_{H, e}(c_2)}{|c_2|} \right] m_2 \cdot x^{|V(G)| c_2}$$

and

$$\begin{aligned} \Omega_e(G \times H, x) &= \sum_c m(G \times H, c) \cdot x^c \\ &= \sum_{c_1} \left[\frac{w_{G, e}(c_1)}{|c_1|} \right] m_1 \cdot x^{|V(H)| c_1} \\ &\quad + \sum_{c_2} \left[\frac{w_{H, e}(c_2)}{|c_2|} \right] m_2 \cdot x^{|V(G)| c_2} \end{aligned}$$

where, $m_1 = m(G, c_1)$, $m_2 = m(H, c_2)$ and this completes the proof.

Theorem 4. Let G_1, G_2, \dots, G_n be connected co-graphs. Then we have:

$$\Omega_e(G_1 \times G_2 \times \dots \times G_n, x) = \sum_{i=1}^n \sum_{c_i} \left[\frac{w_{G_i, e}(c_i)}{|c_i|} \right] m(G_i, c_i) \cdot x^{|\bigcup_{j=1}^n V(G_j)| c_i}$$

Proof. We use induction on n . By Theorem 3, the result is valid for $n = 2$. Let $n \geq 3$ and assume the theorem holds for $n - 1$. Set $G = G_1 \times \dots \times G_{n-1}$. Then we have

$$\begin{aligned} \Omega_e(G \times G_n, x) &= \sum_c \left[\frac{w_{G, e}(c)}{|c|} \right] m(G, c) \cdot x^{|\bigcup_{j=1}^n V(G_j)| c} \\ &\quad + \sum_{c_n} \left[\frac{w_{G_n, e}(c_n)}{|c_n|} \right] m(G_n, c_n) \cdot x^{|\bigcup_{j=1}^n V(G_j)| c_n} \\ &= \sum_{i=1}^{n-1} \sum_{c_i} \left[\frac{w_{G_i, e}(c_i)}{|c_i|} \right] m(G_i, c_i) \cdot x^{|\bigcup_{j=1}^n V(G_j)| c_i} \\ &\quad + \sum_{c_n} \left[\frac{w_{G_n, e}(c_n)}{|c_n|} \right] m(G_n, c_n) \cdot x^{|\bigcup_{j=1}^n V(G_j)| c_n} \\ &= \sum_{i=1}^n \sum_{c_i} \left[\frac{w_{G_i, e}(c_i)}{|c_i|} \right] m(G_i, c_i) \cdot x^{|\bigcup_{j=1}^n V(G_j)| c_i} \end{aligned}$$

One can compute same results for the Sadhana and Theta polynomials as previously.

Examples

Example 1. Suppose Q_n denotes a hypercube of dimension n . Then by Theorem 2,

$$\begin{aligned} \Omega_e(Q_n, x) &= \Omega_e(K_2^n, x) = n \cdot \sum_c \left[\frac{w_{K_2, e}(c)}{|c|} \right] m(K_2, c) \cdot x^{|\bigcup_{j=1}^n V(K_2)| c} \\ &= n \cdot [w_e(K_2)] \cdot x^{2^{n-1}} \end{aligned}$$

Example 2. Let P_n be a path of length n and C_n an n -cycle. Then

$$\Omega_e(C_n, x) = \begin{cases} \sum_{i=1}^n \left[\frac{w_{C_n, e}(c_i)}{2} \right] x^2 & 2|n \\ \sum_{i=1}^n [w_{C_n, e}(c_i)] x & 2|n \end{cases}$$

Also we have $\Omega_e(P_n, x) = \sum_{i=1}^{n-1} [w_{P_n, e}(c_i)] x$. So,

$$\Omega_e(P_n \times P_m, x) = \sum_{i=1}^{n-1} [w_{P_n, e}(c_i)] x^m + \sum_{j=1}^{m-1} [w_{P_n, e}(c_j)] x^n .$$

In the other words

$$\Omega_e(P_n \times C_m, x) = \begin{cases} \sum_{i=1}^{n-1} [w_{P_n, e}(c_i)] x^m + \sum_{j=1}^{\frac{m}{2}} \left[\frac{w_{C_m, e}(c_j)}{2} \right] x^{2n} & 2|m \\ \sum_{i=1}^{n-1} [w_{P_n, e}(c_i)] x^m + \sum_{j=1}^m [w_{C_m, e}(c_j)] x^n & 2 \nmid m \end{cases} ,$$

$$\Omega_e(C_n \times C_m, x) = \begin{cases} \sum_{i=1}^n [w_{C_n, e}(c_i)] x^m + \sum_{j=1}^m [w_{C_m, e}(c_j)] x^n & 2|m, 2 \nmid n \\ \sum_{i=1}^n [w_{C_n, e}(c_i)] x^m + \sum_{j=1}^{\frac{m}{2}} \left[\frac{w_{C_m, e}(c_j)}{2} \right] x^{2n} & 2|m, 2 \nmid n \\ \sum_{i=1}^{\frac{n}{2}} \left[\frac{w_{C_n, e}(c_i)}{2} \right] x^{2m} + \sum_{j=1}^m [w_{C_m, e}(c_j)] x^n & 2 \nmid m, 2|n \\ \sum_{i=1}^{\frac{n}{2}} \left[\frac{w_{C_n, e}(c_i)}{2} \right] x^{2m} + \sum_{j=1}^{\frac{m}{2}} \left[\frac{w_{C_m, e}(c_j)}{2} \right] x^{2n} & 2 \nmid m, 2|n \end{cases} .$$

CONCLUSIONS

In this paper we defined three weighted versions of Omega, Theta and Sadhana polynomials and then we established some theoretical relations for them. We can apply the concept of weighted graph in molecular graph theory. The most important weight for edge/bond is the (covalent) bond length while for the vertex/atom, we can use the atomic radius, the partial charge in an optimized molecule by a quantum method, and so one. The topological indices derived from weighted polynomials, reflecting more properly the chemical characteristics of bonds/atoms, could be better used in QSAR/QSPR studies.

REFERENCES

1. P.E. John, A.E. Vizitiu, S. Cigher, M.V. Diudea, *MATCH Commun. Math. Comput. Chem.*, **2007**, 57, 479.
2. M.V. Diudea, S. Cigher, A.E. Vizitiu, O. Ursu, P.E. John, *Croat. Chem. Acta*, **2006**, 79, 445.
3. A.E. Vizitiu, S. Cigher, M.V. Diudea, M.S. Florescu, *MATCH Commun. Math. Comput. Chem.*, **2007**, 57, 457.
4. M.V. Diudea, *Carpath. J. Math.*, **2006**, 22, 43.
5. A.R. Ashrafi, M. Ghorbani, M. Jalali, *Ind. J. Chem.*, **2008**, 47A, 535.
6. P.V. Khadikar, S. Joshi, A.V. Bajaj, D. Mandloi, *Bioorg. Med. Chem. Lett.*, **2004**, 14, 1187.
7. P.V. Khadikar, V.K. Agrawal, S. Karmarkar, *Bioorg. Med. Chem.*, **2002**, 10, 3499.
8. M. Ghorbani, A.R. Ashrafi, *J. Comput. Theor. Nanosci.*, **2006**, 3, 803.
9. A.R. Ashrafi, M. Jalali, M. Ghorbani, M.V. Diudea, *MATCH Commun. Math. Comput. Chem.*, **2008**, 60(3), 905.
10. A.R. Ashrafi, M. Ghorbani, *MATCH Commun. Math. Comput. Chem.*, **2008**, 60, 359.
11. M. Ghorbani, M. Jalali, *Studia UBB Chemia*, **2009**, 2, 145.
12. M. Ghorbani, M. Jaddi, *Optoelectron. Advan. Mater.-Rapid Commun.*, **2010**, 4(4), 540.
13. M. Ghorbani, *Iranian J. Math. Chem.*, **2010**, 1(1), 105.
14. M. Ghorbani, *Iranian J. Math. Chem.*, **2011**, 2(2), 1.

GENERALIZED DEGREE DISTANCE OF TREES, UNICYCLIC AND BICYCLIC GRAPHS

ASMA HAMZEH^a, ALI IRANMANESH^{a*},
SAMANEH HOSSEIN-ZADEH^a, MIRCEA V. DIUDEA^b

ABSTRACT. A generalization of degree distance of graphs we recently proposed as a new topological index. In this paper, the new index is studied in trees, in unicyclic graphs of girth k and in some special classes of bicyclic graphs. Lower-bound and upper-bound values and analytical formulae to calculate this index in the studied graphs are given.

Keywords: Generalized degree distance, unicyclic graphs, bicyclic graphs, trees.

INTRODUCTION

A graph invariant is any function on a graph that does not depend on the labeling of its vertices. Topological indices TIs are graph invariants calculated on the graphs associated to molecules. The distance-based TIs have been widely used in theoretical chemistry to establish relations between the structure and the properties of molecules: correlations with physical, chemical and biological properties of chemical compounds have been reported [1]. In this paper, only simple graphs are considered.

Let G be a connected graph with vertex and edge sets $V(G)$ and $E(G)$, respectively, their cardinalities being $n=|V(G)|$ and $m=|E(G)|$. In a molecular graph, the vertices represent atoms and the edges the covalent bonds. The distance between the vertices u and v of G is denoted by $d_G(u,v)$ ($d(u,v)$ for short), and represent the length of a minimum path connecting them. Let $d_G(v)$ be the degree of a vertex v or the valence of a given atom in the hydrogen depleted molecular graph. The eccentricity, denoted

^a Department of Mathematics, Faculty of Mathematical Sciences, Tarbiat Modares University, P.O. Box: 14115-137, Tehran, Iran, iranmanesh@modares.ac.ir

^b Faculty of Chemistry and Chemical Engineering, "Babes-Bolyai" University, 400028 Cluj, Romania

by $\varepsilon(v)$, is defined as the maximum distance from vertex v to any other vertex in G . The diameter of a graph, $d(G)$, is the maximum eccentricity over all vertices in G . For any vertex $v \in V(G)$, the open neighborhood of v is the set $N(v) = \{u \in V(G) | uv \in E(G)\}$ and the closed neighborhood of v is the set $N[v] = N(v) \cup \{v\}$. The girth of a graph is the length of a shortest cycle contained in the graph. A connected graph G with n vertices and m edges is called unicyclic if $m = n$; G is called bicyclic if $m = n + 1$.

The additively weighted Harary index was defined in [2] as follows:

$$H_A(G) = \sum_{\{u,v\} \subseteq V(G)} d^{-1}(u,v)(d_G(u) + d_G(v)).$$

Dobrynin and Kochetova in [3] and Gutman in [4] introduced a new graph invariant, called the degree distance. It is defined as:

$$D'(G) = \sum_{\{u,v\} \subseteq V(G)} d(u,v)(d_G(u) + d_G(v)).$$

The first Zagreb index was originally defined as [5]:

$$M_1(G) = \sum_{u \in V(G)} d_G(u)^2$$

The first Zagreb index can also be expressed as the sum over all the edges of G :

$$M_1(G) = \sum_{uv \in E(G)} [d_G(u) + d_G(v)].$$

We refer the readers to [6] for the proof of this fact and for more information on the Zagreb index.

The first Zagreb co-index of a graph G is defined in [7] as:

$$\bar{M}_1(G) = \sum_{uv \notin E(G)} [d_G(u) + d_G(v)].$$

Let $d(G, k)$ be the number of pairs of vertices of a graph G located at distance k , λ be a real number, and

$$W_\lambda(G) = \sum_{k \geq 1} d(G, k)k^\lambda$$

be a Wiener-type invariant of G associated to a real number λ , see [8, 9] for details.

A generalization of the degree distance, denoted by $H_\lambda(G)$ was proposed [10]. For every vertex u , the "degree distance sum" is defined as:

$$H_\lambda(u) = D^\lambda(u)d_G(u)$$

where the distance sum is calculated on the distance matrix raised at power λ :

$$D^\lambda(u) = \sum_{v \in V(G)} d^\lambda(u, v).$$

So we have:

$$H_\lambda(G) = \sum_{u \in V(G)} H_\lambda(u) = \sum_{u \in V(G)} D^\lambda(u) d_G(u) = \sum_{\{u,v\} \subseteq V(G)} d^\lambda(u, v) (d_G(u) + d_G(v))$$

where λ is a real number. If $\lambda = 0$, then $H_\lambda(G) = 4m$. When $\lambda = 1$, this new topological index $H_\lambda(G)$ equals the degree distance index (i.e. Dobrynin or Schultz index). The properties of the degree distance index were studied in [11-14]. Also, if $\lambda = -1$, then $H_\lambda(G) = H_A(G)$ (see above). The relation of our new index with other intensely studied indices motivated our present (and future) study.

Throughout this paper, C_n , P_n , K_n and S_n denote the cycle, path, complete and star graphs on n vertices, respectively. The complement of a graph G is a graph H on the same vertices such that two vertices of H are adjacent if and only if they are not adjacent in G . The graph H is usually denoted by \overline{G} . Our other notations are standard and taken mainly from [1, 15, 16].

Extremal graph theory is a branch of the mathematical field of graph theory. Extremal graph theory studies extremal (maximal or minimal) graphs which satisfy a certain property. Extremality can be taken with respect to different graph invariants, such as order, size or girth. The problem of determining extremal values and corresponding extremal graphs of some graph invariants is the topic of several papers [11-14, 17-26]. In this paper, we characterize n -vertex unicyclic graphs with girth k , having minimum and maximum generalization degree distance and we derive the formula of this index for some special classes of bicyclic graphs. Furthermore, we determine the minimum and maximum of this index for trees.

RESULTS AND DISCUSSION

Let us construct the graph G as follows: Let H and H' be two disjoint connected graphs such that $|V(H)| \geq 1$ and $|V(H')| \geq 1$. Suppose that there is $w \in V(H)$ such that $d_H(w) \geq 2$, $u \in V(H')$ and $P = wv_1v_2 \dots v_p$ is a pendant path of length $p \geq 1$ attached at w , and the edge wu is connecting H and H' (see Figure 1). Let $G' = \pi(H, w, P, H')$ be the graph obtained from the graph G by removing the edge wu and inserting the edge v_pu .

We call such a transformation from G to G' a π -transform of a graph G . Note that if $d_G(w) = 2$, then G and G' are isomorphic [27].

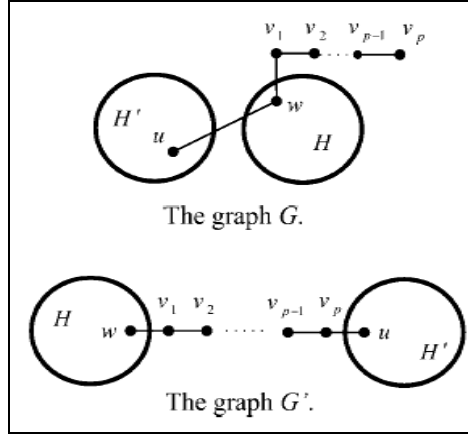


Figure 1. π -transform applied to G at vertex w .

Theorem 2.1. Let $G' = \pi(H, w, P, H')$ be a π -transform of a graph G and λ be a positive integer. Then $H_\lambda(G') \geq H_\lambda(G)$, and the equality is held if and only if $d_G(w) = 2$.

Proof. If $d_G(w) = 2$, then it is obvious the isomorphism $G \cong G'$, so assume that $d_G(w) > 2$. The only vertices that change degree after performing the π -transform are w and v_p . So

$$\begin{aligned}
 H_\lambda(w, G) &= d_G(w) \left(\sum_{v \in V(H)} d^\lambda(v, w) + (1^\lambda + 2^\lambda + \dots + p^\lambda) \right) \\
 &\quad + \sum_{v \in V(H')} (d(u, v) + 1)^\lambda, \\
 H_\lambda(w, G') &= (d_G(w) - 1) \left(\sum_{v \in V(H)} d^\lambda(v, w) + (1^\lambda + 2^\lambda + \dots + p^\lambda) \right) \\
 &\quad + \sum_{v \in V(H')} (d(u, v) + p + 1)^\lambda, \\
 H_\lambda(v_p, G) &= \left(\sum_{v \in V(H)} (d(v, w) + p)^\lambda + (1^\lambda + 2^\lambda + \dots + (p-1)^\lambda) \right) \\
 &\quad + \sum_{v \in V(H')} (d(u, v) + p + 1)^\lambda,
 \end{aligned}$$

$$H_\lambda(v_p, G') = 2\left(\sum_{v \in V(H)} (d(v, w) + p)^\lambda + (1^\lambda + 2^\lambda + \dots + (p-1)^\lambda)\right) + \sum_{v \in V(H')} (d(u, v) + 1)^\lambda.$$

Put $A = (H_\lambda(w, G') + H_\lambda(v_p, G')) - (H_\lambda(w, G) + H_\lambda(v_p, G))$, so we have:

$$\begin{aligned} A &= (d_G(w) - 2) \sum_{v \in V(H')} (d(u, v) + p + 1)^\lambda + \sum_{v \in V(H)} (d(v, w) + p)^\lambda - p^\lambda \\ &\quad + (2 - d_G(w)) \sum_{v \in V(H')} (d(u, v) + 1)^\lambda - \sum_{v \in V(H)} d^\lambda(v, w) \\ &= (d_G(w) - 2) \left(\sum_{v \in V(H')} ((d(u, v) + p + 1)^\lambda - (d(u, v) + 1)^\lambda) \right) \\ &\quad + \sum_{v \in V(H) - \{w\}} (d(v, w) + p)^\lambda + p^\lambda - p^\lambda - \sum_{v \in V(H)} d^\lambda(v, w) \\ &= (d_G(w) - 2) \left(\sum_{v \in V(H')} ((d(u, v) + p + 1)^\lambda - (d(u, v) + 1)^\lambda) \right) \\ &\quad + \sum_{v \in V(H) - \{w\}} ((d(v, w) + p)^\lambda - d^\lambda(v, w)). \end{aligned}$$

Since λ is a positive integer and $d_G(w) > 2$, thus $A \geq 0$. Let $V(P) = \{v_1, v_2, \dots, v_p\}$, then for every vertex $x \in \{v_1, v_2, \dots, v_{p-1}\}$, we have $H_\lambda(x, G') = H_\lambda(x, G)$. Now we assume $x \in V(H) - \{w\}$. So

$$\begin{aligned} H_\lambda(x, G) &= d_G(x) \left(\sum_{v \in V(H)} d^\lambda(x, v) + \sum_{v \in V(H')} (d(u, v) + 1 + d(w, x))^\lambda \right. \\ &\quad \left. + (1 + d(w, x))^\lambda + \dots + (p + d(w, x))^\lambda \right), \\ H_\lambda(x, G') &= d_G(x) \left(\sum_{v \in V(H)} d^\lambda(x, v) + \sum_{v \in V(H')} (d(u, v) + 1 + p + d(w, x))^\lambda \right. \\ &\quad \left. + (1 + d(w, x))^\lambda + \dots + (p + d(w, x))^\lambda \right). \end{aligned}$$

Thus for every vertex $x \in V(H) - \{w\}$, $H_\lambda(x, G') \geq H_\lambda(x, G)$. Now we assume $x \in V(H')$. So

$$\begin{aligned} H_\lambda(x, G) &= d_G(x) \left(\sum_{v \in V(H')} d^\lambda(x, v) + \sum_{v \in V(H)} (d(w, v) + 1 + d(u, x))^\lambda \right. \\ &\quad \left. + (2 + d(u, x))^\lambda + \dots + (p + 1 + d(u, x))^\lambda \right), \\ H_\lambda(x, G') &= d_G(x) \left(\sum_{v \in V(H')} d^\lambda(x, v) + \sum_{v \in V(H)} (d(w, v) + 1 + p + d(u, x))^\lambda \right. \\ &\quad \left. + (1 + d(u, x))^\lambda + \dots + (p + d(u, x))^\lambda \right). \end{aligned}$$

Thus for every vertex $x \in V(H')$, we have $H_\lambda(x, G') \geq H_\lambda(x, G)$. Considering the above inequality, we obtain, $H_\lambda(G') \geq H_\lambda(G)$ and the proof is completed.

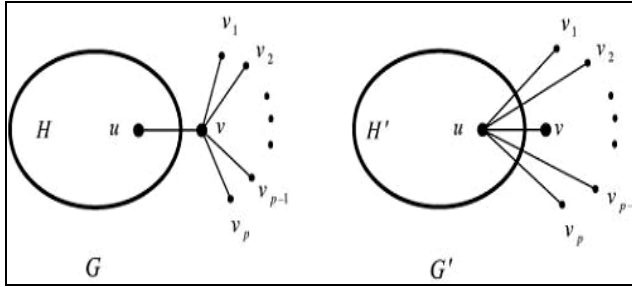


Figure 2. σ -transform applied to G at vertex v .

Let v be a vertex of degree $p+1$ in a graph G , which is not a star, such that vv_1, vv_2, \dots, vv_p are pendant edges incident with v and u is the neighbor of v distinct from v_1, v_2, \dots, v_p . We form a graph $G' = \sigma(G, v)$ by removing edges vv_1, vv_2, \dots, vv_p and adding new edges uv_1, uv_2, \dots, uv_p . We say that G' is a σ -transform of G (see Figure 2). Note that if $d_G(u) = 1$, then G and G' are isomorphic [27].

Theorem 2.2. Let $G' = \sigma(G, v)$ be a σ -transform of G and λ be a positive integer. Then $H_\lambda(G) \geq H_\lambda(G')$, and the equality is held if and only if $d_G(u) = 1$.

Proof. The only vertices that change the degree after performing the σ -transform are u and v . So

$$\begin{aligned}
 H_\lambda(u, G) &= d_G(u) \left(\sum_{x \in V(H)} d^\lambda(x, u) + 1 + 2^\lambda p \right), \\
 H_\lambda(u, G') &= (d_G(u) + p) \left(\sum_{x \in V(H)} d^\lambda(x, u) + 1 + p \right), \\
 H_\lambda(v, G) &= (p+1) \left(\sum_{x \in V(H)} (d(x, u) + 1)^\lambda + p \right), \\
 H_\lambda(v, G') &= \sum_{x \in V(H)} (d(x, u) + 1)^\lambda + 2^\lambda p.
 \end{aligned}$$

Put $A = (H_\lambda(u, G) + H_\lambda(v, G)) - (H_\lambda(u, G') + H_\lambda(v, G'))$, thus

$$\begin{aligned}
 A &= p \sum_{x \in V(H)} (d(x,u)+1)^\lambda + 2^\lambda p d_G(u) - p d_G(u) - p \sum_{x \in V(H)} d^\lambda(x,u) - 2^\lambda p \\
 &= p \left(\sum_{x \in V(H)} (d(x,u)+1)^\lambda - \sum_{x \in V(H)} d^\lambda(x,u) \right) + 2^\lambda p (d_G(u)-1) - p d_G(u).
 \end{aligned}$$

For every vertex $x \in V(P) = \{v_1, v_2, \dots, v_p\}$, we have:

$$\begin{aligned}
 H_\lambda(x, G) &= \sum_{x \in V(H)} (d(x,u)+2)^\lambda + 1 + 2^\lambda (p-1), \\
 H_\lambda(x, G') &= \sum_{x \in V(H)} (d(x,u)+1)^\lambda + 2^\lambda p.
 \end{aligned}$$

Then

$$H_\lambda(x, G) - H_\lambda(x, G') = \sum_{x \in V(H)} ((d(x,u)+2)^\lambda - (d(x,u)+1)^\lambda) + 1 - 2^\lambda.$$

For every vertex $x \in V(H) - \{u\}$, we have:

$$\begin{aligned}
 H_\lambda(x, G) &= d_G(x) \left(\sum_{y \in V(H)} d^\lambda(x,y) + (d(x,u)+1)^\lambda + p(d(x,u)+2)^\lambda \right), \\
 H_\lambda(x, G') &= d_G(x) \left(\sum_{y \in V(H)} d^\lambda(x,y) + (d(x,u)+1)^\lambda + p(d(x,u)+1)^\lambda \right).
 \end{aligned}$$

It is clear that for every vertex $x \in V(H) - \{u\}$, $H_\lambda(x, G) \geq H_\lambda(x, G')$.

If $d_G(u) = 1$, then $G \cong G'$, so we assume that $d_G(u) \geq 2$. By considering the above inequality, we have, $H_\lambda(G) \geq H_\lambda(G')$ and the proof is completed.

Corollary 2.3. Let T be a tree on $n \geq 2$ vertices and λ be a positive integer. Then $H_\lambda(S_n) < H_\lambda(T) < H_\lambda(P_n)$.

Proof. Let T be a tree on n vertices. By using of Theorem 2.1, we easily get that $H_\lambda(T) < H_\lambda(P_n)$ and by using of Theorem 2.2, we easily get that $H_\lambda(S_n) < H_\lambda(T)$.

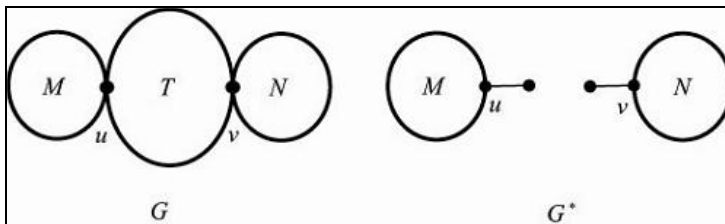


Figure 3. The graphs G and G^* .

Let T be a tree on $n \geq 2$ vertices. Then $D'(S_n) < D'(T) < D'(P_n)$. In the following Corollary, we will find a bound for H_λ in bicyclic graphs.

Corollary 2.4. Let G and G^* be two graphs which is shown in Figure 3, where M and N are vertex disjoint cycles, T is a tree with $k \geq 3$ vertices, $V(M) \cap V(T) = \{u\}$, $V(N) \cap V(T) = \{v\}$, G^* is formed from G by setting the tree T to be P_k with end vertices u and v . Suppose that $G \neq G^*$ and λ is a positive integer. If $|V(M)|, |V(N)| \geq 2$, then $H_\lambda(G) < H_\lambda(G^*)$.

Proof. The proof follows from Corollary 2.3.

Lemma 2.5. Let G be a connected graph with at least three vertices and λ be a negative integer.

- (i) If G is not isomorphic to K_n , then $H_\lambda(G) < H_\lambda(G+e)$, where $e \in E(\overline{G})$,
- (ii) If G has an edge e not being a cut edge, then $H_\lambda(G) > H_\lambda(G-e)$.

Proof. (i) Suppose that G is not a complete graph. Then there exists a pair of vertices u and v in G such that $uv \in E(\overline{G})$. It is obvious that $d_G(x, y) \geq d_{G+uv}(x, y)$ for any pair of vertices x and y in G . Also, we have $d_G(u, v) > 1 = d_{G+uv}(u, v)$. Moreover, $d_{G+uv}(w) \geq d_G(w)$ for any w in G . Because λ is negative integer, we have $d_{G+uv}^\lambda(u, v) > d_G^\lambda(u, v)$, so $H_\lambda(G) < H_\lambda(G+e)$.

(ii) Since the edge e is not a cut edge in G , we have $G-e$ is connected and not isomorphic to the complete graph of the same order. Thus, by (i), we have $H_\lambda(G-e) < H_\lambda((G-e)+e) = H_\lambda(G)$, as expected.

Let $U_{n,k}$ be the set of all unicyclic graphs of order $n \geq 3$ with girth $k \geq 3$. Also, let $H_{n,k}$ be a subset of $U_{n,k}$ such that contain a cycle C_k and the remaining vertices of graph make up only a subgraph that has exactly a common vertex with C_k . Obviously this subgraph is a tree. By $L_{n,k}$, we denote the graph obtained from C_k and P_{n-k+1} by indentifying a vertex of C_k with an end vertex of P_{n-k+1} and by $S_{n,k}$ we denote the graph obtained from C_k and S_{n-k+1} by indentifying a vertex of C_k with a vertex of maximum degree of S_{n-k+1} . Now we characterize the minimum and maximum generalization degree distance over this special classes of unicyclic graphs.

Theorem 2.6. If $G \in H_{n,k}$, and λ is a positive integer, then $H_\lambda(G) \leq H_\lambda(L_{n,k})$, and equality is held if and only if $G \cong L_{n,k}$.

Proof. Since $H_{n,k}$ contain only one cycle and one tree, according to Corollary 2.3, the maximum H_λ occur when tree is a path. If path is connected to cycle with vertex of minimum degree, by π -transform, H_λ is more than of the case that path connected to cycle with vertex of maximum degree. Therefore bound is obtained by calculating $H_\lambda(L_{n,k})$ and the proof is completed.

Theorem 2.7. If $G \in H_{n,k}$, and λ is a positive integer. Then $H_\lambda(G) \geq H_\lambda(S_{n,k})$, and equality is held if and only if $G \cong S_{n,k}$.

Proof. Since $H_{n,k}$ contain only one cycle and one tree, according to Corollary 2.3, the minimum H_λ occur when tree is a star. If star is connected to cycle with vertex of maximum degree, by σ -transform H_λ is less than of the case that star connected to cycle with vertex of minimum degree. Therefore bound is obtained by calculating $H_\lambda(S_{n,k})$ and the proof is completed.

Let λ be a negative integer. Define $D^{\lambda^*}(u) = \sum_{v \in V(G) - \{u\}} d^\lambda(u, v)$.

Theorem 2.8. Let G be a connected graph of order $n \geq 2$ and size $m \geq 1$ and λ is negative integer. Then

$M_1(G) + 2d^\lambda mn - d^\lambda M_1(G) - 2d^\lambda m \leq H_\lambda(G) \leq (1 - 2^\lambda)M_1(G) + 2^{\lambda+1}mn - 2^{\lambda+1}m$ and equality is held if and only if $d \leq 2$, where d is the diameter of G .

Proof. First, let us prove that the right-hand side inequality holds. For each vertex x in G , we have

$$\begin{aligned} D^{\lambda^*}(x) &= d_G(x) + \sum_{y \in V(G) - N[x]} d_G^\lambda(x, y) \\ &\leq d_G(x) + 2^\lambda(n - d_G(x) - 1), \end{aligned}$$

where the equality is attained if and only if $\varepsilon(x) \leq 2$. So

$$\begin{aligned} H_\lambda(G) &= \sum_{x \in V(G)} d_G(x) D^{\lambda^*}(x) \\ &\leq \sum_{x \in V(G)} d_G(x) (d_G(x) + 2^\lambda(n - d_G(x) - 1)) \\ &= (1 - 2^\lambda)M_1(G) + 2^{\lambda+1}mn - 2^{\lambda+1}m, \end{aligned}$$

where the equality is attained if and only if for each x , $\varepsilon(x) \leq 2$. So, $H_\lambda(G) \leq (1-2^\lambda)M_1(G) + 2^{\lambda+1}mn - 2^{\lambda+1}m$ with equality if and only if the diameter of G is at most 2, as desired. Now, we turn to the left-hand side inequality. For each vertex x in G ,

$$\begin{aligned} D^{\lambda^*}(x) &= d_G(x) + \sum_{y \in V(G) - N[x]} d_G^\lambda(x, y) \\ &\geq d_G(x) + d^\lambda(n - d_G(x) - 1), \end{aligned}$$

where the equality is attained if and only if for any $y \in V(G) - N[x]$, $d(x, y) = d$, implying that $d \leq 2$. Therefore,

$$\begin{aligned} H_\lambda(G) &= \sum_{x \in V(G)} d_G(x) D^{\lambda^*}(x) \\ &\geq \sum_{x \in V(G)} d_G(x) (d_G(x) + d^\lambda(n - d_G(x) - 1)) \\ &= M_1(G) + 2d^\lambda mn - d^\lambda M_1(G) - 2d^\lambda m, \end{aligned}$$

where the equality is attained if and only if $d \leq 2$. This completes the proof.

A cactus is a connected graph each of whose blocks is either a cycle or an edge. If a cactus has no cycles, then it is just a tree, and if it has exactly a cycle, then it is a unicyclic graph. For $0 \leq k \leq \frac{n-1}{2}$, we let G_n^k be an n -vertex k -cycle cactus obtained from the n -vertex star by adding k independent edges among $n-1$ pendant vertices.

The following Lemma is a result of [28].

Lemma 2.9. Let G be an n -vertex k -cycle cactus with $0 \leq k \leq \frac{n-1}{2}$.

Then $M_1(G) \leq n^2 - n + 6k$, and equality is held if and only if $G \cong G_n^k$.

Theorem 2.10. Let G be an n -vertex k -cycle cactus with $0 \leq k \leq \frac{n-1}{2}$

and λ be a negative integer. Then we have:

$$H_\lambda(G) \leq (1-2^\lambda)(n^2 - n + 6k) + 2^{\lambda+1}(n^2 - 2n + kn + 1 - k),$$

and equality is held if and only if $G \cong G_n^k$.

Proof. Note that G has $n+k-1$ edges. By Theorem 2.8 and Lemma 2.9, we have

$$H_\lambda(G) \leq (1-2^\lambda)M_1(G) + 2^{\lambda+1}mn - 2^{\lambda+1}m$$

$$\begin{aligned} &\leq (1-2^\lambda)(n^2 - n + 6k) + 2^{\lambda+1}(n-1)(n+k-1) \\ &= (1-2^\lambda)(n^2 - n + 6k) + 2^{\lambda+1}(n^2 - 2n + kn + 1 - k). \end{aligned}$$

The equality is held if and only if the diameter of G is 2 and $G \cong G_n^k$. Note that G_n^k has diameter 2. Thus,

$$H_\lambda(G) \leq (1-2^\lambda)(n^2 - n + 6k) + 2^{\lambda+1}(n^2 - 2n + kn + 1 - k)$$

with equality if and only if $G \cong G_n^k$, so completing the proof.

By Theorem 2.8, we immediately have the following results for H_λ of trees and unicyclic graphs, respectively.

Corollary 2.11. Let G be a unicyclic graph on $n \geq 3$ vertices and λ be a negative integer. Then $H_\lambda(G) \leq (1-2^\lambda)(n^2 - n + 6) + 2^{\lambda+1}(n^2 - n)$ and equality is held if and only if $G \cong G_n^1$.

The final result in this paper is related to trees and we obtain an upper and lower bound for generalization degree distance of trees.

Corollary 2.12. Let T be a tree on $n \geq 2$ vertices and λ be a negative integer. Then $H_\lambda(P_n) < H_\lambda(T) \leq (1-2^\lambda)(n^2 - n) + 2^{\lambda+1}(n^2 - 2n + 1)$, and the right equality is held if and only if the tree is a star, $T \cong S_n$.

Proof. By Theorem 2.8, the right-hand side inequality is held. Now, we turn to the left-hand side inequality. We prove among all nontrivial connected graphs of order n , the graphs with the maximum and minimum H_λ are K_n and P_n , respectively. The case of $n = 2$ is trivial. So we suppose that $n \geq 3$ and we first prove that K_n is maximal with respect to H_λ . If G is not a complete graph, then we can add some edges into G such that we obtain $G \cong K_n$. By Lemma 2.5, $H_\lambda(G) \leq H_\lambda(K_n)$, with equality if and only if $G \cong K_n$. Now, let us prove that P_n is minimal with respect to H_λ . Suppose first that G is not isomorphic to a tree. Let $T(G)$ be a spanning tree of G . It then follows from Lemma 2.5, that $H_\lambda(G) > H_\lambda(T(G))$. So we need only to consider the case of G is a tree. If G is not isomorphic to the path, then by using the π -transform on G for some times according to the status of graph G we obtain the path P_n . Then by Theorem 2.1 and negative integer λ , we have $H_\lambda(P_n) < H_\lambda(G)$, as expected.

By the above Corollary, if T is a tree on $n \geq 2$ vertices, then $H_\lambda(P_n) < H_\lambda(T) \leq H_\lambda(S_n)$.

ACKNOWLEDGMENTS

This work was partially supported by Center of Excellence of Algebraic Hyperstructures and its Applications of Tarbiat Modares University (CEAHA). Also the authors would like to thank the referee for the valuable comments.

REFERENCES

1. M.V. Diudea, I. Gutman, L. Jantschi, "Molecular Topology", Huntington, NY, **2001**.
2. Y. Alizadeh, A. Iranmanesh, T. Došlić, *Discret Math.*, **2013**, 313, 26.
3. A.A. Dobrynin, A. A. Kochetova, *J. Chem. Inf. Comput. Sci.*, **1994**, 34, 1082.
4. I. Gutman, *J. Chem. Inf. Comput. Sci.*, **1994**, 34, 1087.
5. I. Gutman, N. Trinajstić, *Chem. Phys. Lett.*, **1972**, 17, 535.
6. S. Nikolić, G. Kovačević, A. Miličević, N. Trinajstić, *Croat. Chem. Acta*, **2003**, 76, 113.
7. T. Došlić, *Ars Math. Contemp.*, **2008**, 1, 66.
8. I. Gutman, *Indian J. Chem.*, **1997**, 36A, 128.
9. I. Gutman, A. A. Dobrynin, S. Klavžar, L. Pavlović, *Bull. Inst. Combin. Appl.*, **2004**, 40, 23.
10. A. Hamzeh, A. Iranmanesh, S. Hossein-Zadeh, "On the generalization of degree distance of graphs", submitted.
11. P. Dankelmann, I. Gutman, S. Mukwembi, H.C. Swart, *Discrete Appl. Math.*, **2009**, 157, 2773.
12. S. Hossein-Zadeh, A. Hamzeh, A. R. Ashrafi, *Miskolc Math. Notes*, **2010**, 11, 129.
13. I. Tomescu, *Discrete Appl. Math.*, **2008**, 156, 125.
14. I. Tomescu, *Discrete Appl. Math.*, **1999**, 98, 159.
15. F. Harary, "Graph Theory", Addison-Wesley, Reading, MA, **1969**.
16. N. Trinajstić, "Chemical Graph Theory", CRC Press, Boca Raton, FL. **1992**.
17. A.R. Ashrafi, T. Došlić, A. Hamzeh, *MATCH Commun. Math. Comput. Chem.*, **2011**, 65, 85.
18. O. Bucicovschi, S. M. Cioabă, *Discrete Appl. Math.*, **2008**, 156, 3518.
19. Z. Du, B. Zhou, N. Trinajstić, *MATCH Commun. Math. Comput. Chem.*, **2011**, 66, 681.
20. H. Deng, *MATCH Commun. Math. Comput. Chem.*, **2007**, 57, 597.
21. L. Feng, W. Liu, *MATCH Commun. Math. Comput. Chem.*, **2011**, 66, 699.
22. Y. Huang, B. Liu, M. Zhang, *MATCH Commun. Math. Comput. Chem.*, **2010**, 63, 453.
23. O. Khormali, A. Iranmanesh, I. Gutman, A. Ahmadi, *MATCH Commun. Math. Comput. Chem.*, **2010**, 64, 783.

24. L. Sun, S. Wei, *MATCH Commun. Math. Comput. Chem.*, **2009**, 62, 699.
25. D. Vukičević, S. M. Rajtmajer, N. Trinajstić, *MATCH Commun. Math. Comput. Chem.*, **2008**, 60, 65.
26. H. Zhang, X. Jiang, Y. Yang, *MATCH Commun. Math. Comput. Chem.*, **2009**, 61, 697.
27. A. Ilić, D. Stevanović, L. Feng, G. Yu, P. Dankelmann, *Discrete Appl. Math.*, **2011**, 159, 779.
28. B. Zhou, N. Trinajstić, *J. Math. Chem.*, **2008**, 44, 235.

EFFECT OF ENZYME DEGLYCOSYLATION ON THE AMPEROMETRIC DETECTION OF GLUCOSE AT PDH-MODIFIED ELECTRODE

ANIKÓ KILLYÉNI^a, MARIA E. YAKOVLEVA^b,
CLEMENS K. PETERBAUER^c, DÓNAL LEECH^d,
LO GORTON^b, IONEL CATALIN POPESCU^{a,*}

ABSTRACT. The effect of deglycosylation of pyranose dehydrogenase (PDH), obtained from *Agaricus meleagris* and recombinantly expressed in *Pichia pastoris*, on the amperometric detection of glucose was investigated. Glycosylated (gPDH) and deglycosylated (dgPDH) PDH were immobilized on spectrographic graphite (G) simultaneously with an Os redox polymer (Os-RP). The amperometric response of G/Os-RP/gPDH and G/Os-RP/dgPDH to glucose was recorded using flow injection measurements and cyclic voltammetry. A significant increase in the maximum catalytic current density was observed for G/Os-RP/dgPDH [$(148.7 \pm 0.14) \mu\text{A}/\text{cm}^2$] compared with G/Os-RP/gPDH [$(81.4 \pm 1.4) \mu\text{A}/\text{cm}^2$]. Additionally, the deglycosylation of the enzyme resulted in a higher substrate-enzyme affinity ($K_M^{\text{app}} = 2.44 \pm 0.10 \text{ mM}$), compared with glycosylated PDH ($K_M^{\text{app}} = 7.52 \pm 0.34 \text{ mM}$).

Keywords: *pyranose dehydrogenase, enzyme deglycosylation, glucose amperometric detection, Os-redox polymer*

INTRODUCTION

PDH (EC 1.1.99.29) is a monomeric sugar oxidoreductase and is produced in a narrow group of fungi, classified based on ecophysiological characteristics as litter-decomposing fungi. PDH contains a covalently bound flavin adenine dinucleotide (FAD) [1] as a prosthetic group and was originally isolated from the edible mushroom *Agaricus bisporus* [2-4]. Beside *Agaricus bisporus* it was also purified from *Agaricus xanthoderma* [5], *Agaricus rhacodes* [6] and *Agaricus meleagris* (*Am*) [1, 7].

^a *Universitatea Babeş-Bolyai, Facultatea de Chimie și Inginerie Chimică, Str. Kogălniceanu, Nr. 1, RO-400084 Cluj-Napoca, Romania, * cpopescu@chem.ubbcluj.ro*

^b *Department of Analytical Chemistry/Biochemistry and Structural Biology, Lund University, P.O. Box 124, SE-22155 Lund, Sweden*

^c *Food Biotechnology Laboratory, Department of Food Science & Technology, BOKU-University of Natural Resources and Life Sciences, Muthgasse 18, A-1190 Vienna, Austria*

^d *School of Chemistry, National University of Ireland, University Road, Galway, Ireland*

Structurally and catalytically PDH is related to two other enzymes: pyranose oxidase (POx) and cellobiose dehydrogenase (CDH). However, in contrast to POx, PDH displays broader substrate specificity and variable regioselectivity. Moreover, PDH is inactive with molecular oxygen as electron acceptor.

Depending on the substrate and enzyme source PDH is able to catalyze mono- as well as dioxidation reactions. Monoxidation occurs at C-1, C-2 or C-3 position and dioxidation at C-2,3 or C-3,4 positions [8]. All these characteristics made PDH very attractive for utilization in membraneless enzymatic biofuel cells (EBFCs). Another feature of PDH is its ability to work under physiological conditions (pH ~7), which is a significant advantage in the construction of implantable EBFCs.

Due to these unique properties, PDH was found to be very attractive for a number of technological applications and, consequently, its simple and effective production was considered. Thus, the *Amp*PDH genes were expressed in various heterologous expression hosts such as *Aspergillus spp.* [9], *Escherichia coli* (*E. coli*) and *Pichia pastoris* (*P. pastoris*) [10].

The expression in *Aspergillus spp.* was shown to be time consuming and involving a rather complicated genetic manipulation process. At the same time, PDH expression in *E. coli* resulted in no soluble or active enzyme [10]. A successful expression of *Amp*PDH using *P. pastoris* as host organism was recently reported [10], and this approach allowed a large-scale production of PDH based on a simplified purification scheme. The MW of *Amp*PDH expressed in *P. pastoris* was determined by SDS-PAGE to be ~93 kDa with an overglycosylation of ~30%, whereas the native *Amp*PDH has a MW of ~66.5 kDa with 7 % glycosylation [1].

The removal of the glycan shell from the enzyme molecule decreases the distance between the enzyme redox center and the electrode surface [11-14] and, according to the Marcus equation [15], direct electron transfer should be facilitated. Therefore, *Amp*PDH was deglycosylated with endoglycosidase H_f (Endo H_f) and the effect was studied in both direct and mediated electron transfer mode [16]. It was found that by removing the glycan shell from the *Amp*PDH one can achieve direct electron transfer between the bound FAD in the enzyme active site and the electrode [16].

At the same time, it was shown that deglycosylation of *Amp*PDH has a favorable effect on the biocatalytic oxidation of glucose.

Furthermore, aiming at investigating the use of PDH in the development of EBFCs, PDH was immobilized together with different Os redox polymers [17, 18]. Additionally, in order to increase the catalytic current output as well as the coulombic efficiency, PDH was co-immobilized with CDH [19].

In this work a comparative study of the behavior of glycosylated (gPDH) and deglycosylated PDH (dgPDH) was carried out by the separate immobilization of the above mentioned enzymes, coupled with an Os redox polymer (Os-RP), onto the surface of spectrographic graphite electrodes.

The bioelectrocatalytic activity for glucose oxidation of the so obtained modified electrodes was investigated by using flow injection (FI) and cyclic voltammetry (CV) measurements under different experimental conditions.

RESULTS AND DISCUSSION

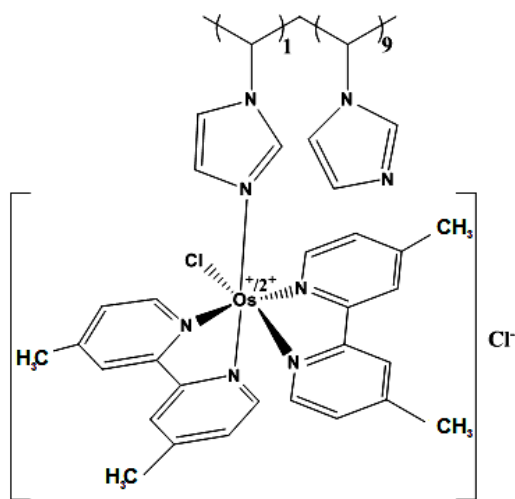
Optimization of bioelectrodes

The effect of deglycosylation on the bioelectrocatalytic activity of PDH was investigated by carrying out the immobilization of gPDH or dgPDH on the surface of graphite electrode. The enzyme immobilization was done by simple adsorption of the dissolved enzymes from a mixture containing the Os-RP and a cross-linking agent [poly(ethylene glycol) diglycidyl ether 400] (PEGDGE). In order to perform a reliable comparison, equal amounts (in terms of activity) of gPDH and dgPDH were deposited on the electrode surface (for more details see the Experimental section).

It is well known that an efficient electron transfer between the enzyme redox center, the redox mediator and the electrode surface requires a careful choice of the value of the applied potential. Thus, taking into account that the value of the formal standard potential (E°) of the mediator must be ~50 mV higher than the corresponding value of the enzyme redox center [20], an Os-RP (Scheme 1) having a E° value of +32 mV vs. Ag|AgCl, 0.1M KCl was chosen to connect the enzyme redox center to the electrode. At the same time, the E° value of the selected Os-RP was more positive with ~170 mV than that of the bound FAD cofactor of AmPDH (-140 mV vs. Ag|AgCl, 0.1 M KCl (pH 7.4); [19]).

In order to find the optimum value for the applied potential, the amperometric response of the G/Os-RP/gPDH and G/Os-RP/dgPDH modified electrodes was recorded operated under flow conditions (a constant flow rate of 0.45 mL/min) at different applied potentials, gradually varied from -200 to +300 mV vs. Ag|AgCl, 0.1 M KCl in steps of 50 mV. For each value of the applied potential, the current response of the investigated modified electrodes was monitored during the injection of 50 μ L of 5 mM glucose solution (Figure 1). Glucose was chosen as substrate for all measurements performed with the modified bioelectrodes because it was shown that glycosylated PDH exhibits a high activity towards this substrate [18].

As can be seen in Figure 1, the bioelectrocatalytic current recorded for both modified electrodes becomes significant at potential values higher than -50 mV vs. Ag|AgCl, 0.1M KCl. Furthermore, an increase in the applied potential results in an increase in the amperometric response until values higher than +200 mV vs. Ag|AgCl, 0.1M KCl when a plateau is reached. Consequently, in order to achieve the highest sensitivity for all investigated bioelectrodes an applied potential of +200 mV vs. Ag|AgCl, 0.1M KCl was used for all further measurements.



Scheme 1. Structure of the Os redox polymer (Os-RP).

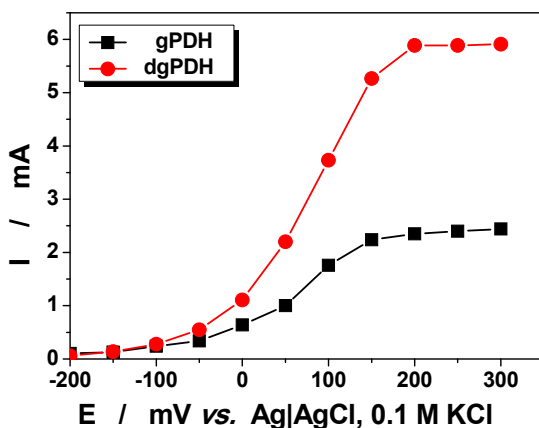


Figure 1. Dependence of the biocatalytic current on the applied potential observed at G/Os-RP/gPDH and G/Os-RP/dgPDH modified electrodes. *Experimental conditions: supporting electrolyte, 50 mM PB containing 137 mM NaCl (pH 7.4); flow rate, 0.45 mL/min; injected sample, 50 μ L of 5 mM glucose.*

At the same time, the data from Figure 1 show that the maximum current response recorded at G/Os-RP/dgPDH electrode is approximately two-fold higher than that measured at G/Os-RP/gPDH. This behavior indicates that the deglycosylated PDH possesses a much higher bioelectrocatalytic activity than the glycosylated PDH.

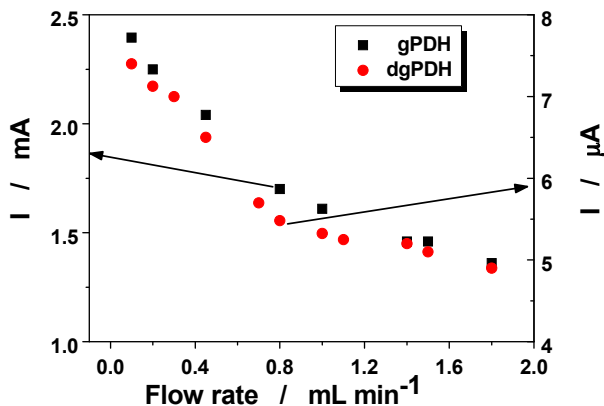


Figure 2. Influence of the flow rate on the amperometric response recorded at G/Os-RP/gPDH and G/Os-RP/dgPDH modified electrodes.

Experimental conditions: applied potential, 200 mV vs. Ag|AgCl, 0.1M KCl; supporting electrolyte, 50 mM PB containing 137 mM NaCl (pH 7.4); injected sample, 50 μ L of 3 mM glucose.

PDH from *Agaricus meleagris* can oxidize D-glucose transiently to 2-dehydro-D-glucose or 3-dehydro-D-glucose and, further, to 2,3-didehydro-D-glucose [8]. Therefore, taking into account this complex behavior of PDH it was interesting to evaluate the influence of the flow rate on the current response of the modified bioelectrodes (Figure 2). The increase in the flow carrier rate leads, as expected for FI measurements, to a clear decrease into the current response as the time for the enzyme reaction to occur at the electrode surface decreases and also the enzyme product, which for glucose as substrate is also a substrate for PDH, is more rapidly removed from the electrode surface. Thus, for example at 1.8 mL/min for G/Os-PR-gPDH modified electrodes the decrease was \sim 50 % and for G/Os-PR-dgPDH modified electrodes was \sim 30 %. In order to choose an optimum value of the flow rate (high enough for shortening the time spent for a measurement, but not too high to significantly diminish the bioelectrode sensitivity), all further measurements were performed at a flow rate of 0.45 mL/min. For this flow rate value both types of biosensors showed a minor decrease in the current response (less than 10%).

Bioelectrodes characterization

Cyclic voltammograms recorded at both modified electrodes, in the absence and presence of glucose (Figure 3), gave evidence for the electrocatalytic activity of the investigated bioelectrodes. In Table 1 are summarized the values for the catalytic efficiency $[CE = 100 \cdot (I_{p, \text{substrate}} - I_{p, 0}) / I_{p, 0}]$, where $I_{p, \text{substrate}}$ and $I_{p, 0}$ stand for the peak current in presence and in absence

of the substrate, respectively, estimated at the same potential value]. It can be noticed that the catalytic efficiency corresponding to the G/Os-RP/dgPDH modified electrode is slightly higher than the value estimated for the G/Os-RP/gPDH modified electrode.

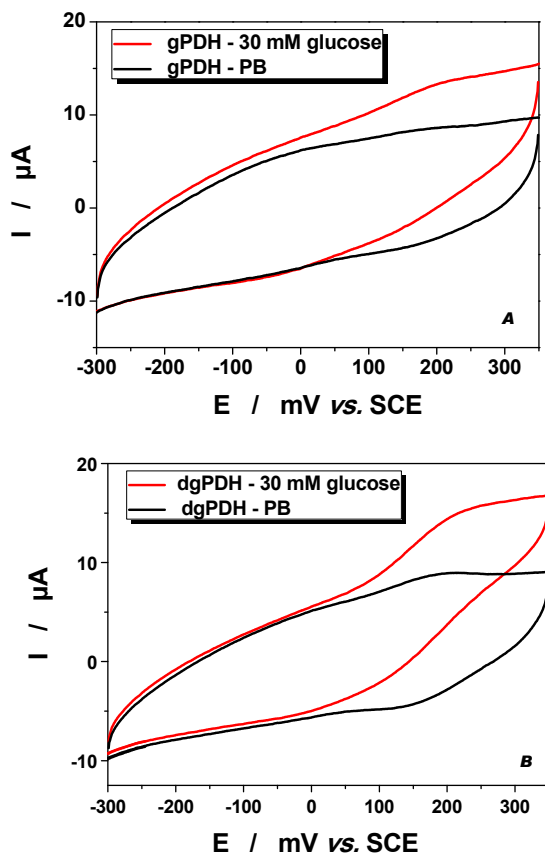


Figure 3. CV response recorded at G/Os-RP/gPDH (A) and G/Os-RP/dgPDH (B) modified electrodes in absence and in presence of 30 mM glucose.

Experimental conditions: supporting electrolyte, 50 mM PB containing 137 mM NaCl (pH 7.5); scan rate, 10 mV/s; starting potential, -0.300 V vs. SCE.

Table 1. Bioelectrocatalytic efficiency of the *Am*PDH modified electrodes estimated for 30 mM glucose (for experimental conditions see Figure 3).

Bioelectrode	CE (%)
G/Os-RP/gPDH	56
G/O-RP/dgPDH	67

Moreover, the CV recorded at G/Os-RP/dgPDH in absence of the substrate shows a pair of better defined redox peaks, which can not be observed on the CV recorded at G/Os-RP/gPDH. This peculiar behavior of the G/Os-RP/dgPDH modified bioelectrode can be attributed to a better electrical connection existing in the electrochemical chain deglycosylated PDH – Os-RP - graphite electrode.

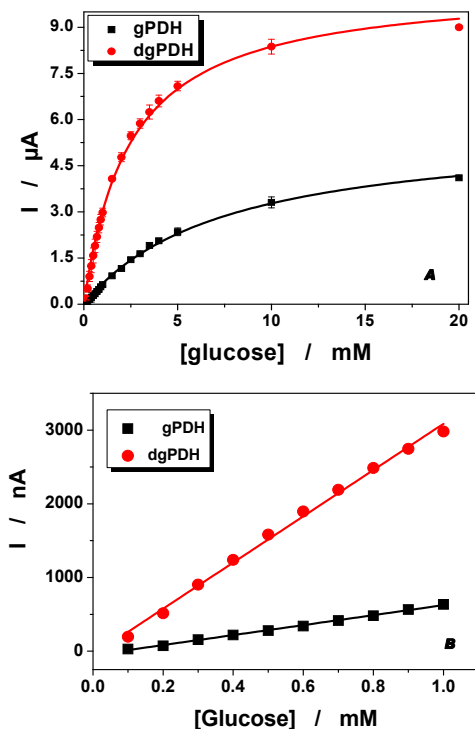


Figure 4. Calibration curves (A), and the linear range (B) of G/Os-RP/gPDH and G/Os-RP/dgPDH using glucose as substrate. *Experimental conditions: applied potential, 200 mV vs. Ag|AgCl, 0.1M KCl; supporting electrolyte, 50 mM PB containing 137 mM NaCl (pH 7.4); flow rate, 0.45 mL/min.*

The kinetic parameters corresponding to the modified bioelectrodes were estimated by using nonlinear fitting of the calibration curves to glucose exhibited in Figure 4A. The results are summarized in Table 2. It can be noticed that the biosensor based on dgPDH showed a much higher catalytic current density [$I_{\max} = (148.7 \pm 0.14) \mu\text{A}/\text{cm}^2$] than that measured for gPDH [$I_{\max} = (81.4 \pm 1.4) \mu\text{A}/\text{cm}^2$]. This finding proves once again the higher bioelectrocatalytic activity of the deglycosylated PDH.

Table 2. The kinetic parameters estimated for the modified bioelectrodes (for experimental conditions see Figure 4).

Biosensor	K_M^{app} (mM)	J_{max} ($\mu A/cm^2$)	Sensitivity ($\mu A/mMcm^{-2}$)	R^2/N
G/Os-RP/dgPDH	2.4 ± 0.1	148.7 ± 0.14	61.4 ± 2.9	0.996 / 19
G/Os-RP/gPDH	7.5 ± 0.3	81.4 ± 1.4	10.9 ± 0.3	0.996 / 19

At the same time, deglycosylation of PDH resulted in a lower value of the apparent Michaelis-Menten constant ($K_M^{app} = 2.4 \pm 0.1$ mM) compared with that estimated for gPDH ($K_M^{app} = 7.5 \pm 0.3$ mM). This behavior suggests either a higher enzyme-substrate affinity for dgPDH, or a higher permeability to glucose of the deglycosylated enzyme matrix associated with a higher accessibility of the Os-RP for the deglycosylated enzyme.

For both modified bioelectrodes the linear range was practical the same, being placed between 0.1 up to 1 mM (Figure 4B).

The increase in the maximum current response and the substrate affinity for the G/Os-RP/dgPDH bioelectrode could be due to: (i) a faster electron transfer between the Os-RP and the covalently bound FAD cofactor of dgPDH; (ii) an increase in the substrate accessibility at the dgPDH active center, due to a higher permeability of the Os-RP – dgPDH network [14].

dgPDH selectivity

*Am*PDH showed a noticeable bioelectrocatalytic activity toward various sugars such as: 2-deoxy-D-galactose, 2-deoxy-D-glucose, cellobiose, fucose, lactose, maltose, mannose, sucrose, trehalose, galactose, xylose [18]. Aiming to investigate the selectivity of deglycosylated PDH, the sensitivities of the G/Os-RP/dgPDH bioelectrode towards galactose, xlyose, mannose, and lactose were estimated as the I_{max}/K_M^{app} ratios, calculated with the values obtained by the fitting of the experimental calibration curves to the Michaelis-Menten equation. The obtained results are shown in Figure 5.

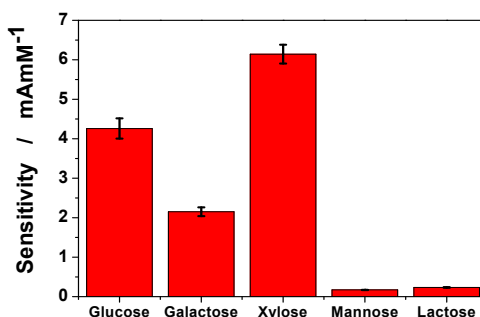


Figure 5. Sensitivity of G/Os-RP/dgPDH modified electrodes towards different substrates. The error bars correspond to the standard deviation for 3 successive measurements.

Experimental conditions: see Figure 4.

The dgPDH modified electrodes show a noticeable sensitivity for all investigated substrates. It is interesting to notice that dgPDH exhibits the highest sensitivity for xylose, contrarily to gPDH which showed the highest sensitivity for glucose [18]. This unexpected change in the enzyme selectivity after its deglycosylation is not explained until now.

Short term stability of bioelectrodes

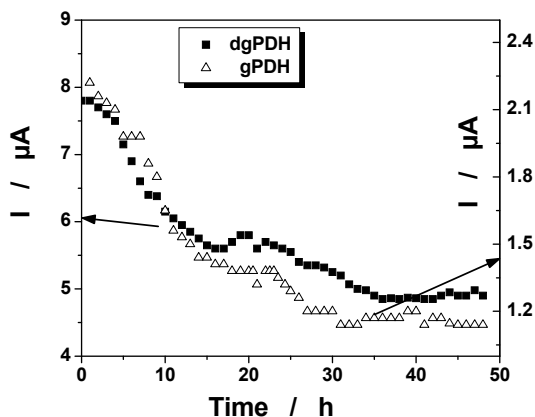


Figure 6. Time evolution of the amperometric response of G/Os-RP/gPDH and G/Os-RP/dgPDH modified electrodes for glucose.

Experimental conditions: applied potential 200 mV vs. Ag|AgCl, 0.1M KCl; 50 mM PB, 137 mM NaCl, 5 mM glucose, pH 7.4; flow rate 0.450 mL/min

The operational stability of the bioelectrode is one of its key parameters and, consequently, it was evaluated further. Figure 6 shows the results of the test of the stability performed for both bioelectrodes based on *Am*PDHs, under a constant flow of 5 mM glucose.

For both modified electrodes, a pronounced decrease in the current response was observed during the first 20 h. Thus, for G/Os-RP/gPDH electrode the current decreases to ~37% of the initial response, while for G/Os-RP/dgPDH electrode the decrease was slightly smaller (~25%). Furthermore, after ~35 h spent under a constant flow of glucose, the current response of both bioelectrodes reached a plateau placed at ~63% for G/Os-RP/dgPDH and at ~56% for G/Os-RP/gPDH.

CONCLUSIONS

In the present study the effect of deglycosylation of PDH on the amperometric response to glucose of G/Os-RP/PDH modified electrodes was investigated. The obtained results confirmed the beneficial effect of the removal of the glycan shell on the behavior of the bioelectrode. This effect

materialized as: (i) an increase in the sensitivity of the bioelectrode for amperometric detection of glucose; (ii) an increase in the enzyme affinity towards its main substrate (glucose); (iii) an unchanged short term operational stability; (iv) a change of the enzyme selectivity towards its substrates.

In conclusion, it was established that, by simple immobilization of the deglycosylated PDH simultaneously with a convenient Os redox polymer and a cross-linker (PEGDGE) on the surface of a graphite electrode, a modified bioelectrode with a good sensitivity, selectivity and short term operational stability can be obtained. The bioelectrochemical characteristics of this bioelectrode recommend it as a suitable transducer for biofuel cells.

EXPERIMENTAL SECTION

Materials

Pyranose dehydrogenase from *Agaricus meleagris* (AmPDH) was recombinantly expressed in *Pichia pastoris* and deglycosylated with Endo Hf (New England Biolabs, Bionordiska AB, Stockholm, Sweden) as described elsewhere [10]. Poly(ethylene glycol)(400) diglycidyl ether (PEGDGE), ferricinium hexafluorophosphate and D(+)-glucose were purchased from Sigma-Aldrich Chemie GmbH (Steinheim, Germany). The osmium redox polymer ($[\text{Os}(\text{dmbpy})_2(\text{PVI})_{10}\text{Cl}]^{+2/+}$, $E^{\circ} = +76$ mV vs. SCE, where dmbpy stands for 4,4'-dimethyl-2,2'-bipyridine and PVI is poly(N-vinylimidazole)) was synthesized as described in [21].

In all experiments the supporting electrolyte was 50 mM phosphate buffer at pH 7.4, containing 137 mM NaCl salt. The phosphate buffer solution was prepared using Na_2HPO_4 and NaH_2PO_4 (Sigma-Aldrich Chemie GmbH, Steinheim, Germany) and its pH value was adjusted to 7.5 by using 4M NaOH (Fischer Scientific) or 5 mM HCl (Sigma-Aldrich Chemie GmbH, Steinheim, Germany).

The water was purified with a Milli-Q purification system (Millipore, Bedford, MA, USA).

Equipment

Flow injection measurements were performed with a flow-through amperometric cell of the wall-jet type [22], containing a platinum wire as counter electrode and an Ag|AgCl, 0.1M KCl as a reference electrode. The applied potential to the working electrode was controlled by using a low currents potentiostat (Zäta Electronics, Höör, Sweden). The response of the working electrode, (spectrographic graphite, Ringsdorff Werke GmbH, Bonn, Germany, type RW001; 3.05 mm diameter and 13% porosity) was registered using a chart recorder (BD 112, Kipp & Zonen, Utrecht, The Netherlands). An injector (Rheodyne, type 7125 LabPR, Cotati, CA, USA) with a 50 μL sample loop was used to inject the samples.

CV measurements were performed with a standard three electrodes electrochemical cell connected to a computer controlled potentiostat (AutoLab PGSTAT30, Metrohm Nordic AB, Bromma, Sweden). The modified graphite electrode was used as working electrode, a SCE as reference electrode and a platinum foil as counter electrode. Before every measurement argon was purged through the solution for 10 min.

Enzyme assay

For the determination of the *Amp*PDH activity the protocol described previously [16, 23] was used. It consists of spectrophotometric monitoring of ferricenium (Fc^+) reduction to ferrocene at 300 nm [molar absorptivity $4.3 \text{ mM}^{-1}\text{cm}^{-1}$], for 3 min at 20 °C in a standard cuvette [23]. One milliliter of the standard solution contained 100 μmol of phosphate buffer (pH 7.4), 50 μmol of D-glucose, 0.4 μmol of Fc^+PF_6^- (prepared daily by dissolving 3.3 mg of salt in 5 ml of 5 mM HCl) and the appropriately diluted enzyme. One unit of enzyme activity was defined as the amount of the enzyme necessary for the reduction of 2 μmol of Fc^+ per 1 min at 20 °C.

Preparation of bioelectrodes

Graphite electrodes were prepared using the procedure described elsewhere [16, 18]. Spectrographic graphite rods (geometric area of 0.071 cm^2) were polished on wet emery paper (Tufbak, Durite, P1200). Afterwards, they were carefully rinsed with Milli-Q water and dried at room temperature. *Amp*PDH was immobilized on graphite electrodes by adsorbing the enzyme solution prepared in the presence of Os redox polymer and the cross-linking agent (PEGDGE) by using the following procedure: 2 μl of an aqueous Os-RP solution (10 mg/ml) and 1 μl of freshly prepared PEGDGE (68% v/v, in water) were placed on the top of the electrode.

After 10 min of incubation 5 μl of enzyme solution (250 U/ml) was added. The modified electrodes were left overnight at 4° C to complete the cross-linking.

ACKNOWLEDGMENTS

AK thanks for the financial support received from “The Sectorial Operational Program for Human Resources Development 2007-2013, co-financed by the European Social Fund, under the project number POSDRU/107/1.5/S/76841 with the title “Modern Doctoral Studies: Internationalization and Interdisciplinarity”. LG thanks the Swedish Research Council (2010-5031) and LG and DL the European Commission (project “3D-Nanobiodevice” NMP4-SL-2009-229255) for financial support. CKP is grateful to the Austrian Science Fund (FWF) for financial support (grant TRP218).

REFERENCES

1. C. Sygmond, R. Kittl, J. Volc, P. Halada, E. Kubatova, D. Haltrich, C.K. Peterbauer, *Journal of Biotechnology*, **2008**, *133*, 334.
2. J. Volc, P. Sedmera, P. Halada, V. Prikrylova, G. Daniel, *Carbohydrate Research*, **1998**, *310*, 151.
3. J. Volc, P. Sedmera, P. Halada, V. Prikrylova, D. Haltrich, *Carbohydrate Research*, **2000**, *329*, 219.
4. J. Volc, E. Kubátová, D.A. Wood, G. Daniel, *Archives of Microbiology*, **1997**, *167*, 119.
5. J. Volc, P. Sedmera, M. Kujawa, P. Halada, E. Kubatova, D. Haltrich, *Journal of Molecular Catalysis B: Enzymatic*, **2004**, *30*, 177.
6. J. Volc, E. Kubátová, G. Daniel, P. Sedmera, D. Haltrich, *Archives of Microbiology*, **2001**, *176*, 178.
7. R. Kittl, C. Sygmond, P. Halada, J. Volc, C. Divne, D. Haltrich, C. Peterbauer, *Current Genetics*, **2008**, *53*, 117.
8. C. Peterbauer, J. Volc, *Applied Microbiology and Biotechnology*, **2010**, *85*, 837.
9. I. Pisanelli, M. Kujawa, D. Gschnitzer, O. Spadiut, B. Seiboth, C. Peterbauer, *Applied Microbiology and Biotechnology*, **2010**, *86*, 599.
10. C. Sygmond, A. Gutmann, I. Krondorfer, M. Kujawa, A. Glieder, B. Pscheidt, D. Haltrich, C. Peterbauer, R. Kittl, *Applied Microbiology and Biotechnology*, **2012**, *94*, 695.
11. E.E. Ferapontova, V.G. Grigorenko, A.M. Egorov, T. Börchers, T. Ruzgas, L. Gorton, *Journal of Electroanalytical Chemistry*, **2001**, *509*, 19.
12. A. Lindgren, M. Tanaka, T. Ruzgas, L. Gorton, I. Gazaryan, K. Ishimori, I. Morishima, *Electrochemistry Communications*, **1999**, *1*, 171.
13. G. Presnova, V. Grigorenko, A. Egorov, T. Ruzgas, A. Lindgren, L. Gorton, T. Börchers, *Faraday Discussions*, **2000**, *116*, 281.
14. A. PrévotEAU, O. Courjean, N. Mano, *Electrochemistry Communications*, **2010**, *12*, 213.
15. R.A. Marcus, *Annual Review of Physical Chemistry*, **1964**, *15*, 155.
16. M.E Yakovleva, A. Killyéni, R. Ortiz, C. Schulz, D. MacAodha, P.Ó. Conghaile, D. Leech, I.C. Popescu, C. Gonaus, C.K. Peterbauer, L. Gorton, *Electrochemistry Communications*, **2012**, *24*, 120.
17. M.N. Zafar, F. Tasca, S. Boland, M. Kujawa, I. Patel, C.K. Peterbauer, D. Leech, L. Gorton, *Bioelectrochemistry*, **2010**, *80*, 38.
18. F. Tasca, S. Timur, R. Ludwig, D. Haltrich, J. Volc, R. Antiochia, L. Gorton, *Electroanalysis*, **2007**, *19*, 294.
19. F. Tasca, L. Gorton, M. Kujawa, I. Patel, W. Harreither, C.K. Peterbauer, R. Ludwig, G. Nöll, *Biosensors and Bioelectronics*, **2010**, *25*, 1710.

20. A. Heller, *Physical Chemistry Chemical Physics* **2004**, *6*, 209.
21. S. Rengaraj, P. Kavanagh, D. Leech, *Biosensors and Bioelectronics*, **2011**, *30*, 294.
22. R. Appelqvist, G. Marko-Varga, L. Gorton, A. Torstensson, G. Johansson, *Analytica Chimica Acta*, **1985**, *169*, 237.
23. M. Kujawa, J. Volc, P. Halada, P. Sedmera, C. Divne, C. Sygmund, C. Leitner, C. Peterbauer, D. Haltrich, *FEBS Journal*, **2007**, *274*, 879.

SYNTHESIS AND STRUCTURAL ANALYSIS OF SOME NEW ARYLBROMIDE DECORATED AZOBENZENE DERIVATIVES

ISTVAN KOCSIS^a, NICULINA HĂDADE^a and ION GROSU^{a*}

ABSTRACT. We describe the synthesis and structural analysis of some new bi-functionalized compounds containing azobenzene units decorated with bromoaryl groups. The *trans-cis* equilibrium of the central azobenzene unit, induced by photochemical isomerization, is investigated by NMR experiments.

Keywords: azobenzene, podands, photoisomerization, *cis-trans* isomers, NMR

INTRODUCTION

Controlled dynamics at the molecular level has become a subject of close examination over the last two decades. [1] Structural transitions of a molecule between two or several stable states, triggered by external stimuli (e.g. pH, temperature, light) opens new ways for the construction of molecular devices [2], which are the foundation of nanoscale science. [3] To date, the large majority of the existing molecular devices consist of two-state molecular switches. [4, 5].

The aim of our work was to design and synthesize podands which incorporate switchable building blocks and which may be valuable candidates for preparation of photochemically driven molecular devices. One of the most interesting and well studied systems that are used to convert light-energy into “mechanical motion” is based on the photochemical *cis-trans* isomerization of azobenzene derivatives. [6] The isomerisation process can be controlled both by UV light irradiation and thermal relaxation. [6] Thereby, conversion of the thermodynamically stable *trans* configuration to metastable *cis* configuration is achieved using UV light, while heating in the dark or irradiation with visible light of the *cis* isomer yields the thermodynamically stable *trans* form.

Photoisomerisation of azobenzene derivatives found important applications in the synthesis of photoresponsive host-guest systems [7] and polymers [8], as well as in the generation of photoswitchable dynamic

^a Babeş-Bolyai University, Faculty of Chemistry and Chemical Engineering, 11 Arany Janos str., RO-400028 Cluj-Napoca, Romania, * igrosu@chem.ubbcluj.ro

combinatorial libraries. [9] Moreover, photoisomerisation of azobenzene derivatives has been successfully used to control electronic properties [10] or catalysis [11] and to initiate folding/unfolding of oligopeptide chains. [12] In this context, we considered of interest to obtain and to investigate the photochemical properties of some new podands bearing an azobenzene central unit decorated with reactive functional groups. Such compounds might be used for macrocyclization reactions and they seem to be good candidates as building blocks for photochemically controlled molecular devices.

RESULTS AND DISCUSSIONS

Viewing the significance of azobenzene as one of the most familiar unit in the construction of photochemically controlled molecular devices, we focused our attention on the synthesis and structural analysis of new difunctionalised 4,4'-azobenzene derivatives (**I** and **II**, Figure 1).

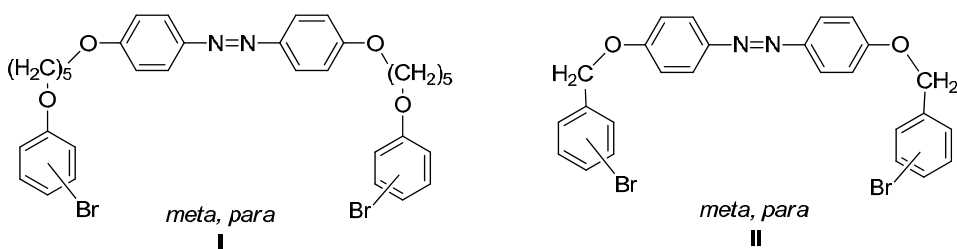
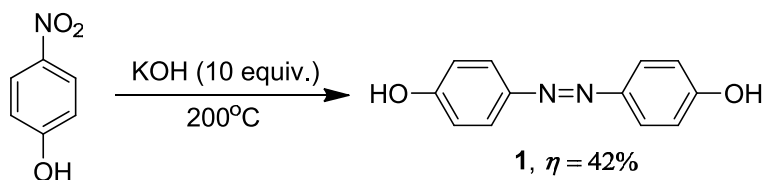


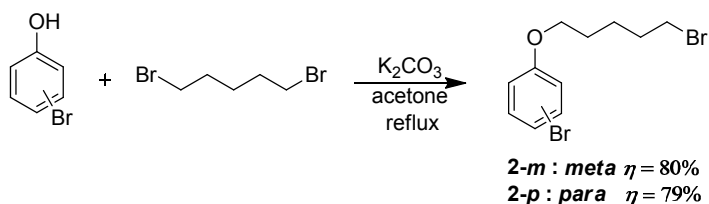
Figure 1. Target azobenzene derivatives **I** and **II**

The *p,p'*-azophenolic unit **1** (Scheme 1) was obtained starting from *p*-nitrophenol, following a previously reported procedure. [13]

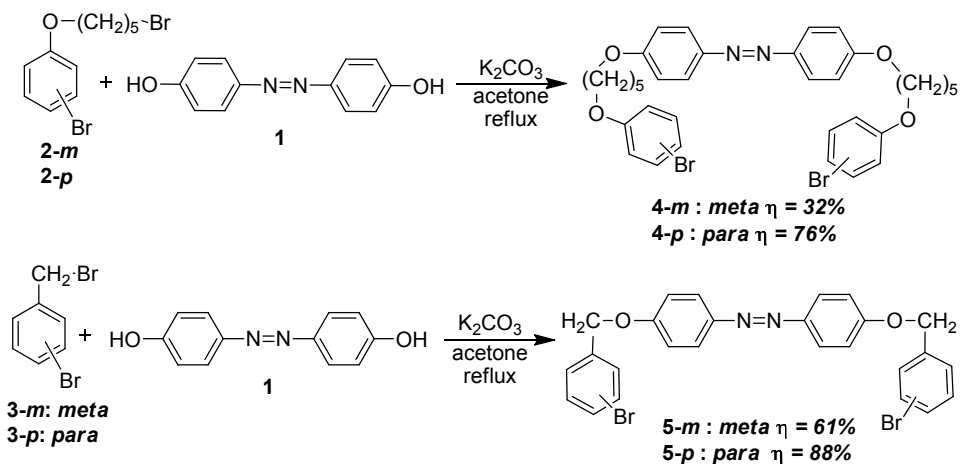


Scheme 1

Next, the dibrominated phenolic ethers **2-m** and **2-p** (Scheme 2) were obtained in good yields upon treatment of *m*- and *p*-bromophenol respectively with five fold excess of 1,5-dibromopentane in the presence of potassium carbonate as proton scavenger. A large excess of 1,5-dibromopentane was used in order to statistically favor the formation of the monosubstituted compounds **2-m** and **2-p**. However, small amounts of disubstituted byproducts (< 6%) also were formed, which were not isolated or investigated.

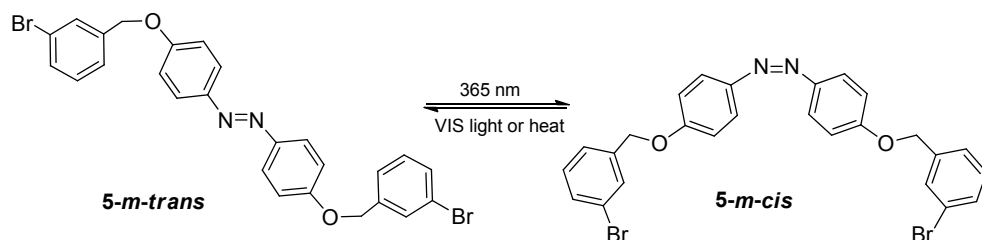


With the building-blocks **1**, **2-m** and **2-p** in our hands, we proceeded to the synthesis of the target azobenzene derivatives (Scheme 3). Compounds **4-m**, **4-p**, **5-m** and **5-p** were obtained in yields ranging between 32 – 88 % from the reaction of *p,p'*-azobenzene **1** with dibromo derivatives **2-m**, **2-p**, **3-m** and **3-p** (dibromo derivatives **3-m** and **3-p** are commercially available).



All reaction products were purified by column chromatography and their structure was confirmed by ^1H and ^{13}C NMR spectroscopy.

Next, we took a preliminary insight into the photoisomerization process of our azobenzene derivatives. For the present discussion we will refer hereafter to compound **5-m** only. The isomerization (*trans* \rightarrow *cis*) (Scheme 4) was achieved at 0 °C by irradiation with UV light (365 nm) and the reaction evolution was monitored by ^1H -NMR (CDCl_3 on 300 MHz time scale; Figure 2).



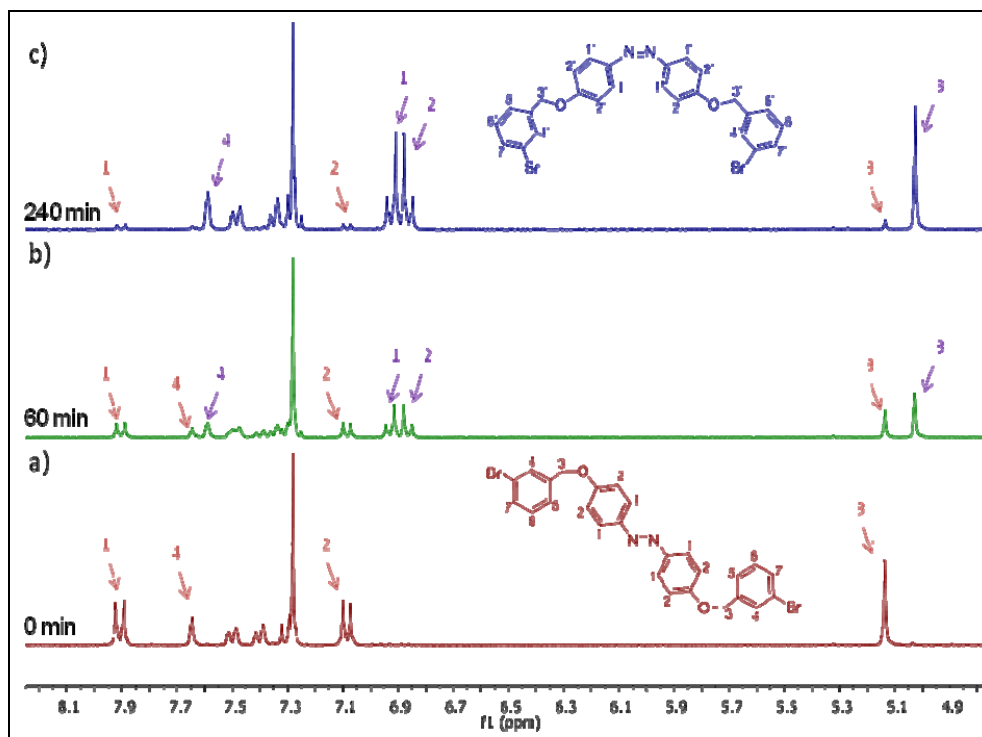


Figure 2. ¹H-NMR (CDCl₃, 300 MHz, rt) spectra of compound **5-m**: a) prior to irradiation (*trans* isomer only); b) after 60 min. of irradiation with UV light (365 nm), as a *cis* : *trans* = 1 : 1.6 mixture; c) after 240 min. of irradiation as a *trans* : *cis* = 1 : 11.4 mixture.

The atom numbering schemes shown in this figure are used for ¹H-NMR assignments and do not correspond to IUPAC numbering rules.

¹H-NMR spectrum of **5-m**, recorded before UV light irradiation (Figure 2a) revealed a single set of signals corresponding to the *trans* isomer. Irradiation with UV light (365 nm) for one hour yielded a mixture of *cis* and *trans* isomers as inferred from the Figure 2b, in a *cis* /*trans* ratio of 1.6/1 (determined by integration of the singlets at 5.03 ppm and 5.11 ppm corresponding to the CH₂ protons of *trans* and *cis* isomers, respectively). The ¹H-NMR spectrum of the *cis* isomer (Figure 2c) shows an identical pattern of signals as the *trans* one, but displaying different chemical shifts. The reaction mixture, after irradiation for four hours displayed a composition of isomers in a ratio *cis*/*trans* = 11.4/1 (inferred from NMR integration). The *trans* isomer of **5-m** was totally reformed when **5-m-cis** was kept under visible light for 24 h.

CONCLUSIONS

In summary, we carried out the efficient synthesis of a new series of *p,p'*-disubstituted azobenzene derivatives containing arylbromine units. For this purpose, the Williamson type reaction between 4,4'-(diazene-1,2-diyl) diphenol and different dibromoderivatives was used. Photoisomerisation studies conducted on compound **5-m** and monitored by ¹H-NMR spectroscopy showed almost quantitative *trans* to *cis* transformation under UV light irradiation and total *cis* to *trans* conversion under visible light irradiation.

EXPERIMENTAL SECTION

¹H and ¹³C-NMR spectra were recorded at room temperature in CDCl₃ or CD₃OD as solvents on a Bruker Advance 300 spectrometer. Multiplicities are abbreviated as follows: br.-broad; s-singlet; d-doublet; t-triplet; q-quadruplet; and m-multiplet. Melting points were measured with a Kleinfeld Apotec melting point apparatus and are uncorrected. Thin layer chromatography (TLC) was carried out on silica gel 60 F₂₅₄ coated aluminium sheets using UV visualization. Isomerisation studies were realised by UV irradiation using a Vilber Lourmat 12 W UV lamp operating at 254 nm and 365 nm.

Compound **1** was already reported [13] and compounds **3-m** and **3-p** are commercially available.

General procedure for synthesis of derivatives 2-m and 2-p

A mixture of bromophenol (0.346 g; 0.002 mole), 1,5-dibromopentane 2.3 g; 0.01 mole) and potassium carbonate (2.76 g; 0.02 mole) in acetone (50 mL) is refluxed overnight. The resulted solid is filtrated and the liquid phase is evaporated *in vacuo*. The residue is chromatographed on silica gel using as mobile phase an elution system of pentane and ethylacetate 90:1 to yield colorless liquids (R.f. = 0.3).

3-bromophenyl, 5'-bromopentylether (2-m). Colorless liquid. MW for C₁₂H₁₆Br₂O: 336.06 g/mol. ¹H NMR (300 MHz, CDCl₃) δ: 7.12 (1H, dd, *J* = 8.1 Hz, *J'* = 7.5 Hz), 7.09-7.07(1H, m), 7.06-7.03 (1H, m), 6.82 (1H, ddd, ³*J* = 8.1 Hz, ⁴*J* = 2.3 Hz, ⁴*J'* = 1.3 Hz), 3.94 (2H, t, *J* = 6.3 Hz), 3.44 (2H, t, *J* = 6.6 Hz), 2.01-1.87 (2H, m), 1.81 (2H, cv, *J* = 6.3 Hz), 1.69-1.54 ppm (2H, m). ¹³C NMR (75 MHz, CDCl₃) δ: 159.6, 130.4, 123.6, 117.6, 113.4, 67.7, 33.5, 32.3, 28.2, 24.7 ppm.

4-bromophenyl, 5'-bromopentylether (2-p) Colorless liquid. MW for C₁₂H₁₆Br₂O: 336.06 g/mol. ¹H NMR (300 MHz, CDCl₃) δ: 7.36 (2H, d, *J* = 9 Hz), 6.76 (2H, d, *J* = 9 Hz), 3.92 (2H, t, *J* = 6.3 Hz), 3.43 (2H, t, *J* = 6.9 Hz), 1.93 (2H, m), 1.80 (2H, m), 1.61 ppm (2H, m). ¹³C NMR (75 MHz, CDCl₃) δ: 170.3, 132.1, 116.1, 101.3, 67.8, 33.5, 32.3, 28.2, 24.7 ppm.

General procedure for synthesis of derivatives 4-m, 4-p, 5-m and 5-p

A mixture of diphenol **1** (0.214 g; 0.001 mole), bromoderivative **2-m**, **2-p**, **3-m** or **3-p** (0.003 mole), and potassium carbonate (1.38 g; 0.01 mole) in acetone (30 mL) was refluxed overnight. The resulted solid is filtered and the liquid phase is evaporated *in vacuo*. The residue was chromatographed on silica gel.

Trans-1,2-bis[4-(7-m-bromophenyl-1,7-dioxaheptane-1-yl)phenyl] diazene (4-m) Yellow solid, yield 36%, (pentane/ethylacetate =6:1; Rf = 0.57), m.p. = 125°C. MW for C₃₄H₃₆N₂O₄ : 696.47 g/mol. ¹H NMR (300 MHz, CDCl₃) δ: 7.86 (4H, d, J = 9.0 Hz), 7.13 -7.00 (6H, overlapped peaks), 6.98 (4H, d, J = 9.0 Hz), 6.84-6.81 (2H, m), 4.06 (4H, t, J = 6.3 Hz), 3.98 (4H, t, J = 6.0 Hz), 1.92-1.82 (8H, overlapped peaks), 1.65-1.64 ppm (4H, m). ¹³C NMR (75 MHz, CDCl₃) δ: 161.0, 159.8, 146.9, 130.5, 124.3, 123.6, 122.8, 117.7, 114.6, 113.5, 67.9, 29.7, 28.9, 28.9, 22.7 ppm.

Trans-1,2-bis[4-(7-p-bromophenyl-1,7-dioxaheptane-1-yl)phenyl] diazene (4-m) Yellow solid, yield: 76% (pentane/ethylacetate = 6:1; Rf = 0.57) m.p. = 138°C. MW for C₃₄H₃₆N₂O₄:696.47 g/mol. ¹H NMR (300 MHz, CDCl₃) δ: 7.87 (4H, d, J = 9 Hz), 7.35 (4H, d, J = 9 Hz), 6.98 (4H, d, J = 9 Hz), 6.77 (4H, d, J = 9 Hz), 4.06 (4H, t, J = 6 Hz), 3.95 (4H, t, J = 6.3 Hz), 1.90 (8H, overlapped peaks), 1.68 ppm (4H, m). ¹³C NMR (75 MHz, CDCl₃) δ: 161.0, 158.1, 146.9, 132.2, 124.3, 116.2, 114.6, 112.7, 68. 0, 67.9, 30.9, 28.9, 22.7 ppm.

Trans-1,2-bis[4-(2-m-bromophenyl-1-oxaethane-1-yl)phenyl]di azene (5-m) Yellow solid, yield; 61%, (pentane/ethylacetate =6:1; Rf = 0.44), m.p. = 181°C. MW for C₂₆H₂₀Br₂N₂O₂: 552.26 g/mol. ¹H NMR (300 MHz, CDCl₃) δ: 7.88 (4H, d, J = 9.0 Hz), 7.62 (2H, s), 7.47 (2H, d, J = 7.8 Hz), 7.37 (2H, d, J = 7.8 Hz), 7.27 (2H, t, J = 7.8 Hz), 7.06 (4H, d, J = 9.0 Hz), 5.11 ppm (4H, s). ¹³C NMR (75 MHz, CDCl₃) δ: 158.5, 142.7, 138.7, 131.2, 130.3, 130.2, 125.8, 115.0, 87.5, 69.2 ppm.

Trans-1,2-bis[4-(2-p-bromophenyl-1-oxaethane-1-yl)phenyl]di azene (5-p). Yellow solid. Yield: 88%, (pentane/ethylacetate = 6:1; Rf = 0.44), m.p. = 228°C. MW for C₂₆H₂₀Br₂N₂O₂: 552.26 g/mol. ¹H NMR (300 MHz, CDCl₃) δ: 7.87 (4H, d, J = 8.7 Hz), 7.53 (4H, d, J = 8.1 Hz), 7.33 (4H, d, J = 8.1 Hz), 7.05 (4H, d, J = 8.7 Hz), 5.09 ppm (4H, s). ¹³C NMR (75 MHz, CDCl₃) δ: 170.4, 135.9, 131.8, 129.1, 124.9, 122.1, 115.1, 87.6, 32.4 ppm.

General procedure for the photoisomerization of derivative 5-m

A solution of compound **5-m** (10 mg) in deuterated chloroform (1.5 ml) was prepared in a quartz tank. The solution was cooled at 0 °C using a mixture of water ice and salt. Under magnetic stirring the solution was subjected to UV irradiation in a darkroom. Each 60 minutes, an aliquot of 0.2 ml was collected in order to prepare the NMR samples. The ¹H-NMR spectra (rt) were immediately recorded. After 4 hours almost the entire quantity of *trans* isomer was transformed into the *cis* one (see Figure 2).

Cis-1,2-bis[4-(2-*m*-bromophenyl-1-oxaethane-2-yl)phenyl]di azene (5-*m*-cis)

¹H NMR (300 MHz, CDCl₃) δ: 7.57 (2H, s), 7.46 (2H, d, *J* = 9 Hz), 7.32 (2H, d, *J* = 9 Hz), 7.25 (2H, t, *J* = 9 Hz), 6.90 (4H, d, *J* = 9 Hz), 6.83 (4H, d, *J* = 9 Hz), 5.00 ppm (4H, s). ¹³C NMR (75 MHz, CDCl₃) δ: 157.5, 147.0, 138.7, 131.2, 130.3, 130.2, 125.8, 122.8, 114.8, 87.6, 69.2 ppm.

ACKNOWLEDGEMENTS

We acknowledge the financial support of this work awarded by Babeş-Bolyai University as scholarship granted to Istvan-Zsolt Kocsis.

REFERENCES

1. E.R. Kay, D.A. Leigh, F. Zerbetto, *Angew. Chem. Int. Ed.*, **2007**, *46*, 72.
2. a) N.D. Bogdan, E. Condamine, L. Toupet, Y. Ramondenc, I. Silaghi-Dumitrescu, I. Grosu, *Tetrahedron Lett.*, **2008**, *49*, 5204. b) N. Bogdan, I. Grosu, G. Benoit, L. Toupet, Y. Ramondenc, E. Condamine, I. Silaghi-Dumitrescu, G. Ple, *Org. Lett.*, **2006**, *8*, 2619. c) M. Balog, I. Grosu, G. Ple, Y. Ramondenc, E. Condamine, R. A. Varga, *J. Org. Chem.*, **2004**, *69*, 1337.
3. J.K. Gimzewski, C. Joachim, *Science*, **1999**, *283*, 1683.
4. a) B.L. Feringa, *Acc. Chem. Res.*, **2001**, *34*, 504; b) M. C. Basheer, Y. Oka, M. Mathews, N. Tamaoki, *Chem. Eur. J.*, **2010**, *16*, 3489.
5. G. Haberhauer, C. Kallweit, *Angew. Chem. Int. Ed.*, **2010**, *49*, 2418.
6. B. Bruin, P. Hauwert, J.N.H. Reek, *Angew. Chem. Int. Ed.*, **2006**, *45*, 2660.
7. Y. Norikane, K. Kitamoto, N. Tamaoki, *J. Org. Chem.*, **2003**, *68*, 8291.
8. G.S. Kumar, D.C. Neckers, *Chem. Rev.*, **1989**, *89*, 1915.
9. L.A. Ingeman, M.L. Waters, *J. Org. Chem.*, **2009**, *74*, 111.
10. B. Jusselme, P. Blanchard, N. Gallego-Planas, J. Delaunay, M. Allain, P. Richomme, E. Levillain, J. Roncali, *J. Am. Chem. Soc.*, **2003**, *125*, 2888.
11. R. Cacciapaglia, S.D. Stefano, L. Mandolini, *J. Am. Chem. Soc.*, **2003**, *125*, 2224.
12. J. Bredenbeck, J. Helbing, A. Sieg, T. Schrader, W. Zinth, C. Renner, R. Behrendt, L. Moroder, J. Wachtveitl, P. Hamm, *Proc. Natl. Acad. Sci. U.S.A.*, **2003**, *100*, 6452.
13. G. Bratulescu, Y.L. Bigot, M. Delmas, *Revue Roumaine de Chimie*, **1998**, *43*, 525.

CHARACTERIZATION OF HYDROXYAPATITE COATINGS ON DIFFERENT PRETREATED Ti_6Al_7Nb ALLOY SUBSTRATES

TEODORA MARCU^{a,*}, OVIDIU NEMES^a, MILICA TODEA^b,
DAN LEORDEAN^c, CATALIN POPA^a

ABSTRACT. The aim of the present work was to characterize the influence of the surface conditioning treatment of a medical grade Ti_6Al_7Nb alloy substrate on the homogeneity, morphology and adhesion strength of hydroxyapatite coatings. The substrates were obtained by means of a Selective Laser Melting process using different laser powers. The deposition of hydroxyapatite was performed by dip-coating, followed by a heat treatment at 600°C for 30 min., in air. The morphology of the coatings was studied by means of scanning electron microscopy. Bonding strength was evaluated by pull-off tests.

Keywords: Ti_6Al_7Nb alloy, hydroxyapatite, dip-coating, coating morphology, bonding strength

INTRODUCTION

Titanium alloys are widely used in the medical field for hard tissue replacement, due to their favorable combination of mechanical properties, corrosion resistance, low density, and biocompatibility. Even if well tolerated by the human body, they are bio inert materials. For an improved osteointegration, the surface of the future implant could be coated with bioactive ceramics as hydroxyapatite, bio glass, etc [1].

Hydroxyapatite (HA , $Ca_{10}(PO_4)_6(OH)_2$) is often used to this aim. Techniques such as plasma spray, sputter coating, electron beam deposition, spin-coating, or dip-coating may be employed to coat the biomaterial substrate. HA coatings obtained by high temperature processes are characterized by

^a *Universitatea Tehnică din Cluj-Napoca, Facultatea de Ingineria Materialelor și a Mediului, B-dul Muncii, Nr. 103-105, RO-400641 Cluj-Napoca, Romania.*

* *Corresponding author: teodora.marcu@stm.utcluj.ro.*

^b *Universitatea Babeș-Bolyai, Facultatea de Fizică și Institutul de Cercetări Interdisciplinare în Bio-Nano-Științe, RO-400084 Cluj-Napoca, Romania.*

^c *Universitatea Tehnică din Cluj-Napoca, Facultatea de Construcții de Mașini, B-dul Muncii, Nr. 103-105, RO-400641 Cluj-Napoca, Romania.*

good adhesion to the substrate, with bonding strengths up to 30 MPa [2]. On the other side, the high processing temperature and the rapid heating and cooling rate could affect both the surface structure of the implant and the structure of HA [3]. Low-temperature processes such as dip-coating, which do not affect the structure of HA or of the substrate, result in low adhesion strength of the coating to the implant surface. Several mechanical and chemical surface treatments could be applied to the substrate in order to increase the surface roughness and to modify the surface chemistry for an improved adhesion of the coating [4 - 6].

In the present work, a substrate of medical grade - $\text{Ti}_6\text{Al}_7\text{Nb}$ alloy obtained by Selective Laser Melting (SLM) technique - was coated with HA employing the dip-coating method. Different surface pretreatments were performed on $\text{Ti}_6\text{Al}_7\text{Nb}$ alloy substrate, in order to improve both HA bonding strength and morphology. The conditioning treatments aimed to increase the amount of Ti oxides on the surface, which are benefic to the HA adhesion [7].

RESULTS AND DISCUSSION

The surface roughness R_a of the $\text{Ti}_6\text{Al}_7\text{Nb}$ alloy obtained with 120 W and 200 W was 15 μm and 7 μm , respectively. Thus, as expected, it decreased by increasing the applied laser power. The micro hardness HV0.1 was 455 ± 11 for the substrate obtained with 120 W and 481 ± 8 for the substrate obtained with 200 W. It is well known that the structures obtained by the SLM technique have residual stresses which may be estimated, among other methods, by micro hardness measurements. The residual stresses may contribute to the surface energy, which plays an important role in the interaction between the substrate surface and the coating. Since the micro hardness values of the Ti alloy substrates obtained with 120 W and 200 W are quite close, it could be presumed that the possible contribution of the residual stresses to the surface energy is roughly the same for the two different processed substrates.

The SEM images of the $\text{Ti}_6\text{Al}_7\text{Nb}$ substrate surface processed with 120 W before and after dip-coating with HA are shown in Figure 1 and Figure 2, respectively. The surface of the as-processed material, Figure 1, was characterized by the presence of porosity. After dip-coating, the coverage with HA was lower than 100%, as shown in Figure 2; areas of uncoated substrate could be seen by SEM. The surface topology was not of primary importance in this study. In consequence, only the $\text{Ti}_6\text{Al}_7\text{Nb}$ substrate obtained with a laser power of 200 W was considered for the future work. In order to facilitate the bonding strength determination, the surfaces on which the HA would be deposited were ground and polished. The polished $\text{Ti}_6\text{Al}_7\text{Nb}$ samples were subjected to various pretreatments as specified in the Experimental section.

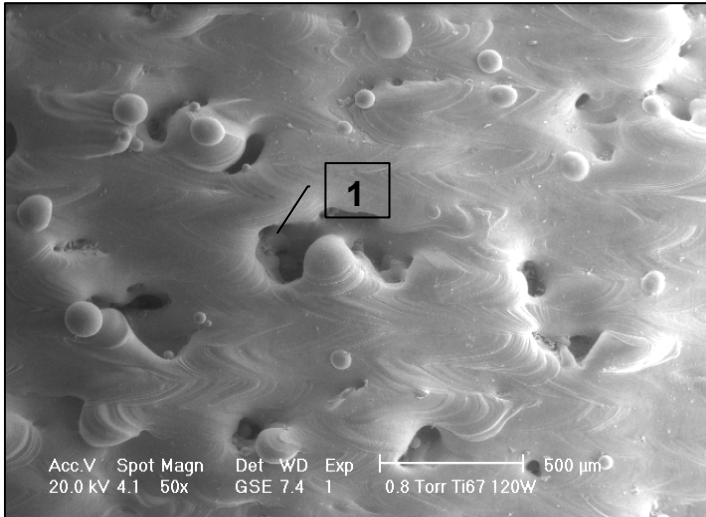


Figure 1. SEM image of the surface of the Ti_6Al_7Nb substrate processed with 120 W; 1 – pore.

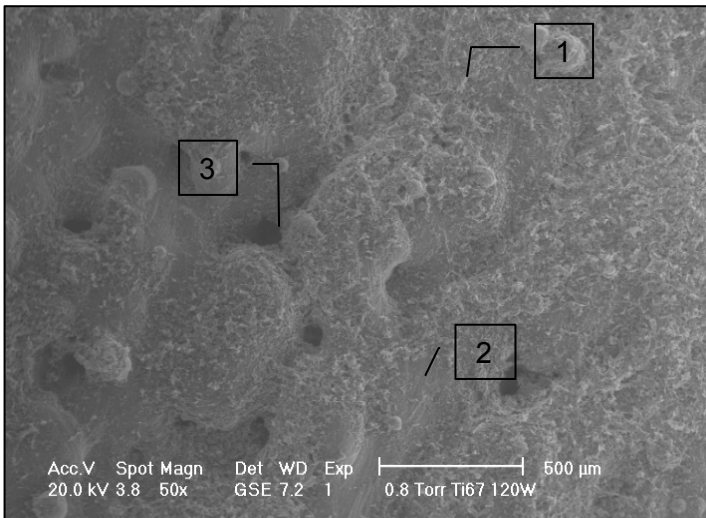


Figure 2. SEM image of the HA coated Ti_6Al_7Nb substrate processed with 120 W 1 - HA coating; 2 – substrate; 3 – pore.

The aspect of the substrate obtained with 200 W, ground and polished, is shown in Figure 3. The surface was smooth, without pores. After the alkali surface treatment in NaOH 5M and heat treatment at 600°C, the surface was characterized by the presence of micro pores, as shown in Figure 4, which are expected to enhance the coverage and bonding strength of the HA to the substrate.

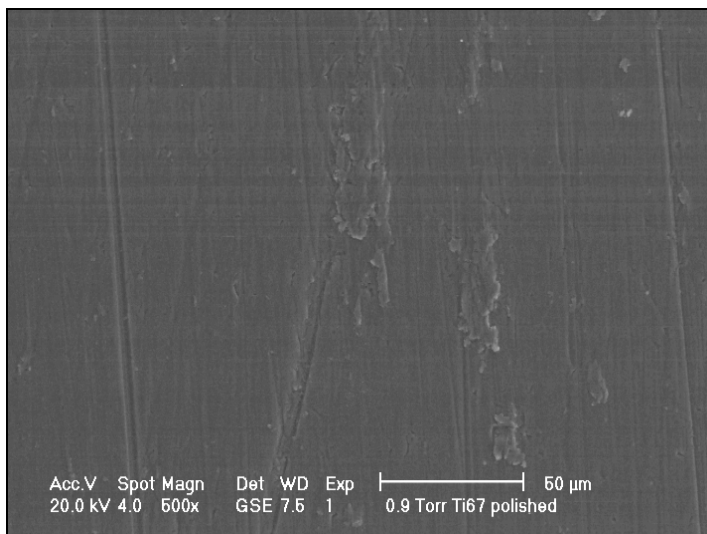


Figure 3. SEM image of the surface of Ti₆Al₇Nb substrate obtained with 200 W, ground and polished.

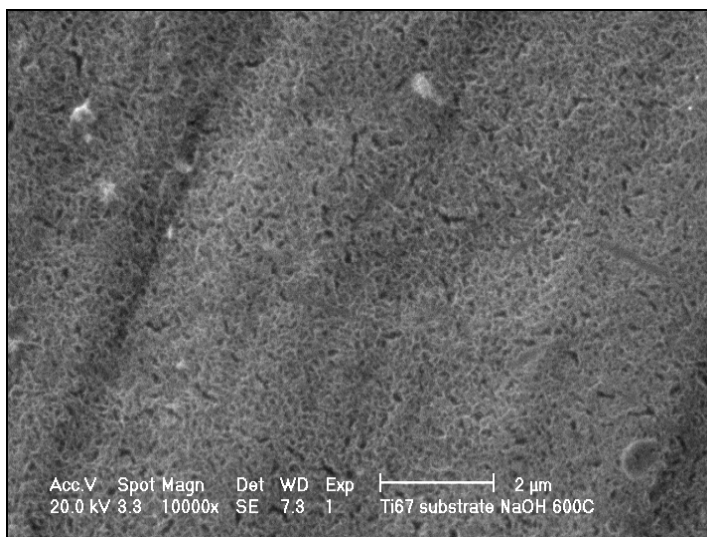


Figure 4. SEM image of the surface of Ti₆Al₇Nb substrate obtained with 200 W, ground and polished, treated in NaOH 5M.

The SEM aspect of the polished surface of Ti₆Al₇Nb after dip-coating with HA is shown in Figure 5 and Figure 6. Some uncoated areas, light colored in Figure 5, were observed. A higher magnification revealed the presence of some micro cracks in the HA coating, Figure 6.

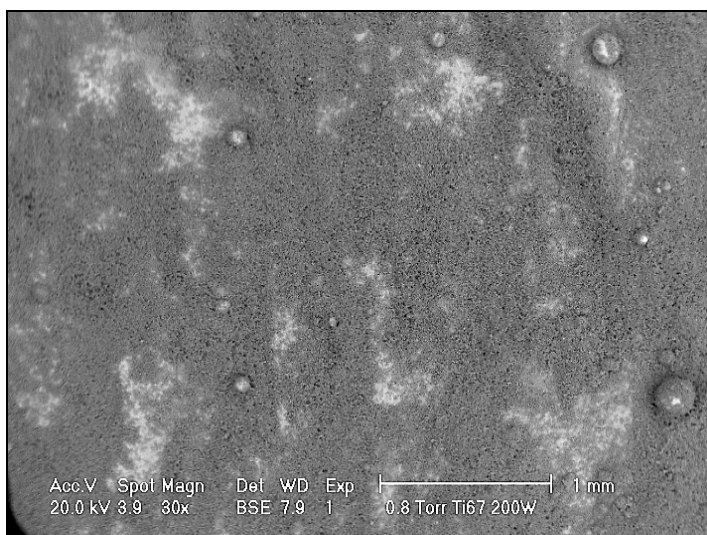


Figure 5. SEM image of the HA coating on the surface of Ti_6Al_7Nb substrate obtained with 200 W, ground and polished.

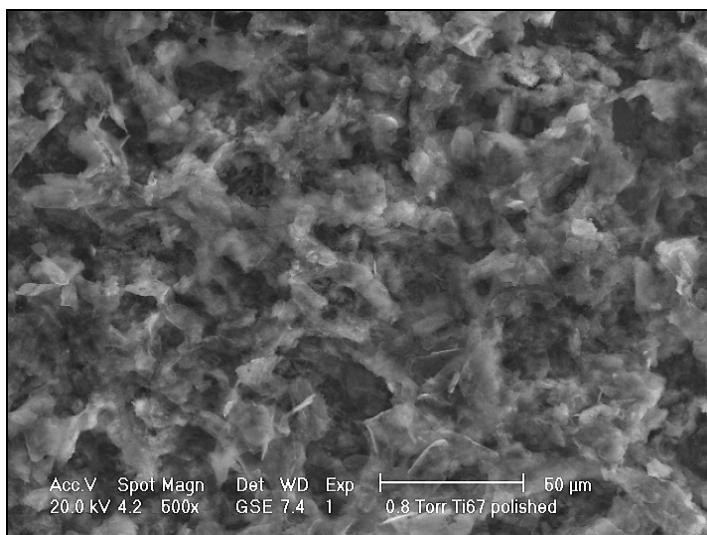


Figure 6. SEM image of the HA coating on the surface of Ti_6Al_7Nb substrate obtained with 200 W, ground and polished. Higher magnification.

A higher coverage and a better homogeneity characterized the HA coated on the alkali-treated substrate surface (Figure 7), even though at a high magnification the SEM analyses evidenced some uncoated substrate, as shown in Figure 8.

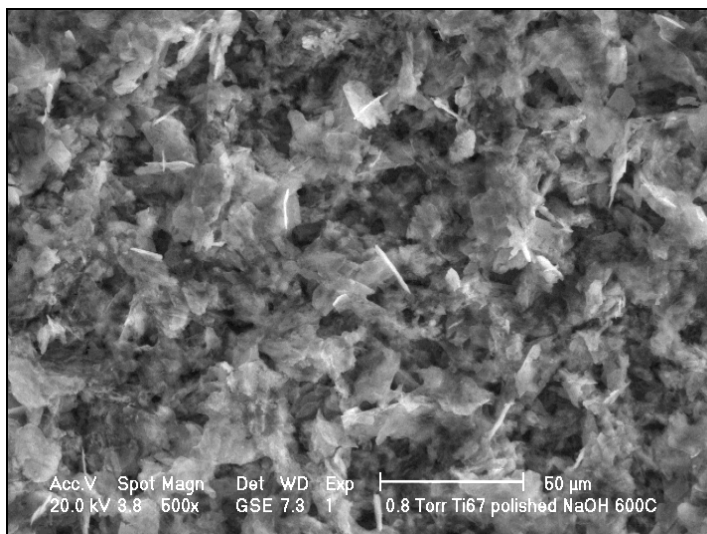


Figure 7. SEM image of the HA coating on the surface of Ti₆Al₇Nb substrate obtained with 200 W, ground and polished, then alkali treated in NaOH 5M.

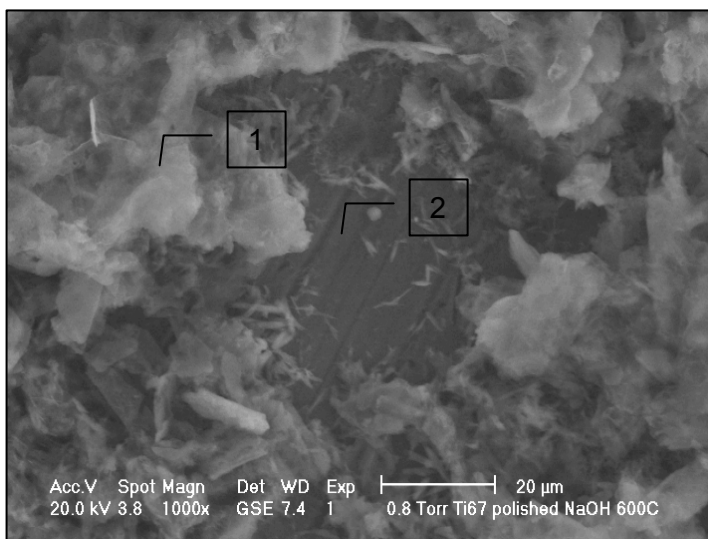


Figure 8. SEM image of the HA coating on the surface of Ti₆Al₇Nb substrate obtained with 200 W, ground and polished, then alkali-treated in NaOH 5M. Higher magnification. 1-HA; 2-substrate.

A small number of small micro cracks, as indicated by the arrow in Figure 10, appeared in the structure of HA coatings deposited on the alkali treated substrate.

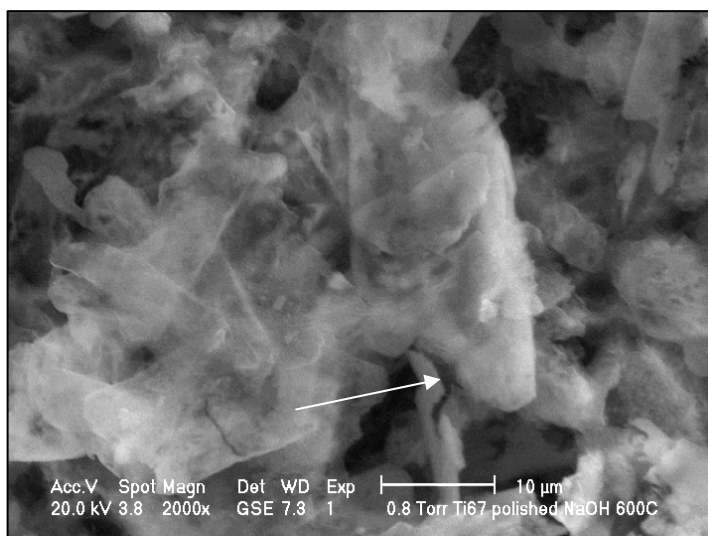


Figure 10. SEM image of the HA coating on the surface of Ti_6Al_7Nb substrate obtained with 200 W, ground and polished, then alkali treated in NaOH 5M. Micro crack indicated by the arrow.

The most affected HA coating with regard to the micro cracking occurrence was that deposited on the surface of the substrate heat treated at 400°C, whose morphology is shown in Figure 11 and in Figure 12.

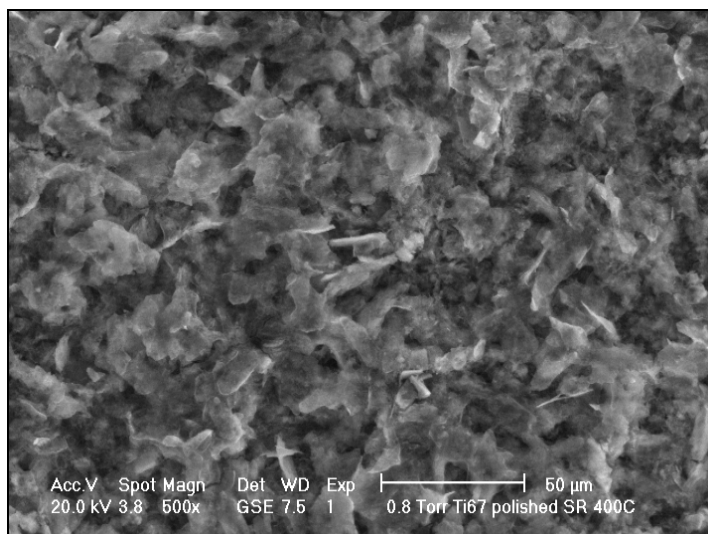


Figure 11. SEM image of the HA coating on the surface of Ti_6Al_7Nb substrate obtained with 200 W, ground and polished, then heat treated in air at 400°C.

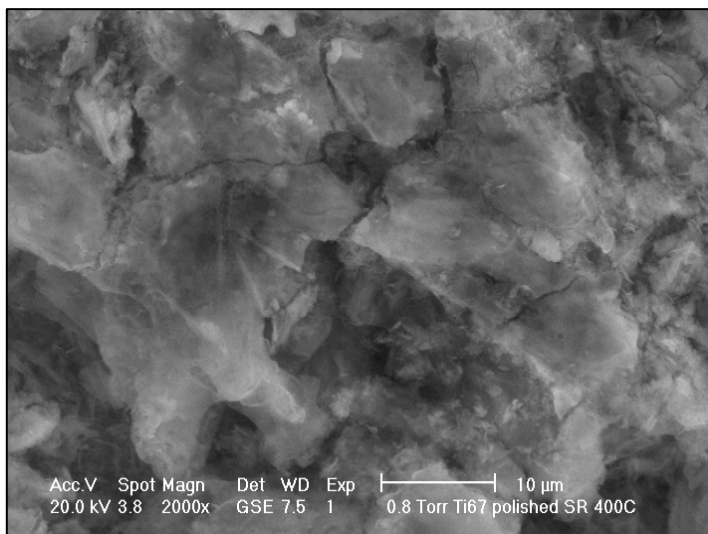


Figure 12. SEM image of the HA coating on the surface of Ti₆Al₇Nb substrate obtained with 200 W, ground and polished, then heat treated in air at 400°C. Presence of micro cracks.

The EDS analyses performed on the HA coatings on different pre-treated substrates revealed the presence of Ca, P, O; the ratio Ca/P was between, 1.78 and 1.90. As an example, Figure 13 shows the EDS spectrum corresponding to the HA coating on the polished Ti₆Al₇Nb.

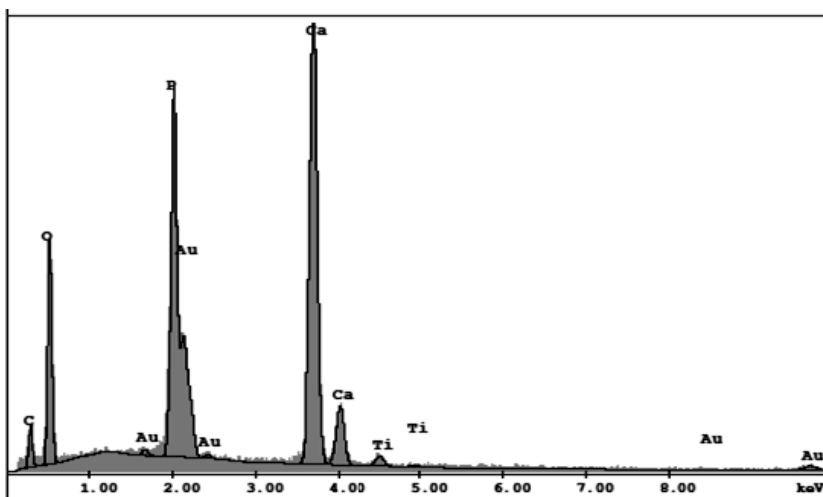


Figure 13. EDS analysis of the HA coating on the surface of Ti₆Al₇Nb substrate obtained with 200 W, ground and polished.

The formation of the micro cracks in the HA coatings could be attributed to an improper heating rate during the final heat treatment at 600°C. For the future experiments, the heating rate will be lowered in order to minimize the micro cracking occurrence in the structure of the HA coatings.

The bonding strength and failure mode of the HA coating on the different pre-treated Ti₆Al₇Nb substrates are given in Table 1. The values are in good agreement with those reported by the literature [4, 8, 9]. The highest bonding strength was displayed by the HA coating on the alkali treated Ti₆Al₇Nb substrate.

Table 1. Bonding strength and failure mode of HA coatings on different treated Ti₆Al₇Nb substrates

Substrate surface condition	Bonding strength MPa	Failure mode
Ground and polished	3.1±0.7	Mainly cohesive
Alkali and heat treated at 600°C	4.0±0.6	Mainly cohesive
Heat treated at 400°C	2.7±1.2	Mainly adhesive

CONCLUSIONS

The present work aimed to define the best surface conditioning treatment of a medical grade Ti₆Al₇Nb alloy substrate obtained by Selective Laser Melting technology with a laser power of 200 W with the aim of coating with hydroxyapatite. The deposition was performed by the dip-coating method. The polished substrates were subjected to two different treatments, as follows: a) alkali surface treatment in NaOH followed by a heat treatment at 600°C and b) heat treatment at 400°C, in air. The best coverage, morphology and bonding strength were displayed by the HA coating on the alkali treated Ti₆Al₇Nb substrate.

EXPERIMENTAL SECTION

The substrates were obtained by SLM of the medical grade Ti₆Al₇Nb alloy powder (MCP HEK GmbH), surface conditioned [10]. Specimens with dimensions of 42 mm x 13 mm x 3 mm were produced with the same scanning strategy. Two different laser powers, 120 W and 200 W, were employed with a Realizer (MCP) Nd: YAG (Fiber Laser) machine.

The substrates were ground with 180, 400, 600 and 1000 grit SiCabrasive paper. Polishing was performed on a special cloth with 3 μm alumina powder. Ground and polished substrates were ultrasonically washed in distilled water for 10 min, and then dried at 80°C for 30 min. Different surface conditioning treatments were applied to the substrates, as follows:

- Alkali heat treatment consisting in the immersion of the substrates in a NaOH 5M solution at 60°C for 24 h, followed by a final heat treatment at 600°C for 60 min, in air, with furnace cooling;
- Heat treatment at 400°C in air for 60 min., with furnace cooling.

All heat treatments were performed in a Programix (UGIN-Dentaire) furnace.

For dip-coating, a HA solution with pH 4.5 was used. The substrates were immersed in the HA solution for 10 sec., then withdrawn at a rate of 0.6 mm/sec, and dried at 120°C for 15 min. This sequence was repeated for five times. At the end, the coated substrates were heat-treated at 600°C for 30 min, in air, with furnace cooling. The heating rate up to the treatment temperature was 2°C/min.

Coating morphology analyses were carried out with a scanning electron microscope Philips XL30 ESEM equipped with a sapphire Si(Li) EDS detector.

The surface roughness of the SLM specimens was determined with a Mitutoyo tester.

The micro hardness HV0.1 of the Ti alloy substrates was measured with a Paar MHT-4 tester.

Pull-off tests were carried out on a Zwick Z005 Roell universal testing machine, according to ASTM C 633-01. A steel rod with 12 mm diameter was carefully glued on the HA coating surface with an ABRO epoxy resin and hardener. The rod was fixed in the upper grip of the testing machine, while the substrate was fixed in the lower grip by means of a dispositive especially designed to minimize the eventual shear stresses in the coating, during the test. The test speed was 0.5 mm/min.

ACKNOWLEDGMENTS

Teodora Marcu, Ovidiu Nemes and Milica Todea acknowledge financial support from the project "Progress and development through post-doctoral research and innovation in engineering and applied sciences - PRIDE - Contract no. POSDRU/89/1.5/S/57083", co-funded from the European Social Fund via the Sectorial Operational Program Human Resources 2007-2013.

The research was carried out within the BIOMAPIM project, financed by the Romanian National Council for the Higher Education Scientific Research.

Special thanks are addressed to the Metallurgy Research Group (Department of Materials Engineering and Industrial Technologies, University of Trento, Italy) headed by Professor Alberto Molinari, for the support with SEM-EDS analyses.

REFERENCES

1. M. Geetha, A.K. Singh, R. Asokamani, A.K. Gogia, *Progress in Materials Science*, **2009**, 54, 397.
2. H.Li, K.A. Khor, P. Cheang, *Engineering Fracture Mechanics*, **2007**, 74, 1894.
3. Y.C. Tsui, C. Doyle, T.W. Clyne, *Biomaterials*, **1998**, 19, 2015.
4. L.D. Piveteau, B. Gasser, L. Schlapbach, *Biomaterials*, **2000**, 21, 2193.
5. P.C. Rath, L. Besra, B.P. Singh, S. Bhattacharjee, *Ceramics International*, **2012**, 38, 3209.
6. R. Rohanizadeh, R.Z. LeGeros, M. Harsono, A. Bendavid, *Journal of Biomedical Materials Res*, **2005**, 72A, 428.
7. D.G. Wang, C.Z. Chen, J. Ma, T. He, *Applied Surface Science*, **2011**, 257, 2592.
8. S. Zhang, Z. Xianting, W. Yongsheng. C. Kui, W. Wenjian, *Surface&Coating Technology*, **2006**, 200, 6350.
9. I.H. Oh, N. Nomura, A. Chiba, Y. Murayama, N. Masahashi, B.T. Lee, S. Hanada, *Journal of Materials Science: Materials in Medicine*, **2005**, 16, 635.
10. T. Marcu, M. Todea, I. Gligor, P. Berce, C. Popa, *Applied Surface Science*, **2012**, 258, 3276.

QSPR STUDY ON THE CHROMATOGRAPHIC BEHAVIOR OF A SET OF THIAZOLE DERIVATIVES BY AUTO-CORRELATION ANALYSIS

RALUCA MATIES^a, BEATA SZEFLER^b, IOANA IONUT^c,
BRANDUSA TIPERCIUC^{c,*}

ABSTRACT. A set of twenty six thiazole derivatives, synthesized in our laboratory and measured for chromatographic retention, was submitted to a QSPR study by auto-correlation analysis on the hypermolecule model. As predictor variables, mass fragments, Cluj indices and the HOMO energy, computed at the Hartree-Fock level of theory, are used. Several QSPR models were derived while the leave-one-out procedure was used to evaluate the predictive ability of the main model.

Key words: *thiazoles, hypermolecules, QSPR, topological descriptors*

INTRODUCTION

Quantitative structure-property relations (QSPR) have become a fundamental tool for property prediction in various scientific fields including chemistry, biology, pharmacology, and chemical engineering. Accordingly, relations between molecular structure and macroscopic quantities have been established in diverse areas ranging from thermophysics [1–7] carcinogenicity and toxicity, [8–10] and catalytic activity [11] up to combustion kinetic properties [12–15] and lubricity [16] of biofuels. Quantitative structure-activity relations (QSAR) are employed in drug design to identify molecules with high binding affinity to receptors in order to maximize biological activity.[17–20] A recent review about theory and applications of QSPR was provided by Katritzky et al. [21].

Any QSPR and QSAR approach assumes that a macroscopic property of a chemical compound depends on the molecular structure, as described,

^a Faculty of Chemistry and Chemical Engineering, Babeş-Bolyai University, 400028 Cluj, Romania.

^b Department of Physical Chemistry, Collegium Medicum, Nicolaus Copernicus University, Kurpińskiego 5, 85-950, Bydgoszcz, Poland.

^c Department of Pharmaceutical Chemistry, Faculty of Pharmacy, Iuliu Hatieganu University of Medicine and Pharmacy, Cluj-Napoca, Romania. * brandu32@yahoo.com

e.g. by the topological indices TIs, which are derived from the molecular topology or geometry. In the last years, thousands of TIs have been proposed and used in predicting various molecular properties. Among these, the Cluj indices play an important role [22], even we cannot hide a sentimental relation with them. They have been defined by Diudea at the end of the 2nd millennium [23,24], as shown below.

A Cluj fragment $CJ_{i,j,p}$ collects vertices v lying closer to i than to j , the endpoints of a path $p(i,j)$. Such a fragment collects the vertex proximities of i against any vertex j , joined by the path p , with the distances measured in the subgraph $D_{(G-p)}$, as shown in the following equation:

$$CJ_{i,j,p} = \left\{ v \mid v \in V(G); D_{(G-p)}(i, v) < D_{(G-p)}(j, v) \right\} \quad (1)$$

In graphs containing rings, more than one path could join the pair (i, j) , thus resulting more than one fragment related to i (with respect to j and a given path p). The entries in the Cluj matrix are taken, by definition, as the maximum cardinality among all such fragments:

$$[UCJ]_{i,j} = \max_p |CJ_{i,j,p}| \quad (2)$$

Indices I_e and I_p are calculated, from the Cluj topological matrices UCJ_e , and UCJ_p , respectively (see above), as half sum of matrix entries. In the above symbols, e refers to edge-calculated matrix while p refers to the path-calculated ones.

The chromatographic behavior of a molecule reflects its interaction with two phases: a mobile phase (i.e., the eluent) and a stationary one. This interaction is a function of more than one factor, polarity, lipophylicity and the size of the molecule being included. Lipophilicity is related to the chromatographic behavior and controls the passive transport of a medicinal molecule through the cell membranes (of lipidic nature) [25].

AUTO-CORRELATION METHOD

In order to achieve the QSPR, the structure is encoded in a numerical form. The arrangement of substituent groups, on the Thiazole derivatives herein discussed, can be accounted for by the *hypermolecule* HM concept [26], viewed as the union of the molecules forming the correlating space. In the construction of the hypermolecule, a property *row-vector* P_i is attached to each molecule i :

$$P_i = \{ P_{ij}; j = 1, 2, \dots, n_{HM} \} \quad (3)$$

where n_{HM} is the number of vertices in the hypermolecule. The molecules of the set are superimposed according to their maximal common substructures.

This superposition is indicated by an associated vector X_i , in which the matching positions take $X_{ij} = 1$ while for the non-matching ones $X_{ij} = 0$.

The molecules under study can be numerically described by using a global molecular descriptor AD_i , calculated as a linear combination of the property descriptors $P_j X_{ij}$, multiplied by the regression coefficients b_j performed on the all or most important positions j in the hypermolecule HM:

$$AD_i = \sum_j b_j P_j X_{ij} \quad (4)$$

The above AD_i are called *auto-correlation* descriptors [27,28] and they are *ad-hoc* ones, depending on the chosen set of molecules.

The general regression equations are of the form:

$$Y_i = a + \sum_{j=1}^m b_j \cdot Z_{ij} \quad (5)$$

where Y_i is the dependent variable, Z_{ij} are the predictor variables, $m < n$, n being the number of structures in the set.

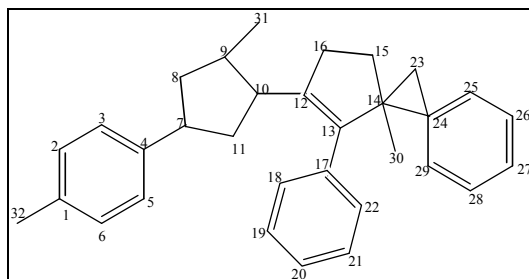
The correlating algorithm followed the steps:

1. generate the *hypermolecule*
2. calculate the molecular descriptors by using a chosen property P_i
3. find the best regression equations
4. test the predictive capability of the model

In this paper, the property P_i was taken the mass fragment M_i while the correlated property was the measured chromatographic retention.

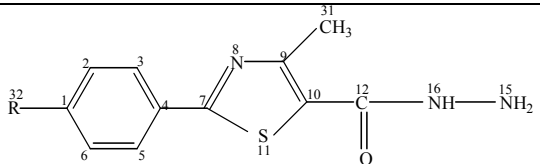
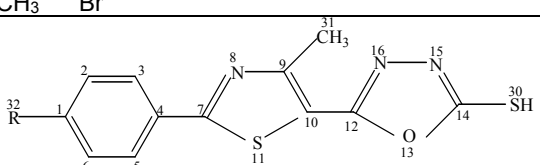
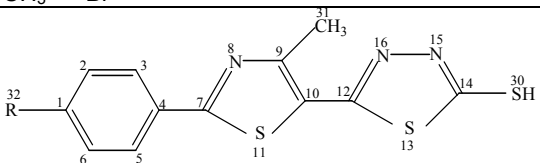
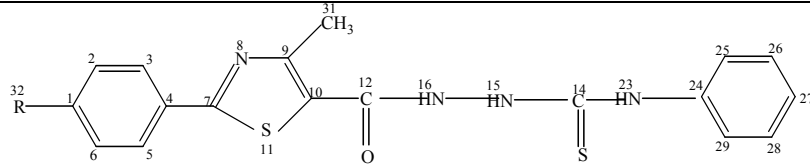
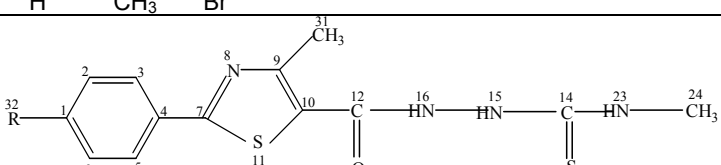
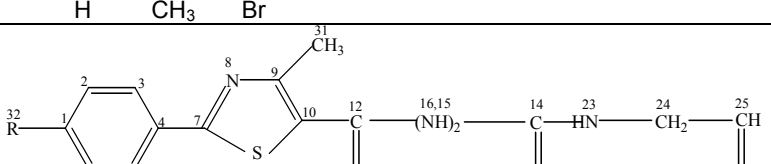
STRUCTURAL DATA

Statistics were done on the set of 26 thiazole derivatives illustrated in Table 1 (see also the experimental part). Numbering refers to the numbering of the hypermolecule, built up as the union of all molecules in the studied set. Chromatographic retention index is listed in Table 2, for each faze F_k , $k=1$ to 5. Details are given in the Experimental section.



Hypermolecule

Table 1. Structural formulas for the studied thiazoles

	Formulas			
1				
Struct.	R	1 H	2 CH ₃	3 Br
2				
Struct.	R	4 H	5 CH ₃	6 Br
3				
Struct.	R	7 H	8 CH ₃	
4				
Struct.	R	9 H	10 CH ₃	11 Br
5				
Struct.	R	12 H	13 CH ₃	14 Br
6				
Struct.	R	15 H	16 CH ₃	17 Br

Formulas				
7				
Struct.	R	18 H	19 CH ₃	20 Br
8				
Struct.	R	21 H	22 CH ₃	23 Br
9				
Struct.	R	24 H	25 CH ₃	26 Br

Table 2. Chromatographic retention values R_f for the Thiazoles in five mobile fazes F_i

Structure	i-propanol:water ratio				
	45:55:00	50:50:00	55:45:00	60:40:00	65:35:00
	F_1	F_2	F_3	F_4	F_5
1	0.400	0.510	0.588	0.552	0.694
2	0.352	0.482	0.529	0.576	0.670
3	0.247	0.376	0.458	0.470	0.611
4	0.658	0.729	0.723	0.764	0.835
5	0.600	0.682	0.676	0.711	0.729
6	0.576	0.670	0.658	0.694	0.729
7	0.470	0.540	0.517	0.547	0.647
8	0.410	0.470	0.482	0.470	0.576
9	0.376	0.494	0.552	0.600	0.688

Structure	i-propanol:water ratio				
	45:55:00	50:50:00	55:45:00	60:40:00	65:35:00
	F_1	F_2	F_3	F_4	F_5
10	0.305	0.435	0.505	0.541	0.647
11	0.282	0.400	0.458	0.494	0.611
12	0.529	0.635	0.670	0.705	0.788
13	0.458	0.588	0.623	0.664	0.752
14	0.388	0.517	0.564	0.611	0.717
15	0.435	0.564	0.600	0.635	0.735
16	0.376	0.505	0.541	0.588	0.705
17	0.329	0.447	0.482	0.529	0.658
18	0.317	0.447	0.482	0.517	0.647
19	0.247	0.400	0.423	0.464	0.611
20	0.153	0.305	0.294	0.435	0.435
21	0.329	0.505	0.482	0.611	0.600
22	0.247	0.447	0.435	0.552	0.553
23	0.211	0.388	0.376	0.482	0.505
24	0.258	0.435	0.429	0.552	0.494
25	0.200	0.376	0.376	0.494	0.505
26	0.152	0.317	0.305	0.670	0.458

RESULTS AND DISCUSSION

The local property P_{ij} chosen here was the hydride fragment mass M_{ij} (listed in Table 3, for each j -position of the hypermolecule). It will be used in the calculation of the auto-correlation property descriptor AD (see below).

Table 3. Hydride fragment mass M_{ij} , for each j -position of the hypermolecule

j	1	2	3	4	5	6	7	8	9	10	11	12	13	14	15	16	17	18	19	20	21	22	23	24	25	26
1	12	12	12	12	12	12	12	12	12	12	12	12	12	12	12	12	12	12	12	12	12	12	12	12	12	12
2	12	12	12	12	12	12	12	12	12	12	12	12	12	12	12	12	12	12	12	12	12	12	12	12	12	12
3	12	12	12	12	12	12	12	12	12	12	12	12	12	12	12	12	12	12	12	12	12	12	12	12	12	12
4	12	12	12	12	12	12	12	12	12	12	12	12	12	12	12	12	12	12	12	12	12	12	12	12	12	12
5	12	12	12	12	12	12	12	12	12	12	12	12	12	12	12	12	12	12	12	12	12	12	12	12	12	12
6	12	12	12	12	12	12	12	12	12	12	12	12	12	12	12	12	12	12	12	12	12	12	12	12	12	12
7	12	12	12	12	12	12	12	12	12	12	12	12	12	12	12	12	12	12	12	12	12	12	12	12	12	12
8	14	14	14	14	14	14	14	14	14	14	14	14	14	14	14	14	14	14	14	14	14	14	14	14	14	14
9	12	12	12	12	12	12	12	12	12	12	12	12	12	12	12	12	12	12	12	12	12	12	12	12	12	12
10	12	12	12	12	12	12	12	12	12	12	12	12	12	12	12	12	12	12	12	12	12	12	12	12	12	12
11	32	32	32	32	32	32	32	32	32	32	32	32	32	32	32	32	32	32	32	32	32	32	32	32	32	32
12	12	12	12	12	12	12	12	12	12	12	12	12	12	12	12	12	12	12	12	12	12	12	12	12	12	12
13	16	16	16	16	16	16	32	32	16	16	16	16	16	16	16	16	16	14	14	14	14	14	14	14	14	14
14	0	0	0	12	12	12	12	12	12	12	12	12	12	12	12	12	12	12	12	12	12	12	12	12	12	12

<i>j</i>	1	2	3	4	5	6	7	8	9	10	11	12	13	14	15	16	17	18	19	20	21	22	23	24	25	26
15	14	14	14	14	14	14	14	14	14	14	14	14	14	14	14	14	14	14	14	14	14	14	14	14	14	14
16	14	14	14	14	14	14	14	14	14	14	14	14	14	14	14	14	14	14	14	14	14	14	14	14	14	14
17	0	0	0	0	0	0	0	0	0	0	0	0	0	0	0	0	0	12	12	12	12	12	12	12	12	12
18	0	0	0	0	0	0	0	0	0	0	0	0	0	0	0	0	0	12	12	12	0	0	0	12	12	12
19	0	0	0	0	0	0	0	0	0	0	0	0	0	0	0	0	0	12	12	12	0	0	0	12	12	12
20	0	0	0	0	0	0	0	0	0	0	0	0	0	0	0	0	0	12	12	12	0	0	0	0	0	0
21	0	0	0	0	0	0	0	0	0	0	0	0	0	0	0	0	0	12	12	12	0	0	0	0	0	0
22	0	0	0	0	0	0	0	0	0	0	0	0	0	0	0	0	0	12	12	12	0	0	0	0	0	0
23	0	0	0	0	0	0	0	0	14	14	14	14	14	14	14	14	14	0	0	0	0	0	0	0	0	0
24	0	0	0	0	0	0	0	0	12	12	12	12	12	12	12	12	12	0	0	0	0	0	0	0	0	0
25	0	0	0	0	0	0	0	0	12	12	12	0	0	0	12	12	12	0	0	0	0	0	0	0	0	0
26	0	0	0	0	0	0	0	0	12	12	12	0	0	0	12	12	12	0	0	0	0	0	0	0	0	0
27	0	0	0	0	0	0	0	0	12	12	12	0	0	0	0	0	0	0	0	0	0	0	0	0	0	0
28	0	0	0	0	0	0	0	0	12	12	12	0	0	0	0	0	0	0	0	0	0	0	0	0	0	0
29	0	0	0	0	0	0	0	0	12	12	12	0	0	0	0	0	0	0	0	0	0	0	0	0	0	0
30	0	0	0	32	32	32	32	32	32	32	32	32	32	32	32	32	32	32	32	32	32	32	32	32	32	32
31	12	12	12	12	12	12	12	12	12	12	12	12	12	12	12	12	12	12	12	12	12	12	12	12	12	12
32	0	12	80	0	12	80	0	12	0	12	80	0	12	80	0	12	80	0	12	80	0	12	80	0	12	80

Topological Cluj descriptors were computed by TOPOCLUJ software and listed in Table 4 along with the number of atoms N in molecules and the energy of the highest occupied molecular orbital HOMO, computed on the optimized molecules, at the Hartree-Fock level of theory (see the experimental part).

Table 4. Topological and energetic descriptors of the optimized molecules at the Hartree-Fock level of theory

Molecule	N	I_e	I_p	HOMO (au)
1	16	310	1400	-1778.65
2	17	380	1800	-1817.691
3	17	380	1800	-4347.955
4	18	430	2500	-1588.141
5	19	520	3000	-1627.187
6	19	520	3000	-4157.45
7	18	430	2500	-1665.028
8	19	520	3000	-1704.068
9	25	1100	7500	-1702.554
10	26	1300	8600	-1741.595
11	26	1300	8600	-4271.859
12	20	570	3000	-1512.092
13	21	670	3600	-1551.132
14	21	670	3600	-4081.396

Molecule	N	I_e	I_p	HOMO (au)
15	22	740	4200	-1588.973
16	23	860	5000	-1628.013
17	23	860	5000	-4158.278
18	24	930	6700	-1492.878
19	25	1100	7800	-1531.919
20	25	1100	7800	-4062.183
21	19	480	2900	-1815.518
22	20	580	3500	-1854.559
23	20	580	3500	-4234.319
24	21	620	3900	-1891.562
25	22	720	4600	-1930.602
26	22	720	4600	-1058.682

The best QSPR model, without auto-correlation descriptors are listed in Table 5. The descriptors named by numbers represent the mass fragments in the given positions of the hypermolecule. Even the models are statistically significant, the number of predictor variables is too large for the set of 26 thiazole derivatives, according to [29]. By this reason, we calculated the auto-correlation descriptors AD, cf. [4] (see below).

Table 5. Regressions without auto-correlation; the descriptors named by numbers represent the mass fragments in the given positions of the hypermolecule

Descriptors	F_1			
	R^2	Adjus. R^2	St. Error	F
IE, 13, 17, 24, 25, 30, 32	0.957	0.940	0.033	56.592
IE, IP, 13, 17, 25, 30, 32, HOMO	0.969	0.955	0.029	67.008
IE, 13, 17, 24, 30, 32	0.941	0.922	0.037	50.464
IE, IP, 13, 17, 25, 30, HOMO	0.954	0.936	0.034	53.425
F_2				
IE, 13, 17, 24, 30, 32, HOMO	0.949	0.929	0.029	47.577
IE, 13, 17, 24, 30, 32	0.943	0.926	0.030	52.806
IP, 13, 17, 24, 30, 32	0.937	0.917	0.031	47.162
F_3				
IE, 13, 17, 25, 30, 32, HOMO	0.947	0.926	0.030	45.614
IE, 13, 17, 25, 30, 32	0.938	0.919	0.032	48.169
IP, 13, 17, 25, 30, 32	0.932	0.911	0.033	43.432
F_4				
IE, IP, 13, 17, 22, 25, 30, 32, HOMO	0.957	0.932	0.023	39.275
IE, 13, 17, 22, 25, 30, 32, HOMO	0.913	0.872	0.031	22.359
IE, 13, 17, 25, 30, 32, HOMO	0.913	0.879	0.031	27.044
F_5				
IE, 13, 17, 22, 29, 30, 32	0.933	0.906	0.031	35.598
IP, 13, 17, 22, 29, 30, 32	0.937	0.913	0.030	38.378
IE, 13, 17, 22, 29, 30, HOMO	0.918	0.885	0.035	28.619

Table 6 lists the global auto-correlating descriptor $AD_{(13, 17, 19, 24, 25, 30, 32)}$ calculated cf (4) (on the positions 13, 17, 19, 24, 25, 30, 32 of the hypermolecule), the F_1 values, observed and estimated, the corresponding residuals (i.e., the difference between the experimental and calculated F -values) for eq. (6) and the predicted *leave-one-out* $F_{1,loo}$ -values cf (7).

$$F_1 = 0.575 + AD(F_1); n=26; R^2=0.950; s=0.031; F=454.567 \quad (6)$$

$$F_{1,loo} = 0.002 + 0.994 AD(F_1)_{loo}; n=25; R^2=0.942; s=0.033; F=391.815 \quad (7)$$

One can see a good predictive ability of the $AD(F_1)_{loo}$ descriptors by the small drop of the correlation coefficient R^2 in a monovariate regression (eqs. 6 and 7). The subscript numbers in AD_i symbols represent the positions in hypermolecule and suggest these are responsible of the chromatographic retention. The large values of Fischer ratio F in (6) in comparison to the multivariate regressions listed in Table 5 suggest a higher level of (statistical) significance for the monovariate regression in comparison to that of multivariate ones. Table 7 lists the best model using the auto-correlating descriptors and some other molecular: Cluj indices and the energy of HOMO, for all the 5 mobile phases F_i . One can see a similar chromatographic behavior in all the phases except F_4 , which is the worst one.

It is noteworthy the adjusted R^2 speaks clearly that the additional variables (i.e., Cluj indices and HOMO) are not necessary, thus proving the utility of the auto-correlating descriptors.

Table 6. Auto-correlating descriptors $AD_{(13, 17, 19, 24, 25, 30, 32)}$ in the learning (calcd) and predicting (*loo*) steps, respectively

Molecule <i>i</i>	AD_i	$F_{1,obs}$	$F_{1,calcd.}$	$Resid_{calcd}$	$F_{1,loo}$
1	-0.203	0.4	0.372	0.028	0.371
2	-0.218	0.352	0.357	-0.005	0.357
3	-0.305	0.247	0.270	-0.023	0.271
4	0.075	0.658	0.651	0.007	0.648
5	0.060	0.6	0.635	-0.035	0.645
6	-0.027	0.576	0.548	0.028	0.544
7	-0.128	0.47	0.448	0.022	0.446
8	-0.143	0.41	0.432	-0.022	0.434
9	-0.185	0.376	0.390	-0.014	0.39
10	-0.201	0.305	0.374	-0.069	0.377
11	-0.288	0.282	0.287	-0.005	0.288
12	-0.078	0.529	0.498	0.031	0.495
13	-0.093	0.458	0.482	-0.024	0.484
14	-0.180	0.388	0.395	-0.007	0.395
15	-0.185	0.435	0.390	0.045	0.388
16	-0.201	0.376	0.374	0.002	0.374

Molecule <i>i</i>	AD_i	$F_{1,obs}$	$F_{1,calcd.}$	$Resid_{calcd}$	$F_{1,lo}$
17	-0.288	0.329	0.287	0.042	0.285
18	-0.315	0.317	0.260	0.057	0.257
19	-0.330	0.247	0.245	0.002	0.245
20	-0.417	0.153	0.158	-0.005	0.159
21	-0.274	0.329	0.302	0.027	0.300
22	-0.289	0.247	0.286	-0.039	0.288
23	-0.376	0.211	0.199	0.012	0.198
24	-0.315	0.258	0.260	-0.002	0.261
25	-0.330	0.200	0.245	-0.045	0.248
26	-0.417	0.152	0.158	-0.006	0.159

Table 7. Regressions with auto-correlation descriptors

Descriptors	F_1			
	R^2	Adjust. R^2	St. Error	F
$AD_{(13, 17, 19, 24, 25, 30, 32)}$	0.950	0.948	0.031	454.567
IE, AD	0.952	0.948	0.031	228.094
IE, IP, AD	0.952	0.946	0.031	146.168
IE, AD, HOMO	0.952	0.946	0.031	146.705
IE, IP, AD, HOMO	0.953	0.944	0.032	106.068
F_2				
$AD_{(13, 17, 18, 24, 26, 30, 32)}$	0.944	0.942	0.026	403.468
AD, HOMO	0.944	0.939	0.027	194.442
IE, IP, AD	0.949	0.943	0.026	137.740
IP, AD, HOMO	0.950	0.943	0.026	138.406
IE, IP, AD, HOMO	0.950	0.940	0.027	99.095
F_3				
$AD_{(13, 17, 24, 25, 30, 32)}$	0.940	0.937	0.028	372.732
AD, HOMO	0.942	0.937	0.028	186.190
IE, IP, AD	0.945	0.937	0.028	125.169
IE, AD, HOMO	0.947	0.940	0.027	131.604
IE, IP, AD, HOMO	0.947	0.937	0.028	94.370
F_4				
$AD_{(13, 17, 22, 24, 25, 30, 32)}$	0.776	0.766	0.943	82.981
IE, IP, AD	0.781	0.751	0.044	26.084
AD, HOMO	0.805	0.788	0.041	47.424
IP, AD, HOMO	0.809	0.783	0.041	31.037
IE, IP, AD, HOMO	0.809	0.773	0.042	22.294
F_5				
$AD_{(13, 17, 18, 22, 26, 29, 30, 32)}$	0.926	0.923	0.029	298.865
AD, HOMO	0.926	0.919	0.029	143.519
IE, AD, HOMO	0.926	0.916	0.030	92.332
IE, IP, AD	0.929	0.919	0.029	95.325
IE, IP, AD, HOMO	0.929	0.915	0.030	68.276

EXPERIMENTAL

Twenty six thiazole derivatives (thiazolyl-carbonyl-thiosemicarbazides and hybrid thiazolyl-1,3,4-oxadiazoles, thiazolyl-1,3,4-triazoles, and thiazolyl-1,3,4-triazoles - Table 1), synthesized in our laboratory, according to a previously described procedure [30,31], were investigated for chromatographic behavior. Chromatography was performed on 20 X 20 cm RP-18F_{254s} TLC precoated silica plates (Merck; Darmstadt, Germany). Solutions (1 mg mL⁻¹) of the tested compounds were prepared in *iso*-propanol, and 3 μ l in duplicate were spotted on the plates by hand, 10 mm from the bottom edge and 20 mm apart. The mobile phases were composed of the *iso*-propanol-water binary mixtures, with a varying content of organic modifier between 45-65% (v/v) in 5% increments, as the study compounds differed considerably in their retention. Chromatography was performed in a normal developing chamber at room temperature, the developing distance being 10 cm. The chromatography chamber was saturated with the mobile phase for 30 minutes before use. After the development (30-60 minutes), the plates were air dried at room temperature and examined under UV lamp ($\lambda = 254$ nm) and the R_f (retardation factor) values were measured manually by a digital caliper. The experiments were made in triplicate. All components of the mobile phases used were of the analytical grade of purity. Table 2 lists the data for each phase F_k , $k=1$ to 5. The results were addressed to statistical correlational analysis.

Topological indices were computed by the TOPOCLUJ [32] software while the HOMO energy was computed by single point on the optimized molecules at the Hartree-Fock HF/6-31G(d,p) level of theory.

CONCLUSIONS

A set of twenty six thiazole derivatives, synthesized in the laboratory of Faculty of Pharmacy, "Iuliu Hatieganu" University of Medicine and Pharmacy, and measured for chromatographic retention was submitted to a QSPR study by auto-correlation analysis within the hypermolecule model. As predictor variables, mass fragments, Cluj indices and the HOMO energy, computed at the Hartree-Fock level of theory, have been used. Several QSPR models were derived while the leave-one-out procedure was used to prove the predictive ability of the main model. The auto-correlation descriptors behaved statistically better than the normal descriptors, according to the parameters of regression equations.

ACKNOWLEDGEMENTS

The authors acknowledge to Prof. Mircea V. Diudea for useful discussions.

REFERENCES

1. W. Herndon, P. Biedermann, I. Agranat, *J. Org. Chem.*, **1998**, 63, 7445.
2. N. Zefirov, V. Palyulin, A. Oliferenko, A. Ivanova, A. Ivanov, *Dokl. Chem.*, **2001**, 381, 356.
3. N. Brauner, M. St. Shacham, G. Cholakov, R. Stateva, *Chem. Eng. Sci.*, **2005**, 60, 5458.
4. A. Vatani, M. Mehrpooya, F. Gharagheizi, *Int. J. Mol. Sci.*, **2007**, 8, 407.
5. G.S. Cholakov, R. Stateva, N. Brauner, M. Shacham, *J. Chem. Eng.*, **2008**, 53, 2510.
6. M. Shacham, G. Cholakov, R. Stateva, N. Brauner, *Ind. Eng. Chem. Res.*, **2010**, 49, 900.
7. A. Katritzky, I. Stoyanova-Slavova, K. Tämm, T. Tamm, M. Karelson, *J. Phys. Chem. A*, **2011**, 115, 3475.
8. S. Sixt, J. Altschuh, R. Brüggemann, *Chemosphere*, **1995**, 30, 2397.
9. A. Helguera, M. Cordeiro, D. Natalia, M. Perez, R. Combes, M. Gonzalez, *Bioorg. Med. Chem.*, **2008**, 16, 3395.
10. I. Shamovsky, L. Ripa, L. Börjesson, C.D. Mee, B. Norden, P. Hansen, C. Hasselgren, M. O'Donovan, P. Sjö, *J. Am. Chem. Soc.*, **2011**, 133, 16168.
11. G. Occhipinti, H. Bjørsvik, V. Jensen, *J. Am. Chem. Soc.*, **2006**, 128, 6952.
12. B. Creton, C. Dartiguelongue, T. de Bruin, H. Toulhoat, *Energy Fuels*, **2010**, 24, 5396.
13. Y. Pan, J. Jiang, X. Ding, R. Wang, J. Jiang, *AIChE J.*, **2010**, 56, 690.
14. M. Hechinger, W. Marquardt, *Comput. Chem. Eng.*, **2010**, 34, 1507.
15. A. Katritzky, D. Fara, *Energy Fuels*, **2005**, 19, 922.
16. K. Masuch, A. Fatemi, H. Murrenhoff, K. Leonhard, *Lubrication*, **2011**, 23, 249.
17. H. Kubinyi, *Drug Discovery Today*, **1997**, 2, 457.
18. S. Jonsdottir, F. Jorgensen, S. Brunak, *Bioinformatics*, **2005**, 21, 2145.
19. R. Perkins, H. Fang, W. Tong, W. Welsh, *Environ. Toxicol. Chem.*, **2003**, 22, 1666.
20. M. Devereux, P. Popelier, I. McLay, *J. Chem. Inf. Model*, **2009**, 49, 1497.
21. A. Katritzky, M. Kuanar, S. Slavov, C. Hall, *Chem. Rev.*, **2010**, 110, 5714.
22. D. Janežič, A. Miličević, S. Nikolić, and N. Trinajstić, *Graph Theoretical Matrices in Chemistry*, Math. Chem. Monographs, Univ. Kragujevac, **2007**.
23. M.V. Diudea, *MATCH Commun. Math. Comput. Chem. (MATCH)*, **1997**, 35, 169.
24. M.V. Diudea, *J. Chem. Inf. Comput. Sci.*, **1997**, 37, 300.
25. H. Kubinyi, *Quant. Struct.-Act. Relat.*, **1994**, 13, 285

26. A.T. Balaban, A. Chiriac, I. Motoc, and Z. Simon, *Steric Fit in QSAR (Lectures Notes in Chemistry, Vol. 15)*, Springer, Berlin, **1980**, Chap. 6.
27. M. Wagener, J. Sadowski, and J. Gasteiger, *J. Am. Chem. Soc.*, **1995**, *117*, 7769.
28. A.A. Toropov, and A.P. Toropova, *Internet El. J. Molec. Design*, **2002**, *1*, 108.
29. J.G. Topliss and R.P. Edwards, *J. Med. Chem.* **1979**, *22*, 1238.
30. B. Tipericiuc, V. Zaharia, I. Colosi, C. Moldovan, O. Crisan, A. Parnau, L. Vlase, M. Duma, O. Oniga, *J. Het. Chem.*, **2012**, *49(6)*, 1407.
31. B. Tipericiuc, C. Sârbu, *Journal of Liquid Chromatography & Related Technologies*, **2006**, *29:15*, 2257.
32. O. Ursu, M.V. Diudea, "TOPOCLUJ software program", Babes-Bolyai University, Cluj, **2005**.

PHYSICAL-CHEMICAL AND STRUCTURAL CHARACTERIZATION OF AMBAZONE AND OF ITS SYNTHESIS SECONDARY PRODUCT

HORIA MOCUTA^a, MARIETA MUREȘAN-POP^b, IRINA KACSÓ^b,
GHEORGHE BORODI^b, SIMION SIMON^a and IOAN BRATU^{b,*}

ABSTRACT. 1,4-benzoquinone guanyl-hydrazone thiosemicarbazone (Ambazone) is an antimicrobial compound, usually employed in Faringosept drug preparation. During the Ambazone synthesis some secondary products appear. One of these secondary products - (1,4-benzoquinon-guanyl-semicarbazone - BGHS) has a chemical structure similar to Ambazone one. In order to investigate the monohydrate and anhydrous forms of Ambazone and of BGHS several techniques were employed such as: powder X-ray diffraction (PXRD), Fourier transform infrared (FTIR) spectroscopy and differential scanning calorimetry (DSC) analysis. It was established that the ambazone monohydrate crystallizes in monoclinic system having $P_{21/c}$ space group. Details of the structures and spectroscopic properties for studied compounds are discussed. The stretching vibrations of primary and secondary amine have been identified by FTIR spectroscopy and showed changes in their characteristic absorption regions during water loss upon heating the ambazone monohydrate sample at 140°C. In the dehydration process, a change in molecular rearrangement was evidenced and the anhydrous ambazone was obtained. DSC data confirm the water molecules loss after 37.5 min. of heating treatment at 140°C and XRPD indicates a new crystalline phase.

Keywords: *ambazone, BGHS, PXRD, DSC, FTIR*

INTRODUCTION

The biologically active compound Ambazone (monohydrate form) (AMB) is an antimicrobial substance with very slightly solubility in water. The studies performed on AMB revealed the fact that this drug has local antibacterial properties if it is administrated at bucofaringeal cavity and it has an antiseptic

^a „Babes-Bolyai” University Cluj-Napoca, Faculty of Physics, 1 Kogalniceanu Str., Cluj-Napoca, Romania.

^b National Institute for Research and Development of Isotopic and Molecular Technologies, 65-103 Donath Str., RO-400293, Cluj-Napoca, Romania.

effect against the viruses that produce infections of that type. There is used as active pharmaceutical principle to obtain the Faringosept medicinal product. The investigations regarding AMB in 1990 have described some antineoplastic properties and antitumor effect [1, 2]. Although discovered in 1950's by Domagk, it is less characterized from the point of view of its structural properties. The chemical formula of AMB is $C_8H_{11}N_7SxH_2O$ ($M=255.37$) (Figure 1a). In the AMB synthesis process some secondary compounds are obtained such as BGHS with molecular formula $C_8H_{12}N_7O$ ($M=221$) (Fig.1b) [3].

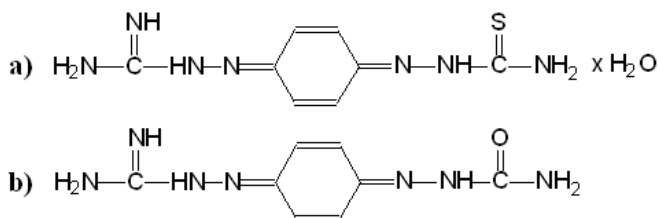


Figure 1. Molecular structures of AMB (a) and BGHS (b) compounds

This investigation shows a comparison between structural characteristics of AMB and of BGHS compounds due to the similarity of their structural formula (sulfur atom being replaced with oxygen one). Another important process that was investigated refers to the transition of AMB from hydrate phase to anhydrous one when heat treatment was applied.

The common techniques applied for characterized these compounds include: powder X-ray diffraction (PXRD), differential scanning calorimetry (DSC) and infrared spectroscopy (FTIR).

RESULTS AND DISCUSSION

Powder X-ray diffraction studies

X-ray powder diffraction patterns for AMB and BGHS are shown in Fig. 2. One can see that the X-ray reflections for BGHS are broader than those for AMB. The crystallinity degree for BGHS is weaker than the corresponding one for AMB. The crystallite size was evaluated using Scherrer relation [6], as being $D = 1300\text{\AA}$ for AMB and $D = 195\text{\AA}$ for BGHS.

Using MS Reflex Plus from Accelerys Material Studio suite (Accelerys Software Inc., 2010), the crystallinity degree was evaluated based on the ratio of crystalline peaks to amorphous halos (Neumann, 2003) [4]: 92% for AMB and 44% for BGHS.

The powder-diffraction pattern of AMB was indexed using the XCell (Neumann, 2003) [4] and Dicvol [5] computer programs implemented in the MS Reflex Plus of Accelrys Material Studio suite (Accelrys Software Inc., 2010).

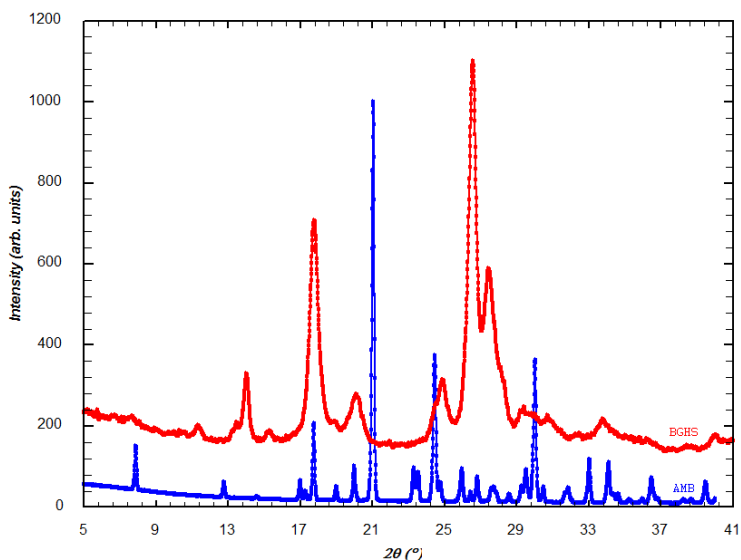


Figure 2. X-ray powder diffraction patterns of AMB and BGHS

From the indexing procedure it was found that AMB crystallizes in monoclinic system, having the following lattice parameters: $a = 7.21 \text{ \AA}$, $b = 7.27 \text{ \AA}$, $c = 22.43 \text{ \AA}$; $\beta = 90.16^\circ$ and unit cell volume is $V = 1176 \text{ \AA}^3$. From forbidden reflection it was found that the space group is $P2_{1/c}$ with $Z=4$ (number of molecule in the unit cell). From molecular weight, the unit cell volume and Z we obtained the calculated density $\rho = 1.447 \text{ g/cm}^3$, which is a reasonable value for such compounds.

AMB monohydrate was submitted to a thermal treatment at 140°C for different time intervals. X-Ray powder diffraction patterns for several relevant thermal treatment time intervals are presented in Fig. 3.

After 5 min of thermal treatment the diffraction patterns changes are observed, *i.e.* the diffraction intensities of the starting phase are diminished and diffraction lines, characteristic to a new phase appear. X-ray diffractograms show that the initial phase is diminished steeply until its complete disappearance after a thermal treatment at 140°C for 37.5 minutes. The crystallinity degree of the new obtained phase is lower than the corresponding one for the starting phase. The crystallite size of the new obtained phase is 590 \AA , as compared to that of the initial phase, which is 1300 \AA .

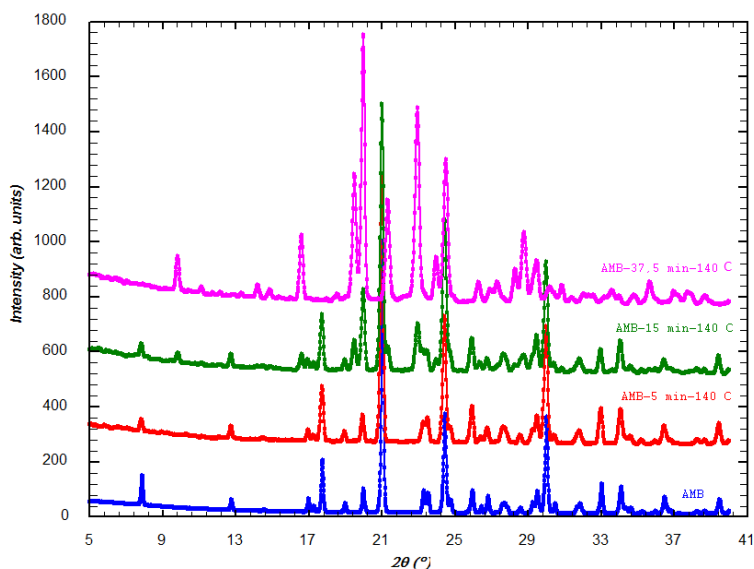


Figure 3. X-ray powder diffraction patterns of AMB compared before and after thermal treatment

FTIR spectroscopy analysis

FTIR spectra of AMB and BGHS are presented in Figs.4 a, b. In the 3400 – 3200 cm^{-1} spectral range (Figure 4a), strong IR absorption bands at ~ 3398 and 3232 cm^{-1} were observed for AMB, respectively at ~ 3463 and 3340 cm^{-1} for BGHS, being assigned to the stretching vibration of primary amino group. The stretching vibrations of secondary amine have been identified at $\sim 3147 \text{ cm}^{-1}$ for AMB, respectively $\sim 3151 \text{ cm}^{-1}$ for BGHS [7, 8].

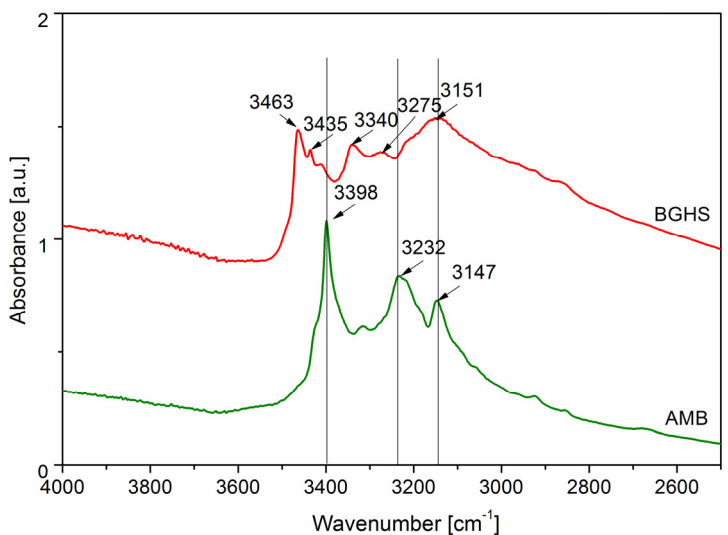
In the 1800-1650 cm^{-1} carbonyl region of BGHS spectrum two peaks at ~ 1750 and 1699 cm^{-1} have been assigned to C=O vibration group (Figure 4.b) [8]. In the 1700–1600 cm^{-1} fingerprint region the medium intensity bands at ~ 1636 and 1613 cm^{-1} for AMB, are attributable to C=N stretching vibration and primary amine bending vibration, respectively.

In the 1600–1500 cm^{-1} spectral range for AMB the primary amino bending at $\sim 1592 \text{ cm}^{-1}$ for AMB and at $\sim 1607 \text{ cm}^{-1}$ for BGHS is identified. The secondary amine deformation vibration is located at $\sim 1509 \text{ cm}^{-1}$ in the spectrum of AMB and at $\sim 1525 \text{ cm}^{-1}$ for BGHS, respectively.

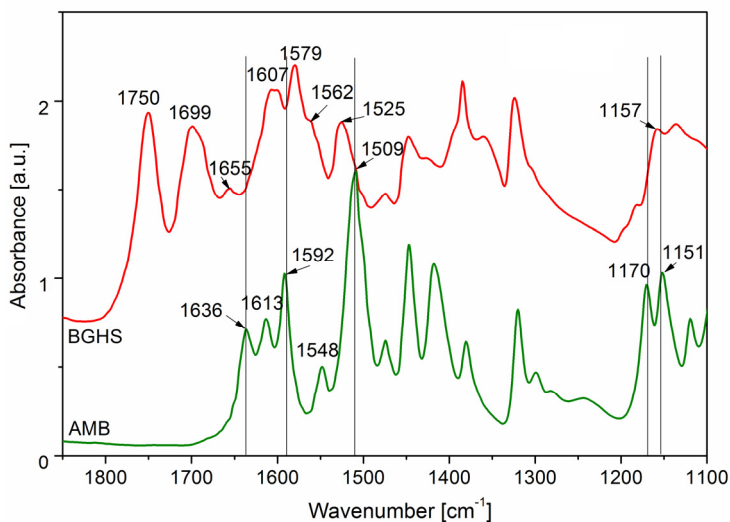
The medium intensity bands at ~ 1548 and 1562 cm^{-1} for AMB and BGHS is assigned to N-C=S and to C=O vibrations, respectively [8].

In the 1230–1030 cm^{-1} spectral range of AMB spectrum, the vibrations at 1170 cm^{-1} (medium intensity) can be associated with C–N bending vibration. The C=S stretching vibration at 1151 cm^{-1} in the spectrum of AMB [10] and in

the spectrum of BGHS the C=O vibration is identified at 1157 cm^{-1} . The differences in peak positions indicate different environments of the carbonyl and amino-groups in these compounds and probably arise from differences in conformation and crystal packing.



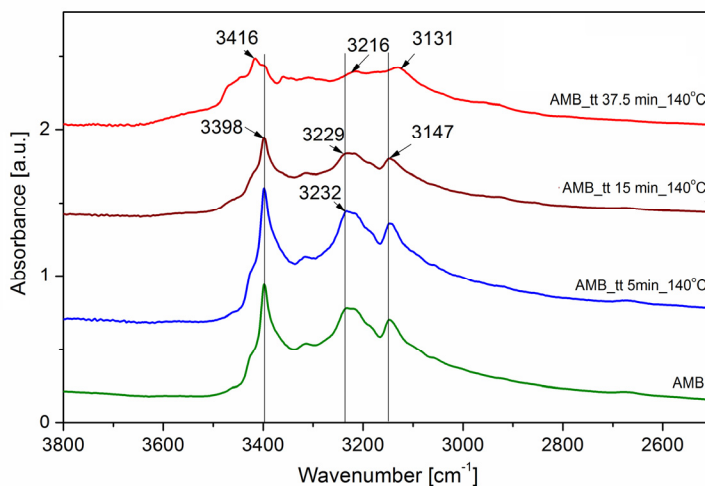
a.



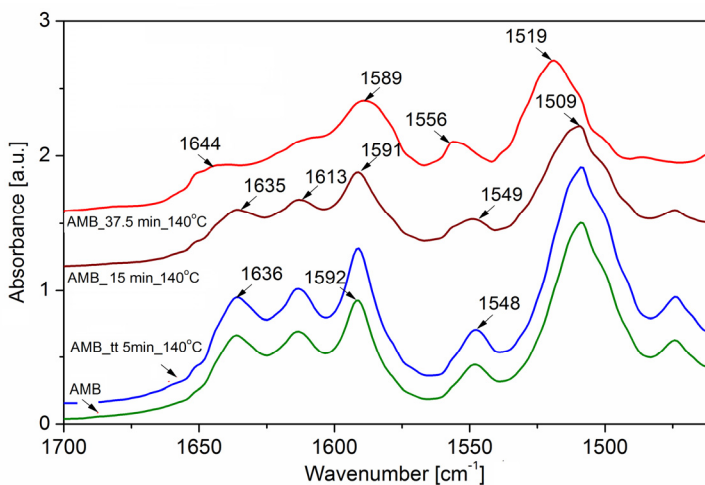
b.

Figure 4. FTIR spectra of AMB monohydrate and of BGHS in the $4000\text{-}2500\text{ cm}^{-1}$ (a); $1850\text{-}1100\text{ cm}^{-1}$ (b) spectral ranges

Upon heating the AMB at 140°C, (Figs. 5a, b), the shift of some absorption bands in the FTIR spectrum were observed, showing a change in force constant, due to a change in molecular rearrangement promptly after hydrogen bond cleavage and were ascribed to crystal collapse due to dehydration. The differences in peak positions indicate different environments of the carbonyl and amino-groups in these compounds and probably arise from differences in conformation and crystal packing.



a.



b.

Figure 5. FTIR spectra of AMB before and after thermal treatment in the 3800-2500 cm^{-1} (a); 1700-1400 cm^{-1} (b) spectral ranges

The band at 3398 cm^{-1} corresponding to primary amine is shifted to higher wavenumbers upon thermal treatments (heating up to 140°C for 37.5 min) whereas the band at 3232 cm^{-1} is shifted to 3216 cm^{-1} (Fig. 5a).

The secondary amine band located at 3147 is shifted to 3131 cm^{-1} for AMB_37.5min_140°C [9-12] that corresponds to broadening by intermolecular association of the C-H group [11].

The pure AMB spectrum contains the secondary amine bending vibration at 1509 cm^{-1} , which is shifted to 1519 cm^{-1} in the case of anhydrous form.

In the carbonyl region (Fig. 5b.) there are differences in peak positions at ~ 1636 and at 1644 cm^{-1} (at 140°C for 37.5 min) showing different environments of the carbonyl groups in AMB, the sample being maintained under thermal treatment for 5, 15 or 37.5 minutes (anhydrate forms) that probably arise from differences in conformation and crystal packing [11, 12]. At the same wavenumber position H-O-H bending vibration of water molecules contributes, also. Its diminishing can support the dehydration of AMB. The C=C stretch at 1613 cm^{-1} shifts to lower wavelength, emphasizing a slight change in orientation of this bond as the water of crystallization bending observed at 1635 cm^{-1} during dehydration is indicative of an alteration in the environment of one of the carbonyl groups. The relatively large intensity increase reflects the loss of hydrogen donation by the water molecule and thus justifies the alterations within the appropriate spectral regions.

Thermal analysis

The DSC thermograms of the AMB, the thermal treated AMB samples and BGHS are presented in Figs. 6, 7. The curve for the pure AMB revealed a broad endothermic signal from 105 to 143°C , with a maximum at 124°C that corresponds to the water molecules loss of the AMB monohydrate structure, followed by a sharp exothermic signal with maximum at 204.5°C , due to the melting with decomposition of AMB.

The BGHS calorimetric curve presents a sharp exothermic signal with maximum at 209°C , attributed to the melting with decomposition of the sample. On this curve any thermal event around 100°C is not observed, so no bounded or unbounded water molecules in the BGHS sample are present.

Comparing the thermally treated samples with starting AMB a decreasing of the dehydration peak intensity was observed with increasing time of the applied heat treatment until the disappearance of this peak for sample heated for 37.5 min (see Fig.7 and Table 1).

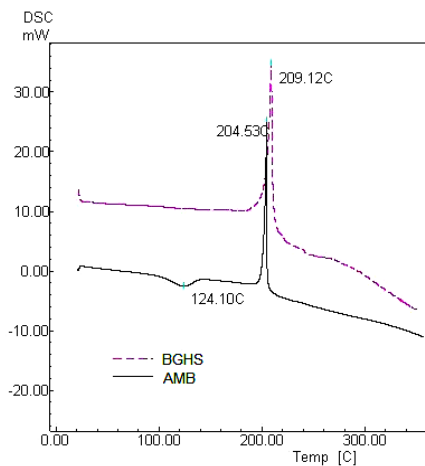


Figure 6. DSC curves of the AMB and BGHS

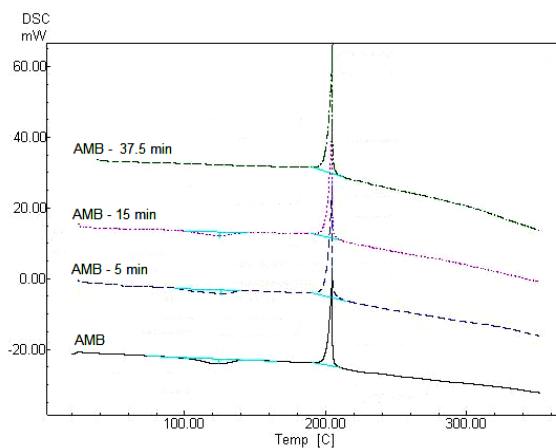


Figure 7. DSC-curves of the AMB monohydrate before and after thermal treatment at 140°C

Table 1. The peaks maxima and heat values for ambazone monohydrate and thermal treated samples at 140°C for different time intervals.

Sample	T peak (°C)	Heat (J/g)	T peak (°C)	Heat (J/g)
AMB	124.1	-215.19	204.5	491.55
Amb (5 min)	126	-182.99	204.5	637.47
Amb (15 min)	124.8	-161.87	204.4	608.00
Amb (37.5 min)	-	-	204.8	732.25

The disappearance of the dehydration peak reveals that water molecule from AMB structure was removed after 37.5 min of heat treatment at 140°C, thus the anhydrous form of the ambazone was obtained.

CONCLUSIONS

From AMB powder diffraction patterns indexing it was established that Ambazone monohydrate crystallizes in the monoclinic system, $P_{21/c}$ space group and the unit cell parameters were determined. The crystallinity and the crystallite size for BGHS are lower than those for AMB. As a result of AMB thermal treatment, its crystalline structure is changed and a new crystalline phase - anhydrous AMB was obtained, its crystallite size (590 Å) being lower than that of the starting compound (1300 Å).

The FTIR analysis showed changes in the characteristic absorption bands of the primary and secondary amines for ambazone monohydrate, BGHS and anhydrous ambazone, respectively.

The BGHS calorimetric curve showed that this compound is an anhydrous form and presents a different melting signal as compared to AMB one. After 37.5 min of the AMB heating treatment at 140°C the water molecule is expelled and the anhydrous form of the ambazone was obtained.

EXPERIMENTAL SECTION

AMB and BGHS investigated in this study were supplied by the Microsin S.A. Bucharest, respectively Research Center for Synthetic Drugs Cluj-Napoca and were used as received.

The thermal treatment of AMB was done maintaining the starting AMB samples at constant temperature (140°C) for different time intervals, starting with 5 minute up to 37.5 minutes.

Powder X-ray diffraction (PXRD) patterns were obtained at room temperature using SHIMADZU XRD-6000 X-ray diffractometer with CuK_α radiation and Ni – filter, ($\lambda = 1.5418\text{Å}$) and (30 mA 40 kV). As standard calibration, a quartz powder had been used. The samples were scanned from 3° to 53°, 2θ at a scan speed of 1°/min.

Fourier transformed infrared spectroscopy (FTIR) measurements were recorded with a JASCO 6100 FTIR spectrometer (number of scans 255; resolution 4 cm^{-1} ; range 4000-400 cm^{-1}). The KBr pellets were prepared by mixing 0.8 mg of sample and 150 mg KBr and pressing the mixture into a 13 mm disks at 12 tones pressure. The spectra were analyzed using Spectra Analysis software.

Thermal analysis (DSC) Calorimetric measurements were performed with DSC-60 Shimadzu differential scanning calorimeter. The 1-2 mg of the accurately weighed samples was heated in crimped aluminium pan from

room temperature up to 350°C under nitrogen flow, the heating rate being 10°C/min. For acquisition and analysis Shimadzu TA-WS-60 and TA60 2.1 system software were used.

ACKNOWLEDGMENTS

Financial support of the PN 09-44 02 05 project is acknowledged.

REFERENCES

1. R. Amlacher, J. Baumgart, A. Hartl, H. Weber, H.J. Kuhnel, W. Schulze, H. Hoffmann, *Arch Geschwulstforsch*, **1990**, *60*, 11.
2. G. Löber and H. Hoffmann, *Biophys Chem*, **1990**, *35*, 287.
3. Applicant S.C. Terapia S.A., „Process for the purification of 1-4-benzoquinone guanylhydrazone thiosemicarbazone (ambazone)“, WO 2005/028431 A1, 31.03.2005.
4. M.A. Neumann, *J Appl Cryst*, **2003**, *36*, 356.
5. A. Boutif, D. Louer, *J Appl Cryst*, **1991**, *24*, 987.
6. P.Klug, L.E. Alexander, “X-Ray Diffraction: Procedure for Polycrystalline and Amorphous Materials”, Willey, New York, **1974**, 966.
7. M. Mureșan-Pop, I. Kacsó, C. Tripon, Z. Moldovan, Gh. Borodi, I. Bratu and S. Simon, *J Therm Anal Calorim*, **2011**, *104*, 299.
8. Z. Dong, B.E. Padden, J.S. Salisbury, E.J. Munson, A. Schroeder, Indra Prakash and David J.W. Grant, *Pharm Res*, **2002**, *19*, 330.
9. G. Socrates, “Infrared and Raman characteristic group frequencies: tables and charts”, 3rd ed. Wiley, West Sussex, **2001**.
10. V. Stilinovic, D. Cincik and B. Kaitner, *Acta Chim*, **2008**, *55*, 874.
11. T.C. Hu, S.L. Wang, T.F. Chen, S.Y. Lin, *J Pharm Sci*, **2002**, *91*, 1351.
12. J.M. Rollinger, A. Burger, *J Therm Anal Calorim*, **2002**, *68*, 361.

NOVEL 1,3-THIAZOLIDINES. SYNTHESIS OF 2-ARYL-4,4-BIS(HYDROXYMETHYL)-1,3-THIAZOLIDINES BY DIRECT THIOAMINALISATION

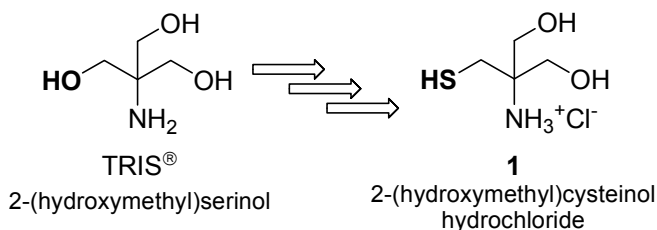
CRISTINA MORAR^a, CARMEN SACALIS^{a*}, PEDRO LAMEIRAS^b,
IOAN BRATU^c, OANA MOLDOVAN^a, YVAN RAMONDENC^d
and MIRCEA DARABANTU^{a**}

ABSTRACT. The direct cyclocondensation between 2-amino-2-(mercaptomethyl)propane-1,3-diol ("hydroxymethyl-cysteinol") with arylaldehydes was investigated as feasibility and efficiency. A new family of C-substituted 1,3-thiazolidines was obtained and fully characterised.

Keywords: cysteinols, thioaminalisation, serinols, 1,3-thiazolidines

INTRODUCTION

We have recently reported [1] our improved three steps synthesis of 2-amino-2-(mercaptomethyl)propane-1,3-diol hydrochloride **1**, an S-analogue of TRIS[®] (Scheme 1).



Scheme 1

^a Babeş-Bolyai[®] University, Department of Chemistry, Laboratory of Fine Organic Stereo- and Heterocyclic Chemistry (L.F.O.S.H.C.) 11 Arany János St., 400028 Cluj-Napoca, Romania.

* cbatiu@chem.ubbcluj.ro; ** darab@chem.ubbcluj.ro

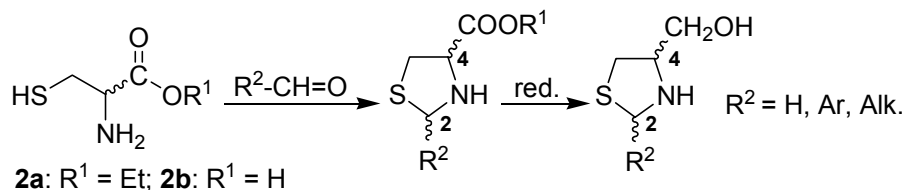
^b University of Reims Champagne-Ardenne, ICMR - LIS, UMR 6229, BP 1039, 51687 Reims, France.

^c INCDTIM, 65-103, Donath St., P.O. Box 700, 400293 Cluj-Napoca 5, Romania.

^d University and INSA of Rouen, IRCOF – LCOFH, UMR 6014 CNRS COBRA, 76821 Mont Saint-Aignan Cedex, France.

Our incipient result prompted other authors to be also interested in exploiting this protocol by using the free base of **1** as starting material in the preparation of new thiazolidinyloxazolidine fused systems [2].

In fact, the “traditional” way by which elaborated-1,3-thiazolidines can be accessed (*Scheme 2*) starts from (*S*)-or (*R*)-ethylcysteinate **2a** (R^1 : Et) (optionally *R* or *S* cysteine **2b**, R^1 : H) upon treatment with aldehydes, followed, optionally, by reduction of the carbonyl functionality [2-5].



Scheme 2

It appears to us that, in the above context, the 1,3-thiazolidine motif was seen rather as an (non)isolable intermediate in the asymmetric synthesis of C-2 substituted analogous of cysteine [4a, 4b], in total synthesis of *Biotin* (vitamin H, coenzyme R) [6a], of antimicrobial *Micacocidin* [6b], of segments of *Farnesyl Transferase* [6c] and, more recently, in dynamic combinatorial libraries (DCLs) [2].

The same “disfavoured” Baldwin’s 5-*endo-trig* cyclisation [7] (*Scheme 2*) was used when the much simpler 2-aminoethanethiol was reacted with various aldehydes [8a, 8b] in order to investigate the behaviour of the resulting 2-substituted-1,3-thiazolidines in ring-chain tautomerism conditions [8c, 8d].

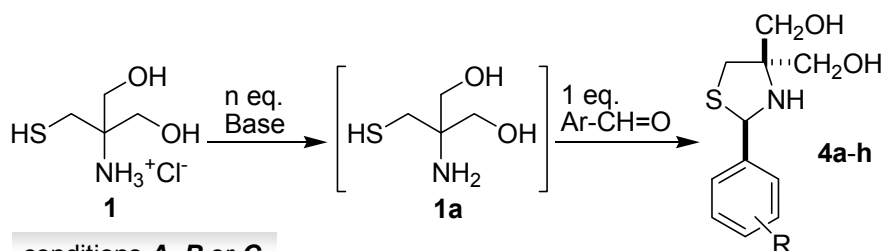
Hence, the aim of the present preliminary report is to account on the synthesis of a new family of condensates of the free base of **1** (*Scheme 1*), the title 2-aryl-4,4-bis(hydroxymethyl)-1,3-thiazolidines, as feasibility and efficiency.

To our knowledge, no similar approach is known up to now.

RESULTS AND DISCUSSION

Scheme 3 depicts our chemistry and the quantitative results. Thus, in the presence of an equimolar amount of an aryl aldehyde, the free base of **1**, the “hydroxymethyl-cysteinol” **1a**, was generated, by acid-base interchange.

Initially, we thought that, when reacted with **1a**, the electrophilicity of the aryl aldehyde could be modulated by an appropriate selection of its withdrawing vs. donating groups C-substitution. Accordingly, three types of reaction conditions, **A-C**, were tested. They all were mandatory to manipulations under mild conditions and inert atmosphere. However, it was rapidly clear to us that our direct thioaminalisation protocol was, in fact, a more or less successful “trapping *in situ*” of the free base **1a** by the chosen carbonyl electrophiles.



conditions **A**, **B** or **C**

A: Benzene / Dean-Stark Trapp / 6-8 h / 0.5 eq. K_2CO_3 aq.

B: EtOH / reflux / 8-10 h / 1.0 eq. Et_3N

C: EtOH / r.t. / 48 h / 1.0 eq. Et_3N

No.	R	Method	Yield (%)	Isolation
4a	<i>p</i> - O_2N	A	15	c.c.*
4b	<i>p</i> -Cl	C	36	d.c.**
4c	<i>p</i> -Br	C	55	d.c.
4d	H	A	51	c.c.
		C	52	d.c.
4e	<i>m</i> -HO	B	40	c.c.
4f	<i>p</i> -HO	B	40	c.c.
4g	<i>o</i> -HO	B	50	c.c.
4h	<i>p</i> - Me_2N	B	44	c.c.

*Column chromatography (see EXPERIMENTAL SECTION for details)

**Direct crystallisations (see EXPERIMENTAL SECTION for details)

Scheme 3

Indeed, **1a** manifested remarkably high redox instability, most likely as $2 R-SH \rightarrow R-S-S-R + 2H$. To this end, we previously reported the isolation of a side dimeric -S-S- cyclisation product resulted upon treatment of the thioaminodiols **1a** (6% conversion) with formaldehyde [1a, 1b]. Soon after, Mahler *et al.* [2] noticed similar intrinsic problems. Actually, we were suspicious ever since that, in the presence of our substrate **1a**, formaldehyde acted not only as an electrophile but, to some extent, *i.e.* 6%, also as an oxidant.

The smallest yield obtained in the case of *p*-nitrobenzaldehyde (compound **4a**, method **A**) confirmed the above hypothesis. If milder conditions we applied, *e.g.* **C** (not depicted in Scheme 1), the result was quite the same. We deduced that *p*-nitrobenzaldehyde behaved, by its nitro functionality, rather like an oxidant of **1a** than like an electrophile. Therefore, the complete failure of a similar attempt in the case of *o*-nitrobenzaldehyde was not surprising at all.

All other investigated cases, **b-h**, showed our protocol being feasible with satisfactory to medium yields.

It was not possible, however, to infer any influence of the aryl aldehyde C-substitution on the reaction conditions **A-C** and yields.

The TLC monitoring (UV, 254 nm) of our thioaminalisations revealed their evolution being directed, almost exclusively, to the desired products. No nucleophilic competition SH vs. OH in the ring closure, previously noticed by Alekseyev and Zelenin [8b] in reaction of sugars with 2-aminoethanethiol was observed.

By contrast, only visualisation in I₂ bath allowed detection of other many side non-aromatic products, issued from the still non-avoidable oxidative degradation of **1a**. That is, in just two cases, compounds **4b** and **4c**, their isolation by direct crystallisation, as pure analytical sample, was fruitful. In all the other manipulations, only column chromatography, with double TLC control (*vide supra*), followed by crystallisation, yielded clean compounds. Once isolated as pure analytical samples, they all were stable indefinitely.

1,3-thiazolidines **4a-h** provided convincing analytical data. As a title example, the ¹H NMR spectrum of compound **4a** is depicted in **Figure 1**.

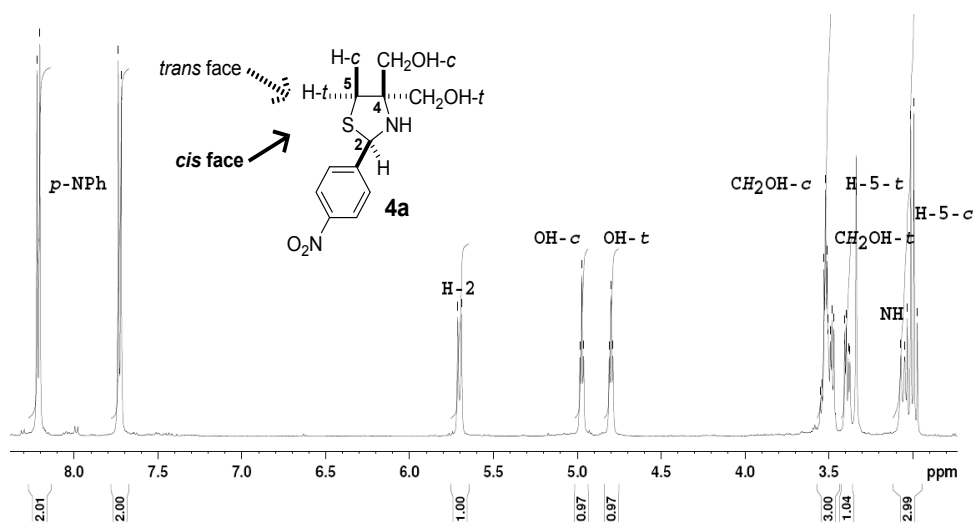


Figure 1. ¹H NMR spectrum of compound **4a** (500 MHz, DMSO-d₆, 298 K)

Figure 2 resumes the most relevant dipolar interactions in the 2D-¹H, ¹H-NOESY Chart of the same compound, illustrating the heterofacial [9] nature of the thiazolidine ring in series **4a-h**.

CONCLUSIONS

In summary, we reported the synthesis of a previously unknown series of C-trisubstituted-1,3-thiazolidines by direct thioaminalisation of 2-amino-2-(mercaptomethyl)propane-1,3-diol with various aryl aldehydes. The efficiency of the protocol is satisfactory up to middle, the feasibility being mandatory to manipulation in mild conditions. The dynamic behaviour of our compounds, as pseudorotation vs. stereoelectronic effects and the extension of their heterofacial skeleton will be reported in the near future.

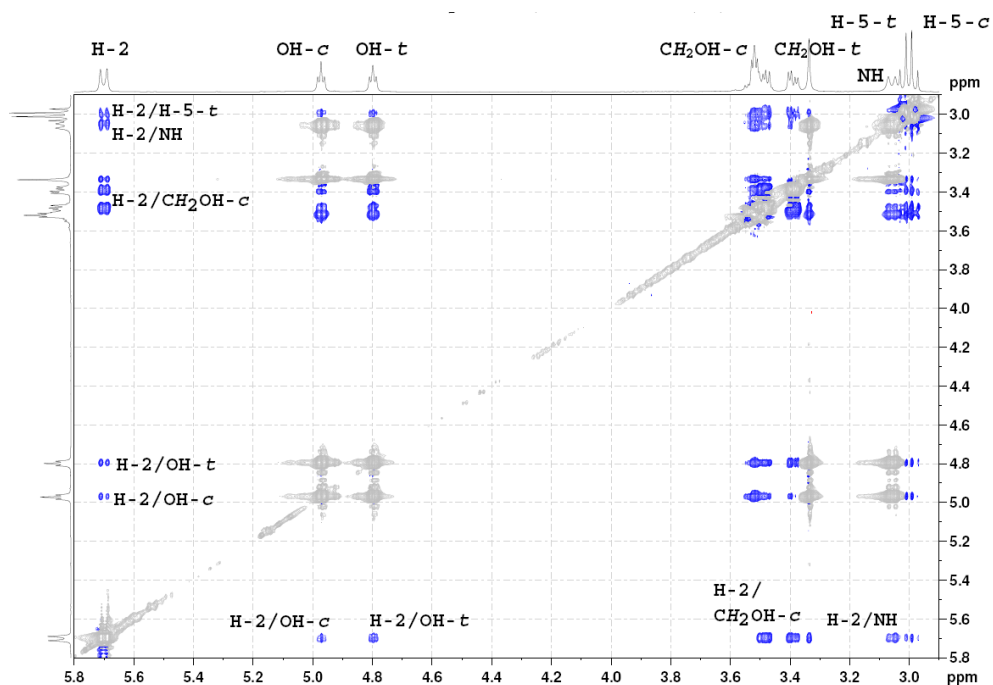


Figure 2. Relevant $^1\text{H}, ^1\text{H}$ dipolar interactions in the 2D- $^1\text{H}, ^1\text{H}$ -NOESY Experiment of compound **4a** (500 MHz, $\text{DMSO}-d_6$ 298 K)

EXPERIMENTAL SECTION

Melting points are uncorrected; they were carried out on ELECTROTHERMAL[®] instrument. Conventional NMR spectra were recorded on a Bruker[®] AM 300 instrument operating at 300 and 75 MHz for ^1H and ^{13}C nuclei, respectively. Related 2D- $^1\text{H}, ^1\text{H}$ -NOESY and DEPT Experiments were recorded on a Bruker[®] AM 500 instrument operating at 500 and 125 MHz for ^1H and ^{13}C nuclei or respectively. All chemical shifts (δ values) are given throughout in parts per million (ppm); all homocoupling patterns ($^nJ_{\text{H,H}}$ values)

are given throughout in Hertz. TLC was performed by using aluminium sheets with silica gel 60 F254 (Merck[®]); column chromatography was conducted on Silica gel Si 60 (40–63 mm, Merck[®]). IR spectra were performed on a JASCO[®] FT-IR 6100 Spectrometer. Only relevant absorption maxima are listed, throughout, in cm^{-1} : s (strong), m (medium) and w (weak). Microanalyses were performed on a Carlo Erba[®] CHNOS 1160 apparatus. Mass spectra (MS) as ESI were recorded on a Bruker[®] Esquire Instrument with ions trapping in electrospray mode.

The synthesis and data of compound **1** (*Scheme 1*) we reported elsewhere [1].

In the NMR descriptions, some specific abbreviations were used: “bt” (broad triplet), “bd” (broad doublet), “bdd” (broad doublet of doublets). Stereochemical descriptors *-c* (*cis*) and *-t* (*trans*) are, throughout, referred to the fiducial substituent [9], the Ar group at position C-2 (see **Figure 2**).

Typical procedures for the preparation of 1,3-thiazolidines 4a-h

Method A

Preparation of compound 4d

Under dry nitrogen atmosphere, to a benzene (40 mL) solution containing benzaldehyde (0.613 g, 0.587 mL, 5.78 mmol), 2-amino-2-(mercaptomethyl)propane-1,3-diol hydrochloride **1** (1.000 g, 5.78 mmol) was added with vigorous stirring. In the resulted suspension, a solution obtained by dissolving anh. K_2CO_3 (0.400 g, 2.89 mmol) in water (1.500 mL) was injected. The reaction mixture was refluxed, under N_2 , for about 8 h. (until no more water separated in a Dean-Stark trap). At room temperature, the suspension was filtered off and minerals were well washed with dry THF (50 mL). The organic filtrate was evaporated under reduced pressure to dryness and the solid residue was chromatographed on silica gel (eluent ligroin/acetone 1.5:1) to provide the desired compound **4d** as a single pure analytical sample fraction (0.665 g, 51% yield).

Method B

Preparation of compound 4g

Under dry nitrogen atmosphere, to an ethanol (25 mL) solution containing 2-hydroxybenzaldehyde (0.247 g, 0.210 mL, 2.022 mmol), 2-amino-2-(mercaptomethyl)propane-1,3-diol hydrochloride **1** (0.350 g, 2.022 mmol) was added with vigorous stirring. To the resulted suspension, triethylamine (0.204 g, 0.280 mL, 2.022 mmol) was injected. The reaction mixture was refluxed for 8 h. At room temperature, the suspension was evaporated under reduced pressure to dryness. The residue was taken with anh. THF on heating (40°C, 3×15 mL) and filtered off. The remaining triethylamine hydrochloride

was well washed with anh. THF, and then the combined THF solution was evaporated under reduced pressure to dryness. The residue was chromatographed on silica gel, the desired compound being isolated as the single fraction. This was additionally triturated with DCM/ligroin at -18°C to yield compound **4g** as pure analytical sample (0.244 g, 50% yield).

Method C

Preparation of compound **4b**

Under dry nitrogen atmosphere, to an ethanol (15 mL) solution containing 4-chlorobenzaldehyde (0.284 g, 2.022 mmol), 2-amino-2-(mercaptomethyl) propane-1,3-diol hydrochloride **1** (0.350 g, 2.022 mmol) was added with vigorous stirring. To the resulted suspension, triethylamine (0.204 g, 0.280 mL, 2.022 mmol) was injected. The reaction mixture was stirred at room temperature for 24 h. and then evaporated under reduced pressure to dryness. The residue was taken with anh. THF on heating (40°C , 3×15 mL) and filtered off. The remaining triethylamine hydrochloride was well washed with anh. THF, and then the combined THF solution was evaporated under reduced pressure to dryness. The residue was first triturated with THF/Et₂O. The resulted product was supplementary crystallised from EtOH/DCM/Et₂O 0.5:5:3 at -18°C to yield the desire compound **4b** as pure analytical sample (0.188 g, 36% yield).

(*rac*)-4,4-Bis(hydroxymethyl)-2-(4-nitrophenyl)-1,3-thiazolidine (**4a**); yield 15% (column chromatography, eluent ligroin/acetone 1.5:1), yellow powder, mp 119 – 121°C ; [Found: C, 49.09; H, 5.31; N, 9.98%. C₁₁H₁₄N₂O₄S (270.07) requires: C, 48.88; H, 5.22; N, 10.36%]; *R*_f (60% ligroin/acetone) 0.48. ν_{max} . (KBr) 3392 (m), 3281 (m), 3214 (m), 2927 (m), 2861 (m), 1608 (m), 1525 (s), 1458 (m), 1353 (s), 1317 (m), 1108 (m), 1094 (m), 1056 (s), 1034 (s), 942 (m), 914 (m), 863 (s), 833 (s), 751 (m), 709 (m), 593 (m) cm⁻¹. ¹H NMR, 2D-¹H, ¹H-COSY and 2D-¹H,¹H-NOESY (500 MHz, DMSO-*d*₆, 298 K) δ_{H} 2.99 (1 H, d, ²*J*_{H,H}=10.2 Hz, H-5-c), 3.02 (1 H, d, ²*J*_{H,H}=10.5 Hz, H-5-t), 3.06 (1 H, d, ³*J*_{H,H}=11.5 Hz, NH), 3.39 (1 H, dd, ²*J*_{H,H}=11.0 Hz, ³*J*_{H,H}=5.0 Hz, CH₂OH-t), 3.48 (1 H, dd, ²*J*_{H,H}=11.0 Hz, ³*J*_{H,H}=6.5 Hz, CH₂OH-t), 3.51 (1 H, dd as t, ²*J*_{H,H}=8.0 Hz, ³*J*_{H,H}=5.0 Hz, CH₂OH-c), 3.54 (1 H, dd, ²*J*_{H,H}=10.5 Hz, ³*J*_{H,H}=5.0 Hz, CH₂OH-c), 4.80 (1 H, dd as t, ³*J*_{H,H}=5.8 Hz, OH-t), 4.97 (1 H, dd as t, ³*J*_{H,H}=5.5 Hz, OH-c), 5.70 (1 H, d, ³*J*_{H,H}=11.0 Hz, H-2), 7.73 (2 H, d, ³*J*_{H,H}=8.5 Hz, H-2, -6, Ar), 8.21 (2 H, d, ³*J*_{H,H}=8.5 Hz, H-3, -5, Ar) ppm. ¹³C NMR, *J*_{mod}, DEPT, HSQS and HMBC (125 MHz, DMSO-*d*₆, 298 K) δ_{C} 37.8 (C-5), 62.5 (CH₂OH-t), 63.3 (CH₂OH-c), 69.5 (C-2), 74.7 (C-4), 124.0 (C-3, -5, Ar), 128.7 (C-2, -6, Ar), 147.4 (C-1, Ar), 149.6 (C-4, Ar) ppm. MS (ESI⁺, ACN) *m/z* (rel. int. %) 272 (M+2H) (19), 271 (M+H) (100), 252 (M-18) (41).

(*rac*)-2-(4-Chlorophenyl)-4,4-bis(hydroxymethyl)-1,3-thiazolidine (**4b**); yield 36% (tritulating with THF/Et₂O then crystallisation from EtOH/DCM/Et₂O 0.5:5:3), white powder, mp 100-102°C; [Found: C, 51.11; H, 5.35; N, 5.61%. C₁₁H₁₄ClNO₂S (259.04) requires: C, 50.86; H, 5.43; N, 5.39%]; *R_f* (CH₂Cl₂/Et₂O/EtOH 0.5:5:3) 0.53. *v*_{max}. (KBr) 3354 (s), 3267 (s), 2927 (m), 2874 (m), 1592 (m), 1490 (m), 1412 (m), 1093 (m), 1027 (s), 1015 (m), 803 (m), 777 (m), 723 (w), 581 (w), 524 (w) cm⁻¹. ¹H NMR and 2D-¹H,¹H-COSY (300 MHz, DMSO-*d*₆, 298 K) δ_H 2.97 (1 H, d, ²*J*_{H,H}=10.2 Hz, H-5-*c*), 3.01 (1 H, d, ²*J*_{H,H}=10.2 Hz, H-5-*t*), 3.33 (1 H, d, ²*J*_{H,H}=10.8 Hz, CH₂OH-*t*), 3.45 (1 H, d, ²*J*_{H,H}=11.1 Hz, CH₂OH-*t*), 3.53 (1 H, d, ²*J*_{H,H}=12.6 Hz, CH₂OH-*c*), 3.57 (1 H, d, ²*J*_{H,H}=12.6 Hz, CH₂OH-*c*), 4.90 (2 H, bs, OH-*c*, -*t*), 5.54 (1 H, s, H-2), 7.42 (2 H, d, ³*J*_{H,H}=8.7 Hz, H-2, -6, Ar), 7.49 (2 H, d, ³*J*_{H,H}=8.4 Hz, H-3, -5, Ar) ppm. ¹³C NMR and *J*_{mod} (75 MHz, DMSO-*d*₆, 298 K) δ_C 37.6 (C-5), 62.6 (CH₂OH-*t*), 63.1 (CH₂OH-*c*), 70.0 (C-2), 74.5 (C-4), 128.8 (C-3, -5, Ar), 129.5 (C-2, -6, Ar), 132.8 (C-4, Ar), 140.3 (C-1, Ar) ppm. MS (ESI⁺, ACN) *m/z* (rel. int. %) 260 (M+H).

(*rac*)-2-(4-Bromophenyl)-4,4-bis(hydroxymethyl)-1,3-thiazolidine (**4c**); yield 55% (tritulating with THF/Et₂O then crystallisation from EtOH/DCM/Et₂O 0.5:5:3), white powder, mp 102-104°C; [Found: C, 43.34; H, 4.46; N, 5.61%. C₁₁H₁₄BrNO₂S (302.99) requires: C, 43.43; H, 4.64; N, 5.60%]; *R_f* (CH₂Cl₂/Et₂O/EtOH 0.5:5:3) 0.53. *v*_{max}. (KBr) 3356 (s), 3321 (s), 3261 (s), 2929 (m), 2869 (m), 1587 (w), 1486 (s), 1458 (s), 1192 (m), 1055 (s), 1044 (s), 1028 (s), 1010 (s), 777 (s), 719 (w), 525 (w) cm⁻¹. ¹H NMR and 2D-¹H,¹H-COSY (300 MHz, DMSO-*d*₆, 298 K) δ_H 2.87 (1 H, d, ³*J*_{H,H}=11.4 Hz, NH), 2.96 (1 H, d, ²*J*_{H,H}=10.2 Hz, H-5-*c*), 3.01 (1 H, d, ²*J*_{H,H}=10.2 Hz, H-5-*t*), 3.33 (1 H, d, ²*J*_{H,H}=10.8 Hz, CH₂OH-*t*), 3.45 (1 H, d, ²*J*_{H,H}=11.1 Hz, CH₂OH-*t*), 3.53 (1 H, d, ²*J*_{H,H}=12.3 Hz, CH₂OH-*c*), 3.57 (1 H, d, ²*J*_{H,H}=11.7 Hz, CH₂OH-*c*), 4.99 (2 H, bs, OH-*c*, -*t*), 5.52 (1 H, d, ³*J*_{H,H}=10.5 Hz, H-2), 7.42 (2 H, d, ³*J*_{H,H}=8.4 Hz, H-2, -6, Ar), 7.55 (2 H, d, ³*J*_{H,H}=8.4 Hz, H-3, -5, Ar) ppm. ¹³C NMR and *J*_{mod} (75 MHz, DMSO-*d*₆, 298 K) δ_C 37.6 (C-5), 62.6 (CH₂OH-*t*), 63.1 (CH₂OH-*c*), 70.1 (C-2), 74.5 (C-4), 121.3 (C-4, Ar), 129.8 (C-2, -6, Ar), 131.7 (C-3, -5, Ar), 140.7 (C-1, Ar) ppm. MS (ESI⁺, ACN) *m/z* (rel. int. %) 306 [M+2] (86), 304 [M+1] (100), 302.13 (15), 273.2 (22), 226.13 (15), 184.13 (16).

(*rac*)-4,4-Bis(hydroxymethyl)-2-phenyl-1,3-thiazolidine (**4d**); yield 51%, (column chromatography, eluent ligroin/acetone 1.5:1), white powder, mp 119-121°C; [Found: C, 58.46; H, 7.05; N, 5.91%. C₁₁H₁₅NO₂S (225.08) requires: C, 58.64; H, 6.71; N, 6.22%]; *R_f* (60% ligroin/acetone) 0.55. *v*_{max}. (KBr) 3368 (s), 3325 (s), 3259 (s), 2959 (m), 2921 (s), 2872 (m), 2361 (m), 1602 (w), 1586 (w), 1492 (s), 1454 (s), 1437 (m), 1231 (m), 1192 (m), 1073 (s), 1044 (s), 1028 (s), 962 (w), 883 (m), 867 (s), 799 (s), 753 (s), 698 (s), 614 (m), 579 (w), 565 (w), 524 (w) cm⁻¹.

^1H NMR and 2D- ^1H , ^1H -COSY (300 MHz, DMSO- d_6 , 298 K) δ_{H} 2.86 (1 H, d, $^3J_{\text{H,H}}=12.0$ Hz, NH), 2.99 (1 H, d, $^2J_{\text{H,H}}=10.2$ Hz, H-5-*c*), 3.04 (1 H, d, $^2J_{\text{H,H}}=10.2$ Hz, H-5-*t*), 3.34 (1 H, dd, $^2J_{\text{H,H}}=11.0$, $^3J_{\text{H,H}}=5.0$ Hz, CH₂OH-*t*), 3.47 (1 H, dd, $^2J_{\text{H,H}}=11.1$ Hz, $^3J_{\text{H,H}}=6.6$ Hz, CH₂OH-*t*), 3.57 (1 H, d, $^2J_{\text{H,H}}=12.3$ Hz, CH₂OH-*c*), 3.63 (1 H, d, $^2J_{\text{H,H}}=12.0$ Hz, CH₂OH-*c*), 4.77 (1 H, dd as t, $^3J_{\text{H,H}}=5.7$ Hz, OH-*t*), 5.07 (1 H, dd as t, $^3J_{\text{H,H}}=5.7$ Hz, OH-*c*), 5.54 (1 H, d, $^3J_{\text{H,H}}=12.0$ Hz, H-2), 7.29 (1 H, m, H-4, Ph), 7.36 (2 H, dd as t, $^3J_{\text{H,H}}=7.2$ Hz, H-3, -5, Ph), 7.47 (2 H, d, $^3J_{\text{H,H}}=6.9$ Hz, H-2, -6, Ph) ppm. ^1H NMR, 2D- ^1H , ^1H -COSY and 2D- ^1H , ^1H -NOESY (500 MHz, DMSO- d_6 , 298 K) δ_{H} 2.85 (1 H, bs, NH), 2.98 (1 H, d, $^2J_{\text{H,H}}=10.0$ Hz, H-5-*c*), 3.02 (1 H, d, $^2J_{\text{H,H}}=10.0$ Hz, H-5-*t*), 3.34 (1 H, d, $^2J_{\text{H,H}}=11.0$, CH₂OH-*t*), 3.45 (1 H, dd, $^2J_{\text{H,H}}=11.0$ Hz, $^3J_{\text{H,H}}=4.0$ Hz, CH₂OH-*t*), 3.57 (1 H, dd, $^2J_{\text{H,H}}=13.0$ Hz, $^3J_{\text{H,H}}=4.0$ Hz, CH₂OH-*c*), 3.58 (1 H, dd, $^2J_{\text{H,H}}=13.2$ Hz, $^3J_{\text{H,H}}=3.5$ Hz, CH₂OH-*c*), 4.72 (1 H, bs, OH-*t*), 5.02 (1 H, bs, OH-*c*), 5.53 (1 H, bs, H-2), 7.30 (1 H, dd as t, $^3J_{\text{H,H}}=7.3$ Hz, H-4, Ph), 7.36 (2 H, dd as t, $^3J_{\text{H,H}}=7.3$ Hz, H-3, -5, Ph), 7.47 (2 H, d, $^3J_{\text{H,H}}=7.0$ Hz, H-2, -6, Ph) ppm. ^{13}C NMR, J_{mod} , DEPT, HSQC and HMBC (125 MHz, DMSO- d_6 , 298 K) δ_{C} 37.6 (C-5), 62.8 (CH₂OH-*t*), 63.2 (CH₂OH-*c*), 71.0 (C-2), 74.5 (C-4), 127.6 (C-2, -6, Ph), 128.4 (C-4, Ph), 128.8 (C-3, -5, Ph), 141.1 (C-1, Ph) ppm. MS (ESI⁺, ACN) m/z (rel. int. %) 226 (M+H) (100), 227 (M+2) (14).

(*rac*)-4,4-Bis(hydroxymethyl)-2-(3-hydroxyphenyl)-1,3-thiazolidine (**4e**); yield 40% (column chromatography, eluent EtOH/CH₂Cl₂/Et₂O 1:5:3, then triturating from THF/ligroine), white powder, mp 133-135°C; [Found: C, 55.05; H, 5.98; N, 5.91%. C₁₁H₁₅NO₃S (241.08) requires: C, 54.75; H, 6.27; N, 5.80%]; R_f (EtOH/CH₂Cl₂/Et₂O 1:5:3) 0.64. ν_{max} (KBr) 3403 (s), 3276 (s), 2928 (m), 2734 (m), 2606 (m), 1599 (s), 1458 (s), 1083 (m), 1040 (s), 867 (m), 795 (w), 772 (w), 694 (w), 583 (w) cm⁻¹. ^1H NMR and 2D- ^1H , ^1H -COSY (300 MHz, DMSO- d_6 , 298 K) δ_{H} 2.79 (1 H, d, $^3J_{\text{H,H}}=12.0$ Hz, NH), 2.98 (2 H, s, H-5), 3.33 (1 H, s, CH₂OH-*t*), 3.42 (1 H, s, CH₂OH-*t*), 3.59 (2 H, s, CH₂OH-*c*), 4.75 (1 H, bs, OH-*t*), 5.07 (1 H, bs, OH-*c*), 5.44 (1 H, d, $^3J_{\text{H,H}}=12.0$ Hz, H-2), 6.70 (1 H, d, $^3J_{\text{H,H}}=7.2$ Hz, H-4, Ar), 6.86 (1 H, s, H-2, Ar), 6.87 (1 H, d, $^3J_{\text{H,H}}=11.4$ Hz, H-6, Ar), 7.14 (1 H, dd as a t, $^3J_{\text{H,H}}=7.1$ Hz, H-5, Ar), 9.48 (1 H, s, Ar-OH) ppm. ^{13}C NMR and J_{mod} (75 MHz, DMSO- d_6 , 298 K) δ_{C} 37.4 (C-5), 62.8 (CH₂OH-*t*), 63.1 (CH₂OH-*c*), 71.0 (C-2), 74.4 (C-4), 114.2 (C-2, Ar), 115.4 (C-4, Ar), 118.2 (C-6, Ar), 129.8 (C-5, Ar), 142.5 (C-1, Ar), 157.8 (C-2, Ar) ppm; MS (ESI⁺, MeOH) m/z (rel. int. %) 242 (M+H) (100).

(*rac*)-4,4-Bis(hydroxymethyl)-2-(4-hydroxyphenyl)-1,3-thiazolidine (**4f**); yield 40% (column chromatography, eluent EtOH/CH₂Cl₂/Et₂O 1:5:3), beige powder, mp 142-144°C; [Found: C, 54.93; H, 6.16; N, 6.11%. C₁₁H₁₅NO₃S (241.08) requires: C, 54.75; H, 6.27; N, 5.80%]; R_f (EtOH/CH₂Cl₂/Et₂O 1:5:3) 0.63. ν_{max} (KBr) 3250 (s), 3033 (m), 2961 (m), 2929 (m), 2807 (m), 2703 (w), 1614 (m),

1594 (m), 1519 (s), 1454 (m), 1378 (w), 1277 (s), 1229 (s), 1171 (m), 1040 (s), 876 (m), 829 (m), 812 (m), 708 (w), 538 (w) cm^{-1} . ^1H NMR and 2D- ^1H , ^1H -COSY (300 MHz, DMSO- d_6 , 298 K) δ_{H} 2.70 (1 H, d, $^3J_{\text{H,H}}=12.3$ Hz, NH), 2.94 (1 H, d, $^2J_{\text{H,H}}=10.2$ Hz, H-5-c), 2.99 (1 H, d, $^2J_{\text{H,H}}=10.2$ Hz, H-5-t), 3.29 (1 H, dd, $^2J_{\text{H,H}}=10.8$, $^3J_{\text{H,H}}=4.8$ Hz, $\text{CH}_2\text{OH-t}$), 3.42 (1 H, dd, $^2J_{\text{H,H}}=10.5$, $^3J_{\text{H,H}}=6.6$ Hz, $\text{CH}_2\text{OH-t}$), 3.55 (1 H, dd, $^2J_{\text{H,H}}=12.3$, $^3J_{\text{H,H}}=5.1$ Hz, $\text{CH}_2\text{OH-c}$), 3.59 (1H, dd, $^2J_{\text{H,H}}=11.4$ $^3J_{\text{H,H}}=5.6$ Hz, $\text{CH}_2\text{OH-c}$), 4.71 (1 H, dd as t, $^3J_{\text{H,H}}=5.6$ Hz, OH-t), 5.04 (1 H, dd as t, $^3J_{\text{H,H}}=5.7$ Hz, OH-c), 5.42 (1 H, d, $^3J_{\text{H,H}}=12.0$ Hz, H-2), 6.73 (2 H, d, $^3J_{\text{H,H}}=8.4$ Hz, H-3, -5, Ar), 7.26 (2H, d, $^3J_{\text{H,H}}=8.4$ Hz, H-2, -6, Ar), 9.48 (1 H, s, Ar-OH) ppm. ^{13}C NMR and J_{mod} (75 MHz, DMSO- d_6 , 298 K) δ_{C} 37.5 (C-5), 62.8 ($\text{CH}_2\text{OH-t}$), 63.1 ($\text{CH}_2\text{OH-c}$), 71.0 (C-2), 74.3 (C-4), 115.5 (C-3, -5, Ar), 128.9 (C-2, -6, Ar), 131.0 (C-1, Ar), 157.6 (C-4, Ar) ppm. MS (ESI $^+$, MeOH) m/z (rel. int. %) 242.02 (M+H) (100).

(*rac*)-4,4-Bis(hydroxymethyl)-2-(2-hydroxyphenyl)-1,3-thiazolidine (**4g**); yield 50% (column chromatography, eluent EtOH/ CH_2Cl_2 /Et $_2\text{O}$ 1:5:3, then triturating from DCM/ligroin), yellow powder, mp 86-88°C; [Found: C, 54.61; H, 6.56; N, 5.98%. $\text{C}_{11}\text{H}_{15}\text{NO}_3\text{S}$ (241.08) requires: C, 54.75; H, 6.27; N, 5.80%]; R_f (EtOH/ CH_2Cl_2 /Et $_2\text{O}$ 1:5:3) 0.65. ν_{max} (KBr) 3374 (s), 3330 (s), 3275 (s), 3220 (s), 2917 (s), 2851 (s), 1604 (m), 1457 (s), 1263 (s), 1229 (m), 1054 (s), 889 (m), 759 (s), 686 (w), 549 (w) cm^{-1} . ^1H NMR and 2D- ^1H , ^1H -COSY (300 MHz, DMSO- d_6 , 298 K); δ_{H} 2.90 (1 H, d, $^2J_{\text{H,H}}=9.9$ Hz, H-5-c), 2.96 (1 H, d, $^2J_{\text{H,H}}=10.2$ Hz, H-5-t), 3.30 (1 H, d, $^3J_{\text{H,H}}=12.3$ Hz, NH), 3.34 (1 H, bd, $^2J_{\text{H,H}}=10.2$ Hz, $\text{CH}_2\text{OH-t}$), 3.45 (1 H, bd, $^2J_{\text{H,H}}=10.5$ Hz, $\text{CH}_2\text{OH-t}$), 3.59 (2 H, bs, $\text{CH}_2\text{OH-c}$), 4.75 (1 H, bs, OH-t), 5.04 (1 H, bs, OH-c), 5.70 (1 H, d, $^3J_{\text{H,H}}=9.9$ Hz, H-2), 6.78 (1 H, d, $^3J_{\text{H,H}}=5.7$ Hz, H-3, Ar), 6.79 (1 H, dd as t, $^3J_{\text{H,H}}=3.5$ Hz, H-5, Ar), 7.10 (1 H, ddd $^3J_{\text{H,H}}=7.6$, 7.6, 1.1 Hz, H-4, Ar), 7.30 (1 H, d, $^3J_{\text{H,H}}=6.6$ Hz, H-6, Ar), 9.98 (1 H, bs, Ar-OH) ppm. ^{13}C NMR, J_{mod} (75 MHz, DMSO- d_6 , 298 K) δ_{C} 36.7 (C-5), 62.4 ($\text{CH}_2\text{OH-t}$), 63.2 ($\text{CH}_2\text{OH-c}$), 65.8 (C-2), 73.6 (C-4), 116.0 (C-3, Ar) 119.3 (C-1, Ar), 126.3 (C-1, Ar), 127.7 (C-4, Ar), 155.6 (C-2, Ar) ppm. MS (ESI $^+$, MeOH) m/z (rel. int. %) 242.13 (M+H) (100).

(*rac*)-4,4-Bis(hydroxymethyl)-2-(4-dimethylaminophenyl)-1,3-thiazolidine (**4h**); yield 44% (column chromatography, eluent EtOH/ CH_2Cl_2 /Et $_2\text{O}$ 1:5:3, then triturating with THF/ligroin), orange powder, mp 145-147°C; [Found: C, 57.88; H, 7.77; N, 10.10%. $\text{C}_{13}\text{H}_{20}\text{N}_2\text{O}_2\text{S}$ (268.12) requires: C, 58.18; H, 7.51; N, 10.44%]; R_f (EtOH/ CH_2Cl_2 /Et $_2\text{O}$ 1:5:3) 0.85. ν_{max} (KBr) 3346 (s), 3261 (s), 3122 (m), 2933 (m), 2873 (m), 2817 (m), 1616 (s), 1530 (s), 1441 (s), 1362 (m), 1222 (s), 1195 (s), 1068 (s), 1032 (s), 892 (m), 818 (s), 539(w) cm^{-1} . ^1H NMR and 2D- ^1H , ^1H -COSY (300 MHz, DMSO- d_6 , 298 K) δ_{H} 2.70 (1 H, bd, $^3J_{\text{H,H}}=11.7$ Hz, NH), 2.88 (6 H, s, NMe $_2$), 2.95 (1 H, bd, $^2J_{\text{H,H}}=10.2$ Hz, H-5-c), 3.00 (1 H, bd, $^2J_{\text{H,H}}=9.9$ Hz, H-5-t), 3.26 (1 H, bdd, $^2J_{\text{H,H}}=10.2$ Hz, $^3J_{\text{H,H}}=2.1$ Hz, $\text{CH}_2\text{OH-t}$),

3.43 (1 H, bdd, $^2J_{\text{H,H}}=11.6$, $^3J_{\text{H,H}}=5.6$ Hz, $\text{CH}_2\text{OH-t}$), 3.56 (1 H, bd, $^2J_{\text{H,H}}=13.2$ Hz, $\text{CH}_2\text{OH-c}$), 3.61 (1 H, bd, $^2J_{\text{H,H}}=13.2$ Hz, $\text{CH}_2\text{OH-c}$), 4.71 (1 H, bt, OH-t), 5.05 (1 H, bt, $^3J_{\text{H,H}}=4.7$ Hz, OH-c), 5.42 (1 H, bd, $^3J_{\text{H,H}}=10.5$ Hz, H-2), 6.69 (2 H, d, $^3J_{\text{H,H}}=8.7$ Hz, H-3, -5, Ar), 7.27 (2 H, d, $^3J_{\text{H,H}}=8.4$ Hz, H-2, -6, Ar) ppm. ^{13}C NMR and J_{mod} (75 MHz, DMSO-d_6 , 298 K) δ_{C} 37.4 (C-5), 40.6 (NMe_2), 62.9 ($\text{CH}_2\text{OH-t}$), 63.2 ($\text{CH}_2\text{OH-c}$), 71.2 (C-2), 74.4 (C-4), 112.5 (C-3, -5, Ar), 127.8 (C-1, Ar), 128.3 (C-2, -6, Ar), 150.7 (C-4, Ar) ppm. MS (ESI^+ , MeOH) m/z (rel. int. %) 291.07 [$\text{M}+\text{Na}$] (7), 269.20 ($\text{M}+\text{H}$) (100).

ACKNOWLEDGMENTS

The financial support from Grant provided by the *Research Council Romania* (Project PN-II-ID-PCE-3-0128) is gratefully acknowledged. Oana MOLDOVAN thanks for "*Investing in people!*" Ph.D. scholarship, Project co-financed by the SECTORAL OPERATIONAL PROGRAM FOR HUMAN RESOURCES DEVELOPMENT 2007 – 2013 Priority Axis 1. "Education and training in support for growth and development of a knowledge based society" Key area of intervention 1.5: Doctoral and post-doctoral programs in support of research. Contract no.: POSDRU/88/1.5/S/60185 – "INNOVATIVE DOCTORAL STUDIES IN A KNOWLEDGE BASED SOCIETY" Babeş-Bolyai University, Cluj-Napoca, Romania".

REFERENCES

1. a) A. But, P. Lameiras, I. Silaghi-Dumitrescu, C. Batiu, S. Guillard, Y. Ramondenc, M. Darabantu, *Lett. Org. Chem.*, **2010**, *7*, 283; b) A. But, C. Batiu, Y. Ramondenc, M. Darabantu, *Rev. Roum. Chim.*, **2009**, *54*, 127; c) A. But, C. Batiu, D. Porumb, M. Darabantu, *Studia UBB Chemia*, **2008**, *LIII*, *4*, 43.
2. a) C. Saiz; P. Wipf; E. Manta; G. Mahler, *Org. Lett.*, **2009**, *11*, 3170; b) C. Saiz, P. Wipf, G. Mahler, *J. Org. Chem.*, **2011**, *76*, 5738.
3. a) W. Enz, M. Cecchinato, *Helv. Chim. Acta*, **1961**, *44*, 706; b) H.S. Broadbent, W.S. Burnham, R.M. Sheely, R.K. Olsen, *J. Het. Chem.*, **1976**, *13*, 337; c) G.G. Habernel, W. Ecsy, *Heterocycles*, **1977**, *7*, 1027.
4. a) D. Seebach, T. Weber, *Tetrahedron Lett.*, **1983**, *24*, 3315; b) D. Seebach, T. Weber, *Helv. Chim. Acta*, **1984**, *67*, 1650; c) A. Gonzales, R. Lavilla, J.F. Piniella, A. Alvarez-Larena, *Tetrahedron*, **1995**, *51*, 3015.
5. J. Sélambaron, F. Carré, A. Fruchier, J.P. Roque, A. Pavia, *Tetrahedron*, **2002**, *58*, 4439.

6. a) F.D. Deroose, P.J. De Clercq, *J. Org. Chem.*, **1995**, *60*, 321; b) A. Ino, Y. Hasegawa, A. Murabayashi, *Tetrahedron Lett.*, **1998**, *39*, 3509; c) H. Yang, X.C. Sheng, E.M. Harrington, K. Ackerman, A.M. Garcia, M. D. Lewis, *J. Org. Chem.*, **1999**, *64*, 242.
7. a) J.E. Baldwin, *J. Chem. Soc. Chem. Commun.*, **1976**, *18*, 734; b) J.E. Baldwin, J. Cutting, W. Dupont, L. Kruse, L. Silberman, R.C. Thomas, *J. Chem. Soc. Chem. Commun.*, **1976**, *18*, 736.
8. a) F. Fülöp, J. Mattinen, K. Pihlaja, *Tetrahedron*, **1990**, *46*, 6545; b) V.V. Alkseyev, K.N. Zelenin, *Khim. Geterosikl. Soedin.*, **1998**, 1068; c) L. Lázár, F. Fülöp, *Eur. J. Org. Chem.*, **2003**, *16*, 3025; d) M. Darabantu, *Curr. Org. Synth.*, **2010**, *7*, 120.
9. E.L. Eliel, H.S. Wilen, „Stereochemistry of the Organic Compounds”, John Wiley & Sons, New York, NY, Chichester, UK, Brisbane, Toronto, Singapore, **1994**, p 1199, 1200.

AFM INVESTIGATION OF MORPHOLOGICAL CHANGES TO *STAPHYLOCOCCUS AUREUS* SURFACE INDUCED BY AgNO₃ AND OXACILLIN ADDITION

OANA PONTA^{a*}, ENDRE JAKAB^b, IOAN BURDA^a, ARTHUR TUNYAGI^a,
ANDREEA SILAGHI^a, SIMION SIMON^a

ABSTRACT. *Staphylococcus aureus* is one of the most common pathogens in hospitals and can be responsible for infections ranging from minor to life-threatening ones, because its strains can acquire very fast resistance to clinically used antibiotics. A heterogeneous methicillin-resistant *S. aureus* (MRSA) strain, UCLA 8076 was selected as a model for this study. AgNO₃ or oxacillin were added to the culture medium and then incubated for 18 hours. Culture with no AgNO₃ and oxacillin addition served as control. For living cells, high-resolution imaging remains challenging, but a wealth of novel structural information can be obtained, such as visualization of surface structure in native conditions and monitoring of physiological changes in real time. The AFM technique was used in order to examine the structures and dynamics of bacteria because it is a powerful technique for imaging biological samples under nondestructive conditions and it was concluded that AgNO₃ inhibits the *S. aureus* development better than oxacillin.

Keywords: AFM, *S. aureus*, silver ions, oxacillin

INTRODUCTION

In recent years, in clinical settings, increases of skin and soft-tissue infections were encountered, particularly due to multidrug-resistant pathogens. The most serious and common infections produced by *S. aureus* are bacteremia, pneumonia, osteomyelitis, endocarditis [1-3], empyema, scalded skin syndrome, toxic shock syndrome [1] and abscesses of the muscle and various intra-abdominal organs [4,5]. It is known [6] that MRSA are inherently resistant to all β -lactam antibiotics, but some lineages (clones) have additionally

^a Babes-Bolyai University, Faculty of Physics & Institute for Interdisciplinary Research in Bio-Nano-Science, 400084 Cluj-Napoca, Romania.

^b Babes-Bolyai University, Faculty of Biology & Institute for Interdisciplinary Research in Bio-Nano-Science, 400084 Cluj-Napoca, Romania. * oana.ponta@phys.ubbcluj.ro

evolved resistance to multiple antibiotic classes. The resistance to the most known antibiotic classes has occurred within the species due to mutation and horizontal gene transfer and this has led to anxiety regarding the future availability of effective chemotherapeutic options [6]. The characteristics of Oxacillin-Susceptible MRSA strains and the possible efficiency of oxacillin against them were strongly investigated [7-9] by in vitro and in vivo experiments, but the improved oxacillin treatment remains a topical issue among researchers [10].

It has been demonstrated [11-14] that silver ions have a strong inhibitory and bactericidal effect; the antimicrobial action of them is closely related to their interaction with thiol groups. Ag^+ has the ability to bind to functional groups of proteins, resulting in protein denaturation [16]. It is believed that cellular proteins become inactivated on Ag^+ treatment due to the loss of replication capacity of DNA [15]. Studies have reported [17-19] that the positive charge of the Ag ions is crucial for its antimicrobial activity through the electrostatic attraction since the microorganism cell membrane has a negative charge. The bacterial plasma membrane, associated with several housekeeping enzymes, is an important target site for silver ions.

The investigation of biological systems on the cellular level, rather than on the population level is permitted by atomic force microscopy (AFM). AFM is a powerful technique used in order to examine the morphology and dynamics of bacteria at the nanometer to micrometer scale under nondestructive conditions and has the resolution to observe small changes in cell morphology, even nanometer-scale features such as bacterial division septa [20-22]. This highly versatile microscopy technique is particularly well suited to the study of microorganisms, because it combines a greatly improved resolution compared to optical microscopy and has no requirement to scan in vacuum or need for a conductive coating compared to scanning electron microscopy. High-resolution images can be obtained with minimal sample fixation and staining. It has been shown that fixation can alter the mechanical properties of bacteria [23] and cells [24].

S. aureus cells treated with antibiotics and ovine antimicrobial peptides isolated from the blood neutrophils were reported in the literature [25, 26], but potential advantage of using Ag^+ for the treatment of topical staphylococcal infections is strongly debated [27]. Beside the effect of silver ions on the viability and membrane integrity of *S. aureus*, the present study reports also an improvement in cell preparation for AFM investigation. This improvement is achieved by using a proper sized nylon filter instead of drying the culture on a glass slide which is reported to involve lysed cells and a covering with a thin layer of material as a result of the drying process and of the remains of the growth media, respectively [25].

RESULTS AND DISCUSSION

1. *Staphylococcus aureus* (control)

The AFM images (topography and phase contrast) of the *S. aureus* culture without AgNO₃ or oxacillin addition used as control are presented in the Figure 1.

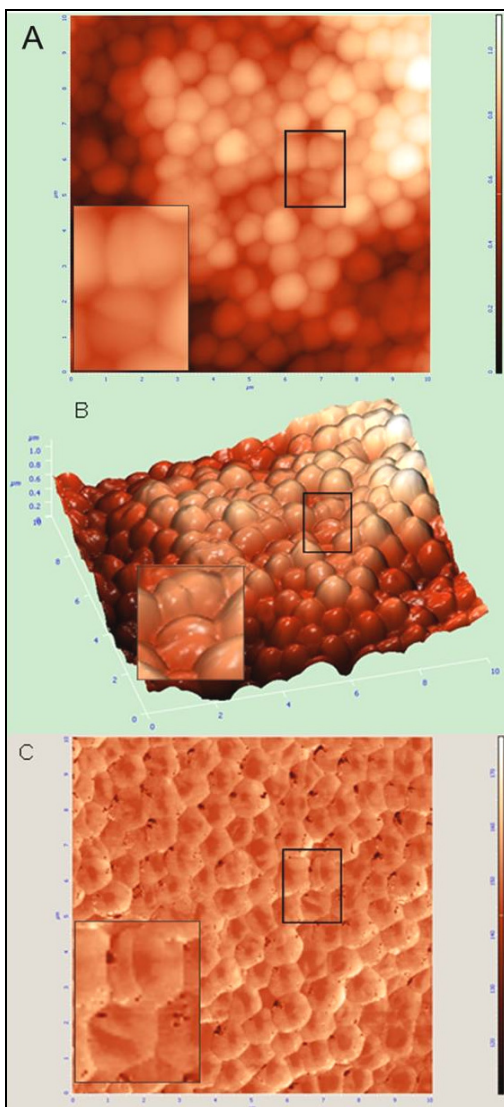


Figure 1. Tapping mode AFM images of *S. aureus* (control) in the 10µm range: A) two-dimensional topography, B) three-dimensional topography, C) phase contrast.

The phase contrast mode is used simultaneously with the tapping mode, so the topography is registered as well. For the phase contrast mode the phase lag of the cantilever oscillation sent to the piezo driver of the cantilever is monitored and recorded, being very sensitive to variations in material properties.

As it is well known, *S. aureus* is a spherical bacterium, about 1µm in size (Figure 1). The presence of a cross wall in some cells shown in the AFM images demonstrates that for these bacteria the early stage of cell division takes place. In the AFM images insets the cells division is more clearly expressed. Cells that are not in the process of dividing do not have a cross wall (Figure 1). This septum will continue its inward growth until a cross-wall is formed that completely separates the two daughter cells. At this point the cells remain joined together but eventually, through a process called splitting, will separate. During separation a small cleft is seen in the periphery of the wall (Figure 1). This stage is the first topological feature that is seen by AFM, where a shallow cleft is found in the relatively smooth homogeneous surface at the midpoint of a cell.

2. Morphological changes induced by oxacillin addition

The AFM images (topography and phase contrast) of the *S. aureus* with 8µg/ml oxacillin addition to the culture medium are presented in the Figure 2. The images obtained revealed not only the weak antibacterial effect of the oxacillin addition, but also the response strategies used by the bacteria. Cell wall collapse and morphological changes reflected some cell death.

3. Morphological changes induced by AgNO₃ addition

The AFM images (topography and phase contrast) of the *S. aureus* with 8µg/ml AgNO₃ addition to the culture medium are presented in the Figure 3 and Figure 4, for two different areas and scales, respectively. From these figures (Figure 3, 4) one can see that all the bacteria present big changes on their surfaces, unlike those subjected to oxacillin treatment (Figure 2).

CONCLUSIONS

By exploiting the natural tendency of many bacteria to thrive on solid surfaces, the air drying of a suspension of *S. aureus* on a filter is a suitable method for imaging bacteria at high resolution by atomic force microscopy. This technique allows simultaneous mapping of the topography and phase contrast. The fact that the cells appear healthy and vigorous when imaging bacteria in air convinced that the cells imaged on filters are quite native. In fact, in this hydrated air–solid interface, the cells grow, divide, multiply, move, and spread outward across the filter.

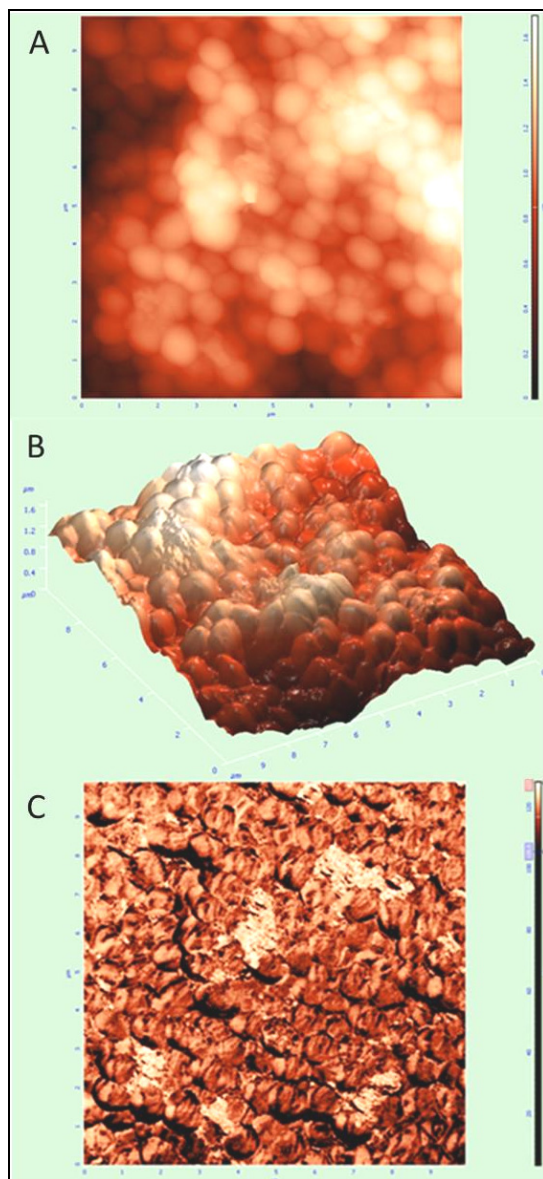


Figure 2. Tapping mode AFM images of *S. aureus* with 8 μg/ml oxacillin addition in the 10 μm range: A) two-dimensional topography, B) three-dimensional topography, C) phase contrast.

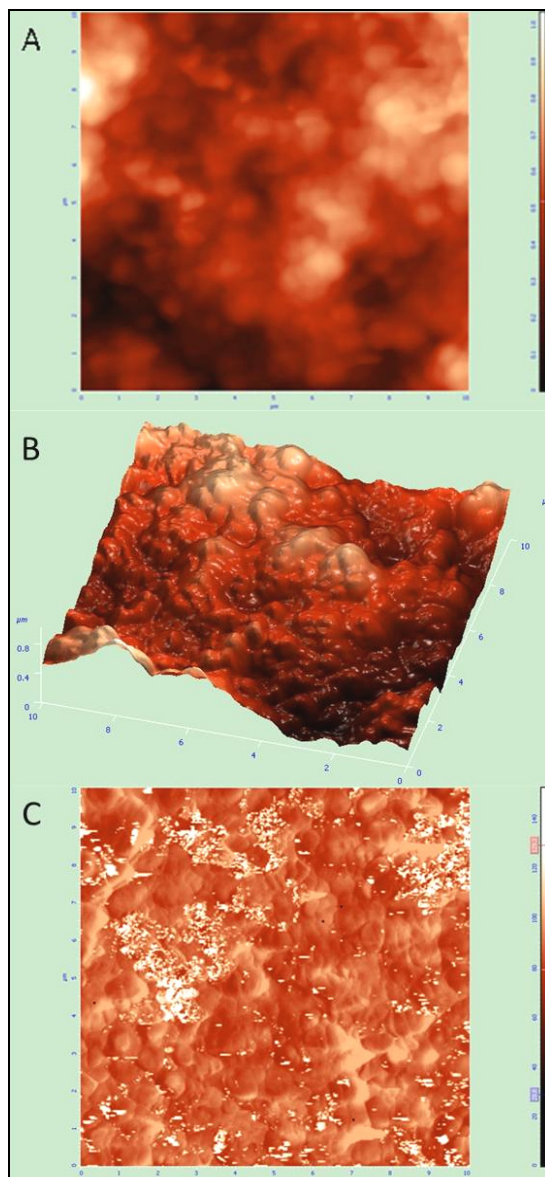


Figure 3. Tapping mode AFM images of *S. aureus* with 8 μg/ml AgNO₃ addition in the 10 μm range: A) two-dimensional topography, B) three-dimensional topography, C) phase contrast.

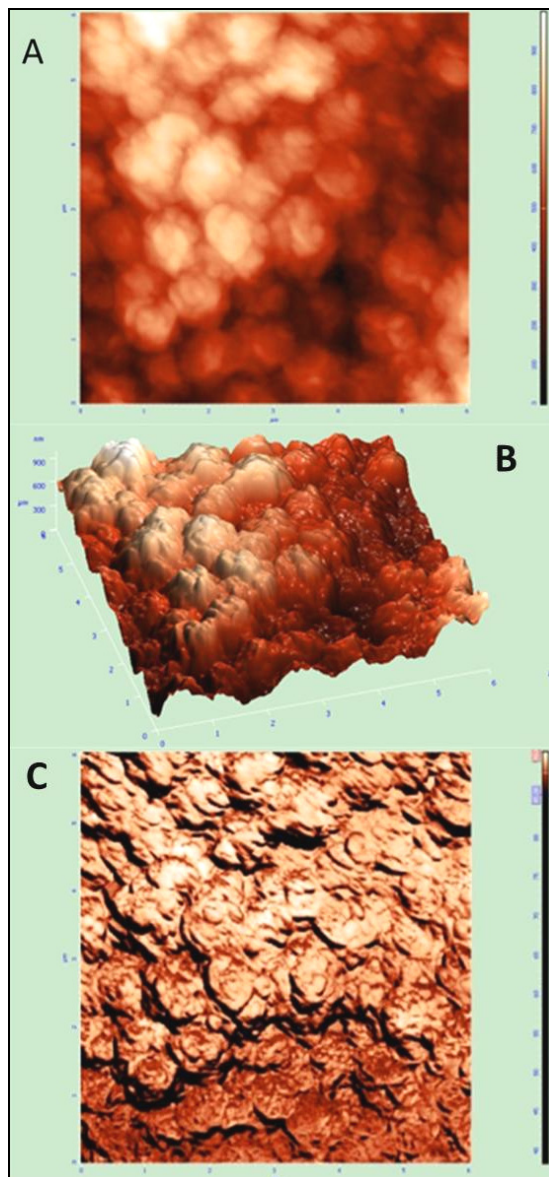


Figure 4. Tapping mode AFM images of *S. aureus* with 8 μg/ml AgNO₃ addition in the 5 μm range: A) two-dimensional topography, B) three-dimensional topography, C) phase contrast.

For the *S. aureus* (control), the AFM technique was able to follow the division process with precision and confirm the initial splitting of the septum.

Atomic force microscopy (AFM) imaging was used to obtain high-resolution images of the effect of silver ions and oxacillin on the bacterial morphology. The mechanism of antibacterial activity of Ag ions and oxacillin were studied by AFM, analyzing the growth and morphology of the bacterium wall.

The topographical imaging completed in tapping mode produced high resolution images demonstrating dramatic differences in surface morphology of the staphylococcal strains, strongly dependent on the AgNO₃ and oxacillin addition. Conformational changes induced by the additions of AgNO₃ and oxacillin were remarked.

The AFM technique, used in order to examine the structures and dynamics of bacteria may prove to be a valuable tool for probing microbial surface at high resolution under nondestructive conditions and it was concluded that AgNO₃ inhibit the *S. aureus* development much better than the oxacillin, confirmed by the fact that the cells walls damage had indeed occurred more in the presence of silver ions than under the oxacillin treatment.

However, researchers should keep in mind that the use of AFM in microbiology remains delicate and that accurate data collection and interpretation require specific expertise. In particular, great care should be taken to optimize sample preparation procedures and imaging conditions when exploring new specimens. Also, the best results will be obtained when AFM is combined with complementary biochemical and structural techniques.

EXPERIMENTAL SECTION

S. aureus growth: The first step was to grow fresh, dense cultures of bacteria (greater than 10⁷ CFU/ml). A heterogeneous methicillin-resistant *S. aureus* strain, UCLA 8076 was selected for this study. The culture was maintained on Mueller-Hinton agar (Fluka, Buchs, Switzerland) plates. Incubation at room temperature is generally sufficient to initiate growth and complex behaviours but the agar plate can also be placed in an incubator, refrigerator, or other controlled environment at this step to encourage the cells to grow. Therefore the strain was cultured at 37°C in Mueller-Hinton broth (Fluka, Buchs, Switzerland) at 150 rpm in a rotary shaker (CERTOMAT BS-T, Sartorius Stedim, Aubagne, France). 8 µg/ml AgNO₃ and oxacillin respectively were added to the culture medium and then were incubated for 18 hours in dark room condition. Culture without AgNO₃ or oxacillin addition served as control.

Preparation for AFM investigation: For AFM investigation bacteria must be immobilized on a surface. Without this strong attachment, cells can move in response to the lateral movement of the tip and can be pushed across the surface during imaging. Air drying a suspension of *S. aureus* on a filter provides sufficient immobilization because this bacterium does not have any appendages

that permit motility. Therefore, the possibility to move out of the area of investigation is not a problem. 5 ml culture broth was centrifuged and washed with sterile, deionized water, the pellet resuspended in 1000 μ l ultrapure water and filtered on 0.45 μ m pore-sized nylon filter (ADVANTEC MFS, Pleasanton, USA). This kind of pore-size filter is recommended since the *S. aureus* diameter is known to be around 0.7 – 1 μ m. The solution containing bacteria, suspended in culture medium is deposited central onto the filters. The solution makes a rounded bubble on top of the filter that soaks through into the plates in about 30 minutes. As long as the pore size is smaller than the bacteria, the bacteria remain on top while the cell debris goes through the filter. If necessary, the excess filter can be cut off with a razor or scissors. The microorganisms can be imaged immediately without any further treatment. This method for imaging bacteria on a nylon filter is a suitable one because even after removing the filter and imaging the bacteria for half an hour, a large fraction of the cells can be scraped off and grown in solution.

Experimental device: The *Staphylococcus aureus*' shape and morphology were accessed using an Atomic Force Microscope: NTEGRA Vita from NT-MDT, combining the strengths of SPM with an inverted optical microscope for biological and medical applications. The topography and phase images were recorded in tapping mode at room temperature in air, using a chemically stable Au reflective coating silicon probe cantilever of 100 μ m length, 35 μ m width, 1.2 μ m thickness and 90 kHz resonance frequency.

ACKNOWLEDGMENTS

This work received financial support from the project 'Education and training in support of economic growth and development of a knowledge-based society', contract code: POSDRU 89/1.5/S/60189, project co-financed from the European Social Fund through the Sectoral Operational Program for Human Resources Development 2007-2013. The research was accomplished in the framework of PN II IDEI PCCE 312/2008 project granted by the Romanian National University Research Council.

REFERENCES

1. M.A. Ansari, H.M. Khan, A.A. Khan, A. Malik, A. Sultan, M. Shahid, F. Shujatullah, A. Azam, *Biology and Medicine*, **2011**, 3 (2) Special Issue, 141.
2. F.D. Lowy, *New England Journal of Medicine*, **1998**, 320, 520.
3. A. Bhatia, S. Zahoor, *Journal of Clinical and Diagnostic Research*, **2007**, 1, 188.
4. L.O. Conterno, S.B. Wey, A. Castelo, *Control and Hospital Epidemiology*, **1998**, 19, 32.

5. J. Romero-Vivas, M. Rubio, C. Fernández, J.J. Picazo, *Clinical Infectious Diseases*, **1995**, 21, 141.
6. R. Augustine, K. Rajarathinam, *International Journal of Nano Dimension*, **2012**, 2(3), 212.
7. S. Rohrer, H. Maki, B. Berger-Bachi, *Journal of Medical Microbiology*, **2003**, 52, 605.
8. G. Sakoulas, H.S. Gold, L. Venkataraman, P.C. DeGirolami, G.M. Eliopoulos and Q. Qian, *Journal of Clinical Microbiology*, **2001**, 39, 3946.
9. A. Ikonomidis, G. Michail, A. Vasdeki, M. Labrou, V. Karavasilis, C. Stathopoulos, A.N. Maniatis, S. Pournaras, *Antimicrobial Agents And Chemotherapy*, **2008**, 52(11), 3905.
10. D.S. Jo, C.P. Montgomery, S. Yin, S. Boyle-Vavra, R.S. Daum, *Antimicrobial Agents and Chemotherapy*, **2011**, 55(6), 2818.
11. K. Satyavani, T. Ramanathan, S. Gurudeeban, *Digest Journal of Nanomaterials and Biostructures*, **2011**, 6 (3), 1019.
12. S. Silver, L.T. Phung, *Annual Review of Microbiology*, **1996**, 50, 753.
13. K. Satyavani, T. Ramanathan, S. Gurudeeban, *Digest Journal of Nanomaterials and Biostructures*, **2011**, 6 (3), 1019.
14. M. Saravanan, World Academy of Science, *Engineering and Technology*, **2010**, 68728.
15. Q.L. Feng, J. Wu, G.Q. Chen, F.Z. Cui, T.M. Kim, J.O. Kim, *Journal of Biomedical Materials Research*, **2000**, 52, 662.
16. J.A. Spadaro, T.J. Berger, S.D. Barranco, S.E. Chapin, R.O. Becker, *Antimicrobial Agents and Chemotherapy*, **1974**, 6, 637.
17. P.K. Stoimenov, R.L. Klinger, G.L. Marchin, K.J. Klabunde, *Langmuir*, **2002**, 18, 6679.
18. I. Sondia, B. Salopek Sondi, *Journal of Colloid and Interface Science*, **2004**, 275, 177.
19. A. Vulpoi, C. Gruian, E. Vanea, L. Baia, S. Simon, H.-J. Steinhoff, G. Göller, V. Simon, *Journal of Biomedical Materials Research Part A*, **2012**, 100(5), 1179.
20. A. Touhami, M.H. Jericho, T.J. Beveridge, *Journal of Bacteriology*, **2004**, 186(11), 3286.
21. S. Boyle-Vavra, J. Hahm, S.J. Sibener, R.S. Daum, *Antimicrobial Agents and Chemotherapy*, **2000**, 44(12), 3456.
22. M.M. Kummali, *Journal of Polymer Physics* **2011**, 49, 1332.
23. A.E. Pelling, Y. Li, W. Shi, *Proceedings of the National Academy of Sciences of the USA*, **2005**, 102, 6484.
24. F. Braet, C. Rotsch, E. Wisse, M. Radmacher, *Applied Physics A*, **1998**, 66, S575.
25. Rachel Claire Anderson, Richard G. Haverkamp, Pak-Lam Yu, *FEMS Microbiology Letters*, **2004**, 240, 105.
26. R.C. Anderson, P.L. Yu, *Aust. J. Agr. Res.*, **2004**, 15, 69.
27. C.P. Randall, L.B. Oyama, J.M. Bostock, I. Chopra, A. J. O'Neill, *J Antimicrob Chemother* **2013**, 68, 131.

THERMAL DECOMPOSITION AND KINETICS OF THE PRECURSORS FOR OBTAINING ZnO AND TEAH MODIFIED ZnO NANOPOWDERS

MIHAELA POPA^{a,*}, AMALIA MESAROS^a, RALUCA A. MEREU^a,
IOANA PERHAITA^b, LELIA CIONTEA^a, TRAIAN PETRISOR^a

ABSTRACT. The thermal decomposition of zinc oxalate, obtained from the precipitation of zinc acetate with oxalic acid, with and without tetraethylammonium hydroxide (TEAH) addition, was investigated. The thermogravimetric analysis (TG) indicated a total mass loss of about 57% in two decomposition steps. FTIR-TG-DTA and MS-TG-DTA indicated mainly CO₂ elimination. The activation energies (E_a) were estimated by Kissinger equation, considering heating rates of 5, 10, 15, 20°C/min. The determined energies were: $E_{a1} = 69$ kJ/mol, for the dehydration process and of about $E_{a2} = 106$ kJ/mol, for organic compounds loss.

Keywords: ZnO, nanopowders, thermal decomposition

INTRODUCTION

Zinc oxide, ZnO, has attracted much interest because of its possible application in distinct technological fields such as magnetic semiconductors, spintronics, catalysts, sensors, field emission devices, solar cells, etc.¹⁻⁵. The preparation conditions of ZnO nanopowders are important since the purity, the particles size and the presence of organic species on the surface of the particles are strongly influenced by this. The precipitation technique provides a facile way for low cost and large-scale production of ZnO in different sizes and shapes, in a reproducible way⁶⁻¹¹. The thermal process is important for the reason that physical and chemical properties of a material varies as function of temperature¹²⁻¹⁴. The conventional thermal analysis technique provides information limited to physical properties and indirect information about the identity of the composition and evolved phases¹⁵. The thermo - FTIR technique provides much more clear information about

^a Technical University of Cluj-Napoca, C4S, 28 Memorandumului Street, 400114, Cluj-Napoca, Romania, Phone +40-264-401475. * mip3pim@yahoo.com

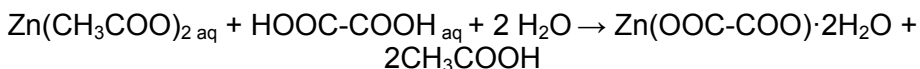
^b "Raluca Ripan" Institute for Research in Chemistry, Babes-Bolyai University of Cluj-Napoca, 30 Fantanele Street, Tel:+40-264-580165 Fax: +40-264-420441

the decomposition pathway, due to the detection of the resulted gases. Such a combination is always an advantage when substances are identified by methods involving a certain loss of mass¹⁶.

In this paper, the thermal decomposition of ZO precursors obtained by precipitation method was performed in order to have an in depth understanding and control of the synthesis process. Furthermore, a small amount of tetraethylammonium hydroxide (TEAH) was added during the precipitation process in order to control the particles shape. Thus, the thermal decomposition in N₂ and static air atmosphere and a kinetic study of TEAH modified ZnO precursor were performed in order to have information about its behavior during the thermal process.

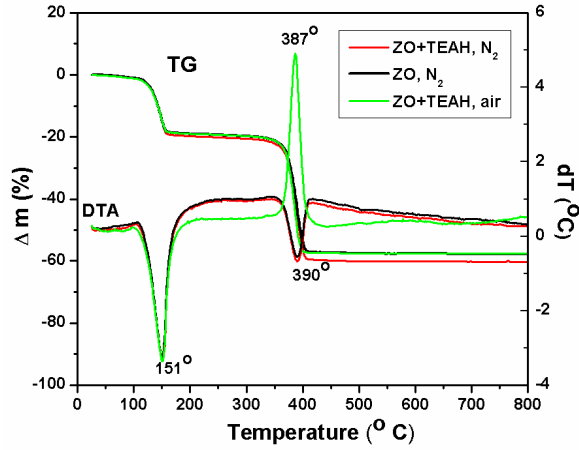
RESULTS AND DISCUSSION

The TG analysis of ZO and ZO+TEAH precursors, performed at a heating rate of 10°C/min, in N₂ and static air atmosphere, indicates a total mass loss of about 57 %, with a ~19 % loss in the first step and ~ 38% in the second step (Fig. 1 a). An insignificantly higher mass loss (57+2.9%) was observed in the case of the ZO+TEAH precursor. The molar masses of ZnO precursors, estimated from the TG curves, were ~ 191 g/mol for the ZO precursor and ~ 204 g/mol for ZO+TEAH precursor. Both values are close to the molar mass of the zinc oxalate hydrated with two molecules of water (189.4 g/mol). This fact suggests that TEAH is present in a very small amount, dispersed in the whole mass of the precursor and that during the synthesis process, zinc acetate has reacted with oxalic acid and deionised water, leading to zinc oxalate and acetic acid elimination, according to the chemical equation:

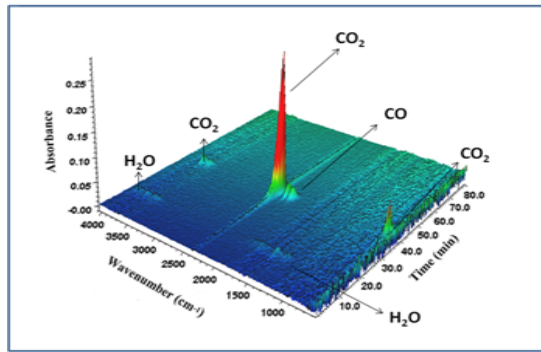


Comparing the DTA curves in N₂ atmosphere of ZO and ZO+TEAH (Fig. 1 a), unnoticeable difference between the two curves can be remarked. Two endothermic peaks (one at 151°C and one at 387°C) are present. When static air was used, an endothermic peak at 151°C and an exothermic peak at 387°C can be observed. The exothermic behavior is related with the oxygen presence from the air. The FTIR coupled TG-DTA experiment, performed on the ZO+TEAH precursor in N₂ atmosphere, indicates that the 151°C DTA peak corresponds to the water loss (its presence is confirmed in the gas loss 3D FTIR spectra (fig.1 b) at ~ 1600 cm⁻¹ and ~ 3600 cm⁻¹ (12.7 min). The DTA peak identified at 390°C corresponds to CO₂ (~2400 cm⁻¹) and to CO (~2100-2200 cm⁻¹) simultaneously loss, according to the 3D FTIR spectra (36.5 min). The chemical equation of the gas loss, in inert atmosphere, can be written as follows:

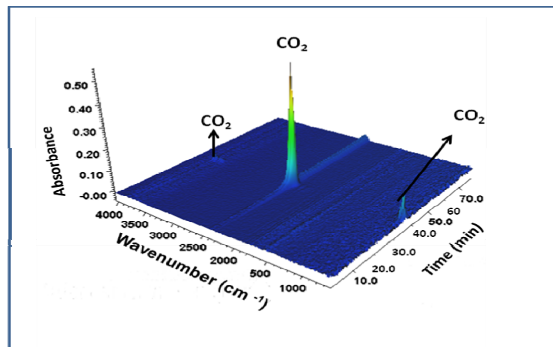




a)



b)



c)

Figure 1. TG-DTA curves in N₂ and static air (a) and FTIR coupled TG - DTA curves of the ZO+TEAH precursor, using a heating rate of 10°C/min, in N₂ atmosphere (b) and static air (c)

The TG-DTA curves of the ZO+TEAH precursor, using different heating rates (5, 10, 15, 20°C/min) - performed in static air, show similar thermograms, with two well defined decomposition steps. A total mass loss in two steps of about 57% was also observed. As can be seen in the DTA curves (Fig.2 a), the mass loss of the ZO+TEAH precursor strongly depends on the heating rate. Using a low heating rate (5°C/min), two peaks can be observed: one endothermic peak at 165°C, corresponding to water elimination and one exothermic peak at 397°C. In disaccord with DTA analysis, the FTIR coupled TG-DTA performed on ZO+TEAH precursor in static air atmosphere and using a heating rate of 10°C/min, indicates only CO₂ (~ 2400 cm⁻¹ at 40 min.) and no water elimination (Fig.1 c). As remarked in previous papers¹⁷, by increasing the heating rate, the DTA curves corresponding to water elimination as well as the organic compounds elimination are shifted towards higher temperatures. Using higher heating rates (10 - 15°C/min) a shoulder at about 392°C was observed. Furthermore, a splitting of this peak in two peaks (one at 396°C and one at 445°C) can be noticed by increasing the heating rate at 20°C/min. MS-TG-DTA analysis was performed for clarifying the gases elimination using a heating rate of 20°C/min (Fig. 2 b). As can be seen, the CO₂ elimination in high proportion is accompanied by some CO and acetic acid gases elimination. Furthermore, some traces of oxalic acid were also identified. No water elimination was observed, sustaining FTIR-TG observation (Fig. 1 c) and no N_xO_y gases elimination was identified, probably due to the small amount of TEAH.

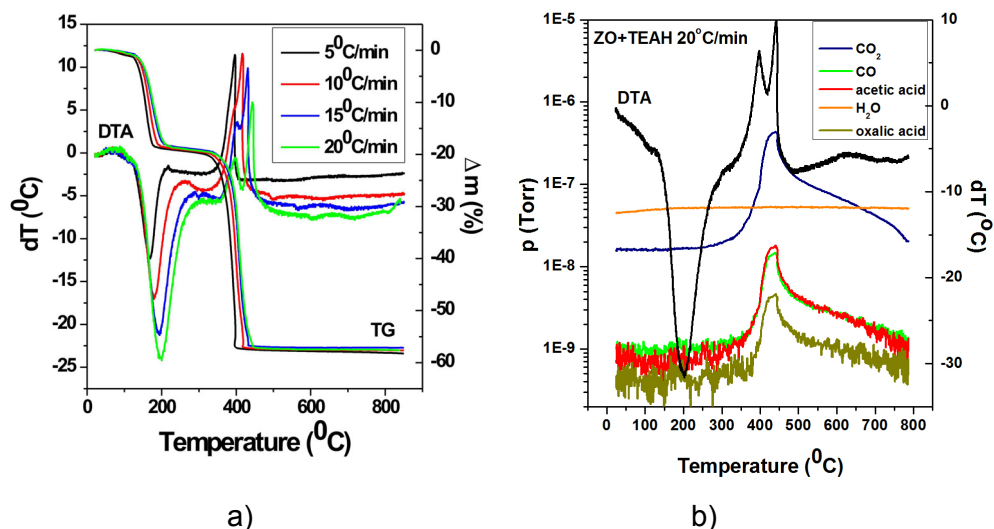


Figure 2. TG-DTA curves, performed in static air, heated using different heating rates (5, 10, 15 and 20 C/min) (a) and TG-DTA-MS curves at 20°C/min (b) of the ZO+TEAH precursor

We have approximated the activation energy, using Kissinger equation:

$$\ln(\phi / T_c^2) = (-E_a / RT_c) + \text{const.},$$

ϕ – heating rate (5, 10, 15, 20 °C/min), T_c – peak temperature, R – gas constant). The activation energy for the dehydration process was $E_{a1} = 69$ kJ/mol (Fig.3 a) and for the organic compounds loss (determined from the main DTA peaks - 397°C to 442°C) followed by crystallization process (Fig.3 b) was $E_{a2} = 106$ kJ/mol. The organic compound loss energy value is smaller than the reported value for the zinc oxalate decomposition in helium atmosphere, calculated using Avrami–Erofeev equation⁸. The authors reported an $E_a = 181.4$ – 186.5 kJ/mol, using heating rates of 2, 4, 7 and 10 K/min.

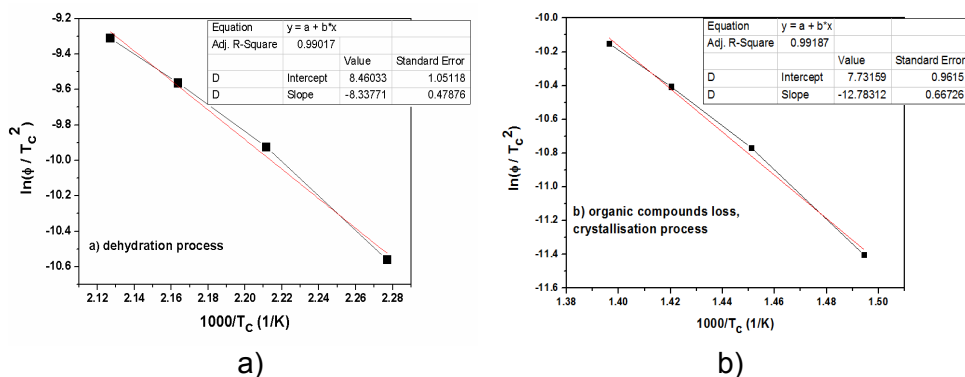


Fig. 3. The activation energy (E_a) determined according to Kissinger equation a) for the dehydration process, b) for organic compound loss

CONCLUSIONS

The thermal decomposition of zinc oxalate, obtained from the precipitation of zinc acetate with oxalic acid, with and without TEAH addition was investigated. TG-DTA, FTIR-TG-DTA and MS-TG-DTA analyses were used in order to determine the thermal behavior of the samples. The thermal decomposition occurred in two steps, having a total mass loss of about 57%. Two peaks at 151°C and at 387°C were detected in the DTA curves, both in the N_2 and static air atmosphere. The peak at 151°C was assigned to water elimination while the peak at 387°C was assigned to the organic compounds loss followed by a crystallization process. However, FTIR-TG-DTA and MS-TG-DTA indicate only a small amount of water elimination, by using N_2 atmosphere and no water elimination, when static air atmosphere was used. Moreover, no N_xO_y gas elimination was remarked for the TEAH modified precursor. The

influences of different heating rates on the decomposition process and kinetics calculations, using Kissinger equation, were also performed. The activation energy was estimated at about $E_{a1} = 69$ kJ/mol, for the dehydration process and $E_{a2} = 106$ kJ/mol, for the organic compounds loss followed by crystallization process.

EXPERIMENTAL SECTION

Sample preparation

High purity chemicals were used in precipitation process. Zinc acetate dihydrate (ZnAc) $Zn(CH_3COO)_2 \cdot 2H_2O$ (Merck, 99,5%), oxalic acid $C_2H_2O_4 \cdot 2H_2O$ (Lach:ner) and deionized water were used. 0.58 M of zinc acetate dihydrate solution and 1.15 M oxalic acid solution were prepared. The two solutions were mixed in stoichiometric ratio, resulting a white precipitate maintained under stirring for 24 h (sample notation – ZO). The mixture pH was 2.8. For one sample, tetraethylammonium hydroxide (Merck, 20% aqueous solution) in 0.0026 volume ratio (TEAH/ZnAc) was added (sample notation ZO+TEAH). The mixture pH increased to 3. The obtained white precipitates were filtered, washed with acetone and then dried at 100°C for 5 h.

Sample characterization

Fourier transform infrared spectroscopy (FTIR) coupled with a thermogravimetric analyser (TG-DTA) (Nicolet 6700 (FTIR) - 851e, 1600°C Mettler-Toledo (TG-DTA)) and thermal analysis coupled with a quadrupole mass spectrometer QMS 200 atmospheric sampling system (Residual Gas Analyzer RGA-Stanford Research System) were used to record the thermal decomposition and the gases loss in the temperature range from 25 to 800°C. The sample mass of about 14 mg was placed in a platinum crucible. Thermal analysis experiments were performed in N_2 and air flow and static state air, using heating rates of 5, 10, 15 and 20 °C/min.

ACKNOWLEDGMENTS

This work was supported by 4D-POSTDOC, contract no. POSDRU/89/1.5/S/52603, project co-funded by the European Social Fund through Sectoral Operational Programme Human Resources Development 2007-2013 (M. Popa) and by CNCSIS-UEFISCU project, n° PN II idei code 106/ 2010 (T. Petrisor)

REFERENCES

- 1 S.J. Pearton, D.P. Norton, K. Ip, Y.W. Heo, T. Steiner, *Progress in Materials Science*, **2005**, *50*, 293.
- 2 M. Popa, R.A. Mereu, M. Filip, M. Gabor, T. Petrisor Jr., L.Ciontea, T. Petrisor, *Materials Letters*, **2013**, *92*, 267.
- 3 L. Li, T. Zhai, Y. Bando, D. Golberg, *Nano Energy*, **2013**, *1*, 91.
- 4 A.B. Djuricic, A.M.C. Ng, X.Y. Chen, *Progress in Quantum Electronics*, **2010**, *34*, 191.
- 5 Y.Q. Fu, J.K. Luo, X.Y. Du, A.J. Flewitt, Y. Li, G.H. Markx, A.J. Walton, W.I. Milne, *Sensors and Actuators B: Chemical*, **2010**, *143*, 606.
- 6 K.G. Kanade, B.B. Kale, R.C. Aiyer, B.K. Das, *Materials Research Bulletin*, **2006**, *41*, 590.
- 7 A. Šaric, S. Music, M. Ivanda, *Journal of Molecular Structures*, **2011**, *993*, 219.
- 8 B. Malecka, E. Drozd-Ciesla, A. Malecki, *Thermochimica Acta*, **2004**, *423*, 13.
- 9 S. Sepulveda-Guzmana, E. de la Rosa, A. Torres-Castroa, V. Gonzalez-Gonzaleza, M. Jose-Yacamane, *Materials Chemistry and Physics*, **2009**, *115*, 172.
- 10 R.Y. Hong, J.H. Li, L.L. Chen, D.Q. Liu, H.Z. Li, Y. Zheng, J. Ding, *Powder Technology*, **2009**, *189*, 426.
- 11 J. Zhou, Y. Wang, Y. Zhang, L. Yang, *Journal of Luminescence*, **2007**, *122*, 195.
- 12 C. C. Lin, Y.-Y. Li, *Materials Chemistry and Physics*, **2009**, *113*, 334.
- 13 J. Chen, W. Lei, J.L. Song, X.W. Sun, X.B. Zhang, W.Q. Deng, *Physica E*, **2009**, *41*, 822.
- 14 E. Darezereshki, M. Alizadeh, F. Bakhtiari, M. Schaffie, M. Ranjbar, *Applied Clay Science*, **2011**, *54*, 107.
- 15 A.V. Ghule, B. Lo, S.-H. Tzing, K. Ghule, H. Chang, Y.C. Ling. *Chemical Physics Letters*, **2003**, *381*, 262.
- 16 G.W. Ehrenstein, G.R., P. Trawiel, "Thermal Analysis", Hanser Publisher, Munich, **2004**.
- 17 T. Aarii, A. Kishi, *Thermochimica Acta*, **2003**, *400*, 175.

PHENOLIC CONTENT AND ANTIOXIDANT CAPACITY OF SWEET AND SOUR CHERRIES

DEJAN PRVULOVIĆ^{a*}, MILAN POPOVIĆ^a, DJORDJE MALENCIĆ^a,
MIRJANA LJUBOJEVIĆ^a, GORAN BARAĆ^a, VLADISLAV OGNJANOV^a

ABSTRACT. Sweet and sour cherries are a valuable natural source of some bioactive compounds important in human health preservation. Total phenolics, tannins, flavonoids and anthocyanins, and antioxidant capacity in a fruits of a two selected sweet cherry genotypes (Szomolyai Gombolyii and Valerij Cskalov) and 2 sour cherry cultivars (Érdi bőtermő and Kántorjánosi) were investigated. Total phenolic content ranged from 76.05 up to 301.19 mg gallic acid equivalents/100 g fresh fruit weight and total tannins content ranged from 32.33 to 236.61 mg gallic acid equivalents/100 g fresh fruit weight. Total flavonoids were within the range 49.47-70.27 mg of rutin equivalents/100 g fresh fruit weight and total anthocyanins content were between 16.86 and 51.16 mg cyanidin 3-glucoside equivalents/100 g fresh fruit weight. Antioxidant activity of sweet and sour cherries is correlated with the total phenolics and total tannins content, and partially related with total anthocyanins, but not with the total flavonoids. Fruits of sour cherries contains more phenolics than fruits of sweet cherries and possess more potent antioxidant activity.

Keywords: antioxidant peroperties, fruit, phenolic compounds, *Prunus avium L.*, *Prunus cerasus L.*

INTRODUCTION

Sweet (*Prunus avium L.*) and sour (*Prunus cerasus L.*) cherries are popular fruit crops across the temperate region of Europe. They are also economically and nutritionally important crops worldwide [1, 2, 3].

Apart from several essential dietary components, such as vitamins, minerals, protein and carbohydrate, cherries also contain other phytonutrients that may provide benefits beyond the prevention of dietary deficiencies such as compacting multiple disease states. The consumption of sweet or sour cherries reduce the risk of cancer, pain from arthritis and inflammation, symptoms of exercise-induced muscle diseases. The beneficial effects of cherries may be attributed to the presence of phenolics such as anthocyanins and melatonin that exert potent antioxidant capacity [4].

^a University of Novi Sad, Faculty of Agriculture, Trg Dositeja Obradovića, Nr. 8, 21000 Novi Sad, Serbia. * dprvulovic@yahoo.com

The genetic background is the first parameter with the potential to influence the antioxidant content in a commodity. Significant inter-cultivar variation in the phenolic content and antioxidant capacity has also been documented in cherries. The biosynthesis of polyphenolic compounds is triggered by exposure to stress conditions, as a natural defense system, generating a significant amount of the above variability [5].

Phenolics are diverse group of aromatic compounds with at least one hydroxyl group, which also include various derivatives. Phenolics are important in determining the sensory quality of food such as colour, taste and flavor. The composition and concentration of phenolics are significantly influenced by the stage of maturity, cultivars, cultural practices, geographic origin, growing season, climate condition, postharvest storage condition, and food-processing procedures [6].

The objectives in this study were to comparatively analyze dietary functional phenolics of fresh sweet and sour cherries and to investigate the antioxidant capacity of these fruits.

RESULTS AND DISCUSSION

In cherries the ripening process is closely related to a change from the initial green colour into red, with degradation of chlorophyll and accumulation of different phenolic compounds and anthocyanins. Phenolic compounds are mostly concentrated in the skin and contribute to sensory and organoleptic qualities of fruits [6].

Table 1. Total phenolics, total tannins and total anthocyanins content of sweet and sour cherry cultivars

Cultivar	Phenolics ¹	Tannins ¹	Anthocyanins ²
Szomolyai Gombolyii	76.05 ± 4.85 ^a	32.33 ± 1.57 ^a	16.86 ± 1.92 ^a
Valerij Cskalov	110.96 ± 13.33 ^b	74.68 ± 11.04 ^b	33.25 ± 2.79 ^b
Érdi bőtermő	300.22 ± 32.44 ^c	236.61 ± 24.45 ^c	38.18 ± 2.76 ^b
Kántorjánosi	301.19 ± 9.16 ^c	227.00 ± 5.03 ^c	51.16 ± 4.66 ^c

The data are mean values ± standard error

^{a,b,c} the values without the same superscript within each column differ significantly ($P < 0.05$)

¹ Expressed as mg of gallic acid equivalents /100 g of fresh plant material.

² Expressed as mg of cyanidin-3-glucoside/100 g of fresh plant material.

The content of total phenolics (TP), total tannins (TT) and total anthocyanins (TA) in two sweet (Szomolyai Gombolyii and Valerij Cskalov) and two sour (Érdi bőtermő and Kántorjánosi) cultivars are given in Table 1. TP, TT and TA content varies among cultivars analyzed in the present study. Previous reported TP content were carried from 4.12 up to 229.00 in sweet

cherries [1, 3, 5, 6, 7, 8, 9] and from 70.70 to 754.00 mg gallic acid equivalents/100 g fresh weight in sour cherries [4, 10, 11, 12, 13]. Valerij Cskalov had the higher amount of TP content (110.96 mg GAE/100 g FW) than Szomolyai Gombolyii cultivar (76.05 mg GAE/100 g FW). Fruits of sour cherry genotypes had a threefold higher content of TP than sweet cherries. TP content in the fruit of Kántorjánosi sweet cherry cultivar was 301.19 mg GAE/100 g FW followed by the Érdi bőtermő cultivar with 300.22 mg GAE/100 g FW. Phenolic compounds serve in plant defense mechanisms, to counteract reactive oxygen species, in order to survive and prevent molecular damage and damaging by microorganisms, insects and herbivores [14].

Great variability exist among the examined cherry cultivars, regarding their content in TT, ranging from 32.33 mg GAE/100 g FW (Szomolyai Gombolyii) and 74.68 mg GAE/100 g FW (Valerij Cskalov) for sweet cherry cultivars, up to 227.00 mg GAE/100 g FW (Kántorjánosi) and 236.61 mg GAE/100 g FW (Érdi bőtermő) for sour cherry cultivars (Table 1). Cherries from the cultivars that are abundant in TP contained also more TT. Tannins are widely distributed in the plant kingdom. The concentration of tannins varies with environmental conditions, plant genotype and tissue development stage. The biochemical activities of tannins range from beneficial antioxidants to damaging prooxidants and toxins. Tannins are feeding deterrents to many herbivores. Feeding deterrence is undoubtedly an important mechanism by which tannins protects from non-adapted animals. For adapted species, tannins can act as stimulants [15]. Tannins markedly affect the flavor and the astringency of fruit [1].

Anthocyanins are water-soluble pigments that contribute the blues, purples and reds in plant food [15]. In cherries, colour is mainly influenced by the concentration and distribution of different anthocyanins in the skin [2, 16]. The TA content of sour cherry genotypes were in range of 38.18 (Érdi bőtermő) and 51.16 (Kántorjánosi) mg cyanidin-3-glucoside equivalents (C3GE) /100 g FW basis (Table 1). The lower content of TA was recorded in sweet cherry genotypes: Szomolyai Gombolyii cultivar (16.86 mg C3GE/100 g FW) and Valerij Cskalov (33.25 mg C3GE/100 g FW). Results from this study are in agreement with results of other authors [9, 10, 11, 12, 18, 19, 20]. Anthocyanins are effective in scavenging reactive oxygen species, in inhibiting lipid peroxidation, in protecting against cardiovascular disease and express antitumor activity [11, 18, 20].

The genotype influences the extent of total flavonoid (TF) accumulation in the cherry fruits. The contents of flavonoids found in sweet and sour cherries are given in Table 2. The genotypes with high flavonoid contents are Valerij Cskalov, Kántorjánosi and Szomolyai Gombolyii with 70.27, 63.67 and 63.35 mg of rutin equivalents (RE)/100 g FW respectively. The cultivar with lowest TF content is Érdi bőtermő with 49.47 mg of RE/100 g FW. Flavonoids were found

to be important part of human diet and are considered as active principles in many medical plants [21]. Flavonoids have been known to reduce oxidative stress in biological systems due to their antioxidant capacities [4, 22]. Most flavonoids are found in nature as O- or C-glycosides. The glycosylation is important to reduce the reactivity and to increase the water solubility of flavonoids, which in turn prevents their cytoplasmic damage and guarantees their storage in the cell vacuole [23]. Flavonoids are reported to have antioxidant, anticancer, antiallergic, antiinflammatory and gastroprotective properties [16].

Table 2. Total flavonoids content and antioxidant activity of sweet and sour cherry cultivars

Cultivar	Flavonoids ¹	DPPH values ²
Szomolyai Gombolyii	63.35 ± 1.14 ^a	33.74 ± 1.69 ^a
Valerij Cskalov	70.27 ± 5.06 ^a	27.15 ± 1.26 ^a
Kántorjánosi	63.67 ± 17.69 ^a	9.30 ± 0.07 ^b
Érdi bőtermő	49.47 ± 6.91 ^b	9.10 ± 0.70 ^b

The data are mean values ± standard error
^{a,b,c} the values without the same superscript within each column differ significantly ($P < 0.05$)
¹ Expressed as mg of rutin/g of dry plant material.
² Expressed as IC₅₀ value (µl of sample).

The antioxidant activity using DPPH method in sweet and sour cherry genotypes are shown in Table 2. All examined cherry extracts showed very high antioxidant activity. A statistical difference was found among genotypes. The IC₅₀ DPPH-values for investigated extracts varied in a wide range between 9.10 and 33.74 µl extract. The highest antioxidant activity was observed in sour cherry genotype Érdi bőtermő, followed by Kántorjánosi genotype.

Table 3. Correlation between DPPH-assay and investigated phenolic compounds in sweet cherry fruits

	Correlation coefficient (<i>r</i>)	Coefficient of determination (<i>r</i> ²)
Total polyphenol content	0.87*	0.75*
Total tannins content	0.95*	0.89*
Total anthocyanins content	0.87*	0.76*
Total flavonoids content	0.28	0.08

* Values marked with asterisk are statistically significant ($P > 0.05$)

The relationship between antioxidant capacity and different phenolic groups varied between cultivars (Table 3). There were statistically significant correlation between antioxidant capacity and TP, TT and TA content ($r^2=0.75$, $r^2=0.89$ and $r^2=0.76$ respectively). In this study, no statistically significant

correlation was observed between antioxidant activity and TF content ($r^2=0.08$). Other authors also found that different phenolic groups influence the antioxidant activity of the fruits, when correlating with DPPH data [5, 8, 18, 20, 24].

CONCLUSIONS

As the conclusion, this investigation show large variability between sweet and sour cherry cultivars in measured chemical attributes. Antioxidant activity of both sweet and sour cherries depends on total phenolics, tannins and anthocyanins, but not on flavonoids. Cherries are a significant source of different phenolic compounds, and could be considered as a good source of natural antioxidants.

EXPERIMENTAL SECTION

Plant material

Fruits of sweet and sour cherry cultivars were collected in 2011 from the productive orchard "Sloga" Kać in vicinity of Novi Sad, Serbia. Fruits of 2 red-coloured sweet cherry cultivars (Valerij Cskalov and Szomolyai Gombolyii) and 2 sour cherry cultivars (Érdi bőtermő and Kántorjánosi) were included in this study. Cherry fruits were picked at commercial maturity on the basis of fruit colour. Approximately 1 kg per cultivar of ripe cherry fruits was harvested from trees. The fruits were selected according to uniformity of size, shape and colour and then transported to the laboratory for analysis.

Extraction and determination of phenolic compounds

Five grams of plant material was extracted with 70% acetone solution (5 ml) by sonication for 20 minutes in an ultrasonic bath at ambient temperature. The extracts were rapidly filtered and kept refrigerated before assay. All extractions were done in triplicate. Total phenolics (TP) in the acetone extracts were determined colorimetrically (Jenway 6505, UK) using Folin-Ciocalteu reagent [25]. Gallic acid (GA) was used as a standard (covering the concentration range between 0.1 and 1.0 mg/ml) and results were expressed as milligram of GAE/100 grams of fresh plant material (FW). Total tannins (TT) content was determined by the Folin-Ciocalteu procedure, after removal of tannins by their adsorption on insoluble matrix (polyvinylpolypyrrolidone) [26]. Calculated values were subtracted from total polyphenol contents, and total tannins contents were expressed as mg GAE per 100 grams of FW. Total flavonoids (TF) were determined according to the procedure of Marckam [27]. The amount of flavonoids was calculated as a rutin equivalent (RE) from the calibration curve of rutin standard solution and expressed as mg of RE per

100 g of FW. The quantification of total anthocyanins (TA) of fresh sweet and sour cherries was evaluated by the pH differential method spectrophotometrically [28]. The content of TA was expressed as mg of cyanidin 3-glucoside equivalents (C3GE)/100 g of FW.

Measurement of antioxidant activity

The potential antioxidant activity of the test samples have been assessed based on scavenging activity of the 70% aqueous acetone sweet and sour cherry extracts of the stable DPPH free radicals [29]. The antioxidant activity of the extracts was expressed as IC₅₀. The IC₅₀ value was defined as the volume in µl of extract that reduce the presence of DPPH radicals in solution by 50% assuming that the sample with the smaller volume has higher scavenging capacity. All measurements were done in triplicate.

Statistical analysis

Results are expressed as mean of determinations of 3 independent samples made in triplicates. Statistical significance was tested by analysis of variance followed by comparison by Duncan's multiple range test ($P < 0.05$) calculated using STATISTICA for Windows version 9.0 (StatSoft, Tulsa, OK, USA). Stepwise multiple regression analyses were used to determine correlation among variables.

ACKNOWLEDGMENTS

This study was carried out within a project No. TR-31038 of Ministry of Education and Science of the Republic of Serbia.

REFERENCES

1. M.J. Bernalte, E. Sabio, M.T. Hernández, C. Gervasini, *Postharvest Biology and Technology*, **2003**, *28*, 303.
2. B. Gonçalves, A.P. Silva, J. Moutinho-Pereira, E. Bacelar, E. Rosa, A.S. Meyer, *Food Chemistry*, **2007**, *103*, 976.
3. V. Usenik, J. Fabčič, F. Štampar, *Food Chemistry*, **2008**, *107*, 185.
4. D. -O. Kim, H.J. Heo, Y.J. Kim, H.S. Yang, C.Y. Lee, *Journal of Agricultural and Food Chemistry*, **2005**, *53*, 9921.
5. D. Faniadis, P.D. Drogoudi, M. Vasilakakis, *Scientia Horticulturae*, **2010**, *125*, 301.
6. G. Ferretti, T. Bacchetti, T. Belleggia, D. Neri, *Molecules*, **2010**, *15*, 6993.

7. A. Chaovanalikit, A. Wrolstad, *Food Chemistry and Toxicology*, **2004**, 69, 73.
8. M.J. Serradilla, A. Martín, A. Hernandez, A. López-Corrales, M. Lozano, M. de Guía Córdoba, *Journal of Agricultural and Food Chemistry*, **2010**, 58, 9157.
9. D. Prvulović, Dj. Malenčić, M. Popović, M. Ljubojević, V. Ognjanov, *World Academy of Science, Engineering and Technology*, **2011**, 59, 1149.
10. V. Dragović-Uzelac, B. Levaj, D. Bursać, S. Pedisić, I. Radojčić, A. Bišo, *Agriculturae Conspectus Scientificus*, **2007**, 72, 279.
11. S. Melicháčová, M. Timoracká, J. Bystrická, A. Vollmannová, J. Čéry, *Acta Agriculturae Slovenica*, **2010**, 95, 21.
12. G.M. Khoo, M.R. Clausen, B.H. Pedersen, E. Larsen, *Journal of Food Composition and Analysis*, **2011**, 24, 772.
13. M.N. Mitić, M.V. Obradović, D.A. Kostić, R.J. Micić, E.T. Pecev, *Chemical Industry & Chemical Engineering Quarterly*, **2012**, 18, 53.
14. G.A. Boeckler, J. Gershenzon, S.B. Unsicker, *Phytochemistry*, **2011**, 72, 1497.
15. R.V. Barbehenn, C.P. Constabel, *Phytochemistry*, **2011**, 72, 1551.
16. L. Dykes, L.W. Rooney, M, *Cereal Foods World*, **2007**, 52, 105.
17. L. Esti, F. Cinquanta, E. Sinesio, E. Moneta, M. Di Matteo, *Food Chemistry*, **2002**, 76, 399.
18. Zs. Veres, I. Holb, J. Nyéki, Z. Szabó, J. Remenyik, M.G. Fári, *International Journal of Horticultural Science*, **2006**, 12, 45.
19. E. Kállay, M. Stéger-Máté, M. Mester-Ficzek, G. Sándor, G. Bujdosó, M. Tóth, *Acta Biologica Szegediensis*, **2008**, 52, 217.
20. N. Papp, B. Szilvássy, Z. Szabó, J. Nyéki, É. Stefanovits-Bányai, A. Hegedűs, *International Journal of Horticultural Science*, **2008**, 14, 59.
21. G.A. Cooper-Driver, *Phytochemistry*, **2001**, 56, 229.
22. D. Prvulović, M. Popović, Dj. Malenčić, M. Ljubojević, V. Ognjanov, *Research Journal of Agricultural Science*, **2011**, 43, 198.
23. F. Cuyckens, M. Claeys, *Journal of Mass Spectrometry*, **2005**, 40, 364.
24. A.T. Serra, R.O. Duarte, M.R. Bronze, C.M.M. Duarte, *Food Chemistry*, **2011**, 21258, 318.
25. G.T. Kroyer, *Inovative Food Science and Emerging Technologies*, **2004**, 5, 101.
26. H.P.S. Makkar, "Quantification of Tannins in tree Foliage-a Laboratory Manual", FAO/IAEA Working Document, Vienna, **2000**.
27. K.R. Marckam, "Methods in Plant Biochemistry", Academic Press, London, **1989**, 16.
28. S.C. Shen, K.C. Tseng, F.T. Chao, S.B. Wu, *Food Quality*, **2007**, 30, 202.
29. N. Abe, T. Murata, A. Hirota, *Bioscience, Biotechnology, Biochemistry*, **1998**, 62, 661.

ANALYSIS AND INTERPRETATION OF COLOURS CHARACTERISTICS OF THE DYED SAMPLES, BASED ON REMISSION CURVES

MONICA PUSTIANU^{a,*}, ADINA BUCEVSCHI^a,
POPA ALEXANDRU^a, ERZSEBET AIRINEI^a

ABSTRACT. In this paper were analyzed and interpreted the colour characteristics of dyed samples, based on remission curves. The correlation between the remission dyeing and the dyes concentration, for wool dyeing with acid dyes was also studied.

There have been dyeing with two acid dyes on 100% wool fabric, six levels of concentration, ranging between 0,1% - 2,0%, in specific conditions of wool dyeing with acid dyes.

Remission curves were drawn for two dyes: red and yellow and mixtures of two dyes take in equal parts, in the visible spectral domain. Based on these remission curves, were analyzed and interpreted the following: the colour characteristics for dyed samples, the correlation between remission colour and the concentration of dyes and the interaction between the dyes in mixing pain.

Keywords: *remission, acid colorants, wool texture, visible spectral domain, dyeing, concentrations, colours characteristics.*

INTRODUCTION

Colour is a subjective phenomenon, a response of the brain at the stimulation of the eye with light. [1].

Perception of colour sensation varies widely limits from individual to individual, depending on age, environment in which observation is made, the level of lighting and other factors. These differences in the subjective assessment of corps colours, including textile materials, imposed the need to introduce methods of objective measurement and numerical assessment of visual sensation and of its size [1].

It was assign three characteristics to colour, as visual sensation: nuance, saturation and brightness [1].

^a Universitatea Aurel Vlaicu, Facultatea de Inginerie, Str. Elena Dragoi, Nr. 2, Arad, Romania.
* pustianumonica@yahoo.com

The colour nuance allows the eye to distinguish different components of white light (daylight): red, orange, green, blue etc. The colour nuance is given by the spectral position in the spectrum of wave length appropriate. The nuance of a certain colour is given by the position in the spectrum of white light of the dominant length of the wave. The nuance of a colours is a quality characteristic [1].

The saturation or purity excitation of a colour represents the amount of pure colour (spectral colour) contained in it, compared with an achromatic colour of the same luminosity (grey). Mixing with other wavelength or white light, colour spectrum undergoes a desaturation. Spectral colours are saturated colours, for which was adopted by convention the value equal to unity ($s=1$), and white saturation is zero. Colour saturation is a quantitative characteristic.[1]

Luminosity of a colour scale is related to sensation of bright that produces. Thus, the different colours appear to emit more or less light. Luminosity is the only characteristic of an achromatic colour and varies from the maximum value conventionally noted with 100 for white to 0 for black. Between these two marks are located grey colours characterized by intermediate values of luminosity [1].

Qualitative description of a colour is done with reference colours: white, black neutral greys and spectral colours. The colour's attributes are described to these guidelines: nuance, saturation, brightness and differences between two or more colours.

Assessing the surfaces colours areas (corps) that haven't their own light requires illumination with light emitted by an illuminator.

Colour is one of the most important attributes of a textile material. A wool sample is composed of several fibres. Fibres have curved surfaces and are oriented in different directions so that the reflection of light is diffused in all directions [2].

When incident light is on a dyed wool material is observed that a small amount of incident light are reflected by the external surface of the sample, and the largest quantity of incident light enters inside the material, where is reflected by the individual fibres in all directions, and then is reflected off the sample.

When incident light is on a non-dyed woollen material it will have the same colour with the reflected light. In daylight non-dyed wool the will be appreciated by the eye as more or less white.

If the material is dyed, a part of incident light is absorbed by molecules of the colorant. Since each colour absorbs light only in a certain region of wavelength, the composition of reflected light depends on the type and the concentration of the colour. In case of light colours, a small amount of light is absorbed, while the rest is reflected and in case of dark colours more light is absorbed and less reflected [2].

RESULTS AND DISCUSSION

For data processing was used Excel program, which provided facilities for database processing and enabled graphical formats as curves of remission [3,4].

The remission curves presented in Figures 1, 2 and 3 shows that:

For all dyeing obtained with Bemacid Gelb GR dye (figure 1) due to changes in concentrations of dyeing, the remission curves aspect is constant. Remissions amplitude decreases with increasing of concentration in dyeing, and with increasing of colour intensity [1,4, 5, 6].

For colour nuance study is made the following interpretation of the curves of remission: maximum remissions of studied colour are located in the spectral range of 580-700 nm. Given that the values of green remissions between 500-560 nm, offset remissions of red of the spectrum between 600-700 nm, because the colours of these two spectral domains are complementary, that blend studied dominant colour is yellow, the same wavelength for all colours. Dominant yellow tone, located in the 580-640 nm spectral colours for all represented, and is highlighted by the very low spectral remissions fields of purple and blue, for $\lambda = 400-500$ nm. The latter include complementary colours yellow colours.

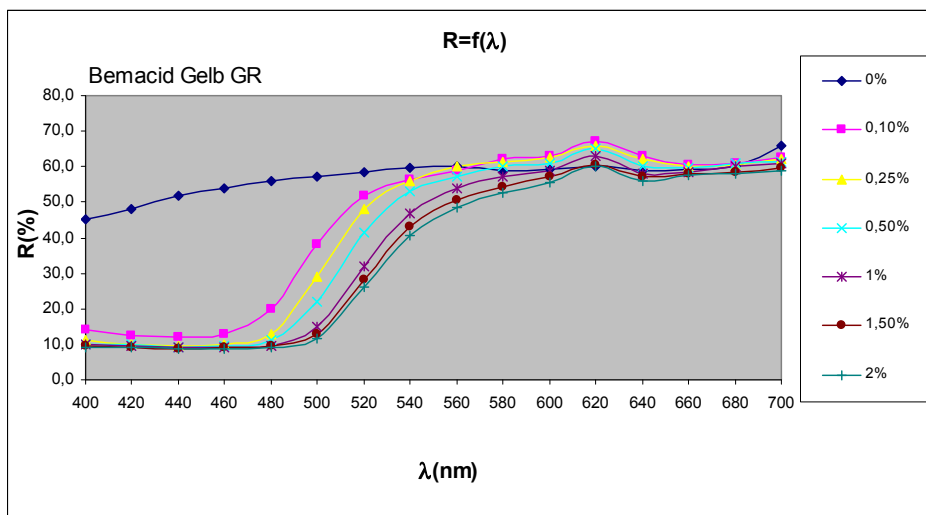


Figure 1. Remission curves of Bemacid Gelb GR

Absences of these colors in visible beam radiation reflected by colored surfaces allow yellow radiation to maintain preponderant. The brightness of studied color (sometimes called luster or clarity) can be expressed by the difference between the maximum of remission value and the value of remission

of complementary color [1,3, 6]. Brightness values are between 55% (for the colors obtained with 0.1% dye) and 51.5% (for the colors obtained with 2% dye). It is noted a very little brightness decreases with increasing of dye concentration. As a result, the yellow colors not lose too much brightness, while increasing their intensity.

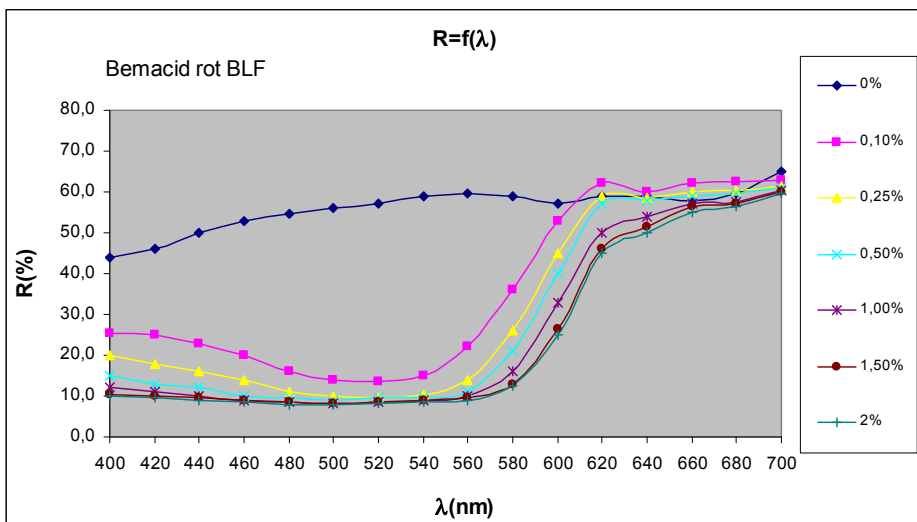


Figure 2. Curves of remission of Bemacid Rot BLF

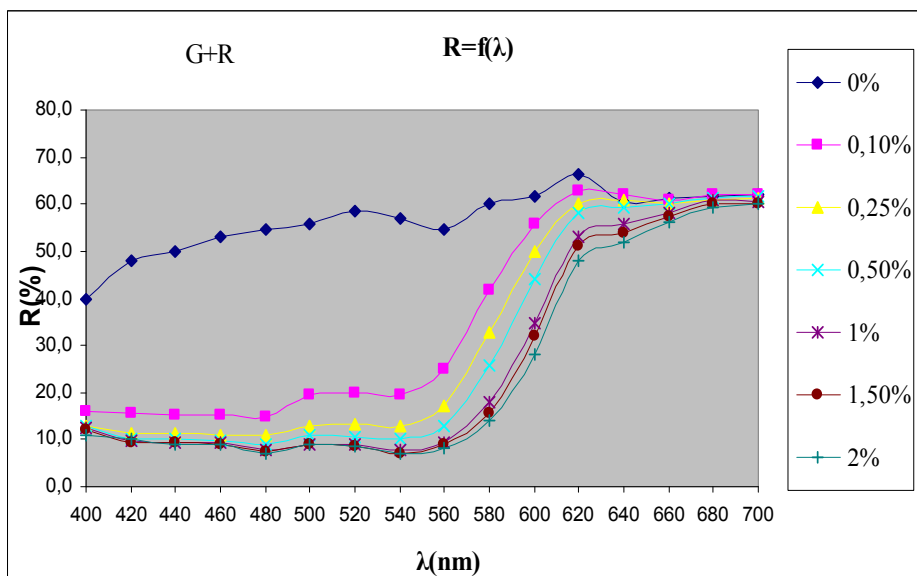


Figure 3. Remission curves of mixtures of Bemacid Gelb GR and Bemacid Rot BLF

For all dyeing with Bemacid Rot BLF dye (figure 2) as a result of changes of the dyeing concentrations, the remission curves remain constant. Remissions amplitude decreases with increasing concentration in dyeing, and with intensity of color increasing. Also found that for concentrations of 1.5% and 2%, the dyeing remissions were very close, the dyeing is very close each to other, although they were dyed with different dye concentrations. This is due to a possible low absorption capacity of colourant, capacity that decreases with increasing concentration so that remission in visible area has close values.

For colors nuance study is made the following interpretation of the curves of remission: maximum remission of studied dyeing are located in the spectral range of 600-700 nm. The maximum length of remissions corresponds to waveform of 700 nm. In the rest of visible spectral domain, remissions values are very low, making the brightness of measured samples to be located, due to radiation, only in a restricted area of the visible spectrum. Applying the method of calculating the color brightness by making the difference between maximum remission and minimum remission, the brightness values are between 49.5% (for dyeing with 0.1% dye) and 51.9% (for coating with 2% dye).

$$R_{\lambda\max} - R_{\lambda\text{complementar}} = 63 - 13.5 = 49.5\% \text{ (for dyeing with 0.1\% dye)}$$

$$R_{\lambda\max} - R_{\lambda\text{complementar}} = 59.8 - 7.9 = 51.9\% \text{ (for dyeing with 2\% dye)}$$

For the colors obtained with mixtures of dyes: Bemacid Gelb GR and Bemacid Rot BLF (figure 3) the curves of remission remain constant. For spectral domain between 420-560 nm, for concentrations higher than 0.5%, their remission values are very close or even equal, so that remission curves overlap in this field. Maximum remission color studied is located in orange, yellow and red between 595-605 nm, 580-595 nm and 605-640 nm. Dyed samples remit in the blue, blue-green, green-blue, green, yellow-green, red spectral domain between 440-540 nm, 540-580 nm, 605-640 nm.

Starting from these premises, to highlight the interaction between the two dyes are analyzed in terms of quality the remission curves for the two colors [1,6-9].

In Figures 4, 5, 6 are illustrated remission curves separately for the two individual dyes and their mixture at different concentrations.

Figure 4, figure 5, figure 6. shows that from a mixture of: 0.25% Bemacid Rot BLF and 0.25% Bemacid Gelb GR; 0.50%, Bemacid Rot BLF and 0.50% Bemacid Gelb GR; 1% Bemacid Rot BLF and 1% Bemacid Gelb GR is obtained orange dyeing. From standard dyeing with each color in hand is observed that in the red area of the spectrum, both colors absorbs very little. The orange color obtained from the yellow color and red color will have the same remission in red, with the two colors. In the field of green will only absorb the color red. The orange color obtained from red and yellow colors, will have the same remission in green, which presents the color red [1,9-11].

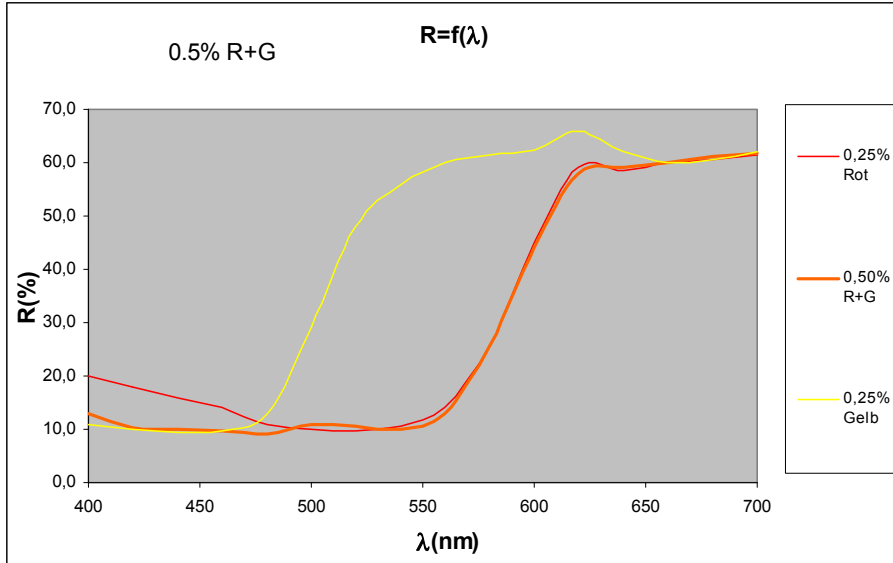


Figure 4. Remission curves for Bemacid Gelb GR, Bemacid Rot BLF and their mixture.

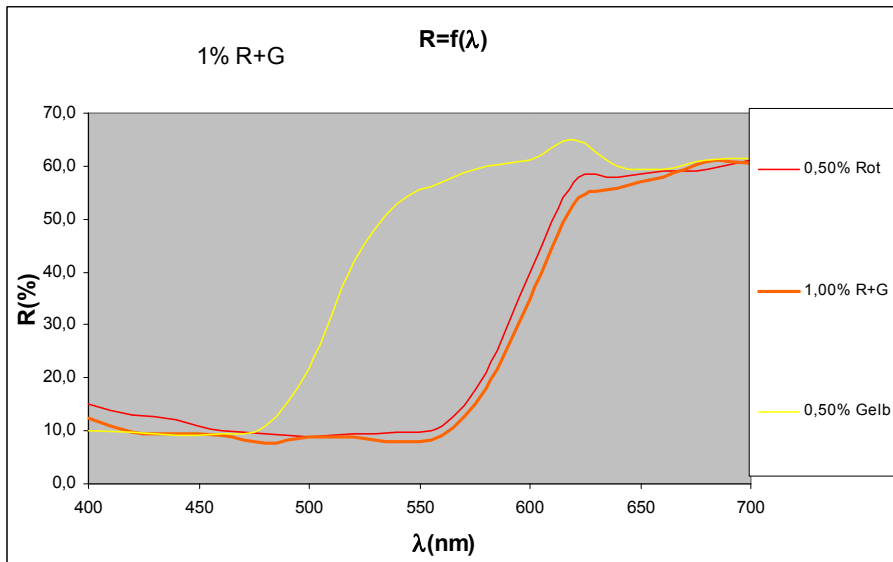


Figure 5. Remission curves for Bemacid Gelb GR, Bemacid Rot BLF and their mixture.

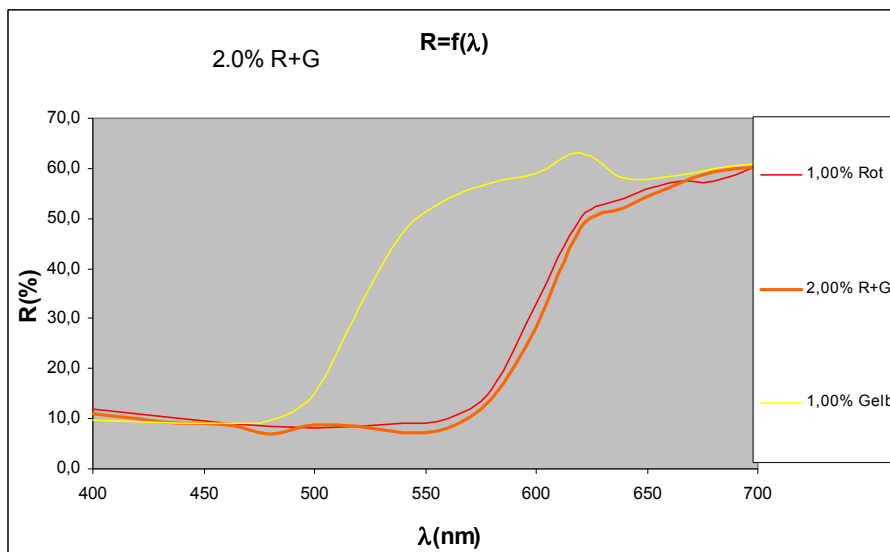


Figure 6. Remission curves for Bemacid Gelb GR, Bemacid Rot BLF and their mixture.

CONCLUSIONS

Remission curves drawn were allowed to discuss color characteristics of standard dyeing obtained with studied colors and the colors obtained by mixing the two dyes and the dependence on the concentration of dye color that was made.

Color shades are interpreted, especially on remission maxim presented on the analysed curves and their modification.

The differences that occur, due to mutual influence the ability of exhaustion of dyes in the bathroom, or a dependency of the ability of the exhaustion of dye bath in dyeing .

Between remissions dyeing with unitary dyes and remissions dyeing with mixed dyes there is interdependence. This interdependence puts in evidence the effect subtractivites manifested by each color on the spectral composition of the other color.

EXPERIMENTAL SECTION

This paper presents the tinctorial characteristics of two acid dyes that will serve at preparing bath dyeing with calculated recipes. Studied dyes are acid dyes produced by Bezema, Switzerland: Bemacid Rot BLF and Bemacid Gelb GR. With these unitary dyes were made standard painting

on 100% wool fabric at concentrations ranging from 0.1% to 2.0%, the specific conditions of wool dyeing with acid dyes. [1, 2, 3, 4, 10, 11]. Dyeing colours obtained were measured on a Specol 10 spectrophotometer, at 16 wavelength of visible located at intervals of 20 nm. In parallel there have been dyeing on wool with mixtures of the two dyes taken in equal parts for the same range of concentrations used for unitary colours.

At present there are spectrophotometer and specialized software that allow the measurement, colorimetric data storage, calculating the coordinates of chromatic colour, intensity of colour, the chromatic parameters of colour and draws automatically the remission curves [12, 13].

REFERENCES

1. L.E. Puscas, D.C. Radu, "Introduction to knowledge and measurement of color", Dosoftedi Ed, Iasi, **1997**.
2. M. Pustianu, M.S. Bucur, *Magazine of chemistry*, **2005**, 7, 746.
3. M. Pustianu, "Instrumental elaboration of optimized recipes dyeing samples of 100% wool"-PhD Thesis, Technical University "Gh.Asachi" Iasi, **2000**.
4. M. Pustianu, *Textile industry magazine*, **2006**, 1, 28.
5. R.H. Wardman, S. Farooq, K.J. Smith, *Coloration Technology*, **2012**, 128, 3, 161.
6. A. Shams-Nateri, *Coloration Technology*, **2009**, 125, 1, 36.
7. L.E. Puscas, "Measurement and color theory", Dosoftedi Ed, Iasi, **1983**.
8. G. Wyozecki, SW Stiles, "Color science. Concepts and methods. Quantitative data and formulas", John Wiley & Sons, ed. II, **1982**.
9. Berger, A., Brockes, A., *Bayer Farben Revue*, No. 3 / 1.
10. ***"Catalog Bezema", **1993**.
11. J.C. Guthrie, J. Moir, *Rev. Progr. Coloration*, **1978**, 9, 1.
12. S. Komboonchoo, T. Bechtold, *Journal of Cleaner Production*, **2009**, 17, 1487.
13. H. Ghouilaa, N. Meksib, W. Haddarb, M.F. Mhennib, H.B. Janneta, *Industrial Crops and Products*, **2012**, 35, 31.

ULTRATHIN ORGANIC COATINGS ON COPPER, COPPER ALLOYS AND STAINLESS STEEL FOR CONTROLLING THE MICROBIOLOGICALLY INFLUENCED CORROSION

LORÁND ROMÁNSZKI*, JUDIT TELEGDI, LAJOS NYIKOS

ABSTRACT. Organic coatings only a few nanometres thick have been prepared on surfaces of pure copper, copper alloys and stainless steel samples by self-assembly, Langmuir–Blodgett technique and dip-coating. The resulted thin films have been characterized by dynamic contact angle measurements as well as by infrared techniques. The stability of the layers in aqueous environment and their protective effect against corrosion in NaCl solution and against bacterial adhesion was investigated.

Keywords: *microbiologically influenced corrosion, self-assembling monolayers, Langmuir–Blodgett-film, copper, stainless steel*

INTRODUCTION

Energy sector is of strategic importance within the industry, where the appearance of microbiologically influenced corrosion (MIC) may have severe consequences. In power plants circulating seawater as cooling agent, the biofouling and corrosion of the condenser tubes is controlled by biocides and corrosion inhibitors [1]. Chlorine and chlorine-related oxidising compounds are the cheapest and most effective chemicals against microorganisms; however, their direct aquatic toxicity and the result of chlorinated organic by-products rigorously limit their dosage [2–3]. In addition, the high amounts of corrosion inhibitors consumed bring on appreciable environmental load. The use of nanocoatings would significantly reduce the consumed chemicals, thus cutting down both expenses and environmental impact.

Nanocoatings are coatings involving primarily organic surfactants, which, by their nature, can readily adsorb to the metal/water interface into compact layers, assuring protection. Although their thickness is only of a few nanometres, these coatings were proved to offer good protection against

* *Department of Interfaces and Surface Modification, Institute of Materials and Environmental Chemistry, Research Centre for Natural Sciences Hungarian Academy of Sciences, Pusztaszeri út 59–67., HU-1025 Budapest, Hungary, romanszki.lorand@ttk.mta.hu*

both corrosion and microbial adhesion. Common features of the molecules involved are a hydrophilic functional group, which can make strong bonds with the metal surface, and a hydrophobic hydrocarbon chain of typically 14-22 carbon atoms long, which accounts for the dense packing of the molecules and for the hydrophobicity of the layer.

Such coatings are prepared and tested in several laboratories worldwide by SAM, Langmuir–Blodgett, dip-coating or other techniques. The number of publications on nanocoatings prepared and tested on pure metals (mainly copper and iron, but also nickel and aluminium) is large. The reported layers include amines [4, 5], thiols [6–10], carboxylic acids [11–16], hydroxamic acids [15–20], amino acids [21–23], phosphonic acids [12], sulphonic acids [12], silane derivatives [24–26], and heterocyclic compounds traditionally used as inhibitors (benzotriazole, benzothiazole, imidazole and their homologues and derivatives) [27, 28]. However, the literature on similar works involving alloys, especially others than stainless steels, is much scarcer [29, 30]. On one hand, this is not surprising, since the surface of an alloy is always a more complicated system than a pure metal, with several new variables and unknowns. On the other hand, alloys have larger field of industrial application, thus studying nanocoatings on alloys is strongly justified and of even bigger possible economic impact. Through our experiments, we try to bring our contribution into this international pioneering work.

RESULTS AND DISCUSSION

Surface free energies of coated alloy samples. There are a few widely acknowledged methods for extracting surface free energy values from contact angle data [31–35]. Most of these require measurement of contact angles with 2-3 polar and non-polar liquids, thus making the procedure long and cumbersome, however, offer the incontestable advantage of obtaining the different components of the total surface free energy. From the available methods, we have chosen the one based on Neumann's equation of state (Eqs. 1 and 2), which makes possible to use only one test liquid, however, at the expense of obtaining only the total surface free energy, without its components [35].

$$\gamma_{SL} = \gamma_S + \gamma_L - 2\sqrt{\gamma_S \gamma_L} e^{-\beta_1(\gamma_L - \gamma_S)} \quad (1)$$

$$\beta_1 = 1.247 \times 10^{-4} \left(\frac{\text{m}^2}{\text{m}} \right)^2 \quad (2)$$

Combining the above expression with Young's equation (Eq. 3), the γ_{SL} solid-liquid interfacial energy term can be eliminated. The resulting transcendental equation in γ_S , the surface free energy of the solid, can be solved numerically, by knowing the γ_L surface tension of the test liquid at a given temperature and the measured value of the θ_Y equilibrium (Young) contact angle. This latter can be calculated from the measured θ_A advancing and θ_R receding contact angles through Tadmor's relation (Eqs. 4–6) [36].

$$\gamma_S = \gamma_{SL} + \gamma_L \cos \theta_Y \quad (3)$$

$$\theta_Y = \arccos \left(\frac{\Gamma_A \cos \theta_A + \Gamma_R \cos \theta_R}{\Gamma_A + \Gamma_R} \right) \quad (4)$$

$$\Gamma_A \equiv \sqrt{\frac{\sin^3 \theta_A}{2 - 3 \cos \theta_A + \cos^3 \theta_A}} \quad (5)$$

$$\Gamma_R \equiv \sqrt{\frac{\sin^3 \theta_R}{2 - 3 \cos \theta_R + \cos^3 \theta_R}} \quad (6)$$

The surface free energies of SAM-coated aluminium brass (Al-b), copper/nickel 70/30 (CuNi) and stainless steel 304 (SS) samples are presented in Table 1. The following observations can be made:

- 1) The surface free energies decrease after applying a SAM-coating. This is an indication of the presence of the hydrophobic alkyl chains on the surface.
- 2) The extent of this decrease depends strongly on the applied compound. Among the four compounds studied, hydroxamic and phosphonic acid coatings exhibited the lowest surface energies. This fact can be explained by the different bond strengths between the functional group of the surface-active compound and the oxidic/hydroxidic surface of the substrate.
- 3) On the surface free energy, the duration of SAM preparation
 - a. has evidently a strong influence in the case of C18-carboxylic acid (lower values measured when preparation time is longer);
 - b. has apparently no influence in the case of C18-amine (no clear trend of the surface free energy with preparation time);
 - and
 - c. has certain influence in the case of the other compounds.

Table 1. The influence of duration of layer preparation on surface free energies of SAM-coated alloy samples

SAM-coating	preparation time (h)	Surface free energy (mJ/m ²)		
		Al-b	CuNi	SS
control (uncoated)	N/A	58.2	61.3	59.6
C18-hydroxamic acid	1	–	44.8	–
	5	44.5	46.0	47.7
	24	44.8	39.5	47.5
C18-phosphonic acid	1	44.3	45.2	45.2
	5	–	44.4	45.4
	24	41.4	43.9	43.5
C18-amine	1	46.1	55.0	57.2
	5	53.8	54.2	58.0
	24	51.6	–	58.7
C18-carboxylic acid	1	50.8	51.5	58.5
	5	47.0	43.5	56.9
	24	41.2	45.0	54.3

Stability of the coatings in aqueous environment. A frequently encountered, justified concern is whether these nanocoatings can withstand flowing water in a possible real application. A simple experiment was conducted in order to get an answer to this question. Samples coated with nanolayers were immersed in gently flowing water (volumetric flux: 1.8 m/h) for 2 weeks. The samples were analysed before and after by reflection absorption infrared spectroscopy (RAIRS) and sum frequency generation spectroscopy (SFS).

In the RAIRS spectra (Figure 1, left), besides the apparent increase of the $\bar{\nu}$ peak at 2962 cm⁻¹ (corresponding to the antisymmetrical stretching mode of the methyl groups), which is an artefact connected to the baseline definition, the intensity of all other characteristic peaks (d^+ symmetrical stretching mode and d_{FR}^+ Fermi resonance of the methylene groups; r^+ symmetrical and \bar{r} antisymmetrical stretching modes of the methyl groups) decreases after the water immersion test; however, the peaks are still traceable, indicating that the nanolayers withstand the aqueous environment.

SFS is a powerful technique to give information about the molecular-level order of the hydrocarbon chains. Due to the nature of the nonlinear optical phenomenon, a strong signal appears only generated by anisotropic moieties. Therefore, in a well-ordered monolayer, with the hydrocarbon chains all aligned and fully extended in all-*trans* conformation, only the characteristic peaks of the terminating methyl groups are present. Methylene groups become visible in the spectrum only when parts of the chains are distorted in *gauche*

conformations. Therefore, the intensity ratios of the methyl/methylene peaks provide information about the conformation of the chains [37]. We found that the methyl peaks appear also after testing in aqueous environment (Figure 1, right). Moreover, the intensity ratios are almost unchanged, which is an unquestionable proof of the layer stability.

This stability depends on the preparation time of the coating. When the immersion time is enough for self-assembled film formation, the result is a properly packed layer of good quality, which can survive the immersion test, as revealed by the stronger IR peaks (Figure 2). Above a threshold time, however, lengthening further the preparation time does not improve further the stability of these layers. According to our results, 5 h preparation time is enough to obtain stable SAM layers.

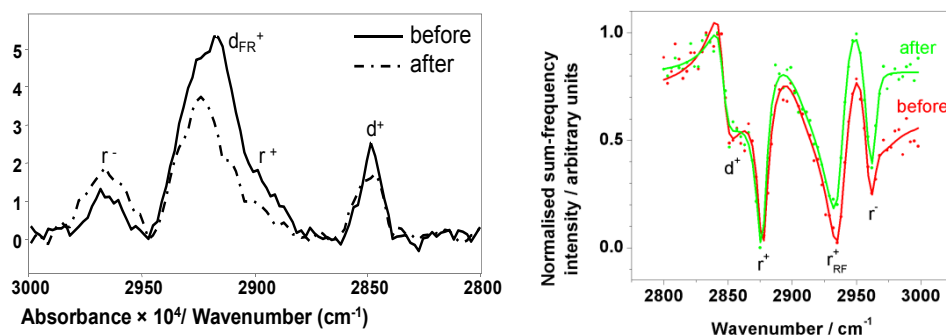


Figure 1. Stability of nanolayers in aqueous environment. Left: RAIRS spectra of C18-hydroxamic acid SAM layer on SS reveals the presence of the layer after the two weeks test in flowing water. Right: SFS spectra of LB-layers of the same hydroxamic acid on copper indicate no alteration of the molecular-level order.

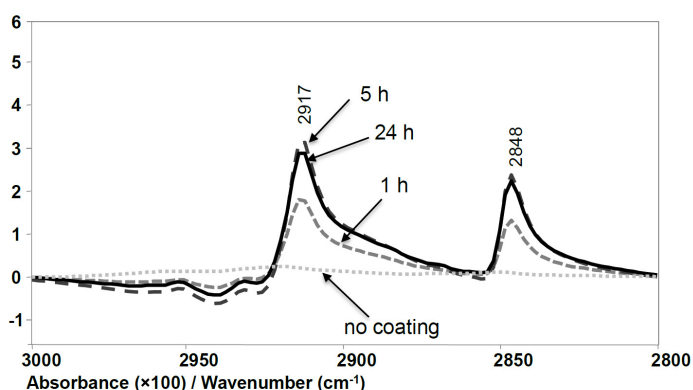


Figure 2. Stability of the nanolayers in aqueous environment: RAIRS spectra of C18-phosphonic acid SAM layers formed in 1, 5, and 24 h on Al-b substrates after the two weeks test in flowing water, as compared to the uncoated reference.

Bacterial adhesion. Samples with different SAM and Langmuir–Blodgett coatings were tested in aqueous environment containing mixed population of microorganisms. The adhesion of cells and formation of biofilm on the coated samples after 48 h immersion time was investigated and visualised by AFM and epifluorescent microscopy. These two techniques revealed that our coatings hamper the adhesion of cells and/or the formation of the biofilm (Figures 3 and 4). The mechanism of action is not completely understood, but we propose the following hypothesis: Bacterial cells are known to adhere to surfaces with the aid of a mixture of secreted macromolecules (proteins, carbohydrates, lipids, uronic acids, nucleic acids etc.), called extracellular polymeric substance (EPS). These macromolecules are mainly hydrophilic by nature. A densely packed hydrophobic nanolayer would not favour the attachment of these macromolecules. In conclusion, the adhesion of the cell is inhibited.

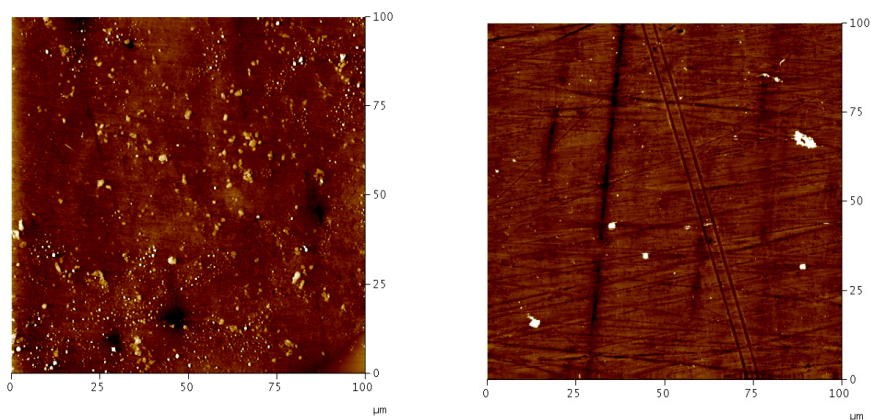


Figure 3. AFM images of copper samples after 48 h immersion in water, containing mixed population of microorganisms. Left: uncoated, right: with stearoyl hydroxamic acid LB1-coating. Scanned area $100 \times 100 \mu\text{m}^2$, height range 500 nm.

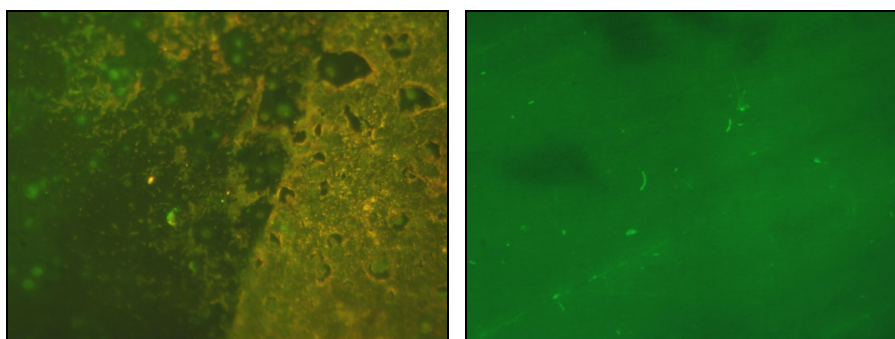


Figure 4. Fluorescent microscope images of an uncoated copper sample (left), respectively a copper sample coated with C18-carboxylic acid LB1 film (right) after being immersed in bacterial environment for 48 h.

CONCLUSIONS

Organic layers already in a few nanometres thickness are able to protect metals against corrosion and to prevent the adhesion of microorganisms. The properties and the efficiency of the protective layers significantly depend on the: type of metal substrate, surface preparation, film forming compound, type of solvent, number of layers.

EXPERIMENTAL SECTION

Metals. The alloys of interest were: aluminium brass (Al-b), copper-nickel 70/30 (CuNi) and stainless steel 304 (SS). Samples cut from standardised condenser tubes of these alloys were used [38, 39]. In addition, pure, polycrystalline copper has been used as model metal.

Preparation and pre-treatment of the substrates. The 10×12 mm² Al-b and CuNi condenser tube samples were used without polishing. Conversely, rectangular copper samples with dimensions of 10×15×1.6 mm³ were consecutively polished in several steps: First, samples underwent consecutive coarse polishing with seven emery papers (220 to 4000 grains/in). After the last, 4000 grains/in paper a fine-polishing procedure followed. In the case of the samples used in corrosion experiments, as well as in AFM and SFS analyses, fine-polishing was done with diamond suspensions of consecutively decreasing grain sizes of 6, 3, 1 and ¼ µm, ended with a final step using 300 nm alumina suspension. For bacterial adhesion experiments the fine-polishing involved only the 1 µm diamond paste, followed by the 300 nm alumina suspension. In order to remove any debris, between each consecutive polishing step the samples were thoroughly cleaned in ultrasonic bath in distilled water, acetone and ethanol. Copper alloys and stainless steel samples were pre-treated for 5 min. in 14 mM HNO₃ in ultrasonic bath, followed by a 5 min. sonication in 5% H₂O₂. The diluted acid removed the inorganic contamination and oxide layers of unknown history, while the diluted peroxide reconstructed the surface oxide in a controllable, reproducible manner, as proven by XPS results (not detailed here). In some cases, this two-step pre-treatment process was substituted by a 10 min. sonication in spectroscopic grade acetone completed by 20 min. cleaning in ozone generated under a UV-lamp.

Film forming compounds. Analytical grade octadecyl amine and stearic acid were used without further purification. Stearoyl hydroxamic acid and oleoyl hydroxamic acid were synthesised in our laboratory from hydroxylamine and the appropriate acyl chlorides, then re-crystallized and characterized by melting points, elemental analysis, infrared spectroscopy and thin layer chromatography. Octadecyl phosphonic acid was synthesised in a Michaelis–Arbusov reaction.

Coating procedure. SAM coatings were prepared by dipping the pre-treated metal samples into 2.0 mM solutions of the film forming compounds in chloroform, dichloromethane, or tetrahydrofurane. Dipping times were 1, 5 and 24 h in the case of the alloys, 20 h in the case of corrosion experiments with copper samples, and 2 h in the case of bacterial adhesion experiments with copper samples. The coated samples were rinsed with the respective solvent in order to remove non-specifically bond excess material and were dried in air or in a stream of nitrogen.

The Langmuir–Blodgett coatings on copper substrates were prepared in a Langmuir–Blodgett trough (NIMA Technology), working with ultra pure water (Milli-Q, 18 M Ω cm) as subphase. The film forming compounds were dissolved in HPLC grade chloroform (Merck) to a concentration of 2.2 mM and spread onto the thermostated subphase. The time allowed for the evaporation of the solvent and the relaxation of the monolayer was 10 min. The organization of the monolayer at the air/water interface was followed by recording the surface pressure vs. molecular area isotherms and also visualised by a Brewster-angle microscope. Stearic acid and stearyl hydroxamic acid monolayers were transferred at 25 °C temperature, 25 mN/m constant surface pressure, compressing the monolayer with 50 cm²/min barrier speed before reaching the target pressure and setting 5 mm/min dipping speed after the target pressure has been reached. The surface pressure was monitored by a Wilhelmy-type pressure gauge and controlled by a feed-back loop.

Contact angle measurements. Copper alloys with and without coatings were characterised by their advancing and receding contact angles. These were measured in a digital surface tensiometer (NIMA Technology) based on the Wilhelmy-method. As measuring liquid ultrapure water (Milli-Q) was used in a clean, thermostated vessel.

Reflection absorption infrared spectroscopy. A Nicolet Magna 750 FTIR spectrometer was used, with the following abilities and parameters: MCT detector, 512 scans, 2 cm⁻¹ resolution, incidence of the IR beam: 68.3°, Au/KRS-5 polarizer, Specac 19650 grazing angle accessory.

Sum frequency generation spectroscopy. An EKSPLA spectrometer was used (visible wavelength: 532 nm, energy: 40 μ J). The description of the setup and the experimental parameters can be found in [40].

Corrosion in NaCl solution. SAM- and Langmuir–Blodgett-coated copper samples were dipped in 0.5 M NaCl for 15 h, then thoroughly rinsed in pure water, in acetone and finally dried. 100 \times 100, 50 \times 50 and 10 \times 10 μ m² areas were scanned in three different points of each sample by a Nanoscope IIIa AFM apparatus (Digital Instruments) equipped with 100 and 10 μ m scanners and silicon nitride tips, operating in contact mode.

Bacterial adhesion. A cooling water sample from the pharmaceutical industry, containing mixed microbial population was used in the adhesion experiments. Bare and coated copper samples were dipped in for 48 h, then rinsed in distilled water and treated with acridine orange in order to dye

the cells. An Axio Imager upright microscope (Carl Zeiss) has been used at 1000× magnification in immersion oil to image the microbial cells and the biofilm. For complementary information, AFM images of 100×100, 50×50, 25×25 and 10×10 μm² areas at three different points of each sample were recorded.

ACKNOWLEDGMENTS

We thank Katalin Tímár for synthesising the hydroxamic acids and the phosphonic acid, Tamás Keszthelyi for the RAIRS and SFS measurements, Pierangela Cristiani for supplying the alloy samples and Zsófia Keresztes for suggestions and advices. The research leading to these results has received funding from the European Community's Sixth and Seventh Framework Programmes under grant agreement numbers 512161/2004 and 238579/2009.

REFERENCES

1. P. Cristiani, *Applied Thermal Engineering*, **2005**, *25*, 2630.
2. P. Cristiani, "Corrosion Monitoring in Microbial Environments", In: L. Yang (ed.), *Techniques for Corrosion Monitoring*, Woodhead Publishing Limited, Cambridge, **2008**, pp. 347–387.
3. P. Cristiani, G. Perboni, A. Debenedetti, *Electrochimica Acta*, **2008**, *54*, 100–107.
4. C.M. Ruan, T. Bayer, S. Meth, C.N. Sukenik, *Thin Solid Films*, **2002**, *419*, 95.
5. Y.Y. Feng, S.H. Chen, J.M. You, W.J. Guo, *Electrochimica Acta*, **2007**, *53*, 1743.
6. G.K. Jennings, P.E. Laibinis, *Colloids and Surfaces A*, **1996**, *116*, 105.
7. Z. Mekhalif, F. Sinapi, F Laffineur, J. Delhalle, *Journal of Electron Spectroscopy and Related Phenomena*, **2001**, *121*, 149.
8. A.T. Lusk, G.K. Jennings, *Langmuir*, **2001**, *17*, 7830.
9. M. Metikoš-Huković, R. Babić, Ž. Petrović, D. Posavec, *Journal of the Electrochemical Society*, **2007**, *154*, C138.
10. P.E. Laibinis, G.M. Whitesides, *Journal of the American Chemical Society*, **1992**, *114*, 9022.
11. Y.T. Tao, G.D. Hietpas, D.L. Allara, *Journal of the American Chemical Society*, **1996**, *118*, 6724.
12. A. Raman, R. Quiñones, L. Barriger, R. Eastman, A. Parsi, E.S. Gawalt, *Langmuir*, **2010**, *26*, 1747.
13. A. Raman, E. S. Gawalt, *Langmuir*, **2007**, *23*, 2284.
14. R.R. Sahoo, S.K. Biswas, *Journal of Colloid and Interface Science*, **2009**, *333*, 707.
15. J. Telegdi, L. Románszki, F. Al-Taher, É. Pfeifer, E. Kálmán, *17th International Corrosion Congress 2008: Corrosion Control in the Service of Society*, NACE International, Houston, **2008**, 2631.

16. L. Románszki, J. Telegdi, E. Kálmán, *Colloids and Surfaces A–Physicochemical and Engineering Aspects* **2008**, 321, 20.
17. J. Telegdi, T. Rigó, E. Kálmán, *Corrosion Engineering, Science and Technology*, **2004**, 39, 65.
18. H.H. Deng, H. Nanjo, P. Qian, Z.B. Xia, I. Ishikawa, T.A. Suzuki, *Electrochimica Acta*, **2008**, 53, 2972.
19. J. Telegdi, T. Rigó, E. Kálmán, *Journal of Electroanalytical Chemistry*, **2005**, 582, 191.
20. J. Telegdi, T. Szabó, F. Al-Taher, É. Pfeifer, E. Kuzmann, A. Vértes, *Materials and Corrosion*, **2010**, 61, 1000.
21. D.Q. Zhang, X.M. He, Q.R. Cai, L.X. Gao, G.S. Kim, *Journal of Applied Electrochemistry*, **2009**, 39, 1193.
22. D.Q. Zhang, L.X. Gao, Q.R. Cai, K.Y. Lee, *Materials and Corrosion*, **2010**, 61, 16.
23. D.Q. Zhang, X.M. He, Q.R. Cai, L.X. Gao, G.S. Kim, *Thin Solid Films*, **2010**, 518, 2745.
24. R. Tremont, H. de Jesús-Cardona, J. García-Orozco, R.J. Castro, C.R. Cabrera, *Journal of Applied Electrochemistry*, **2000**, 30, 737.
25. R. Tremont, C.R. Cabrera, *Journal of Applied Electrochemistry*, **2002**, 32, 783.
26. E. Hoque, J.A. DeRose, P. Hoffmann, H.J. Mathieu, *Surface and Interface Analysis*, **2006**, 38, 62.
27. Y.S. Tan, M.P. Srinivasan, S.O. Pehkonen, S.Y.M. Chooi, *Journal of Vacuum Science and Technology A*, **2004**, 22, 1917.
28. Z. Zhang, S.H. Chen, Y.H. Li, S.H. Li, L. Wang, *Corrosion Science*, **2009**, 51, 291.
29. C. Hao, R.H. Yin, Z.Y. Wan, *Corrosion Science*, **2008**, 50, 3527.
30. K. Mori, N. Fujita, H. Horie, S. Mori, T. Miyashita, M. Matsuda, *Langmuir*, **1991**, 7, 1161.
31. W.A. Zisman, *Industrial and Engineering Chemistry*, **1963**, 55, 19.
32. S. Wu, *Journal of Polymer Science Part C: Polymer Symposia*, **1971**, 34, 19.
33. F.M. Fowkes, *Journal of Adhesion Science and Technology*, **1987**, 1, 7.
34. C.J. van Oss, R.J. Good, M.K. Chaundhury, *Langmuir*, **1988**, 4, 884.
35. A.W. Neumann, R.J. Good, C.J. Hope, M. Sejpal, *Journal of Colloid and Interface Science*, **1974**, 49, 291.
36. R. Tadmor, *Langmuir*, **2004**, 20, 7659.
37. A.G. Lambert, P.B. Davies, D.J. Neivandt, *Applied Spectroscopy Reviews*, **2005**, 40, 103.
38. *Standard specification for copper and copper-alloy seamless condenser tubes and ferrule stock, Designation: B 111 – 98 (Reapproved 2004)*, ASTM International, **2004**.
39. *Standard specification for welded austenitic steel boiler, superheater, heat-exchanger, and condenser tubes, Designation: A 249/A 249M – 04*, ASTM International, **2004**.
40. É. Kiss, T. Keszthelyi, G. Kormány, O. Hakkel, *Macromolecules*, **2006**, 39, 9375.

NEW MATERIALS FROM WASTE GLASS FIBRE

EMILIA SABĂU^a, NICOLAE BÂLC^a,
PAUL BERE^a, OVIDIU NEMEŞ^{b,*}

ABSTRACT. The authors propose a new material obtained from waste composites reinforced with glass fibres, sand, and polyester. Composite plates which contain in the structure waste glass fibre were developed. The obtained material was characterized by compression tests and microstructure analysis by SEM-EDX.

Keywords: *composite materials plates, fibre glass waste, recycling*

INTRODUCTION

Composite materials consist of reinforcement material (glass fibre, carbon fibre, Kevlar, etc.) and a matrix (polyester resin, epoxy resin, and so on). A composite material may contain, in the structure, some auxiliary materials (catalysts, accelerators, coupling agents, pigments, etc.) with the role to give high properties or low price [1, 5].

One problem that we are facing is the storage and recovery of waste composite materials. Composite waste resulting from production processes and composite parts out of use occupy significant space for storage. A solution for recycling such composite materials has been to grind these materials and create new composite products. [6 - 9].

Mixtures of concrete with sand and fiberglass waste are known [10, 11]. However, with the known technical solutions these materials have lower mechanical properties, higher density, and they degrade in time under the influence of external factors: moisture, sunlight, UV radiation.

Dang et al. [12] proposed a chemical recycling protocol for glass fibre reinforced epoxy resin cured with amine using nitric acid. Giraldi et al. [13] recycled PET reinforced with glass fibre, while Bartl et al. [14] investigated the recycling of fibres obtained from tyres. Composite materials obtained from wood fibres were analysed by Nemes et al. [3] and Augier et al. [15].

^a *Universitatea Tehnică din Cluj-Napoca, Facultatea de Construcții de Mașini, B-dul Muncii, Nr. 103-105, RO-400641 Cluj-Napoca, Romania.*

^b *Universitatea Tehnică din Cluj-Napoca, Facultatea de Ingineria Materialelor și a Mediului, B-dul Muncii, Nr. 103-105, RO-400641 Cluj-Napoca, Romania, * Ovidiu.Nemes@sim.utcluj.ro*

In this paper composite plates based on waste fibre glass (Figure 2) are described. Specimens were carried out to determine the physical and mechanical characteristics. The composite plates provide higher mechanical properties, lower costs and reduce waste materials in the environment.

RESULTS AND DISCUSSION

Wastes from composite materials shown in Figure 1 are due to accumulation in time and a poor interest to find solutions for recycling or recovering. By grinding composite waste, one can obtain a material rich in glass fibre (Figure 2) that forms a very valuable reinforcement to be embedded in other materials or to be used for obtaining reinforced composite materials.



Figure 1. Waste composite materials



Figure 2. Ground glass fibre

A manual lay-up technology was used in the manufacturing process for the composite materials as previously described [17]. Cubic specimens were made from the obtained composite material for compression testing. Following the compression load of cubic specimens, the constituent of composite material remains bonded through the filaments of reinforcement material. This paper highlights a new composite material with higher mechanical properties and different possible applications.

Microscopy study in the case of waste materials

The microstructure of fracture samples from waste glass fibres/sand/polyester matrix composites was analysed using a metallographic microscope type Optika XDS-3 MET [16]. The sand was used as a low-cost reinforcement material in the form of particles with transparent aspect. The morphological analysis of the sand is shown in Figure 3. The sand grains contain in the structure over 90% silica (SiO_2). The glass fibres are made from silica sand, which melts at 1720 °C.

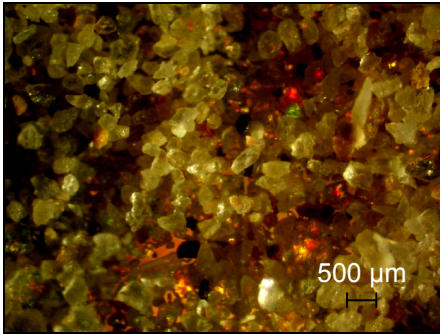


Figure 3. Sand grains

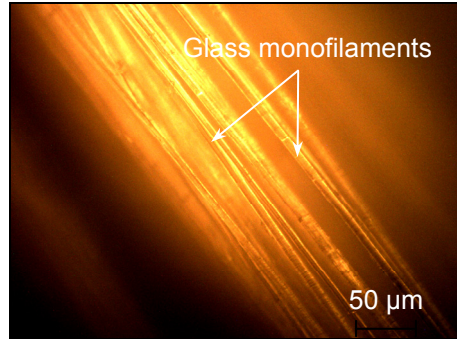
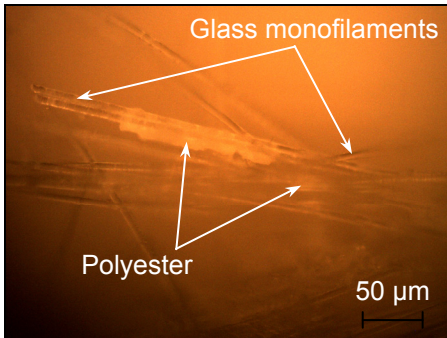
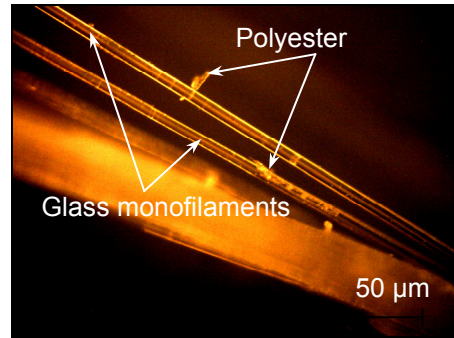


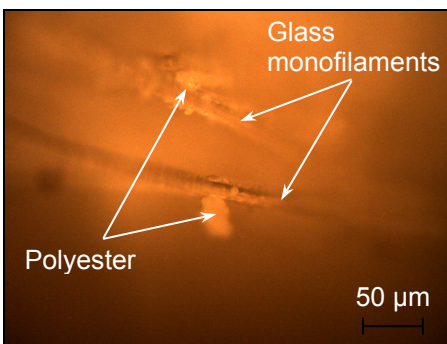
Figure 4. Non-impregnated glass fibre monofilaments



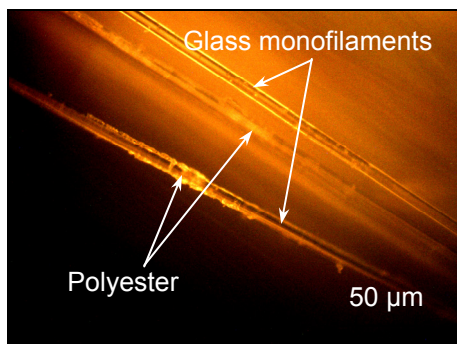
(a)



(b)



(c)



(d)

Figure 5. Waste glass fibre monofilaments impregnated with resin.

The non-impregnated glass fibre monofilaments have a glossy and smooth surface, specific to the glass. The glass fibres surface is treated with silane, which favors good adhesion at the interface between fibres and matrix. The non-impregnated glass fibre was also analysed using optical microscopy, cf. Figure 4.

Figure 5 (a-d) illustrates the adhesion between glass fibre monofilaments and polyester resin. The morphological analysis of the fracture area indicates glass fibre monofilaments and sand grains well impregnated with resin, cf. Figure 6. One may note a good impregnation of the matrix and a good compatibility between filaments, sand and resin.

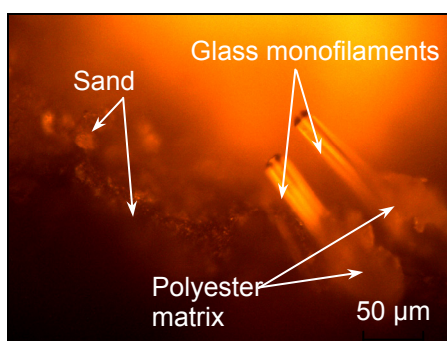


Figure 6. The fracture zone of waste fibre glass/sand/polyester resin plate.

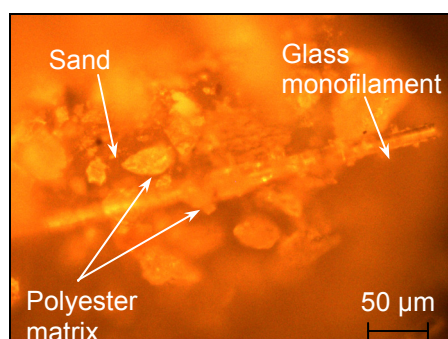


Figure 7. Sand and glass monofilaments in polyester resin.

The particles of polyester resin and sand glued on the glass monofilament indicate that connection between glass fibres, sand and polyester matrix was achieved, cf. Figure 7. One has thus obtained a composite material with high mechanical properties and low density. These materials allow one to reuse waste glass fibre. Using these materials at low temperatures increases their mechanical characteristics.

EDX analysis

Elemental analysis of the waste fibre glass and polyester resin was performed using the energy dispersive x-ray spectroscopy (EDX). Elemental percentages are based on the total weight of the elements detected. Figure 8 shows the elemental EDX analysis of the waste glass fibre, revealing the predominance of silicon and aluminium. Minor amounts of calcium, oxygen, carbon, magnesium and sodium are also detected. Data are expressed as both weight (Wt.%) and atomic per cents (At.%). The weight and the atomic percentages for the contained elements are: Si with 28.19Wt%, 21.12At.%;

Al with 18.50Wt.%, 14.43At.%; Ca with 16.50Wt.%, 8.66At.%; O with 18.34Wt.%, 24.12At.%; C with 17.67Wt.%, 30.96At.%; Mg with 0.43Wt.%, 0.38At.% and Na with 0.37Wt.%, 0.34At.%. Table 1 gives the elements on the surface of a waste glass fibre.

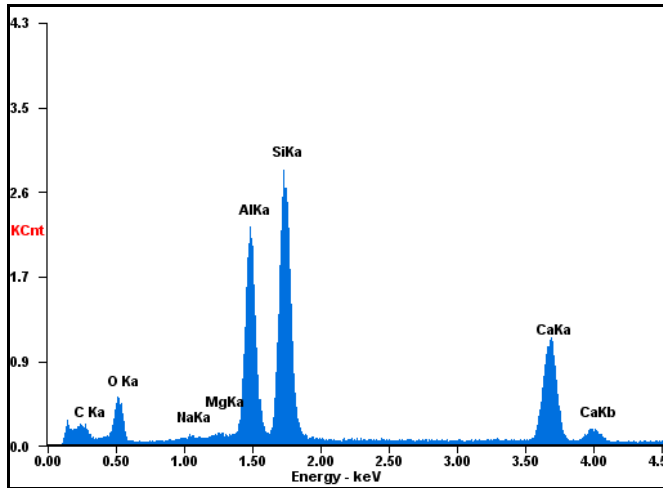


Figure 8. Elemental EDX analysis of the waste glass fibre

Table 1. EDX analysis of the waste glass fibre

<i>Element</i>	<i>Wt%</i>	<i>At%</i>
C	17.67	30.96
O	18.34	24.12
Na	00.37	00.34
Mg	00.43	00.38
Al	18.50	14.43
Si	28.19	21.12
Ca	16.50	08.66

Figure 9 shows the elemental EDX analysis of the polyester resin. These microanalyses reveal the predominance of carbon, oxygen and silicon. Minor amount of calcium, aluminium and sodium have also been detected. The weight and the atomic percentages for the contained elements of the polyester matrix are: C with 62.18Wt.%, 74.80At.%; O with 17.69Wt.%, 15.97At.%; Si with 9.30Wt.%, 4.78At.%; Ca with 7.98Wt.%, 2.87At.%; Al with 2.39Wt.%, 1.28At.% and Na with 0.47Wt.%, 0.29At.%.

Elemental quantitative analyses presented in Table 2 gives the elements on the surface of polyester matrix.

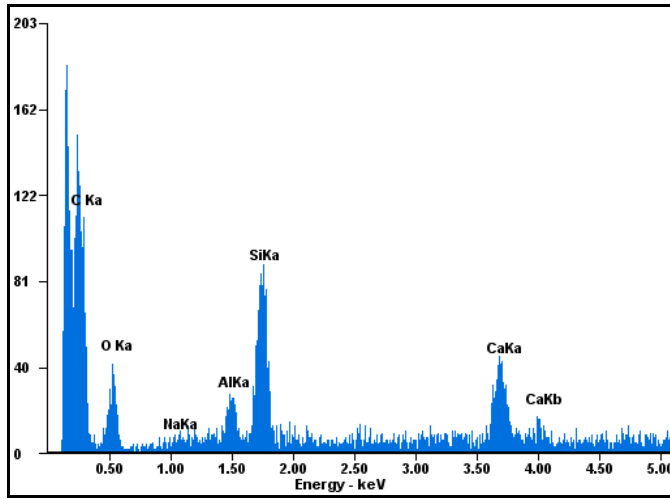


Figure 9. Elemental analysis of the polyester matrix

Table 2. EDX analysis of polyester matrix

<i>Element</i>	<i>Wt%</i>	<i>At%</i>
C	62.18	74.80
O	17.69	15.97
Na	00.47	00.29
Al	02.39	01.28
Si	09.30	04.78
Ca	07.98	02.87

Table 3 shows data following the compressive stress of cubic specimens, the constituent composite material remains bonded through filaments of reinforcement material.

Table 3. Compressive tests results

No.	Force [KN]	Average force [KN]	Average compressive breaking strength [MPa]	Density [Kg/m ³]
1.	185.8	189.96	78.27	1380
2.	191.2			
3.	193.2			
4.	187.3			
5.	192.3			

CONCLUSIONS

This study characterizes a new composite material obtained from recovered materials, with a complete recovery of waste glass fibres.

The experimental data shows that the new materials have good mechanical properties and they can be successfully used in the dimensioning and verification process of composite structures resistance.

The microstructure of fracture samples from waste glass fibres/sand/polyester resin composites was microscopically analysed, noting a good impregnation of the matrix and a good compatibility between filaments, sand and resin. The fracture area indicates monofilaments of glass fibre well wetted by the resin.

The new composite material contained crushed waste glass fibre, sand and polyester matrix all mixed together. After polymerization of the resin we obtain a composite material reinforced with glass fibres which has superior mechanical properties. This can be used in various applications such as: polyester reinforced concrete, strengthening composite parts (ornamental composites plates, ornamental garden stones, garden furniture, additive materials and so on).

EXPERIMENTAL SECTION

The materials used in this study are waste glass fibres, polyester resin, sand of 0.3 mm granulation and gel coat. The polyester resin is type Norpol 440-M750 which is orthophthalic with low styrene emission, tixotropized and pre-accelerated. The technical characteristics of the resin are: Brookfield viscosity: 250 - 350 mPa.s; Density at 25 °C: 1350 kg/m³; Gel time: 2% MEC (methyl-ethyl-ketone): 8 - 15 min; Exothermic peak: 160 - 190 °C; Exothermic peak time: 15 - 23 min; Colour: Transparent blue. The gel coat type Norpol is an isophthalic polyester resin designed to have excellent application properties, good mechanical properties, excellent curing properties, easy to sand and repair. The composite material waste, after grinding, was mixed with the sand and polyester matrix. The quantities of components were as follows: 50% sand, 30% waste glass fibre, 15% polyester matrix and 5% gel coat. From this material cubic specimens were made with the dimensions 50x50x50 mm, according to EN 12320-3 standard.

The composite plates that contain in the structure waste glass fibre were prepared by hand lay-up and compression. To determine the mechanical properties of composite plates experimental testing at compressive load was performed.

ACKNOWLEDGMENT

This paper was supported by the project "Development and support of multidisciplinary postdoctoral programmes in major technical areas of national strategy of Research - Development - Innovation" 4D-POSTDOC, contract

no. POSDRU/89/1.5/S/52603, and project "Progress and development through post-doctoral research and innovation in engineering and applied sciences" - PRiDE, contract no. POSDRU/89/1.5/S/57083, both co-funded by the European Social Fund through Sectorial Operational Programme Human Resources Development 2007-2013.

REFERENCES

1. E.J. Barbero, "Introduction to composite materials design", second edition, CRC Press Taylor & Francis Group, USA, **2010**, chapter 1.
2. L.P. Kollár, G.S. Springer, "Mechanics of composite structures", Cambridge University Press, USA, **2003**, chapter 1.
3. O. Nemes, A.M. Chiper, A.R. Rus, V.F. Soporan, O. Tataru, P. Bere, *Studia UBB Chemia*, **2010**, LV, Sp.Iss.
4. A.M. Gomboş, O. Nemeş, V.F. Soporan, A. Vescan, *Studia UBB Chemia*, **2008**, LIII, 3, 81.
5. O. Nemeş, F. Lachaud, R. Piquet, V.F. Soporan, O. Tătaru, *Studia UBB Chemia*, **2008**, LIII, 3, 25.
6. S.J. Pickering, *Composites: Part A*, **2006**, 37, 1206.
7. T.A. Turner, S.J. Pickering, N.A. Warrior, *Composites: Part B*, **2011**, 42, 517.
8. A. Bernasconi, D. Rossin, C. Armani, *Journal of Engineering Fracture Mechanics*, **2007**, 74, 627.
9. S.J. Pickering, R.M. Kelly, J.R. Kennerley, C.D. Rudd, N.J. Fenwick, *Composites Science and Technology*, **2000**, 60, 509.
10. N. Sebaibi, M. Benzerzour, N.E. Abriak, C. Binetruy, *Construction and Building Materials*, **2012**, 29, 332.
11. S.B. Park, B.C. Lee, J.H. Kim, *Cement and Concrete Research*, **2004**, 34, 2181.
12. W. Dang, M. Kubouchi, H. Sembokuya, K. Tusda, *Polymer*, **2005**, 46, 1905.
13. A.L.F. de M. Giralddi, J.R. Bartoli, J.I. Velasco, L.H.I. Mei, *Polymer Testing*, **2005**, 24, 507.
14. A. Bartl, A. Hackl, B. Mihalyi, M. Wistuba, I. Marini, *Trans IChemE: Part B*, **2005**, 83(B4), 351.
15. L. Augier, G. Sperone, C. Vaca-Garcia, M.E. Borredon, *Polymer Degradation and Stability*, **2007**, 92, 1169.
16. L. Morovič, P. Pokorný, "Optical 3D Scanning of Small Parts, Advanced Materials Research", Vols. 468-471 (2012) pp. 2269-2273, *Trans Tech Publications*, Switzerland, doi:10.4028, www.scientific.net/AMR.468-471.2269.
17. E. Sabau, N. Balc, P. Bere, *Academic Journal of Manufacturing Engineering*, **2011**, 9(3), 100.

COMPARATIVE STUDY OF TURBULENCE PROMOTERS ON PRESSURE LOSS IN HEAT TRANSFER

ANDRA TĂMAȘ^a, SORINA BORAN^a

ABSTRACT. In this paper was studied the influence of some turbulence promoters (annular or spiral baffles), placed in the inner tube of a double pipe heat exchanger, on the pressure losses of the fluid. These studies were conducted in conjunction with the intention to enhance heat transfer by convection of the fluid that moves through these spaces

Keywords: *baffles, heat exchanger, heat transfer, pressure loss, turbulence promoters*

INTRODUCTION

The turbulence in hydraulic systems significantly influences various processes: frictional pressure losses, heat transfer by convection, absorption and adsorption, drying, dissolution; hydrodynamic regime determines the relationships which allow the calculation of the friction coefficient, partial coefficients of heat and mass transfer [1,2]. At the same fluid flow rate, turbulence increasing can be provided by introducing structures into the flow that can successive modify the state of the contact surface and therefore the speed or direction of flow, thus providing an additional local turbulence. Constructively, these changes consist in making artificial roughness in the form of circular or spiral baffles, ribs, channels, conical surfaces or blades swirling etc [3]. Intensification of convective heat or mass transfer considered effective, will be given along with the disadvantage of increasing hydraulic resistance, which leads to the undesired effect of increasing frictional pressure loss [4,5].

When turbulence promoters are used, optimal solutions are obtained by comparing relative changes of partial transfer coefficients with similar changes of the pressure loss. In the case of using turbulence promoters for the intensification of heat transfer by convection, it was compared the ratio between

^a *Universitatea "Politehnica" din Timișoara, Facultatea de Chimie Industrială și Ingineria Mediului, Bd. V. Pârvan Nr. 6, RO-300223 Timișoara, România, andra.tamas@chim.upt.ro; sorina.boran@chim.upt.ro.*

the partial heat transfer coefficients α_i/α_0 with the ratio of frictional pressure losses $\Delta p_i/\Delta p_0$ experimentally determined, under the same conditions [4].

This paper presents the experimental study of frictional pressure losses in a straight pipe, that is part of the tubular heat exchanger, in the presence and absence of turbulence promoters. Were effectively used cylindrical rings located along the length of the tube at different distances, or spirals having the same thickness and winding step equal with the distance between cylindrical rings.

The annulus of the heat exchanger was heated by hot water with known flow rate and temperature, and through the inner tube was ensured the airflow under warming. The determinations are performed both as turbulent and transient flow.

RESULTS AND DISCUSSION

The total heat transfer coefficient K is determined from the energy balance equation:

$$Q_1 = Q_2 + Q_3 = Q_4 \quad (1)$$

$$Q_2 = m_{air} \cdot c_{air} \cdot (\Delta t)_{air} \quad (2)$$

$$Q_4 = K \cdot A \cdot \Delta t_{med} \quad (3)$$

where: Q_1 - heat delivered by the hot fluid (water), W ; Q_2 - heat received by the cold fluid (air), W ; Q_3 - the lost heat, W ; Q_4 - the transmitted heat, W ; m_{air} - the air flow rate, $kg \cdot s^{-1}$; c_{air} - specific heat of air to the average temperature, $J \cdot kg^{-1} \cdot K^{-1}$; $(\Delta t)_{air}$ - the temperature differences for air at the heat exchanger extremities, $^{\circ}C$; Δt_{med} - the average temperature difference between air and water, $^{\circ}C$. The heat transfer area A was calculated with the relationship $A = \pi \cdot d_{med} \cdot H$, where d_{med} and H are the average diameter and the height of the inner pipe ($A = 0.05m^2$).

The partial heat transfer coefficient for air α_{air} was determined from the values of total heat transfer coefficient K , taking into account the thermal resistance to conduction of the pipe wall ($2.6 \cdot 10^{-6} m^2 \cdot K \cdot W^{-1}$) and the partial heat transfer coefficient for water ($\alpha_w = 920 W \cdot m^{-2} \cdot K^{-1}$) analytically calculated in the case of heat transfer in laminar flow through vertical pipes, when the forced movement direction is reversed to the free convection ($Gr \cdot Pr > 5 \cdot 10^5$) [6], Gr and Pr being Grashof and Prandtl criteria.

In Fig. 1 it is comparatively presented the variation of pressure losses caused by the air flow through the central tube, in the absence, respectively, the presence of annular baffles.

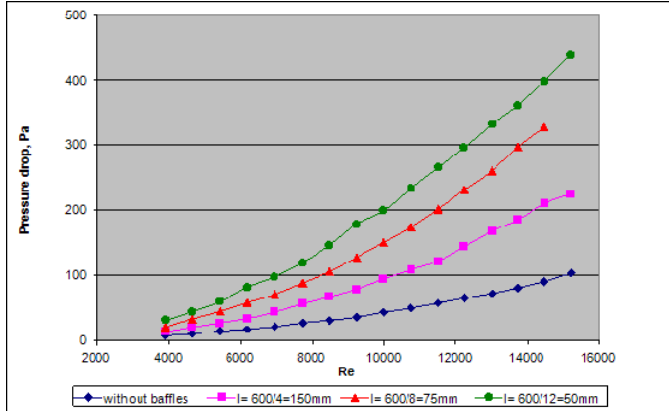


Figure 1. The dependence between the pressure losses and the air hydrodynamic regime, in the presence of annular baffles

It is observed that the presence of annular baffles leads to the pressure losses increasing in the inner tube, the increase is even greater than their number grows.

In the case of annular baffles absence, for the inner tube was analytically calculated the frictional pressure loss. Thus, in Fig.2 it is comparatively presented the evolution of the calculated and experimentally determined pressure losses, as a function of the air hydrodynamic flow regime. It was found a very good correlation of the pairs of values corresponding to the same hydrodynamic regime.

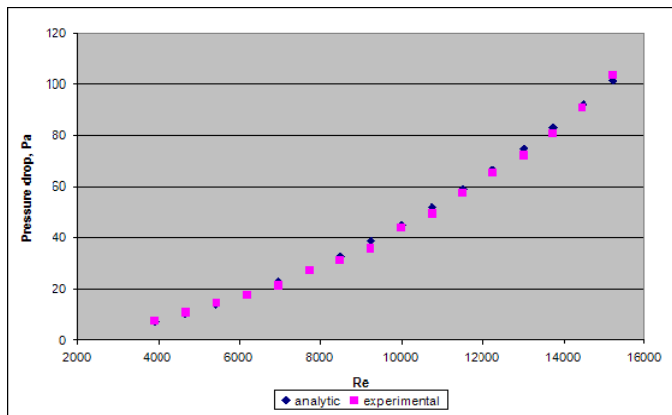


Figure 2. The dependence between the pressure losses and the hydrodynamic regime ($\Delta P = f(Re)$), in the absence of annular baffles

In Table 1 are presented the equations which show the dependence $\Delta P = f(Re)$. It was observed that in all cases the exponent of Re tends to 2, suggesting the correlation with the dynamic pressure $\Delta P_{din} = \rho \cdot w^2 / 2$.

Table 1. The dependence $\Delta P = f(Re)$ for annular baffles

Number of annular baffles and their step	Equation $\Delta P = f(Re)$	r^2
-	$0.85 \cdot 10^{-6} \cdot Re^{1.98}$	0.9984
4 ($l = 600/4 = 150 \text{ mm}$)	$0.28 \cdot 10^{-6} \cdot Re^{2.13}$	0.9992
8 ($l = 600/8 = 75 \text{ mm}$)	$1.56 \cdot 10^{-6} \cdot Re^{2.00}$	0.9955
12 ($l = 600/12 = 50 \text{ mm}$)	$3.70 \cdot 10^{-6} \cdot Re^{1.93}$	0.9995

In Fig. 3a, b is shown the variation of pressure loss through the inner tube in the presence of spiral type turbulence promoters. To obtain an unified expression for the pressure losses values, it was proceeded to the reporting of the experimentally determined values to the inner tube length.

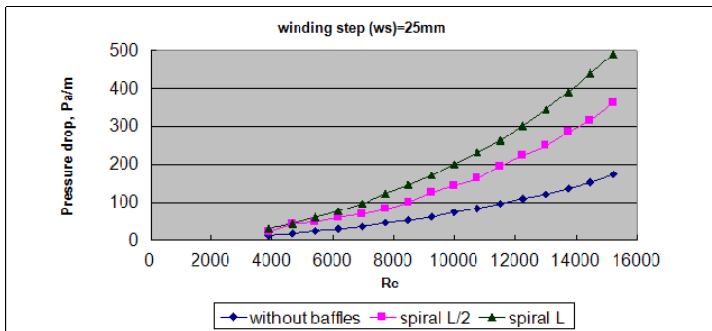


Fig. 3a

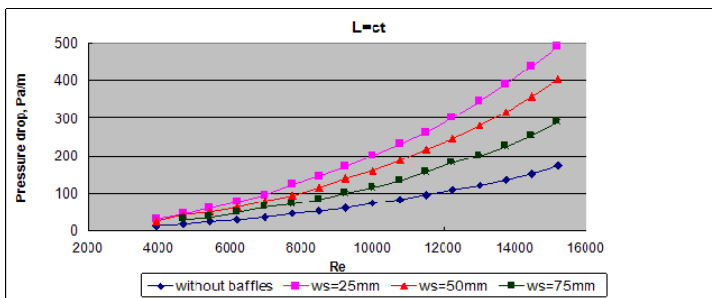


Fig. 3b

Figure 3a,b. The dependence $\Delta P = f(Re)$ for: a) spires with different lengths; b) spires with different winding steps

As you can notice, determinations were made intentionally to higher or less values than 10^4 , to include both turbulent and transient flow. The experimental results lead to different values of the slope of these lines, Table 2.

Table 2. The slope of $\Delta P = f(\text{Re})$ lines

Type of turbulence promoters	Characteristics of promoters	Slope	
		Re<10 ⁴	Re>10 ⁴
Pipe without baffles	-	0.0058	0.0117
Annular baffles	Baffles number		
	4	0.0132	0.0272
	8	0.0208	0.0416
Spire with winding step 25mm	12	0.0281	0.0455
	Spire length		
	L/2	0.0191	0.0433
	L	0.0277	0.0587
Spire with winding step 50mm	L	0.0217	0.0481
Spire with winding step 75mm	L	0.0161	0.0339

Based on these experimental measurements were calculated the ratios between pressure losses caused by the presence of promoters compared with their absence ($\Delta p_i / \Delta p_0$). These results were correlated with the ratios of received heats by the air (Q_i / Q_0) in the same constructive and functional conditions, in order to conclude the overall beneficial effect for heat transfer intensification, Table 3.

Table 3. The average increasing of the received heat and pressure losses in the presence of turbulence promoters

Promoters type	$\Delta p_i / \Delta p_0$		Q_i / Q_0	
	Re<10 ⁴	Re>10 ⁴	Re<10 ⁴	Re>10 ⁴
4 annular baffles	2.09	2.00	1.74	1.70
8 annular baffles	3.24	3.57	2.00	2.24
Spire with length L/2	1.88	2.05	1.48	1.66
Spire with length L	2.62	2.82	1.68	1.75

CONCLUSIONS

It was found the amplification effect due to the increasing of annular baffles number and the decreasing of spire winding step, on the pressure losses. This is illustrated by the upward curves and the increasing slope as a function of the hydrodynamic regime. The increasing of spires length has the same amplifying effect.

The growth ratio of pressure losses is higher than that of the received heats. Thus, for the range $Re \in (1 \div 1.5) \cdot 10^4$, the halving of rings step leads to an increase of 78.5% of the pressure losses compared to a 31.8% increase of the received heats, respectively of partial heat transfer coefficient for air. Instead, to the doubling of the spire length the pressure losses are lower but the received heats decrease substantially (37.6% and 5.4%, respectively).

The intensification of heat transfer needs to be limited by the rapidly increasing of the pressure losses with an unfavorable effect on energy balance.

EXPERIMENTAL SECTION

The heat exchanger used is made of pipes with the following dimensions: the copper inner pipe -diameter $d = 28 \times 1 \text{ mm}$, height $H' = 600 \text{ mm}$, the outer pipe – diameter $D = 49 \times 1.5 \text{ mm}$, height $H = 580 \text{ mm}$. The turbulence promoters of the inner pipe were rings with dimension $25 \times 2 \text{ mm}$ placed at different distances or spires with different winding step and lengths. Both types of promoters were made of copper with $2 \times 2.5 \text{ mm}$ section.

The heat exchanger is vertically positioned. The air enters on the base of the inner pipe where is ensured its flow regulation and measurement. The heat required for the air warming is delivered by the hot water circulating through the annulus and is transmitted through the cylindrical surface of tubular wall. The air temperature was measured with thermometers placed at the top and bottom of the pipe.

The hot water from the annulus is provided by a thermostat and moves upward, being recycled with a rate flow of $0.145 \text{ m}^3 \cdot \text{h}^{-1}$. Its temperature was measured both at the entrance and exit of the annulus, the water cooling has not been greater than 1°C . Determinations were performed at air flow rates from 5 to $20 \text{ m}^3 \cdot \text{h}^{-1}$, leading to mass rates between 3 and $12 \text{ kg} \cdot \text{m}^{-2} \cdot \text{s}^{-1}$.

The pressure loss caused by air flow through the central tube was measured with an inclined-tube manometer.

REFERENCES

1. S.K. Agrawal, "Heat and Mass Transfer", Anshan Limited, Kent, UK, **2005**.
2. J.R. Welty, C.E. Wicks, R.E. Wilson, G.Rorrer, "Fundamentals of Momentum, Heat and Mass Transfer", 4th ed., Wiley&Sons, Inc., **2001**.
3. F. Chiriac, A. Leca, M. Pop, A. Badea, L. Luca, N. Antonescu, D. Peretz, "Procese de transfer de căldură și de masă în instalațiile industriale", Ed. Tehnică, București, **1982**.
4. A. Tamas, M. Vincze, N.A. Ciortan, *Chem.Bull. "POLITEHNICA" Univ. (Timisoara)*, **2011**, 56(70), 1, 52.
5. V. Kumar, V. Shirke, K.D.P. Nigam, *Chem. Eng. J.*, **2008**, 139(2), 284.
6. C.F. Pavlov, P.G. Romankov, A.A. Noskov, "Procese si aparate in ingineria chimica-Exercitii si probleme", Ed. Tehnica, Bucuresti, **1981**.

INVESTIGATION ON THERMODYNAMIC PROPERTIES FOR BINARY SYSTEMS OF WATER + FORMIC, ACETIC, TRICHLOROACETIC, LACTIC, AND CITRIC ACID AT T = 292.15 K AND ATMOSPHERIC PRESSURE

FARDAD KOOHYAR^{a,*}, HASAN GHASEMNEJAD-BOSRA^a,
MEYSAM SHARIFIRAD^b

ABSTRACT. Thermodynamic properties (viscosities, refractive indices, and densities) for aqueous solutions of formic acid, acetic acid, trichloroacetic acid, lactic acid, and citric acid have been measured at $T = 292.15$ K and atmospheric pressure. The measurements were carried out over the whole range of composition. Investigations on these thermodynamic data help us to better understanding of interaction between solvent and solute molecules in these aqueous solutions. Also from these data, for aqueous solution of formic acid and acetic acid the excess molar volumes, viscosity deviations, and change of refractive indices on mixing were calculated and fitted to the Redlich-Kister polynomial equation to estimate the adjustable parameters and the standard errors. Also for aqueous solutions of this study the experimental values of refractive index and viscosity were correlated using the experimental equation and Jones-Dole equation, respectively.

Key words: *Viscosity, Refractive index, Jones-Dole equation, Density, Excess molar volume.*

INTRODUCTION

The study on thermodynamic properties of liquid mixtures and solutions finds direct applications in food, drug, cosmetic and detergent industries [1]. Also, investigations on the thermodynamic properties of binary liquid mixtures have been done to gain information about intermolecular interaction and change in packing efficiencies with compositions [2-4].

There are two prevailing methods for the production of organic acids: fermentation and chemical synthesis. From the viewpoint of sustainable development and human health, the former is preferred to produce the organic acids which are metabolic intermediates or products.

^a Department of Chemistry, Faculty of Science, Babol Branch, Islamic Azad University, Babol, Iran

^b Department of Chemistry, Teacher Research Bojnord, Iran

* Corresponding Author: FardadKoohyar@yahoo.com

Formic acid is an important intermediate in chemical synthesis and occurs naturally, most notably in the venom of bee and ant stings. Owing to its tendency to hydrogen-bond, gaseous formic acid does not obey the ideal gas law [5].

Acetic acid can be extracted from vegetable wastes and found in many manufacturing processes as both a product and precursor for such products as acetate plastic, acetic anhydride, ester solvent, vinegar, and aspirin [6-8].

Trichloroacetic acid is an analogue of acetic acid in which the three hydrogen atoms of the methyl group have all been replaced by chlorine atoms. It is widely used in biochemistry for the precipitation of macromolecules such as proteins, DNA and RNA.

Citric acid is the most widely used organic acid in the field of foods and pharmaceuticals. It is used as an acidulating agent in beverages, confectioneries, in pharmaceutical syrups, elixirs, in effervescent powders and tablets, to adjust the pH of food [9]. It is generally produced by surface or submerged fungal fermentation mainly with *Aspergillus niger*. However, the highest citric acid production has been obtained with the submerged fermentation method [10].

Lactic acid is an important organic acid that is used in various clinical, food and non-food applications [11]. Both fermentation and chemical synthesis are used for producing lactic acid. Lactic acid is of particular interest as a starting material for producing biodegradable poly (lactic acid) plastics [12,13]. A substantial commercial interest exists in producing these plastics from renewable resources such as starch-derived glucose via fermentation, because of increasing emphasis on sustainable production processes [14].

As seen in above phrases, organic acids (and their binary aqueous solutions) have been widely used in foods, fruit and beverages, pharmaceuticals, dental, cosmetics, detergents, plastics, resins, and other biochemical or chemical products [15-20], and thus have a close relationship with human's daily life. Therefore, study on the thermodynamic properties of aqueous solutions of organic acids can be used in the various fields of industry and research.

Also, strong hydrogen bonds can be formed between solute (formic, acetic, trichloroacetic, lactic, and citric acid) and solvent (water) molecules due to their $-OH$ groups. Hydrogen bonding has key role for dissolving the acids in water. Hydrogen bonded systems are very interesting because hydrogen bonds play a vital role in chemical, physical, and biological processes and all of the substrates in this study have strong hydrogen bonds [21].

In this work, we have measured densities (ρ), refractive indices (n_D), and dynamic viscosities (η) for aqueous solution of trichloroacetic acid, lactic acid, and citric acid, also densities (ρ), refractive indices (n_D), dynamic viscosities (η), viscosity deviations ($\Delta\eta$), excess molar volumes (V^E), and change of refractive indices on mixing (Δn_D) for aqueous solution of formic acid and acetic acid at 292.15 K and over entire mole fractions.

RESULTS AND DISCUSSION

The experimental data on densities (ρ), refractive indices (n_D), dynamic viscosities (η), excess molar volumes (V^E), viscosity deviations ($\Delta\eta$), and change of refractive indices on mixing (Δn_D) for aqueous solutions of formic acid and acetic acid at 292.15 K are listed in Table 1. Also, the densities (ρ), refractive indices (n_D), and dynamic viscosities (η) for aqueous solutions of trichloroacetic acid, lactic acid, and citric acid at 292.15 K are listed in Table 2.

It is clear that the density, viscosity, and refractive index at experimental temperature increase as the mole fraction of solutions increases. One of the reasons for this effect can be increasing of the interaction between solute and solvent molecules in solution due to increasing of the number of solute molecules.

Table 1. Densities (ρ), viscosities (η), refractive indices (n_D), excess molar volumes (V^E), viscosity deviations ($\Delta\eta$), and change of refractive indices on mixing (Δn_D) for different aqueous solutions at $T = 292.15$ K as a function of mole fractions (x_2)

Water (1) + Formic acid (2)								
$c_2(\text{mol.L}^{-1})$	x_1	x_2	$\rho(\text{g.cm}^{-3})$	$\eta(\text{mPa.s})$	n_D	$V^E(\text{cm}^3.\text{mol}^{-1})$	$\Delta\eta(\text{mPa.s})$	Δn_D
0.2749	0.9950	0.0050	1.0009	1.0163	1.3335	-0.0107	0.0098	0.0003
0.8192	0.9850	0.0150	1.0071	1.0310	1.3350	-0.0409	0.0167	0.0014
1.8774	0.9650	0.0350	1.0186	1.0593	1.3375	-0.0911	0.0294	0.0032
3.3915	0.9350	0.0650	1.0346	1.0991	1.3410	-0.1574	0.0457	0.0055
5.2798	0.8950	0.1050	1.0537	1.1479	1.3450	-0.2286	0.0633	0.0080
7.0323	0.8550	0.1450	1.0706	1.1926	1.3490	-0.2829	0.0767	0.0104
8.6586	0.8150	0.1850	1.0856	1.2339	1.3515	-0.3226	0.0867	0.0114
10.1671	0.7750	0.2250	1.0987	1.2729	1.3540	-0.3447	0.0945	0.0124
11.5687	0.7350	0.2650	1.1104	1.3103	1.3565	-0.3558	0.1006	0.0133
12.8680	0.6950	0.3050	1.1209	1.3468	1.3585	-0.3577	0.1059	0.0138
13.4935	0.6750	0.3250	1.1258	1.3650	1.3595	-0.3568	0.1084	0.0140
14.3834	0.6450	0.3550	1.1327	1.3926	1.3605	-0.3519	0.1126	0.0139
15.2316	0.6150	0.3850	1.1393	1.4209	1.3615	-0.3475	0.1175	0.0137
15.7759	0.5950	0.4050	1.1436	1.4402	1.3620	-0.3461	0.1211	0.0134
16.5639	0.5650	0.4350	1.1499	1.4702	1.3630	-0.3304	0.1277	0.0133

Water (1) + Acetic acid (2)								
$c_2(\text{mol.L}^{-1})$	x_1	x_2	$\rho(\text{g.cm}^{-3})$	$\eta(\text{mPa.s})$	n_D	$V^E(\text{cm}^3.\text{mol}^{-1})$	$\Delta\eta(\text{mPa.s})$	Δn_D
0	1.0000	0.0000	0.9980	1.0026	1.3330	0	0	0
0.5445	0.9900	0.0100	1.0029	1.0682	1.3355	-0.0617	0.0634	0.0021
1.5988	0.9695	0.0305	1.0113	1.1988	1.3390	-0.1673	0.1895	0.0048
3.1194	0.9370	0.0630	1.0228	1.3919	1.3460	-0.3224	0.3754	0.0106
4.2971	0.9090	0.0910	1.0311	1.5459	1.3505	-0.4432	0.5233	0.0140
5.4419	0.8790	0.1210	1.0387	1.6990	1.3545	-0.5621	0.6697	0.0168
6.5102	0.8480	0.1520	1.0450	1.8451	1.3585	-0.6666	0.8090	0.0196
7.5372	0.8150	0.1850	1.0506	1.9880	1.3620	-0.7666	0.9446	0.0219

8.6484	0.7750	0.2250	1.0558	2.1444	1.3650	-0.8659	1.0922	0.0233
9.5641	0.7380	0.2620	1.0595	2.2730	1.3675	-0.9417	1.2127	0.0244
10.4715	0.6970	0.3030	1.0626	2.3975	1.3700	-1.0098	1.3281	0.0253
11.1098	0.6650	0.3350	1.0643	2.4814	1.3715	-1.0489	1.4050	0.0256
11.5810	0.6395	0.3605	1.0654	2.5397	1.3730	-1.0754	1.4577	0.0261
12.2835	0.5980	0.4020	1.0667	2.6175	1.3740	-1.1076	1.5263	0.0255
13.0381	0.5480	0.4520	1.0676	2.6824	1.3755	-1.1301	1.5802	0.0251
--	0.4640 ^a	0.5360	1.0679	2.7154	1.3765	-1.1321	1.5947	0.0229
--	0.3295 ^a	0.6705	1.0657	2.5221	1.3770	-1.0306	1.3718	0.0182
--	0.2420 ^a	0.7580	1.0627	2.2601	1.3765	-0.8832	1.0905	0.0143
--	0.1450 ^a	0.8550	1.0581	1.8811	1.3745	-0.6350	0.6901	0.0086
--	0.0000 ^a	1.0000	1.0476	1.2229	1.3715	0	0	0

^a: In these mole fractions, acetic acid is solvent and water is solute.

Table 2. Densities (ρ), viscosities (η) and refractive indices (n_D) for different aqueous solutions at $T = 292.15$ K as a function of mole fractions (x_2)

Water (1) + Trichloroacetic acid (2)

c_2 (mol.L ⁻¹)	x_1	x_2	ρ (g.cm ⁻³)	η (mPa.s)	n_D
0.2723	0.9950	0.0050	1.0203	1.1041	1.3390
0.5346	0.9900	0.0100	1.0399	1.2196	1.3440
0.7869	0.9850	0.0150	1.0589	1.3348	1.3485
1.0303	0.9800	0.0200	1.0773	1.4495	1.3530
1.2651	0.9750	0.0250	1.0949	1.5640	1.3575
1.4905	0.9700	0.0300	1.1110	1.6781	1.3615
1.7100	0.9650	0.0350	1.1283	1.7919	1.3655
1.9210	0.9600	0.0400	1.1438	1.9055	1.3695
2.1245	0.9550	0.0450	1.1589	2.0187	1.3730
2.3210	0.9500	0.0500	1.1732	2.1315	1.3765
2.5104	0.9450	0.0550	1.1868	2.2440	1.3797
2.6936	0.9400	0.0600	1.1999	2.3562	1.3830
2.8699	0.9350	0.0650	1.2122	2.4682	1.3855
3.0403	0.9300	0.0700	1.2239	2.5797	1.3880
3.2038	0.9250	0.0750	1.2348	2.6910	1.3905
3.3615	0.9200	0.0800	1.2452	2.8019	1.3930
3.5134	0.9150	0.0850	1.2549	2.9125	1.3950
3.6588	0.9100	0.0900	1.2638	3.0228	1.3970
3.7989	0.9050	0.0950	1.2722	3.1328	1.3985
3.9331	0.9000	0.1000	1.2799	3.2424	1.4000

Water (1) + Lactic acid (2)

0.2725	0.9950	0.0050	1.0026	1.0067	1.3360
0.5379	0.9900	0.0100	1.0080	1.1018	1.3380
0.8464	0.9840	0.0160	1.0141	1.2132	1.3405
1.2197	0.9760	0.0240	1.0221	1.3579	1.3440
1.4344	0.9720	0.0280	1.0259	1.4289	1.3455
1.6684	0.9670	0.0330	1.0307	1.5166	1.3475

INVESTIGATION ON THERMODYNAMIC PROPERTIES FOR BINARY SYSTEMS ...

1.8961	0.9620	0.0380	1.0352	1.6036	1.3495
2.1613	0.9560	0.0440	1.0404	1.707	1.3520
2.4191	0.9500	0.0500	1.0455	1.8102	1.3540
3.5946	0.9200	0.0800	1.0682	2.3347	1.3640
4.2877	0.9000	0.1000	1.0812	2.7100	1.3695
5.0687	0.8750	0.1250	1.0955	3.2326	1.3760
6.1511	0.8350	0.1650	1.1146	4.2484	1.3845
7.1721	0.7900	0.2100	1.1319	5.7484	1.3925
7.7618	0.7600	0.2400	1.1417	7.0047	1.3975
8.2901	0.7300	0.2700	1.1504	8.4923	1.4010
8.7664	0.7000	0.3000	1.1580	10.2274	1.4050
9.2033	0.6700	0.3300	1.1655	12.2207	1.4080
9.5977	0.6400	0.3600	1.1718	14.4772	1.4110
9.9566	0.6100	0.3900	1.1773	16.9966	1.4135
10.2805	0.5800	0.4200	1.1817	19.7729	1.4160
10.4762	0.5600	0.4400	1.1838	21.7612	1.4170

Water (1) + Citric acid (2)

0.0505	0.9990	0.0010	1.0026	1.0321	1.3340
0.1498	0.9970	0.0030	1.0119	1.0840	1.3370
0.2472	0.9950	0.0050	1.0210	1.1399	1.3400
0.3428	0.9930	0.0070	1.0299	1.2000	1.3430
0.4363	0.9910	0.0090	1.0385	1.2643	1.3455
0.5286	0.9890	0.0110	1.0469	1.3330	1.3480
0.6189	0.9870	0.0130	1.0550	1.4061	1.3505
0.7071	0.9850	0.0150	1.0630	1.4837	1.3525
0.7941	0.9830	0.0170	1.0708	1.5660	1.3550
0.8789	0.9810	0.0190	1.0783	1.6530	1.3575
0.9624	0.9790	0.0210	1.0858	1.7448	1.3600
1.0443	0.9770	0.0230	1.0930	1.8416	1.3620
1.1246	0.9750	0.0250	1.1001	1.9434	1.3640
1.2035	0.9730	0.0270	1.1070	2.0504	1.3660
1.2810	0.9710	0.0290	1.1139	2.1625	1.3685
1.3573	0.9690	0.0310	1.1206	2.2801	1.3705
1.4319	0.9670	0.0330	1.1271	2.4030	1.3725
1.5055	0.9650	0.0350	1.1336	2.5315	1.3745

The values of V^E for aqueous solution of formic acid and acetic acid were calculated from the density data using the following equation [22]:

$$V^E = (x_1M_1 + x_2M_2)/\rho - (x_1M_1/\rho_1 + x_2M_2/\rho_2) \quad (1)$$

In this equation x_1, x_2 are mole fractions. M_1, M_2 are the molar masses. ρ_1, ρ_2 are the densities of pure components 1, 2 respectively.

The change of refractive index on mixing (Δn_D) for aqueous solution of formic acid and acetic acid was calculated from following equation [23]:

$$\Delta n_D = n_D - (x_1n_{D1} + x_2n_{D2}) \quad (2)$$

In this equation n_D , n_{D1} , n_{D2} are the refractive index of mixture, pure components 1, 2 respectively.

The viscosity deviation ($\Delta\eta$) for aqueous solution of formic acid and acetic acid was calculated from following equation [24]:

$$\Delta\eta = \eta - (x_1\eta_1 + x_2\eta_2) \quad (3)$$

where η , η_1 , η_2 are the viscosity of mixture, pure components 1, 2 respectively.

The values of excess properties for aqueous solutions were fitted to the Redlich-Kister polynomial equation [25]:

$$Y = x_1(1 - x_1) \sum_{i=0}^n A_i (2x_1 - 1)^i \quad (4)$$

where $Y = V^E$ or Δn_D or $\Delta\eta$, A_i are adjustable parameters, and x_1 is the mole fraction of component 1.

For aqueous solutions of this study the values of these parameters, A_i , along with the standard errors, σ , are listed in Table 3.

Table 3. Coefficients of the Redlich-Kister equation and standard deviations for excess molar volumes, viscosity deviations, and change of refractive indices on mixing for different aqueous solutions at $T = 292.15$ K

Water (1) + Acetic acid (2)					
property	A_0	A_1	A_2	A_3	σ
V^E (cm ³ .mol ⁻¹)	-4.5818	0.3676	-0.8267	-0.8898	0.0140
$\Delta\eta$ (mPa.s)	6.5422	-0.1647	-2.4861	2.6762	0.0258
Δn_D	0.0954	0.0426	0.0302	0.0292	0.0002
Water (1) + Formic acid (2)					
property	A_0	A_1	A_2	A_3	σ
V^E (cm ³ .mol ⁻¹)	-1.6706	4.3653	-15.2023	10.7156	0.0102
$\Delta\eta$ (mPa.s)	0.5442	0.0219	-0.9119	1.4238	0.0045
Δn_D	0.0513	0.0392	-0.0280	0.0491	0.0003

In each case, the optimum number of coefficients A_i was determined from an examination of the variation of the standard deviation [26]:

$$\sigma(Y) = [\sum(Y_{cal} - Y_{exp})^2 / (n - m)]^{(1/2)} \quad (5)$$

where n is the total number of experimental values and m is the number of parameters.

Most studies on viscosity are confined to the description of dilute solutions of solutes via determination of the A - and B -coefficients in the Jones-Dole equation [27]:

$$\frac{\eta}{\eta_0} = 1 + Ac^{1/2} + Bc \quad (6)$$

In this equation c , η , and η_0 are the molar concentration of solution, viscosities of solution, and solvent respectively. Values of the fitted parameters A and B are listed in Table 4.

Table 4. Values of constants A , B , coefficient of determination R^2 (according of Eq 6), and standard deviations σ for different aqueous solutions at $T = 292.15$ K

systems	$A(\text{L}^{1/2} \cdot \text{mol}^{-1/2})$	$B(\text{L} \cdot \text{mol}^{-1})$	R^2	σ
Formic acid + water	-0.0274	0.0331	0.9976	0.0054
Acetic acid + water	-0.0561	0.1473	0.9990	0.0040
Trichloroacetic acid + water	-0.4762	0.7606	0.9986	0.0364
Lactic acid + water	-3.2774	0.1202	0.9970	0.3486
Citric acid + water	-1.5152	1.8882	0.9970	0.0450

The values of refractive index for aqueous solutions can be fitted by following experimental equation [28]:

$$n_D = A_n m + n_{D(c)}^* \quad (7)$$

where m is the molar concentration of the aqueous solution, $n_{D(c)}^*$ is the refractive index of solvent (water) and A_n is an experimental parameter that depends on physical and chemical properties of solute molecules such as molecular weight, polarity, electrical charge, and shape.

For mixtures of this study, the values of A_n , n_D^* and relative deviations between the experimental values of n_D^* (in literatures) [25], and calculated values of n_D^* from Eq. (6) at different temperatures are listed in Table 5.

Table 5. Values of constants A_n and n_D^* (according of Eq 7) and relative deviations $RD(n_D^*)$ for different aqueous solutions at $T = 292.15$ K

systems	$M_{\text{solute}}(\text{g} \cdot \text{mol}^{-1})$	$A_n(\text{L} \cdot \text{mol}^{-1})$	n_D^*	R^2	$RD(\text{for } n_D^*)$
Formic acid + water	46.03	0.0018	1.3346	0.9896	0.0012
Acetic acid + water	60.05	0.0033	1.3351	0.9889	0.0016
Trichloroacetic acid + water	163.38	0.0169	1.3360	0.9966	0.0023
Lactic acid + water	90.08	0.0080	1.3344	0.9995	0.0011
Citric acid + water	192.12	0.0275	1.3332	0.9996	0.0002

The relative deviations (RD) for n_D^* were calculated according to following equation:

$$RD = \left| \frac{n_D^* - n_{D(c)}^*}{n_D^*} \right| \quad (8)$$

where $n_{D(c)}^*$ is the calculated value of refractive index of water from Eq. (7) and n_D^* is the experimental value of refractive index of water (in literature) at same temperature.

The values of thermodynamic properties for solutions of this study can be dependent on two factors. The first factor is the molar concentration of solute in mixture. As seen in Tables 1 and 2 (also in figures 1 and 2), the thermodynamic properties for solution of this study increase as the molar concentration (or mole fraction) of solutes increases. The second factor is the strength of bonds between solvent and solute molecules due to the values of polarity (dipole-dipole interaction and the H-bonds) and electrical charge of solute molecules. In aqueous solutions of organic acids, the type and form of group (or groups) that attached to carbon (in COOH) can be effective on the strength of bonds between solvent and solute molecules. In some cases one factor outbalances another and in some cases both factors are effective. The second factor is important in excess thermodynamic properties (especially in most important of these properties: excess molar volumes) [29].

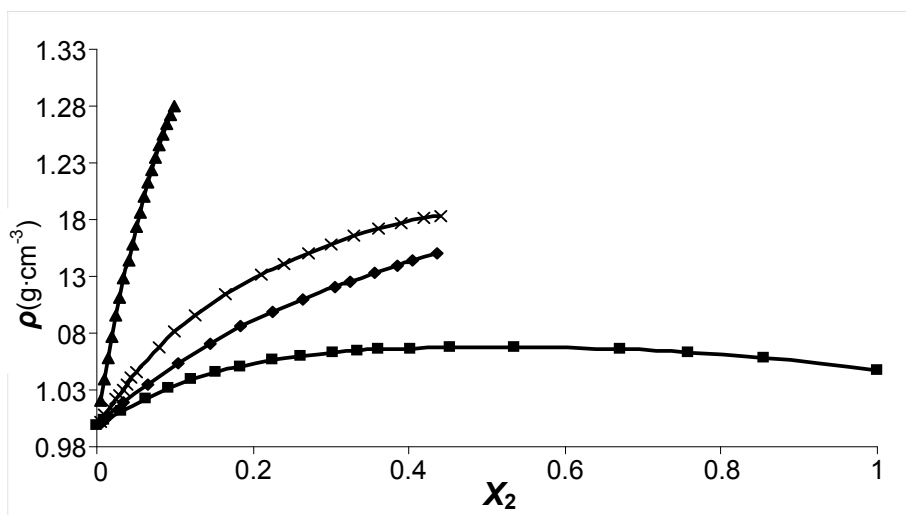


Figure 1. Densities (ρ) plotted against mole fraction of solute (x_2) at $T = 292.15$ K for different aqueous solutions of: ◆, formic acid; ■, acetic acid; ▲, trichloroacetic acid; ×, lactic acid.

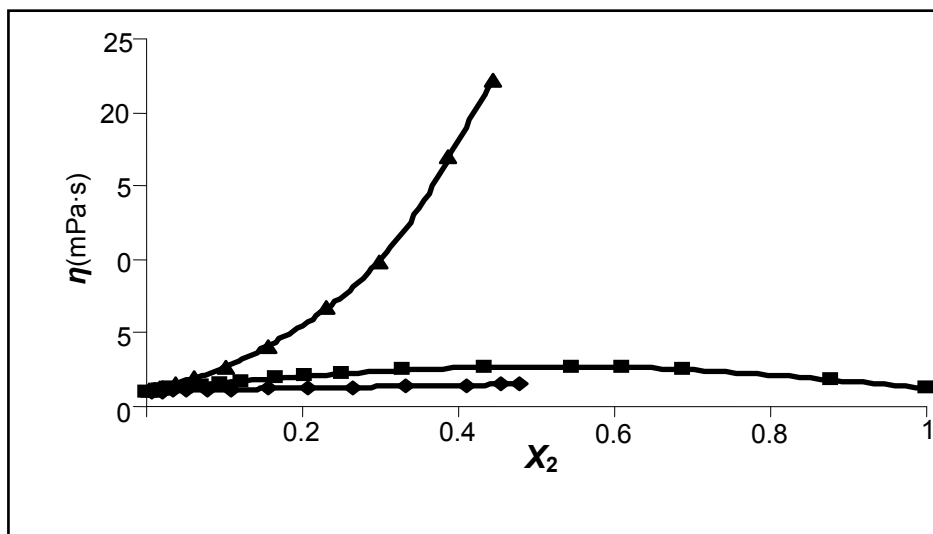


Figure 2. Viscosities (η) plotted against mole fraction of solute (x_2) at $T = 292.15$ K for different aqueous solutions of: \blacklozenge , formic acid; \blacksquare , acetic acid; \blacktriangle , lactic acid.

For mixtures of this study the maximum value of refractive index and viscosity is observed for (lactic acid + water). In this case both factors are effective due to high molar concentration of solution ($10.5213 \text{ mol}\cdot\text{L}^{-1}$) and electron acceptor effect of oxygen in (OH).

Also the maximum value of density is observed for (trichloroacetic acid + water). In this case the second factor exceeds first factor due to more electron acceptor effect of Cl than oxygen atom in (OH).

It can be summarized that V^E values may be affected by three factors. The first factor is the interaction among molecules, such as the formation of hydrogen bonds or of charge transfer complexes. The positive excess molar volumes for the solution can be a result of the breaking of the H-bonds (weaker hydrogen bonds) and complexes between solvent and solute. Forming hydrogen bonds (stronger H-bonds) and complexes bring negative values of excess molar volumes. The second factor is the physical intermolecular forces, including electrostatic forces between charged particles and between permanent dipoles, induction forces between a permanent dipole and an induced dipole, and forces of attraction (dispersion forces) and repulsion between nonpolar molecules. Physical intermolecular forces are usually weak, and the sign of V^E values may be positive or negative, but the absolute values are small. The third factor is the structural characteristics of the component, arising from geometrical fitting of one component into the other's structure,

due to the differences in shape and size of component and free volume. Similar to the excess molar volumes, viscosity deviations are related to the molecular interaction between the components of mixtures as well as to the size and shape of molecules. Positive values of $\Delta\eta$ are indicative of strong interactions whereas negative values indicate weaker interactions [30,31].

As seen in figures 3 and 4, for aqueous solution of formic acid and acetic acid over the entire ranges of mole fractions the values of V^E are negative and also, the values of $\Delta\eta$ and Δn_D are positive at 292.15 K. In these solutions the forces between solute and solvent molecules (formic acid-water and acetic acid-water) are dipole-ionic while there are hydrogen bonds between molecules in pure compounds of these solutions. Ionic-dipole bond (the bond between CH_3COO^- and H_2O also, HCOO^- and H_2O) is stronger than hydrogen bond. Also, the molecules in these solutions are closer together (as compared with acetic acid and formic acid) due to the smaller size of solvent molecules (water) than solute molecules (formic acid and acetic acid). Therefore, interaction between molecules in these solutions is stronger than between pure components. In this case, the first factor and third factor (the structural characteristics of the component, arising from geometrical fitting of one component into the other's structure) are very effective [32].

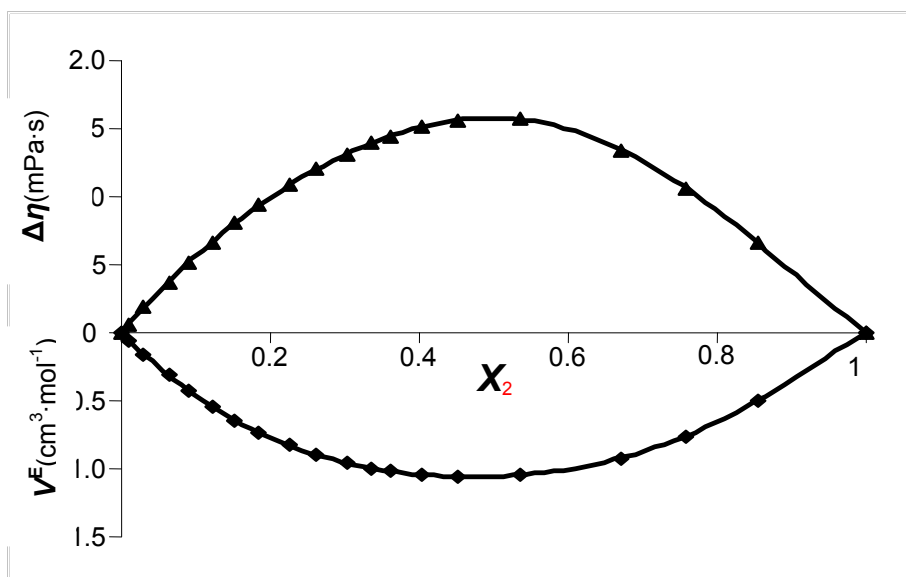


Figure 3. Viscosity deviations (\blacktriangle) and excess molar volumes (\blacklozenge) plotted against mole fraction of acetic acid (x_2) for aqueous solutions of acetic acid at $T = 292.15$ K.

better interaction between solvent-solute molecules in aqueous solution of acetic acid than in aqueous solution of formic acid.

It is clear that according to Table 1 for aqueous solution of acetic acid the minimum and maximum value of V^E and $\Delta\eta$ appears at $x_{\text{acetic acid}} \approx 0.4520$ and 0.5360 , respectively. Also, the maximum value of Δn_D appears at $x_{\text{acetic acid}} \approx 0.3605$.

As can be seen from the Table 5, the values of A_n depend on molecular weight of solute. In solutions of this study, the values of A_n increase as the molecular weight of solute increases.

Also a linear relation between refractive index and molar concentration is observed in figure 5. In addition, all these linear diagrams (n_D vs c) have the high R^2 ($R^2 \approx 0.999$).

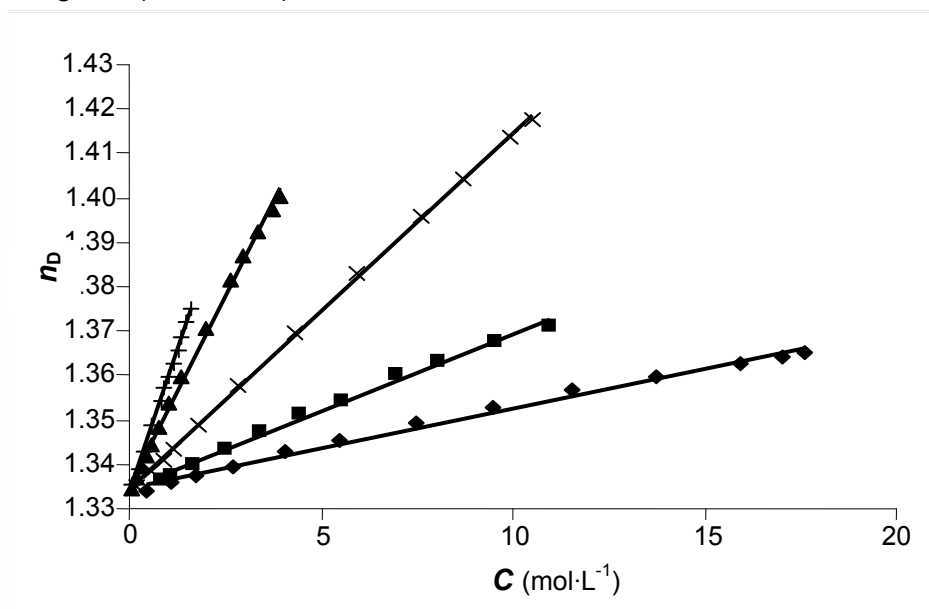


Figure 5. Refractive indices (n_D) plotted against molar concentration of solute (c) at $T = 292.15$ K for different aqueous solutions of: \blacklozenge , formic acid; \blacksquare , acetic acid; \blacktriangle , trichloroacetic acid; \times , lactic acid; $+$, citric acid.

CONCLUSIONS

Experimental viscosities, densities, and refractive indices at 292.15 K data were obtained for (acetic acid + water), (citric acid + water), and (lactic acid + water) over a wide range of composition. From the experimental viscosities, densities and refractive indices, values of viscosity deviations, excess molar volumes and change of refractive indices on mixing for solutions of this study were calculated.

It was found that for binary mixture of (acetic acid + water) all these calculated quantities for change of refractive indices on mixing and viscosity deviations are positive while these calculated quantities for excess molar volumes are negative. The Redlich-Kister polynomial equation was applied successfully for the correlation of V^E , $\Delta\eta$, and Δn_D .

EXPERIMENTAL

Materials

Formic acid, acetic acid, trichloroacetic acid, lactic acid, and citric acid were supplied from Fluka Company. The purity of trichloroacetic acid, lactic acid, and citric acid was 98% and purity of formic acid and acetic acid was 99%. These substances are used without further purification. All dilute solutions were prepared with double-distilled water. Binary mixtures were prepared by known masses of each liquid in air-tight stoppered glass bottles.

Apparatus and procedure

The mass measurements were made on a single pan Mettler balance to an accuracy of ± 0.0001 g. No buoyancy corrections were applied. The possible error in mole fraction is calculated to be less than $\pm 1 \times 10^{-4}$.

Density (ρ) measurements of pure components and binary mixtures over the possible composition range were carried out using a digital vibrating glass tube densimeter (DA-500E, China.). Densities were determined with the uncertainty of ± 0.0001 g·cm⁻³. It was calibrated with double distilled water and air.

The kinematic viscosity was measured with Ubbelohde viscometers with a Schott-Geräte automatic measuring unit model AVS400 provided with a transparent thermostat, which allows temperature stabilization with a tolerance of 0.01 K. Four Ubbelohde tubs with different capillary size (0.36, 0.46, 0.53 and 0.63 mm) were used in the experiments according to the different viscosity values of the mixtures. The calibration was carried out with double distilled water and glycerol (60% w/v). The uncertainty of the viscosity measurement was 0.0001 mPa.s. All of the experiments are repeated three times and then reported the average values. Refractive indices for the sodium D-line (n_D) were measured with an Abbe refractometer (CARL ZEISS, Model A, Germany). A minimum of three independent readings were taken for each composition. The densities, viscosities and refractive indices of pure formic acid, acetic acid, and water were measured by these apparatus at $T = 292.15$ K. The uncertainties of the refractive index and viscosity are $\pm 1 \times 10^{-4}$. Also the uncertainty of the temperature is ± 0.01 K.

REFERENCES

1. M. Kondaiah, D. S. Kumar, K. Sreekanth, D. Krishna Rao, *Journal of Chemical Thermodynamics*, **2011**, *43*, 1850.
2. B. Sathyanarayana, B. Ranjithkumar, T. Savitha Jyostna, N. Satyanarayana, *Journal of Chemical Thermodynamics*, **2007**, *39*, 16.
3. B. Ranjith Kumar, P. Murali Krishna, B. Sathyanarayana, N. Satyanarayana, *Journal of Chemical & Engineering Data*, **2008**, *53*, 2403.
4. P. Murali Krishna, B. Ranjith Kumar, B. Sathyanarayana, K. Jyothi Amara, N. Satyanarayana, *Journal of Pure & Applied Physics*, **2009**, *47*, 576.
5. R. M. Balabin, *Journal of Physical Chemistry, A*, **2009**, *113*, 4910.
6. R. Hattori, K. Yamada, M. Kikuchi, S. Hirano, N. Yoshida, *Journal of Agricultural & Food Chemistry*, **2011**, *59*, 9049.
7. F. Jin, Y. Watanabe, A. Kishita, H. Kishida, H. Enomoto, *Journal of Physics.: Conference Series.*, **2008**, *128*, 1.
8. O.Z. Vogt, E.L. Vogt, W. J. Charyasz, *Polish Journal of Chemical Technology*, **2009**, *11*, 55.
9. K. Zarei, M. Atabati, N. Karimian, *Indian Journal of Chemical Technology*, **2007**, *14*, 417.
10. A. Koparan, A. Guvenc, N. Kapucu, U. Mehmetoglu, A. Calimli, *Turkish Journal of Chemistry*, **2001**, *25*, 477.
11. S. Kowalik, W. Kedzierski, *Polish Journal of Veterinary Sciences*, **2011**, *14*, 373.
12. N. Narayanan, P.K. Roychoudhury, A. Srivastava, *Electronic Journal of Biotechnology*, **2004**, *7*: No 2 (DOI: 10.2225/vol7-issue2-fulltext-7).
13. R. Mehta, V. Kumar, H. Bhunia, S.N. Upadhyay, *Polymer Review C45*, **2005**, *4*, 325.
14. M. Gavrilescu, Y. Chisti, *Biotechnology Advances*, **2005**, *23*, 471.
15. H. Takahashi, K. Ohba, K.I. Kikuchi, *Biochemical Engineering Journal*, **2003**, *16*, 315.
16. H. Takahashi, K. Ohba, K.I. Kikuchi, *Journal of Membrane Science*, **2003**, *222*, 103.
17. C.E. Carpenter, J.R. Broadbent, *Journal of Food Sciences*, **2009**, *74*, 12.
18. A.C.F. Ribeiro, V.M.M. Lobo, D.G. Leaist, J.J.S. Natividade, L.P. Verissimo, M.C.F. Barros, A.M.T.D.P.V. Cabral, *Journal of Solution Chemistry*, **2005**, *34*, 1016.
19. B.G. Green, J. Lim, F. Osterhoff, K. Blacher, D. Nachtigal, *Physiology & Behavior*, **2010**, *101*, 731.
20. T. Umecky, T. Kuga, T. Funazukuri, *Journal of Chemical & Engineering Data*, **2006**, *51*, 1705.
21. E. Zorebski, B. Lubowiecka, *Journal of Chemical Thermodynamics*, **2009**, *41*, 197.
22. A.K. Nain, R. Sharma, A. Ali, *Journal of Molecular Liquids*, **2011**, *158*, 139.
23. A.B. Pereiro, A. Rodriguez, *Journal of Chemical & Engineering Data*, **2007**, *52*, 600.

24. S. Aznarez, M.M.E.F. de Ruiz Holgado, E.L. Arancibia, *Journal of Molecular Liquids*, **2006**, 124, 78.
25. D.R. Chiou, S.Y. Chen, L.J. Chen, *Journal of Chemical & Engineering Data*, **2010**, 55, 1012.
26. A.F. Ribeiro, E. Langa, A.M. Mainar, J.I. Pardo, J.S. Urieta, *Journal of Chemical & Engineering Data*, **2006**, 51, 1846.
27. H. Shekaari, F. Jebali, *Journal of Chemical & Engineering Data*, **2010**, 55, 2517.
28. F. Koohyar, A.A. Rostami, M.J. Chaichi, F. Kiani, *Journal of Solution Chemistry*, **2011**, 40, 1361.
29. M.V. Rathnam, R.K.R. Singh, *Journal of Chemical & Engineering Data*, **2008**, 53, 265.
30. C. Yang, H. Lai, Z. Liu, P. Ma, *Journal of Chemical & Engineering Data*, **2006**, 51, 1345.
31. C. Yang, W. Xu, P. Ma, *Journal of Chemical & Engineering Data*, **2004**, 49, 1794.
32. A.J. Treszczanowicz, O. Kiyohara, G.C. Benson, *Journal of Chemical Thermodynamics*, **1981**, 13, 253.